SLAC-REPORT-299
UC-34D
T/E

A STUDY OF THE STRANGE MESON SPECTRUM AS OBSERVED IN THE REACTION $K^-p \to \bar{K}^0 \pi^+ \pi^- n$ AT 11 GEV/C*

Juha-Pekka Kalervo Sinervo

Stanford Linear Accelerator Center
Stanford University, Stanford, California 94305

May 1986

Prepared for the Department of Energy
under contract number DE-AC03-76SF00515

Printed in the United States of America. Available from the National Technical Information Service, U.S. Department of Commerce, 5285 Port Royal Road, Springfield, Virginia 22161. Price: Printed Copy A12, Microfiche A01.

---

* Ph.D. Dissertation

Abstract

The results of a high statistics study of the reaction $K^- p \to \bar{K}^\circ \pi^+ \pi^- n$ are presented. The data derive from a 4 event/nanobarn exposure of the LASS (Large Aperture Superconducting Solenoid) spectrometer to an 11 GeV/c K^- beam. The $\bar{K}^\circ \pi^+ \pi^- n$ event sample consists of 34 000 events with $\bar{K}^\circ \pi^+ \pi^-$ invariant masses less than 2.4 GeV/c^2 and $|t'| \leq 0.3$ (GeV/c)^2.

The forward-produced $\bar{K}^\circ \pi^+ \pi^-$ events arise predominantly through the production and subsequent strong decay of natural spin-parity strange meson states (J^P=1^-, 2^+, ...). Their production can be understood in the context of an exchange model, while their decay into the $\bar{K}^\circ \pi^+ \pi^-$ final state proceeds through intermediate two-body states such as $K^*(892)^- \pi^+$, $\bar{K}^\circ \rho(770)^\circ$, $K^*(1430)^- \pi^+$, and $\bar{K}^\circ f(1270)^\circ$. A partial wave analysis employing the three-body isobar model successfully describes all of the features of the data.

The J^P=1^+, 2^+, and 3^- partial waves show resonant behavior that is attributed to the production and decay of the 1^+ $Q(1400)$, the 2^+ $K^*(1430)$, and the 3^- $K^*(1780)$. The structure in the 1^- amplitudes can be understood as arising from two vector states, one at ~1.42 GeV/c^2 coupling only to $K^*\pi$ and the other at ~1.73 decaying to both $K^*\pi$ and $K\rho$. The J^P=4^+ waves, required above a mass of 2.0 GeV/c^2, show structure that may arise from the production of the 4^+ $K^*(2060)$. There is a second enhancement in the J^P=2^+ waves at ~2.0 GeV/c^2 that may be evidence for a new resonant state.

The t' dependences of the 2^+, 3^-, and the higher mass 1^- partial waves are steep, whereas the t' dependence of the 1^- amplitude at low mass is shallow. This indicates that the lower mass 1^- state, unlike the other natural spin-parity resonances, does not couple strongly to the $K\pi$ system.

The observed properties of these resonant states can be used to test and further develop models of the strange meson spectrum. The implications of these data for the most successful of these, the non-relativistic quark model, are discussed.

Acknowledgments

The successful completion of the work reported herein was made possible through the efforts of many people. In particular, I would like to thank all of the members of the E-135 collaboration for their painstaking work to ensure that our experiment was a success. All of my collaborators contributed immeasurably to this dissertation, and for this they have my heartfelt gratitude.

David Aston, Bill Dunwoodie, David Leith, and Blair Ratcliff deserve special mention. Their encouragement, support, and guidance have made my graduate school experience particularly rich and rewarding from both a physics and a personal point of view. The invaluable assistance they provided during the preparation of this dissertation served to enhance the final document. Of course, the responsibility for its contents is mine.

Several other people deserve mention as well: Lillian Vasillian, the SLAC Group B secretary who provided an efficient and supportive work environment; Kevin Johnston, Sylvia MacBride, and Terry Anderson, staff in the SLAC illustrations department who drew up the figures with great care and respect for the final product; Paul Kunz, Gerard Oxoby, Mike Gravina, and Quang Trang, the men who built the marvellous computing engines that were essential to my analysis; and all of the other Group B technicians and support personnel without whom the experiment would never have been possible.

My source of greatest inspiration and strength has been my family. The nurturing and love I received from my parents have been the springboard from which I have been able to achieve the goal this dissertation represents, and I am very much in their debt for these gifts. I have to thank my two children, Aviva and Kalervo, who have tolerated my long work hours and absences without recrimination. But finally, I have to acknowledge the love and support of my wife, Pat. She has been the real soldier in the trenches for these last five years, and her patience with and understanding of my own obsession to pursue physics have been completely selfless

and unflagging. This dissertation is dedicated to her; although it bears my name, her contribution is at least as great as mine.

Table of Contents

List of Tables

List of Figures

1. Introduction

By the early 1970's, the known meson and baryon states were qualitatively understood in terms of the allowed quantum numbers predicted by the static quark model involving up, down, and strange quarks. The states could be arranged in SU(3) and SU(6) multiplets, some of which were complete, and the observed decay branching ratios could be described in terms of a small number of coupling constants and mixing angles. In some instances, Regge phenomenology was able to predict the masses and quantum numbers of undiscovered states, but there was no model of the underlying quark-quark interaction that could yield a complete level structure for the hadrons.

In November 1974, meson spectroscopy underwent a revolution with the discovery of the J/Ψ particle.[1,2] This meson was soon identified as the ground state of a charm and anti-charm quark system[3,4] and subsequent investigation revealed an entire family of such states, each having the quantum numbers of the photon, $J^{PC} = 1^{--}$. The spectroscopy of the lowest-lying vector states was quickly uncovered and found to be in good agreement with quark model predictions that employed a naive non-relativistic potential to model the forces between the quark and anti-quark.[5] The more recent discovery of the Υ family has provided another successful test of this quark model. Although it is clear that a potential model approach could only be an approximation to the true situation, it is quite successful in describing the phenomenology of the heavy $q\,\overline{q}$ systems. It also provides a framework within which to test our understanding of what is believed to be a more fundamental description of the strong interaction, namely quantum chromodynamics or QCD.

The systematic study of the heavy-quark mesons in the J/Ψ and Υ families at e^+e^- storage rings has had considerable impact on our understanding of meson states.[6] However, because only vector states can be directly formed in e^+e^- collisions, other excitations of the $q\,\overline{q}$ system have been available for study only as intermediaries in the decays of the heavier vector states. Although many important new discoveries have resulted (*e.g.* the χ, D, D^*, F, $\iota(1440)$, $\theta(1690)$, and $\xi(2260)$ states, to name only a few) certain states are not easily studied in this context. For example, many of the expected meson states corresponding to large $q\,\overline{q}$ orbital

angular momentum excitations are very rarely produced and very few of the light-quark radial recurrences have been observed. Such systems are more copiously produced in fixed target experiments, which therefore play a complementary role in the study of quark spectroscopy.

Knowledge of the masses and widths of the excited mesons provides several important clues to the nature of the forces binding the constituent quarks into hadrons. For example, the mass splittings between triplet states with the same orbital angular momentum (*i.e.* the hyperfine structure) and the splittings of the radial excitations reflect the relative strengths of the terms in the $q\overline{q}$ Lagrangian, so it is important to understand these splittings as a function of both the radial and orbital quantum numbers. Studies of the decays of these excited states are also of considerable value. Since the decay processes are believed to be strongly affected by the $q\overline{q}$ wave function, their variation with the $q\overline{q}$ excited state should yield valuable insights into the dynamics of these systems.

Besides the need to address general questions about meson spectroscopy, there are other reasons to study light-quark meson systems. The speculation that exotic states such as "glueballs" may exist[7] with masses below 2 GeV/c^2 and may mix with the conventional $q\overline{q}$ mesons has increased the need to better understand the spectroscopy of the conventional states. For example, one such glueball candidate, the $\iota(1440)$, can also be interpreted as being a garden-variety $q\overline{q}$ meson[8]; without a precise understanding of the conventional spectroscopy, such ambiguities are difficult to resolve.

The study of light-quark states in production experiments is beset with the problems associated with extracting clear resonance data from the cluttered environment of hadronically-produced systems. Not only is it necessary to have large event samples that are free of contamination, but the unfolding of the resonant structure invariably requires a Partial Wave Analysis, which in addition requires an event sample that is relatively unbiased by acceptance effects. These difficulties are compounded by our poor understanding of the systematics of the excited meson states. The non-relativistic potential models, so successful with the heavy-quark systems, cannot be extended to the light-quark systems without introducing substantial uncertainties. In the charmonium system where a non-relativistic model

appears to work well, typical quark velocities are already about a third of the speed of light; it is difficult to justify applying such a model unaltered in an even more relativistic regime.

Because of these problems, the spectroscopy of the light-quark mesons is still confused, despite the advances made with the heavy meson states. Only three light-quark nonets can be considered complete with well established states: the pseudoscalar nonet comprising the π, K, η, and η'; the vector nonet consisting of the $\rho(770)$, $K^*(892)$, $\phi(1020)$, and $\omega(783)$; and the tensor states, the $A_2(1320)$, $K^*(1430)$, $f(1270)$, and $f'(1525)$. It is important to extend our experimental understanding of mesons so that the systematics can be better understood and new directions for theoretical work established.

These comments notwithstanding, theoretical progress has recently been made in the light-quark meson sector. Several authors have formulated theories that insert the dynamical features expected from QCD into a potential, which they then modify to take into account the relativistic effects in light-quark systems.[9] In particular, Godfrey and Isgur[10] have shown that it is possible to account for the established light and heavy-quark mesons in a theoretical framework that is based on such an approach. Figure 1.1 compares the masses of the strange mesons predicted by Godfrey and Isgur with the experimentally observed states.[11] The figure, known as a Grotrian plot, groups the states according to the quantum numbers predicted by the nonrelativistic quark model. Besides reproducing the spectra of the well-established states, their model has made predictions for the masses and decay rates of the non-leading excited states. A parallel study, employing the dynamics derived by Godfrey and Isgur but introducing an alternative decay model[12] has arrived at even stronger predictions for the decay systematics of these light-quark states. It follows that there now appear to be some credible predictions of the properties of the light-quark mesons.

The strange mesons would appear to be an ideal place to learn about this spectroscopy. Empirically the states tend to be narrower than the corresponding non-strange ones, yielding better signal-to-noise ratios. The expected spectroscopy is simpler for several reasons: (a) the strange mesons have fewer open decay channels compared with the isovector and isoscalar states, which makes the phenomenological

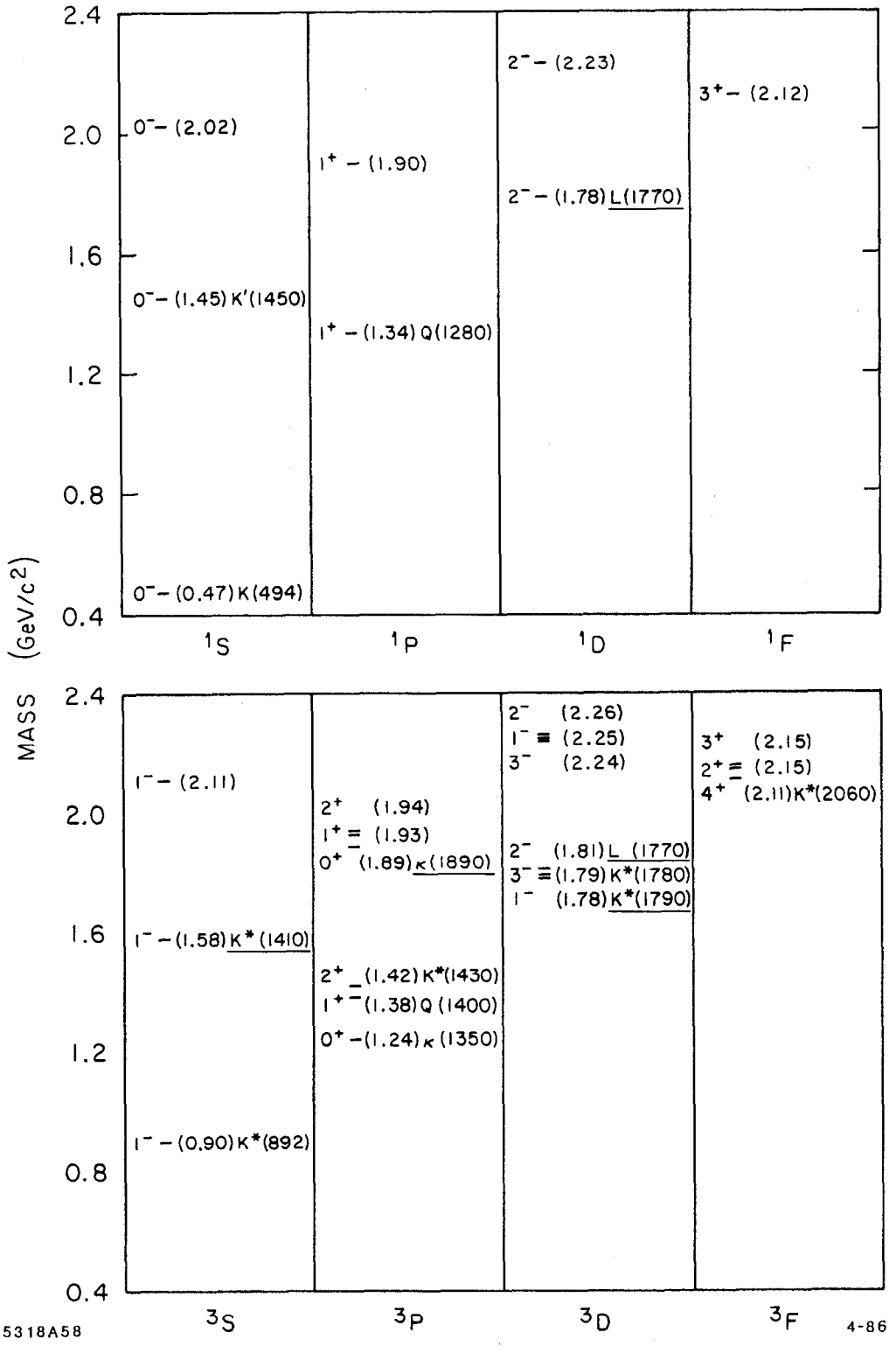

Figure 1.1. The strange meson spectrum. Each state is plotted at the mass predicted in Ref. 10, and the predicted value is shown in the square brackets. The observed states are also shown; those assignments that require confirmation are underlined. In the case of the 1^+ and 2^- assignments, the physical states are believed to be mixtures of the singlet and triplet $q\bar{q}$ systems.

interpretation of the data simpler; (b) pure glueball states are not possible; and (c) the neutral states are free from the ambiguities inherent in the isoscalar-isovector sectors. In addition, the excited strange meson states are experimentally accessible as they can be produced in collisions between high-energy kaon beams and fixed targets. Attempts to unravel the strange meson spectrum have had limited success, however. The spectrum is sufficiently complex that it requires sophisticated analyses of large amounts of data to observe more than the lowest-lying excited K^* states. In addition, these excited states have been studied in only a handful of decay channels. Finally, the availability of strange meson beams of the required purity has been, until recently, a limiting factor.

The two primary sources of data on strange mesons have been the two-body $K\pi$ and three-body $K\pi\pi$ final states. Each of these channels has been observed in either the non-charge-exchange reaction $Kp \rightarrow K^*p$ or the charge-exchange reaction $Kp \rightarrow K^*n$. In the case of the three-meson final states, the unnatural spin-parity states ($J^P = 0^-, 1^+, \ldots$) tend to be preferentially produced in the former whereas the natural spin-parity states ($J^P = 0^+, 1^-, \ldots$) tend to dominate K^* production in the latter.

The two non-charge-exchange reactions that have been studied with the highest statistics are $K^-p \rightarrow \bar{K}^\circ\pi^-p$[13] and $K^\pm p \rightarrow K^\pm\pi^+\pi^-p$.[14–19] The two-body $\bar{K}^\circ\pi^-$ final state is an allowed decay mode for the natural spin-parity mesons and has provided information on the leading K^* resonances, the 1^- $K^*(892)$, the 2^+ $K^*(1430)$, the 3^- $K^*(1780)$, and more recently the 4^+ $K^*(2060)$. The $K^\pm\pi^+\pi^-$ system has been the arena in which properties of the lowest-lying axial-vector mesons, the $Q(1280)$ and $Q(1400)$, have been uncovered. Studies of these channels have also confirmed the existence of the $J^P = 0^-$ $K(1450)$ (the radial excitation of the K), the $J^P = 2^-$ $L(1770)$, and suggested the existence of at least one additional axial-vector state with a mass of 1.8 GeV/c^2. However, one difficulty with the analysis of the diffractive three-body data is the presence of a strong "Deck" background dominating the three-meson production at low three-meson invariant masses. Although the partial wave analyses of these data have readily uncovered the spin-parity structure of this final state, the interpretation of the 1^+ waves requires a detailed model to separate the resonance production from

the Deck effect.

The charge-exchange reactions, on the other hand, do not suffer from these diffractive backgrounds and provide an environment in which leading K^* production dominates the final state. Studies of the two body reaction $K^-p \rightarrow K^-\pi^+n$[20,21] have yielded extensive information on the leading natural spin-parity states up to $J^P = 4^+$, have established the existence of the underlying $J^P = 0^+$ $\kappa(1350)$, and have suggested the possibility of a new vector state in the 1.65–1.80 GeV/c^2 region. There have been several studies of the three-body charge-exchange reaction $K^-p \rightarrow \bar{K}^\circ\pi^+\pi^-n$[22–26] in which the natural spin-parity $2^+K^*(1430)$ and the $3^-K^*(1780)$ have been observed. The three-body analyses have also indicated the existence of a strong 1^- amplitude but the interpretations of this feature have varied. The most recent analysis[22] has shown that it can be understood as arising from the production of two vector states with masses of 1.41 and 1.79 GeV/c^2, respectively.

I will report the results of a new study of the charge-exchange three-body reaction with a data set that is approximately five times larger than any of the samples used previously. The data come from experiment E-135 performed with the Large Aperture Superconducting Solenoid (LASS) spectrometer at the Stanford Linear Accelerator Center. This experiment is a high-statistics study of inelastic $K^\pm$ interactions at 11 GeV/c. The entire K^- data set consists of ~120 000 000 events corresponding to a sensitivity of ~ 4 events/nb. The experiment yields ~50 000 $\bar{K}^\circ\pi^+\pi^-n$ events where the $\bar{K}^\circ$ has decayed weakly into two charged π's.

The analysis of this reaction is performed by selecting the sample of $\bar{K}^\circ\pi^+\pi^-n$ events from the complete data set. This $\bar{K}^\circ\pi^+\pi^-n$ event sample is further analyzed in the context of a specific model that makes use of the three-body isobar formalism. The results of this analysis give a description of the $\bar{K}^\circ\pi^+\pi^-$ system in terms of the spin-parity amplitudes for the specific intermediate states such as $K^*(892)\pi$ and $K\rho(770)$. This relatively simple description of the three-meson final state is then used to extract the properties of the produced K^* states decaying into $\bar{K}^\circ\pi^+\pi^-$.

This thesis is organized as follows: The LASS spectrometer is described in Chapter 2, in which an overview of the detector is presented, followed by a detailed description of each of its components. The manner in which the detector was

operated is described in Chapter 3, where the trigger, data acquisition system, and the calibration procedures are discussed. Chapter 4 describes how the raw event data are processed to yield the trajectories of the charged and neutral tracks along with their production and decay vertices. The Monte Carlo program that simulates the detector is also described in this chapter.

The selection process that isolates the $\bar{K}^\circ \pi^+\pi^- n$ events from the total event sample is described in Chapter 5. The features of the $\bar{K}^\circ \pi^+\pi^- n$ event sample are discussed and motivation is provided for the subsequent analysis of the data. The details of this analysis are described in Chapter 6, where the formalism of the isobar model, the methodology, and the results of the analysis are presented. Chapter 7 describes how the results of the analysis are interpreted, and develops a model to account for the main features of the data. Subsequently, the parameters characterizing the resonant states observed in the $\bar{K}^\circ \pi^+\pi^-$ system are determined. Finally, the conclusions of this study are presented in Chapter 8.

2. The LASS Spectrometer

2.1 Overview

LASS is an acronym for the Large Aperture Superconducting Solenoid. As the name implies, the LASS spectrometer has as its principle component a large superconducting solenoid magnet, but in effect it is actually two detectors combined into one. The first is a solenoidal spectrometer in which collisions between a beam particle and a stationary proton take place. This device measures the trajectories and momenta of particles produced in the target and functions as a sophisticated vertex detector. Its angular acceptance for measuring particle trajectories extends over almost 4π in the lab frame. The second detector is a dipole spectrometer, located down beam of the solenoid magnet, which momentum analyzes fast particles produced close to the solenoid axis. This detector combination yields a powerful spectrometer that has excellent angular and momentum resolution and very good acceptance over most of phase space. The spectrometer has a time of flight (TOF) system and two segmented threshold Čerenkov counters that provide particle identification to assist in the identification of specific final states.

The LASS spectrometer is shown in Fig. 2.1. In the next several sections, I will describe the various components that comprise the device. A more detailed description of the detector (and the E-135 experiment) is given in Ref. 27.

2.2 The Beam line

The 11 GeV/c incident kaons are provided by SLAC beam line 20-21, an RF-separated beam capable of providing mono-energetic particle bunches of high purity.[28] The LASS spectrometer is situated at the downstream end of this beam line.

The beam line is formed by collecting secondary particles produced by bunches of high-energy electrons colliding with a production target. The SLAC linear accelerator produces a 1.6 μsec bunch of electrons at rates up to 180 Hz. Each electron bunch is composed of 5 psec bursts of electrons arriving every 350 psec. This electron beam, with a momentum of 21 GeV/c, is steered onto the primary production target. The target is a water-cooled slab of beryllium, 1.0 radiation length thick, with a 0.25 radiation length thick copper radiator on the upstream

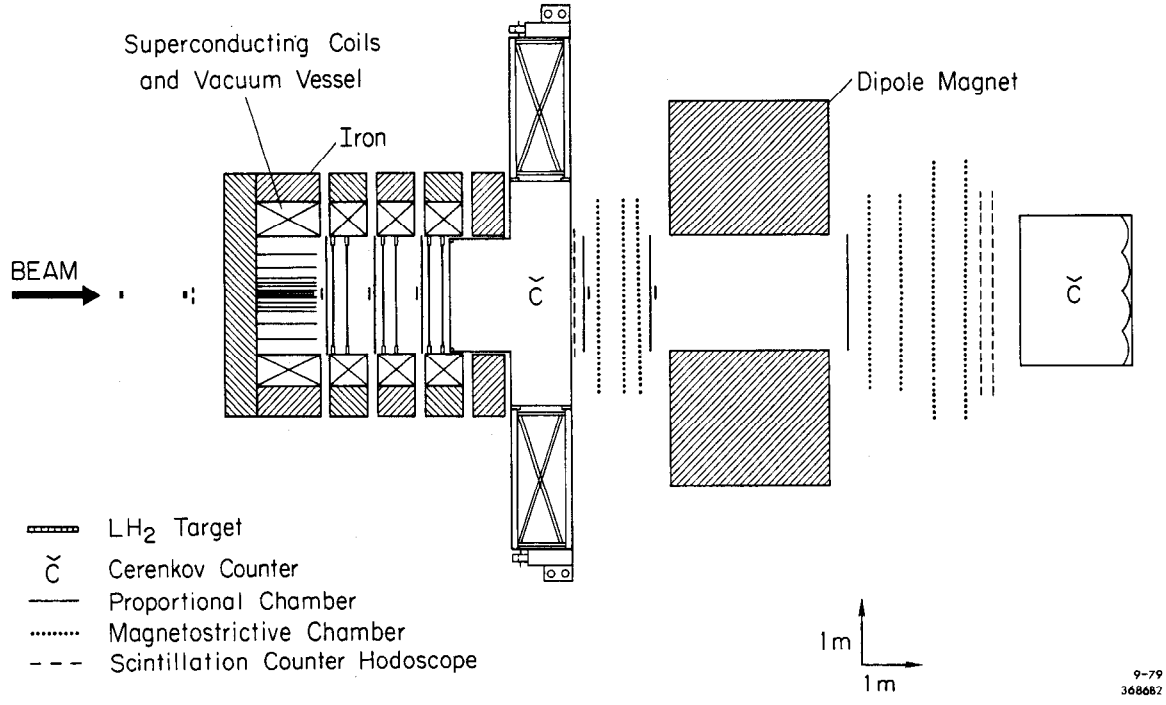

Figure 2.1. The LASS spectrometer. The incoming beam line, the solenoid vertex detector, and the dipole spectrometer are shown in plan view.

face of the slab. The copper increases the probability of the primary electrons showering within the target thereby increasing the secondary particle yield.

The beam line is shown schematically in Fig. 2.2. Secondary particles produced within 3.85 mrad of 1° are captured by the beam line. The beam line has four foci, shown in Fig. 2.2 as F1 through F4, and several instruments that separate the beam into distinct particle species and measure the momentum and position of the individual beam particles.

F1 is a dispersed focus that limits the secondary particle momentum to a range $\Delta p/p \lesssim 2.5\%$ through the use of a collimator. The beam passes through a lead sheet 0.56 radiation lengths thick at this focus in order to reduce the electron contamination of the beam.

Between foci F1 and F2, the particles pass through two RF separators. These separators deflect the particles in the vertical direction by an amount determined by their mass; the time of flight of a particle from the production target to the separators determines the phase of the RF field (*i.e.* the deflecting force) experienced by the particle. By the time the particles pass through F2, an achromatic focus, the different particle species form spatially separated images. A small aperture collimator is positioned at F2 to select preferentially one particle species. Only one separator is necessary with a nominal 11 GeV/c kaon beam and so this was the normal mode of operation when the experiment was conducted.

The momentum of each individual beam particle is determined by its horizontal position at the F3 focus. This horizontal displacement is measured by a group of scintillation counters (the P-hodoscope), shown in Fig. 2.3, which is formed of six overlapping fingers of scintillator plastic that digitize the beam position (*i.e.* momentum) into 11 bins. Each bin is 0.61 cm wide and is equivalent to a momentum bin of width $\Delta p/p = 0.50\%$. At a nominal momentum setting of 11 GeV/c, the mean momentum of a particle measured in bin n is given by

$$p = 10.600 + 0.0495n \text{ GeV/c}. \tag{2.1}$$

The nominal spot size of the beam at F3 and fluctuations in the beam line magnets add an additional uncertainty to the beam momentum that depends on the beam

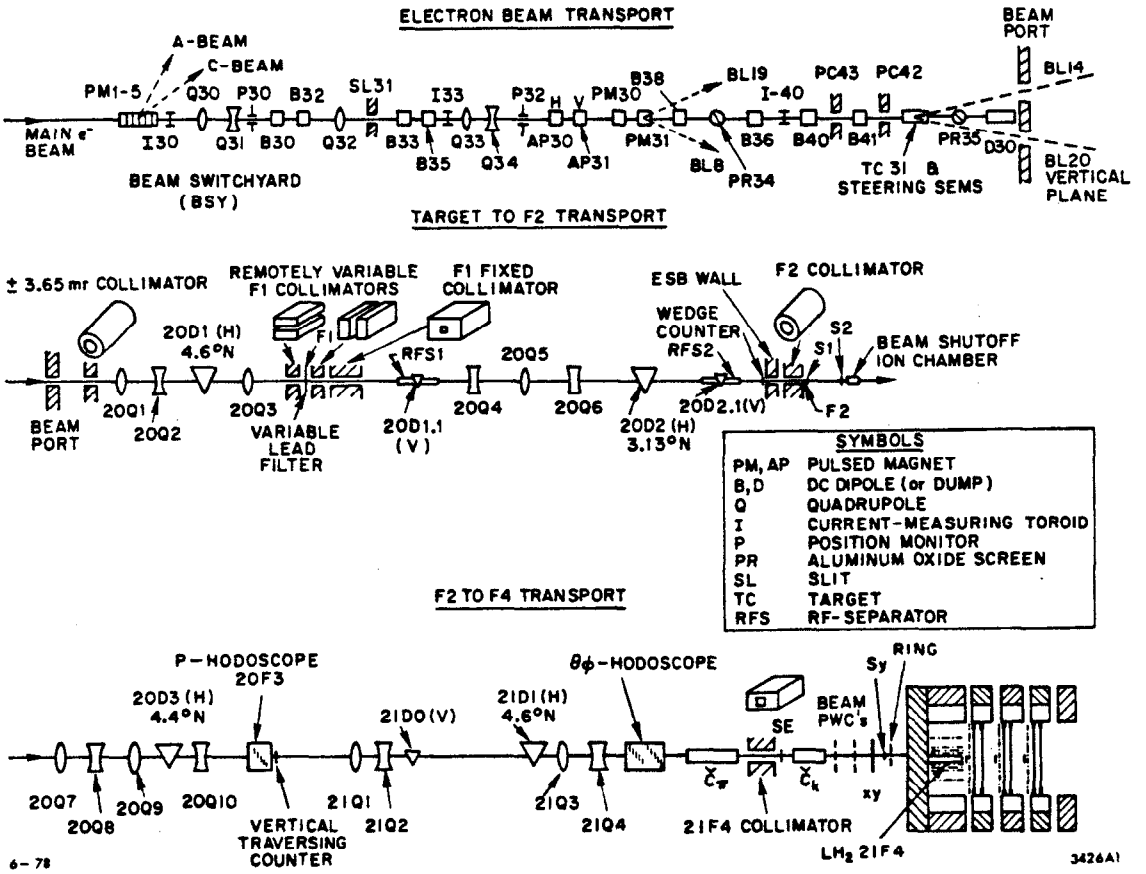

Figure 2.2. SLAC Beam Line 20-21. The locations of the four foci F1-F4 relative to the production target, RF separators and LASS target are shown.

line tuning. From analysis of beam decays where the momenta of the daughter particles are observed in the dipole spectrometer, the overall beam momentum resolution is measured to be ~ 0.040 GeV/c.[29]

The spatial position of each beam particle is measured in a scintillator device known as the $\Theta\Phi$ hodoscope. It is located 13.1 m upstream of the LASS spectrometer and consists of two arrays of 12 1.27 cm wide fingers of plastic scintillator, one array measuring the horizontal position of the beam (the x or Θ coordinate) and the other measuring the vertical position (the y or Φ coordinate). The scintillator fingers are wrapped in 25.4 μ thick aluminum jackets and are butted together and pressed in place to minimize the "dead" region between adjacent fingers. The $\Theta\Phi$ counter is also incorporated in the event trigger logic, its function being to ensure that the spectrometer trigger on one and only one beam particle.

The beam particle is identified as a π, K or p using two threshold Čerenkov counters, $\check{C}_\pi$ and $\check{C}_K$, located downstream of the $\Theta\Phi$ counter. These counters detect the Čerenkov light emitted by the beam particles as they traverse a cylindrical gas volume inside each counter. The Čerenkov photons, produced in a small cone about the beam particle direction, are reflected by an aluminized plane mirror into a parabolic collecting horn that focuses the light onto the photocathode of a photomultiplier tube. The $\check{C}_\pi$ counter is filled with H_2 at 40 psia while $\check{C}_K$ is filled with CO_2 at 75 psia; these gas fills result in refractive indices that cause 11 GeV/c π's to radiate in $\check{C}_\pi$ and $\check{C}_K$ and 11 GeV/c K's to radiate only in $\check{C}_K$. The detection of light in both $\check{C}_\pi$ and $\check{C}_K$ signals a π, light in only $\check{C}_K$ signals a K, and light in neither signals a p. Under typical operating conditions, the RF separators yield a K^- beam with a K/π ratio of ~70–80. The contamination due to anti-protons, electrons and other particle species is negligible.

The trajectory of each beam particle is measured in the beam chamber package, a set of ten planes of small proportional wire chambers (PWC's), the last of which is located 1.2 m upstream of the solenoid. Each anode plane consists of 64 sense wires at a 1.016 mm pitch, the sense wires being 20 μ diameter gold-plated tungsten. The 10 planes are grouped into two packages separated by $\sim$ 1 m. The upstream package has four planes oriented to measure the y, x, p and e coordinates (e and p

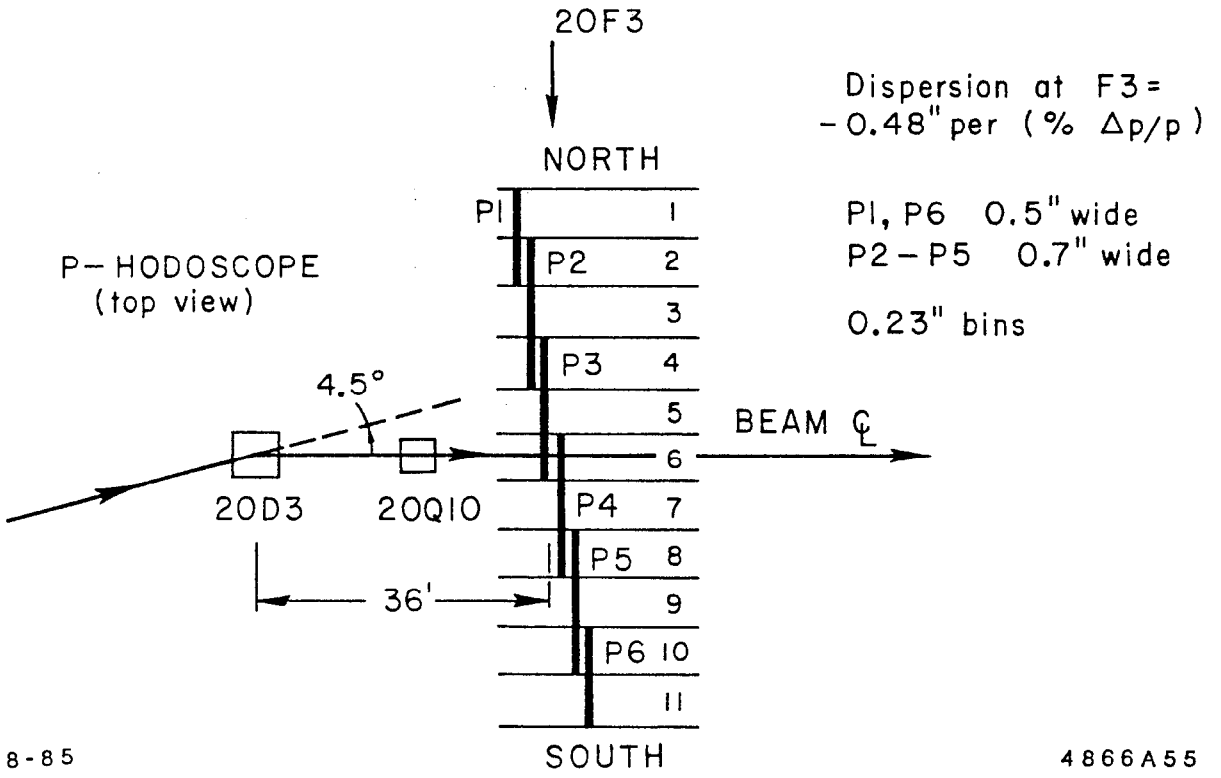

Figure 2.3. The P-hodoscope. This counter is made of six overlapping fingers of scintillator and measures the horizontal displacement of the beam particles at the momentum-dispersed F3 focus.

are the coordinates defined by $e \equiv (x-y)/\sqrt{2}$ and $p \equiv (x+y)/\sqrt{2}$). The six planes in the downstream package are oriented to measure the coordinates in the order y, x, y', x', e and p; x' and y' are a set of xy planes offset by a half-wire spacing in the x and y directions relative to the first xy set. The beam chambers measure the beam track position and direction to within 300 μ and 0.3 mrad respectively.

The final components of the beam line are three scintillator counters located upstream of the liquid H_2 target vessel. The first counter is a slab of plastic scintillator, 0.952 cm in thickness, that is located ~5 m upstream of the spectrometer where the beam enters the building housing the detector. This counter, known as SE, counts both beam particles and any off-axis beam "halo" and is used to form the start pulse for the time of flight system. Because of this function, it is made particularly thick to reduce time jitter in the light pulse. The two other counters, SY and RING, are located immediately upstream of the target and are used to positively tag the incoming beam particle. SY is a 0.318 cm thick, 2.54 cm diameter round counter while RING is a 1.27 cm thick paddle counter with a 2.54 cm diameter hole in the middle. Both counters are aligned on the beam axis, together covering the upstream aperture of the LASS spectrometer, and are used to veto beam halo (one of the counters is slightly over-sized so that there are no cracks between the two counters).

The final focus in the beam line is F4, located a few cm downstream of the end of the hydrogen target. It is an achromatic focus that produces a beam spot size with σ ~0.5 cm in each plane.

Under normal operating conditions, the beam line provides 3-5 beam triggers per linac pulse at the entrance to the LASS spectrometer spread out over the 1.6 μsec duration of the primary beam pulse. During the E-135 data taking the typical linac repetition rate was ~90 Hz.

2.3 The Target

The LASS target cell is 85.04 cm long and 2.54 cm in radius at room temperature and is filled with liquid H_2. A cross-sectional drawing of the target is shown in Fig. 2.4. It consists of a two concentric mylar cylinders, with a mylar window at the upstream end and a pre-formed mylar cap at the downstream end.

The exterior of the target is wrapped in several layers of mylar super insulation and is enclosed in an aluminum vacuum jacket having a wall thickness of 0.71 mm. The entire target is supported on a steel pipe extending upstream of the target and mounted via a flange to the upstream mirror plate of the solenoid magnet. Because of the contraction of the target cell when lowered to liquid H_2 temperature, the operational length of the target is $\sim$ 84.6 cm.

Liquid H_2 is pumped into the inner cylinder of the target and returns through the space between the two mylar cylinders. The pressure and temperature of the H_2 are monitored with four vapor pressure bulbs and three platinum resistors to verify that the liquid remains well below boiling temperature and to determine H_2 density for later normalization calculations. The amount of material presented to a particle produced normal to the beam axis in the target is such that a 0.225 GeV/c proton will range out inside. The average density of the H_2 was 0.0716 ± 0.0004 gm/cm^3 over the duration of the E-135 data collection.

2.4 The Solenoid Vertex Detector

The purpose of the solenoid vertex detector is to measure the trajectories and momenta of the charged tracks produced in the target or arising from secondary decays of neutral and charged particles. These tracks are used to locate the primary and any secondary decay vertices, and to determine the kinematics of the particles at these vertices. Figure 2.5 shows the layout of the solenoid. The following subsections describe the components that comprise the detector.

2.4.1 The Solenoid Magnet

The solenoid magnet produces a magnetic field parallel to the beam axis. It is a superconducting magnet with an inner diameter and length of 185 and 465 cm, respectively. The average magnetic field along the axis is 22.4 kG and is uniform to within 1%. The radial field components are essentially zero on the beam axis and only become sizeable beyond $\sim z = 300$ cm due to the open downstream end of the magnet. A fiducial region of radius 75 cm and length 320 cm defines a magnet volume in which the field variation is less than 3.1%.

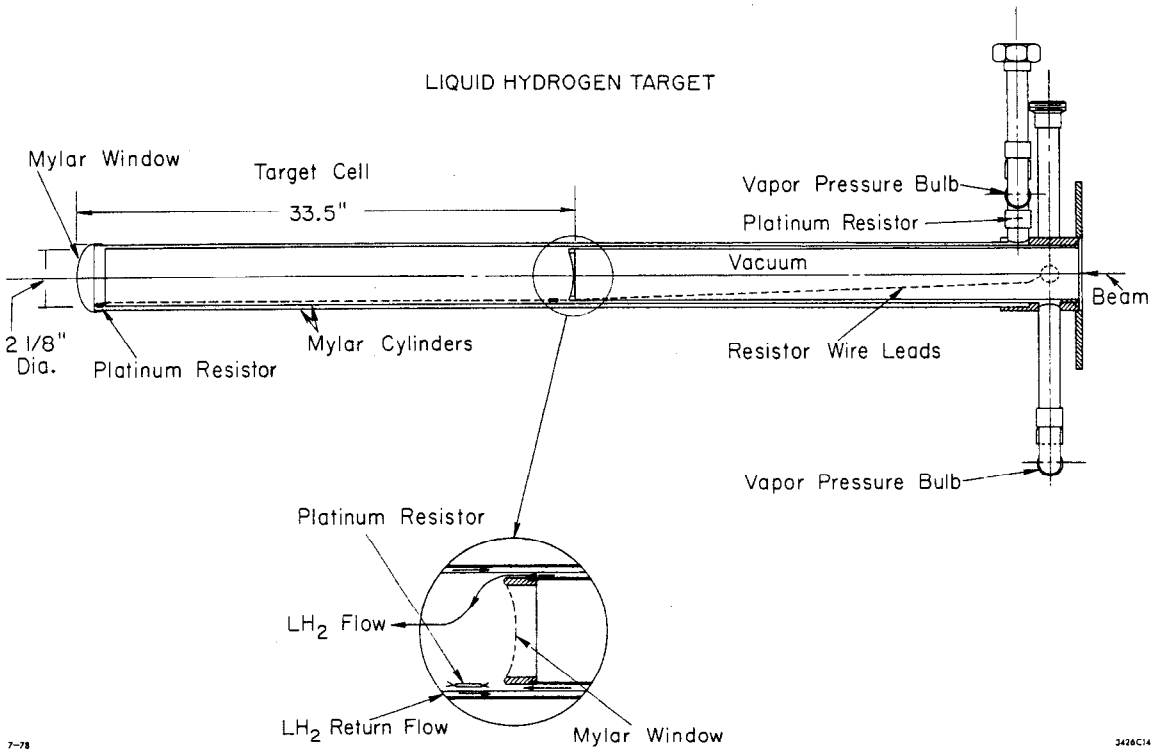

Figure 2.4. The liquid H_2 target cell. The target is composed of two concentric mylar cylinders and is enclosed in a vacuum jacket.

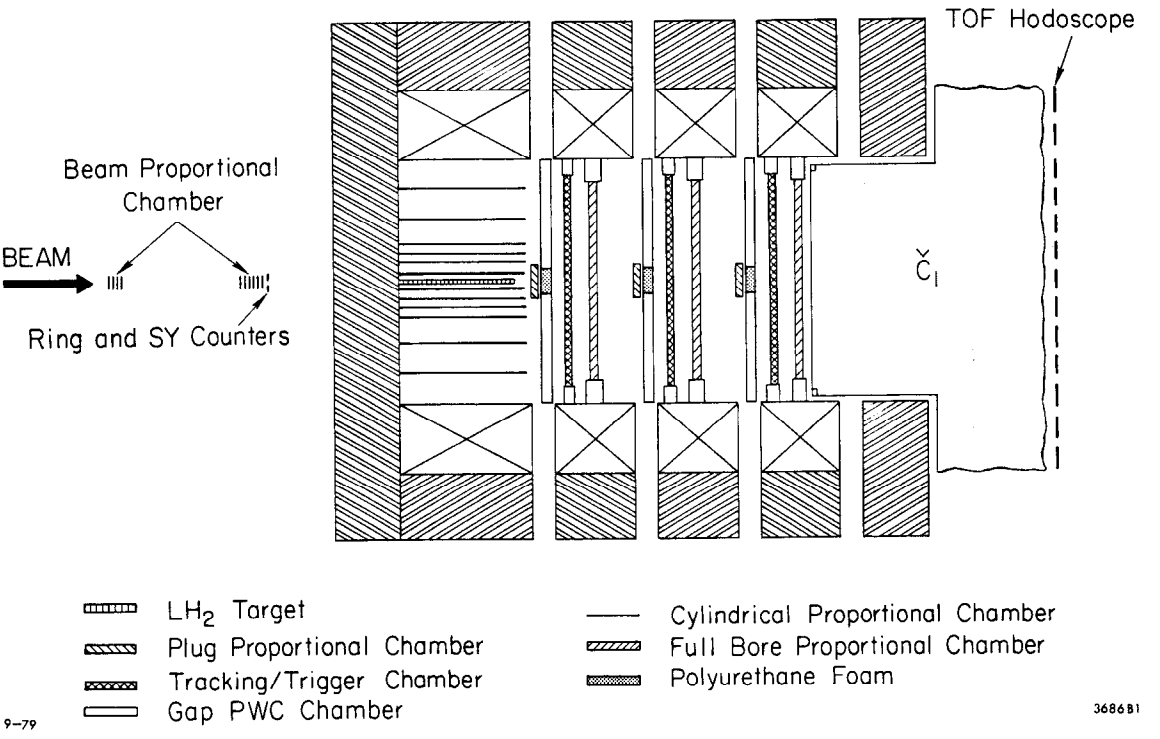

Figure 2.5. The instrumentation of the solenoid vertex detector. The location of the target, the chambers inside the solenoid, and the particle identification devices are shown in relationship to the superconducting magnet coils.

The magnet is made up of four separate superconducting coils arranged so that planar proportional wire chambers can be inserted into three "slots" downstream of the target. It operates at 1600 A and is bath cooled with 5000 l of liquid helium. Helium consumption is $\sim$ 60 l/hour in normal operation and the supply is replenished by two refrigerators located on top of the magnet housing.

2.4.2 The Gap Chambers

Two planar tracking chambers are located in each slot between the magnet coils; a small proportional wire chamber covering the area around the beam axis called a plug chamber, and a large proportional wire chamber with cathode strip readout known as a gap chamber. The plug chambers will be described in the following subsection.

A gap chamber is a single proportional wire plane large enough to cover the entire bore of the solenoid magnet. The active region of the anode plane consists of 758 vertical wires strung at 2.032 mm pitch with 20 μ diameter gold-plated tungsten wire (the same wire is used in all of the PWC devices in the solenoid). The two cathodes for this chamber are single sheets of an aluminum-mylar laminate that are etched into electrically isolated "strips" 6.86 mm wide separated by 1.27 mm insulating gaps. The cathode on the upstream side of the chamber is oriented so that the strips are rotated clockwise 45° with respect to the vertical anode wires as viewed looking downstream along the z-axis (the coordinate measured perpendicular to the strip direction is $e \equiv -(x+y)/\sqrt{2}$). The downstream cathode is oriented with the strips rotated a similar amount in the opposite direction (the coordinate measured by these strips is $p \equiv (-x+y)/\sqrt{2}$). The spacing between the anode plane and each cathode is 0.508 cm. An inner circular region of radius 8.255 cm is deadened with a mylar barrier that is epoxied to styrofoam supports attached to each cathode. This prevents tracks in the high-intensity beam region from filling the central strips of the chamber with data and complicating the coordinate reconstruction (this deadened region is completely covered by the plug chambers). The anode plane has a pair of insulated support wires stretched perpendicular to the anodes and epoxied directly to each sense wire. In addition, 10 polyurethane spacers are epoxied onto each support wire to maintain a constant anode-cathode separation. The spacers

and support wires are necessary to maintain the anode and cathode geometry in the presence of the large electrostatic forces created when voltage is applied to the chamber. A sketch of the anode and cathodes of a gap chamber are shown in Fig. 2.6. A more detailed description of the gap chambers can be found in Ref. 30.

With readout of the induced signal on the individual cathode strips as well as the direct signals on the anode wires, each gap chamber provides three-dimensional space points for tracks at a common z-plane. In operation, the gap chamber behaves as a conventional PWC in that a given charged track produces a cloud of electrons that drifts to the nearest sense wire and generates an avalanche at the wire. A corresponding surface charge is induced on the cathodes in the vicinity of the avalanche by the cloud of positive ions that are repelled from the anode. On each cathode, this image charge is distributed typically over 2–5 strips, the amount of charge per strip depending on the transverse distance of the strip from the avalanche. By measuring the integrated charge on each strip and correlating the charge detected on adjacent strips, the position of the avalanche along the wire can be determined by one cathode and corroborated with the other. This in effect provides a space point measurement at the anode plane. When multiple hits are observed in the same chamber, the large Landau fluctuations in the size of each avalanche are used to pair up the pulse height peaks observed on the two cathode foils. In most cases this pulse-height matching criterion along with the good-spatial resolution of the peaks on the cathode strips allows reconstruction of all the hits within a single chamber with little ambiguity.

The peak position resolutions for the gap chamber foils and the resulting uncertainty of the y coordinates are listed in Table 2.1. The three gap chambers are located between the magnet coils in a mounting system that allows easy extraction of each chamber in the event it needs servicing. The locations of the anode planes along the z-axis are given in Table 2.2.

2.4.3 The Plug Chambers

There are five plug chambers in the LASS spectrometer; one is mounted on the upstream face of each gap chamber and the remaining two are installed in the twixt region of the dipole spectrometer. The five chambers are identical in construction

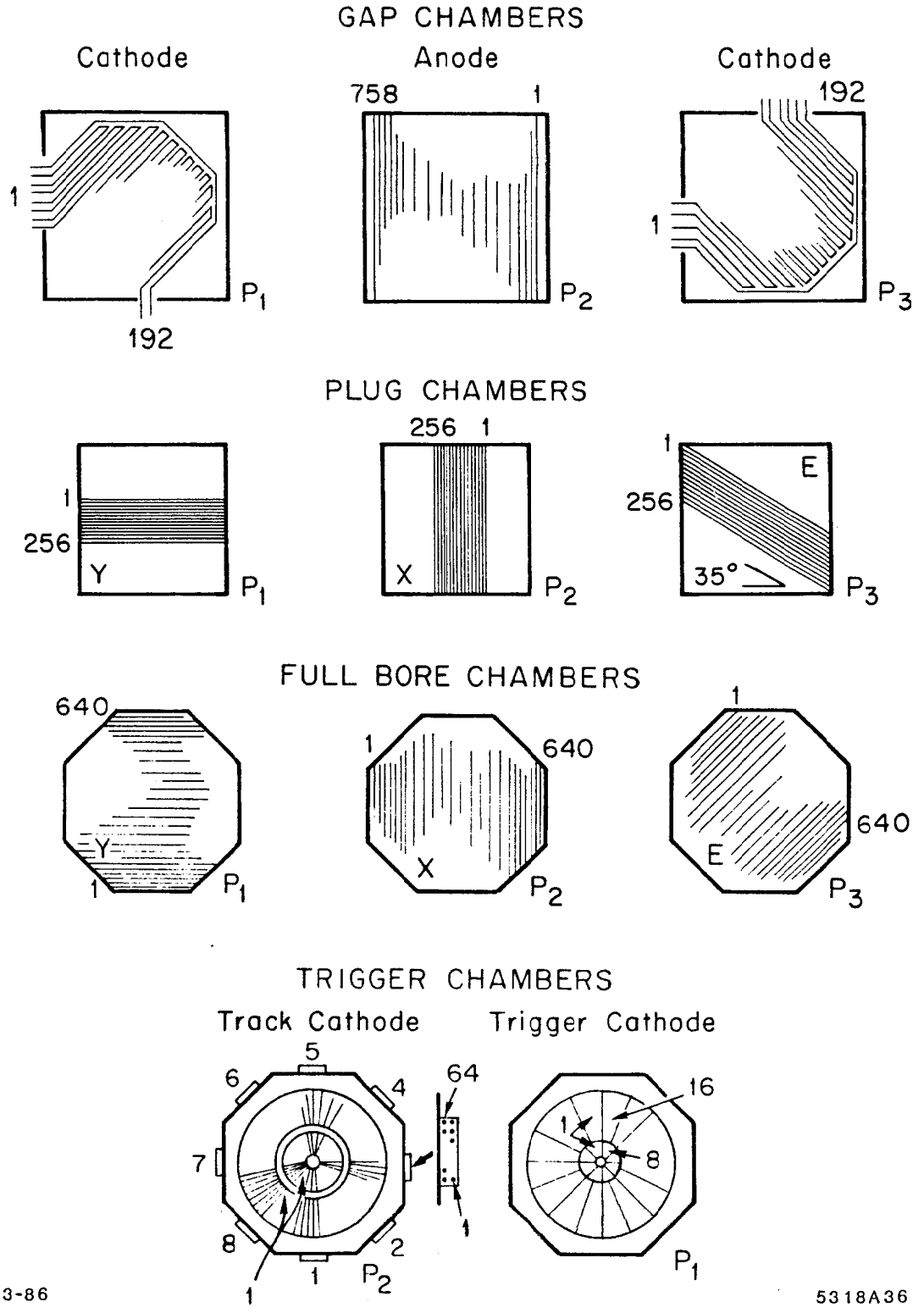

Figure 2.6. The planar PWC devices in the solenoid. The ordering of the planes in each device is according to increasing z. Each plane is viewed looking downstream in the z direction.

Table 2.1. Cathode Coordinate Resolution. These uncertainties are for coordinates with single-anode clusters; the uncertainties for multi-anode coordinates are larger by $30 - 40\%$. The variable θ is the angle between the cathode strips and the corresponding anode wires.

Chamber	Cathode Resolution μ	$1/\tan\theta$	y/z Resolution μ
Gap 1	185	1.00	185
Gap 2	185	1.00	185
Gap 3	226	1.00	226
Cyl 1	175	5.67	700
Cyl 2	155	5.67	620
Cyl 3	195	5.67	780
Cyl 4	185	5.67	740
Cyl 5	220	3.73	580
Cyl 6	220	3.73	580

Table 2.2. Some physical parameters of the planar PWC devices. The z-position of each plane and the anode wire spacing are listed for the solenoid planar proportional wire chambers.

Chamber	z Positions cm			Anode Pitch cm
	y-plane	x-plane	e-plane	
Plug 1	121.58	122.41	123.23	0.1016
Gap 1		130.01		0.2032
1.5	164.92	166.16	167.40	0.2032
Plug 2	198.84	199.61	200.49	0.1016
Gap 2		207.26		0.2032
2.5	242.19	243.43	244.67	0.2032
Plug 3	276.12	276.95	277.77	0.1016
Gap 3		284.54		0.2032
3.5	319.71	320.95	322.19	0.2032

except for minor variations in their frames.

The plug chambers are located along the beam axis where the instantaneous particle flux is high. The first three plug chambers completely cover the deadened area of the gap chambers while the two remaining plug chambers cover a similarly deadened area of the three magnetostrictive spark chambers in the dipole twixt region. The active area of each chamber is small ($\sim 26 \times 28$ cm) but the frame size matches that of the gap chamber so that in the solenoid the pair of devices can be installed as a single unit.

A plug chamber consists of three proportional wire anode planes, strung with 256 sense wires at a pitch of 1.016 mm. The anode planes are oriented so that they measure y, x, and e coordinates ($e \equiv x\cos\theta - y\sin\theta$ with $\theta = 35°$ in the plug chambers). The spacing between each anode plane is 0.825 cm and the anode-cathode gap is 0.406 cm. Each anode plane has its own set of cathodes. However, adjacent cathode planes within the assembly share a common frame to minimize the width of the chamber. The anode planes of a plug chamber are shown in Fig. 2.6.

2.4.4 The Full-Bore Chambers

The three full-bore chambers, labelled the 1.5, 2.5 and 3.5 chambers, are PWC's that are mounted in the inner bore of the magnet coils as shown in Fig. 2.5.

Each chamber consists of three anode planes oriented to measure the y, x and e coordinates ($e \equiv x\cos\theta - y\sin\theta$ with $\theta = 45°$ for the full-bore chambers). The active area of each anode plane is strung with 640 sense wires at a pitch of 2.032 mm. The anode-cathode separation is 0.406 cm, which is maintained by a set of support wires and spacers similar to the ones in the gap chambers. The chamber frame is octagonal in shape in order to cover as much of the solenoid bore as possible. Figure 2.6 shows a drawing of a full bore chamber's anode planes.

2.4.5 The Trigger Chambers

There are three planar cathode foil chambers in the solenoid, located between each set of gap and full-bore chambers. These are the trigger chambers, and are labelled TA, TB, and TC. The trigger chambers cover most of the solenoid bore and are octagonal in shape. Though the original purpose of these chambers was to provide track multiplicity information for the event trigger, their role in experiment

E-135 is to provide additional corroboration for a track candidate during the course of the track-finding process.

Each chamber consists of an anode plane and two segmented cathode planes. The wires in the anode plane, strung 4.064 mm apart, are kept at high voltage and are not read out. The first cathode in each chamber, known as the tracking foil, is segmented into two rings of 8 and 128 pads each. This high level of segmentation is designed with track corroboration in mind. The second cathode, called the trigger foil, is segmented into two rings, with 8 and 16 pads in each ring. As its name implies, it is designed to provide crude track information that could be used in the definition of the event trigger. Figure 2.6 illustrates the segmentation of these foils. The tracking foils are read out for all three trigger chambers. The trigger foils are read out only for TA and TB.

2.4.6 The Cylindrical Chambers

The target vessel is surrounded by six cylindrical PWC devices with cathode strip readout. The six chambers are approximately coaxial with the z axis, with the inner and outer cylinders at radii of 6.05 and 49.02 cm, respectively. The anode wires are strung with a 2.00 mm pitch parallel to the cylinder axis. The cathode strips are oriented at $\pm 10°$ angles to the anode wires for the inner four cylinders and at $\pm 15°$ angles for the outer two cylinders. These devices operate in a manner similar to the gap chambers.

The physical parameters of the devices are listed in Table 2.3. Cylinders 1 through 4 have active lengths of 100 cm and are positioned with their upstream end approx 7 cm upstream of the beginning of the target. Cylinders 5 and 6 have active lengths of 87 cm and are positioned with their upstream end approx 7 cm downstream of the front end of the target. The cylinder cathode resolutions are listed in Table 2.1.

The material presented to outgoing tracks by each cylinder is small ($\sim$ 0.11 gm/cm^2). The cathode foils are supported by a double cylinder of an aluminum-mylar laminate and a paper honeycomb (Hexcel) sheet. The inner cathode covers the outer surface of the inner Hexcel cylinder while the outer cathode covers the inner surface of the outer Hexcel cylinder. The anode wires are attached to ring-

Table 2.3. The physical parameters of the six cylindrical PWC devices. The anodes in cylinders 5 and 6 are ganged together in groups of four to reduce the number of electronics channels.

Cylinder Number	Anode Radius cm	Anode Pitch cm	Cathode Pitch cm	Stereo Angle
1	6.05	0.20	0.500	10°
2	9.55	0.20	0.500	10°
3	12.99	0.20	0.800	10°
4	16.55	0.20	0.800	10°
5	29.41	0.20	1.035	15°
6	49.02	0.20	1.035	15°

shaped PC boards, located at either end of each cylinder, and are glued to a lucite support ring midway down the length of the cylinder. A detailed description of these chambers can be found in Ref. 31.

Besides providing excellent solid angle coverage for particles produced at large angles in the target, a by-product of the pulse height information on the cathode foils is the ability to perform ionization measurements of tracks that pass through several cylinders and have momenta below ~0.6 GeV/c. The avalanches on the anode wires do not saturate the gas gain of the cylinders for tracks near normal incidence, resulting in cathode pulse heights that are proportional to the particle's ionization in the chamber gas. Correlating the measured ionization from several coordinates provides a modest dE/dx measurement that can be compared with the expected ionization for different particle hypotheses.

2.4.7 The $\check{C}_1$ Čerenkov Counter

The $\check{C}_1$ Čerenkov counter is located inside the downstream aperture of the solenoid magnet and extends beyond the last magnet coil. The device is a segmented, threshold Čerenkov counter filled with Freon 114 at atmospheric pressure. In this gas the momentum threshold for π's to emit light is $\sim$ 2.6 GeV/c while the momentum threshold for K's is $\sim$ 9.2 GeV/c. The path length presented to a particle traversing the counter is $\gtrsim$ 180 cm. The counter is segmented into 38

physically and optically isolated cells so that the light emitted by a particle is usually collected by one cell. The counter performs well in a multi-particle environment because of this segmentation.

Figure 2.7 shows the segmentation of the $\check{C}_1$ counter. A cylinder with radius 8.5 cm centered on the beam line is divided into two half-cylindrical volumes called the "D" cells. The counter is then partitioned into three conical shells whose radii increase as they extend downstream. Each of these shells (labelled the C, B and A rings in order of increasing radii) is further divided in azimuth into 12 cells. This partitioning is achieved with sheets of aluminum-mylar foil that have been given a double coat of aluminum using a vacuum deposition technique. The counter segmentation begins at the plane $z = 370.2$ cm but the gas volume extends upstream to $z = 329.6$ cm in order to enhance the Čerenkov photon yield. This results in a Čerenkov ring radius of approximately 2 cm for a radiating π at the beginning of the counter segmentation so that it is possible for one particle to deposit light into more than one cell even though it traverses only one cell as it passes through $\check{C}_1$. At the downstream end of each of the cells, the light is reflected normal to the beam axis into an optical assembly consisting of a plastic Fresnel lens, a light collection horn and a photomultiplier tube. The optical assemblies extend away from the beam axis ~ 4.3 m.

The bottom three cells in the A, B and C rings require a somewhat different geometrical arrangement because of the proximity of the floor. Their optical assemblies are substantially shorter in length and the light collection horns on the phototubes are a more critical feature. Unfortunately these horns have proved to be inefficient in collecting light from a particular region of the optical cell resulting in a degradation of the counter's performance in these bottom three cells of each ring.

Because of the large stray magnetic fields in this region, the phototubes are carefully shielded with a set of iron and μ-metal pipes. In addition, a set of bucking coils are wound to the inner magnetic shield in order to expel remaining magnetic fields parallel to the phototube axis. The photomultiplier tubes are read out with ADC modules that digitize the observed pulse height. The tubes chosen for this counter are RCA 8850 Quantacon photomultipliers, which have exceptionally good

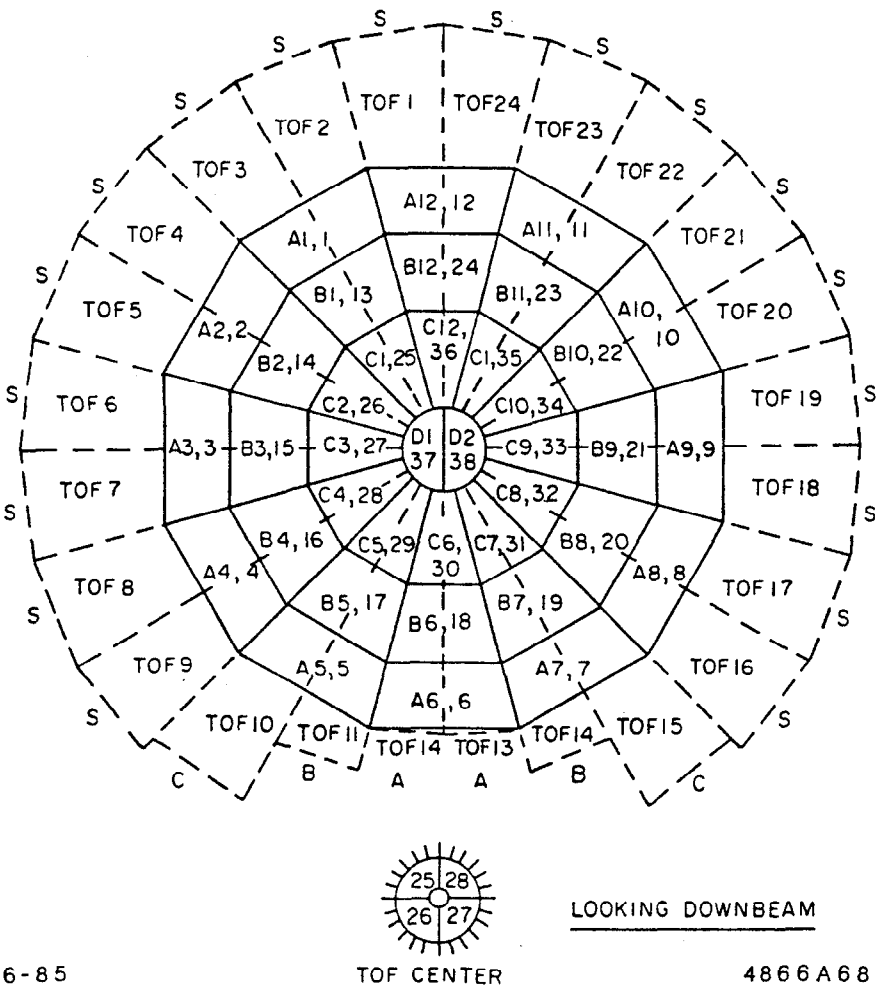

Figure 2.7. The optical cells in $\check{C}_1$. The outline of the TOF hodoscope is shown in dashed lines; the Quad counter located at the center of the TOF array is also shown.

single-photon response and high quantum efficiency.

The $\check{C}_1$ counter's threshold behavior and efficiency as a function of particle trajectory inside the counter is known empirically by studying a large sample of π's identified by requiring them to be daughters from K° decays. The π's are used to measure the probability of detecting light in a cell as a function of momentum and the impact position of the particle at the front face of the cell. The particle trajectory is extrapolated as a helix down to the gap 3 chamber and then Runge-Kutta integrated through the known solenoid field into the $\check{C}_1$ counter and out to the TOF array. The cell entered by the particle at the beginning of the counter's segmented region is defined to be the cell "hit" by the particle. If the particle trajectory is near or above threshold, the impact position of the particle and the particle's momentum determines the combined probability that the particle will radiate light and that the light will be detected by the phototube. This procedure takes into account cases where a particle passes through more than one cell and also allows for the imprecision with which the particle trajectory is known; if a particle passes within 2 cm of a cell boundary, the adjacent cell is also checked for light.

The momentum threshold for light in the $\check{C}_1$ counter is shown in Fig. 2.8. The π's used to measure this threshold behavior have been selected to ensure that cell edge effects have been removed. The lower three inefficient counters in the A, B and C rings have also been excluded in this measurement. The result of a simultaneous fit to the threshold behavior is also shown in Fig. 2.8. The fit takes into account an asymptotic efficiency for each counter, a constant background, and a threshold rise parametrized by the expected photon yield as the particle's velocity passes through the threshold for Čerenkov radiation.

The asymptotic efficiencies are 0.971 ± 0.006, 0.987 ± 0.002 and 0.998 ± 0.002 for the A, B and C rings respectively. The average efficiency of the counter for particles above threshold is 0.975 when the inefficient regions of the bottom quadrant and the D cells are excluded. The efficiency rises to 0.995 when tracks are excluded that pass near the vicinity of a cell partition.

2.4.8 The Time of Flight System

The time of flight (TOF) system consists of the SE counter located upstream

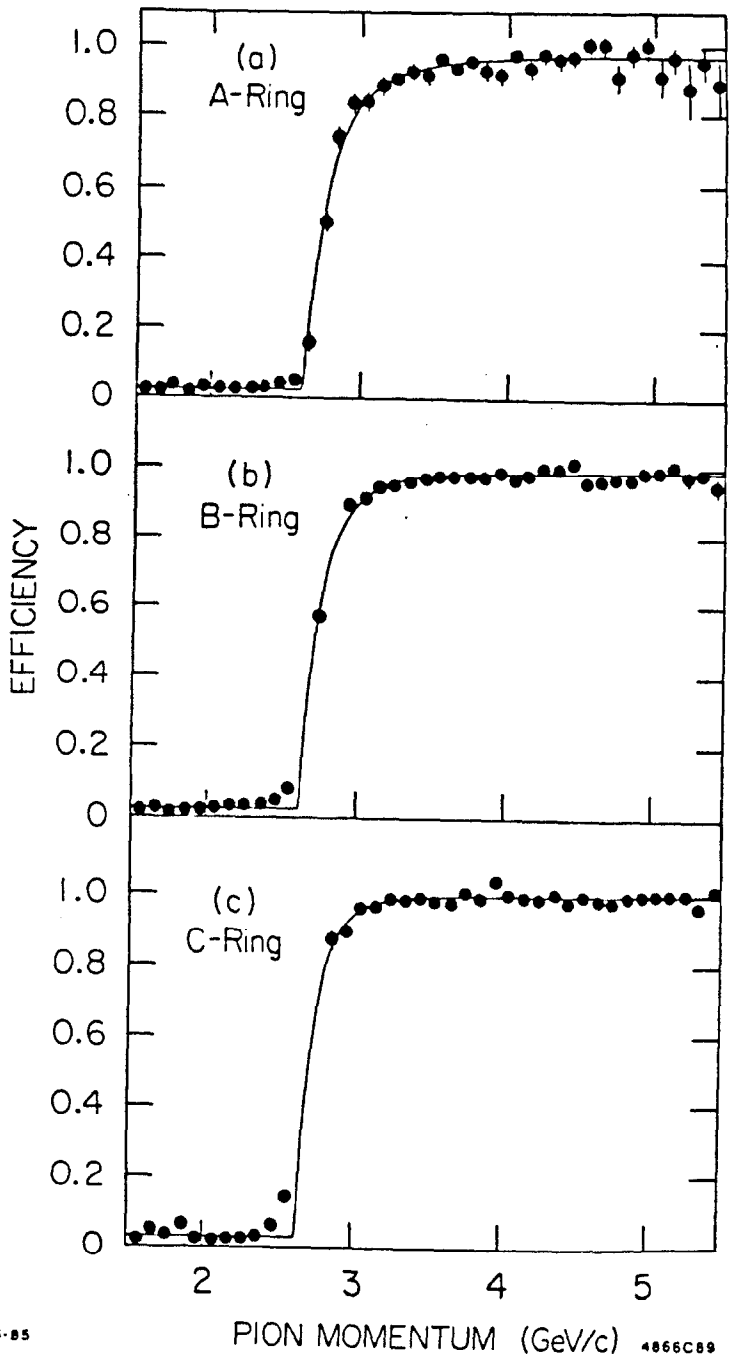

Figure 2.8. The momentum threshold of the $\check{C}_1$ counter. The curves shown in the figure are fits to the data described in the text.

of the target and a segmented scintillator hodoscope located at $z = 573$ cm immediately downstream of the $\check{C}_1$ counter. The hodoscope is shown in Fig. 2.9. It is approximately circular in shape and composed of 24 15° wedge-shaped paddles with a hole of radius 15.24 cm in the center of the hodoscope. The scintillator paddles are 1 cm thick and are viewed from one end by phototubes using a lucite light guide consisting of a light pipe, an elbow and a Winston cone. The hole in the center of the counter is partly filled by a ring-shaped scintillator divided into four quadrants, called the Quad counter. The inner radius of this counter is 3.81 cm, which defines a beam hole centered on the beam axis. The TOF and Quad counter together form one of the inputs to the event trigger logic.

Because of the large solenoid fringe field in this region, each phototube in the TOF counter is magnetically shielded with two steel and μ-metal pipes. To provide additional magnetic shielding, a 250 turn "bucking" coil is wound on each phototube. To further minimize the effect of any stray fields, the elbows in the light pipes are fashioned so that each phototube axis is approximately perpendicular to the magnetic field lines.

The SE counter provides a start signal for 24 TDC modules. The output from a TOF paddle photomultiplier tube is discriminated and used to stop the corresponding TDC. The integrated signal from the last dynode in each photomultiplier is also recorded in an ADC unit. This pulse height measurement and the corresponding ADC output of the SE counter are used to correct the observed TDC measurement for the "time walk" of the discriminated light pulse due to the variation in pulse height. The time resolutions of the individual paddles are listed in Table 2.4.

Each track reconstructed in the solenoid is swum out to the TOF array and is associated with a particular paddle. The swum path length is used, along with the particle's momentum and production vertex, to determine the expected time of flight assuming the particle is a π, K and p. Corrections to the measured and expected time include the pulse height corrections, the transit time of the light in the scintillator and the dispersion of the light pulse in the scintillator due to the paddle's wedge shape. The observed elapsed time is compared with the expected times for the three mass hypotheses to determine the probability of each mass

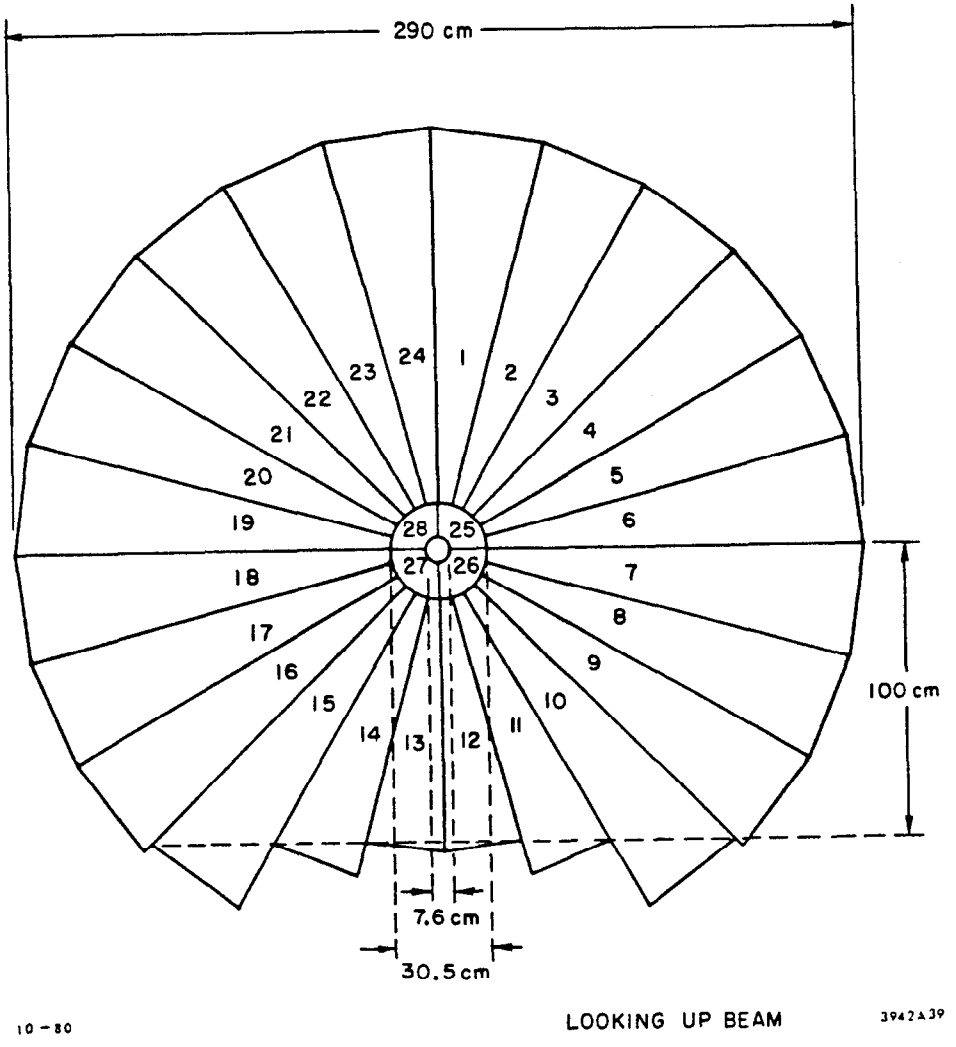

Figure 2.9. The time of flight hodoscope.

Table 2.4. The resolution of the time of flight system.

Paddle #	Resolution psec	Paddle #	Resolution psec
1	605	13	422
2	521	14	437
3	710	15	392
4	580	16	551
5	675	17	534
6	510	18	516
7	631	19	506
8	427	20	564
9	501	21	512
10	445	22	601
11	458	23	547
12	504	24	490

assignment. Using this method, three standard deviation separation is obtained for π's and K's up to momenta of $\sim$ 1.1 GeV/c and for π's and p's up to momenta of $\sim$ 2.5 GeV/c.

The phase space acceptance of the counter is limited primarily by the location of the device at $\sim$ 5 m from the interaction vertex. The advantage of the wedge geometry of the paddles is the good match to the geometry of the $\check{C}_1$ counter for triggering purposes, but this implies that the paddles can only be viewed from one end. The thickness of the scintillator is limited by the desire to keep multiple scattering of particles to a minimum as they pass from the solenoid to the dipole spectrometer. The design of this counter is therefore a compromise, but one that yields an effective identification device that complements the two Čerenkov counters.

2.5 The Dipole Spectrometer

The dipole spectrometer measures the momenta of particles produced within 50–100 mrad of the beam axis with momenta $p \gtrsim 1.5$ GeV/c. It consists of a dipole bending magnet with magnetostrictive readout spark chambers and PWC devices instrumenting the regions upstream and downstream of the magnet. The volume

upstream of the magnet is known as the "twixt" region. Figure 2.10 shows the layout of the dipole spectrometer.

2.5.1 The Dipole Magnet

The horizontal aperture of the dipole magnet is 185 cm and its vertical aperture is 102 cm. It consists of four conventional water-cooled aluminum pancake coils that together draw 7050 A at full excitation. The magnet field is oriented in the $-y$ direction and has a maximum strength (at full-power) of 18 kG, which results in a total field integral along the z-axis of 30.1 kG m (kilogauss-meter). The p_t "kick" experienced by an 11 GeV/c particle passing through the dipole is $\sim$ 0.9 GeV/c. The upstream and downstream mirror plates are located at $z = 725.2$ cm and $z = 1010.4$ cm, respectively.

Over half of the E-135 data acquisition took place with the magnet operating at full power. Because of economic constraints, the remainder of the data were taken with the magnet operating at 3750 A. This power level produces a field that is $\sim 2/3$ of the full field strength, with a total field integral of 21 kG m.

2.5.2 The Magnetostrictive Spark Chambers

Seven magnetostrictive readout (MS) spark chambers are used in the dipole spectrometer to provide the majority of the particle coordinate information. There are three chambers in the twixt region, labelled MST1, MST2, and MST3. The remaining MS chambers are positioned in the downstream region and are labelled MSD1, MSD2, MSD3, and MSD4. These chambers are designed to provide accurate coordinate information over a large area with high multiple-hit efficiency.

Each chamber consists of two spark gaps. The spark gap is defined by two planes of wires, separated by 1 cm, one pulsed to high voltage and the other remaining at ground. The wire planes are formed from wire cloth, a material consisting of parallel aluminum wires with a pitch of 11.2 wires/cm cross-woven with polyester fibres. Five of the chambers have active areas of 150×300 cm and the other two are larger with active areas of 200×400 cm (these latter two "super-chambers" are MSD3 and MSD4). The first gap in each of the chambers has the wires running horizontally and vertically to measure y and x coordinates. In the second gap, the

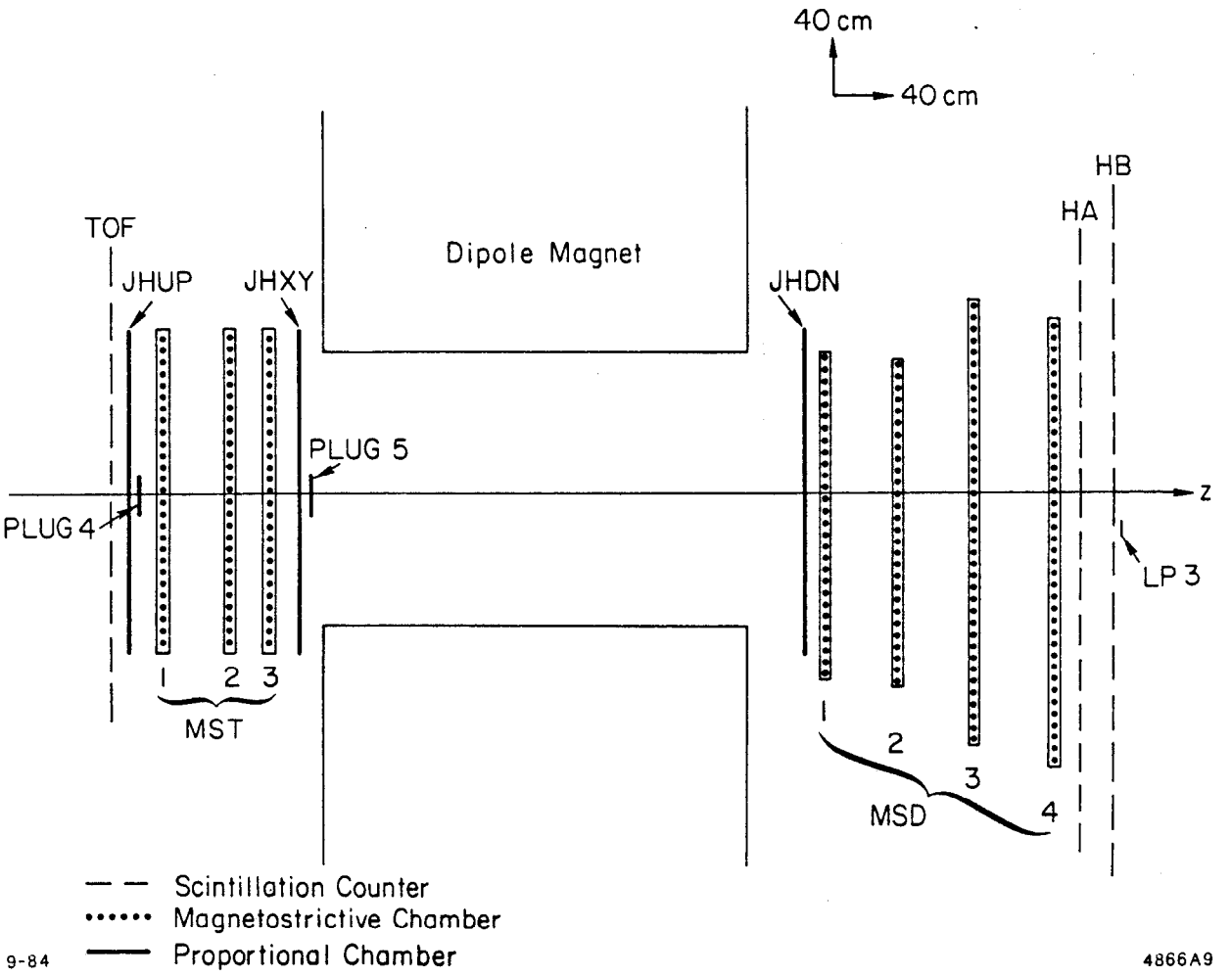

Figure 2.10. The instrumentation of the dipole spectrometer in plan view.

wires are oriented $\pm 30°$ from the vertical ($\pm 25°$ for the super-chambers) to measure the e and p coordinates ($e \equiv x\cos\theta - y\sin\theta$ and $p \equiv x\cos\theta + y\sin\theta$ with $\theta = 30°$ and 25°). Polyurethane plugs are installed in the center of each chamber in order to deaden the spark gaps to particles in the high-flux beam region, as otherwise these chambers, which have long memory times, would detect too many particles from previous interactions. The plugs in the twixt and downstream MS chambers have radii of 3.81 and 7.62 cm, respectively. The downstream chambers are offset in the horizontal bend plane so that 11 GeV/c particles entering the dipole along the beam axis pass through the deadened regions in the chamber centers.

Each of the MS wire planes is instrumented with magnetostrictive wands. The y planes of each chamber and the planes in MSD1 and MSD2 are read out using a single wand. The other planes are read out with two wands, each wand extending over little more than half the plane width, *i.e.* the pair of wands overlap in the middle of the chamber. Each wire plane has two "fiducial" wires located at either side of the plane on which a voltage pulse is induced that is detected on the wand. On planes having a pair of wands, a third fiducial wire is located in the center of the plane that provides a fiducial pulse common to both wands. Figure 2.11 show the orientation of the fiducial wires and active areas for the two spark gaps in each MS chamber.

At every event trigger, a thyratron generates a high voltage pulse across each gap, and a spark occurs across the gap where a particle has left a trail of ionization. The current pulse associated with the spark travels down the wire mesh cloth and induces an acoustic signal on the wand. The fiducial wires are simultaneously pulsed so that acoustic pulses at the location of each fiducial wire are induced. These acoustic signals travel down to the end of the wand where they are detected with a pickup coil. The time of arrival of each pulse is digitized and stored away in a time digitizer circuit located in an ANNA module.[32]

The time of arrival of each pulse is digitized with a 20 MHz clock. For a typical wand, this implies a wand coordinate digitization of $\sim$ 0.027 cm. The resolution of each chamber is a function of the wand as shown in Table 2.5. The wands are oriented horizontally for the e and p planes so that the coordinate uncertainty for

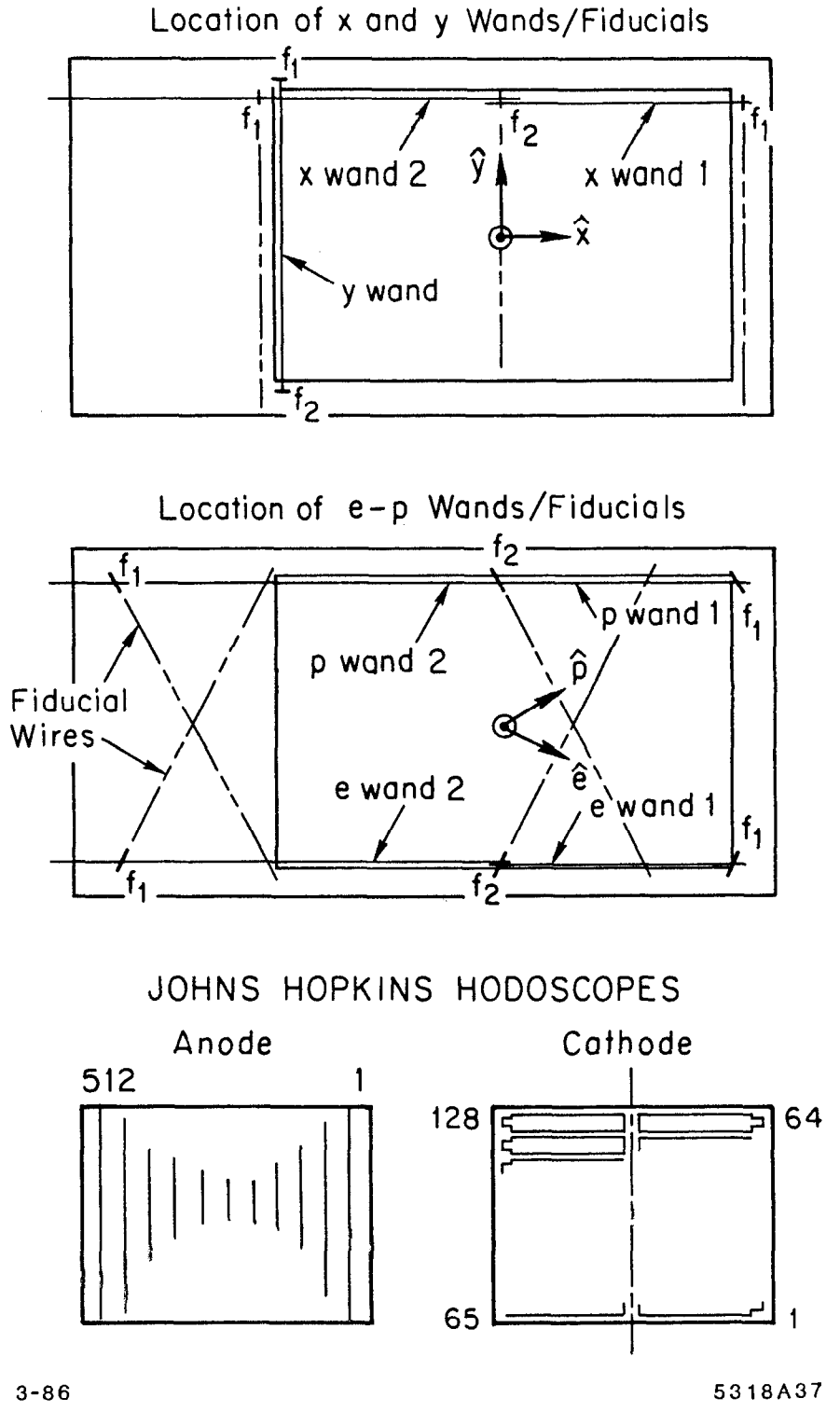

Figure 2.11. The chambers in the dipole spectrometer. The active areas and fiducial wire locations for shown for an x–y and e–p spark gap. A Johns Hopkins anode plane and the cathode segmentation of JHXY are also illustrated.

Table 2.5. The resolution of the MS chambers. The table lists the coordinate setting error for each wand.

Plane	Resolution cm		Plane	Resolution cm	
	Wand 1	Wand 2		Wand 1	Wand 2
MST1 x	0.0648	0.0706	MSD1 x	0.0830	
MST1 y	0.0539		MSD1 y	0.0400	
MST1 e	0.0745	0.0646	MSD1 e	0.1056	
MST1 p	0.0708	0.0576	MSD1 p	0.0926	
MST2 x	0.0564	0.0583	MSD2 x	0.0852	
MST2 y	0.0637		MSD2 y	0.0876	
MST2 e	0.0921	0.0740	MSD2 e	0.0768	
MST2 p	0.0944	0.0722	MSD2 p	0.0603	
MST3 x	0.0501	0.0516	MSD3 x	0.0709	0.0758
MST3 y	0.0569		MSD3 y	0.0598	
MST3 e	0.0883	0.0684	MSD3 e	0.0625	0.0535
MST3 p	0.0882	0.0665	MSD3 p	0.0473	0.0598
			MSD4 x	0.0683	0.0760
			MSD4 y	0.0463	
			MSD4 e	0.0641	0.0678
			MSD4 p	0.0641	0.0678

these wands is reduced by a factor of $\cos\theta$ ($\theta = 30°$ and $25°$ for the normal and super-chambers respectively).

Successful operation of an MS wand is possible only if the ambient magnetic fields do not change the direction of the wand's magnetization. The twixt region has strong stray fields so that it is necessary to magnetically bias the wands of the three twixt MS chambers. This is done with a coil of wire wound around each wand that is pulsed with approximately 10-30 A of current during the beam spill. Despite this, the MS chambers in the twixt region have substantially lower efficiency for detecting particles relative to the efficiencies of the downstream chambers.

2.5.3 The Proportional Hodoscopes

There are three PWC devices in the dipole spectrometer, known as JHUP, JHXY, and JHDN. These chambers, constructed by a group from Johns Hopkins

University, consist of a single plane of 512 vertical wires with a wire spacing of approx 4.23 mm. The cathodes of JHUP and JHDN are made of an aluminum wire and polyester fibre mesh, positioned to form a nominal gap width of 1.27 cm. The cathode of JHXY is a segmented aluminum-mylar foil similar to the ones used in the other PWC chambers. The segmentation is in the form of 64 horizontal strips 2.62 cm wide with a 0.16 cm gap between each strip. The strips are divided at the mid-plane of the cathode resulting in 128 half-strips, each of which is electrically connected to the corresponding half-strip on the adjacent cathode in order to improve the signal strength. Figure 2.11 shows a sketch of a JH anode plane and the JHXY cathode segmentation.

These devices provide in-time corroboration and position information for tracks passing through the dipole spectrometer; JHUP and JHXY are located at the upstream and downstream ends of the twixt region respectively, and JHDN is located immediately downstream of the dipole gap. The JHXY cathode efficiency is quite poor (~50%) and so it is of marginal benefit in the dipole track reconstruction algorithm.

2.5.4 The Scintillator Hodoscopes

Two large scintillator hodoscope arrays, HA and HB, are located immediately behind the last MS chamber in the downstream region. The two counters are constructed of two rows of scintillator paddles, as shown in Fig. 2.12. Each row in the HA hodoscope consists of 21 paddles, the center paddle having dimensions of 10.16×83.82 cm and the remaining paddles being 20.32×83.82 cm. The center paddle in each row is positioned to form a 10.16×10.16 cm hole in the middle of the array through which non-interacting beam particles pass. The HB array is composed of two rows of 38 counters. The paddles are 83.82 cm long, with the center 24 paddles having widths of 10.16 cm and the outer 14 paddles having widths of 15.24 cm. The center paddles are arranged to form a 10.16×10.16 cm beam hole. These counters are used to trigger the spectrometer on events that have particles in the dipole spectrometer and provide in-time corroboration of tracks during the dipole track reconstruction.

A circular counter with a radius of 9.84 cm, called LP3, covers the beam hole

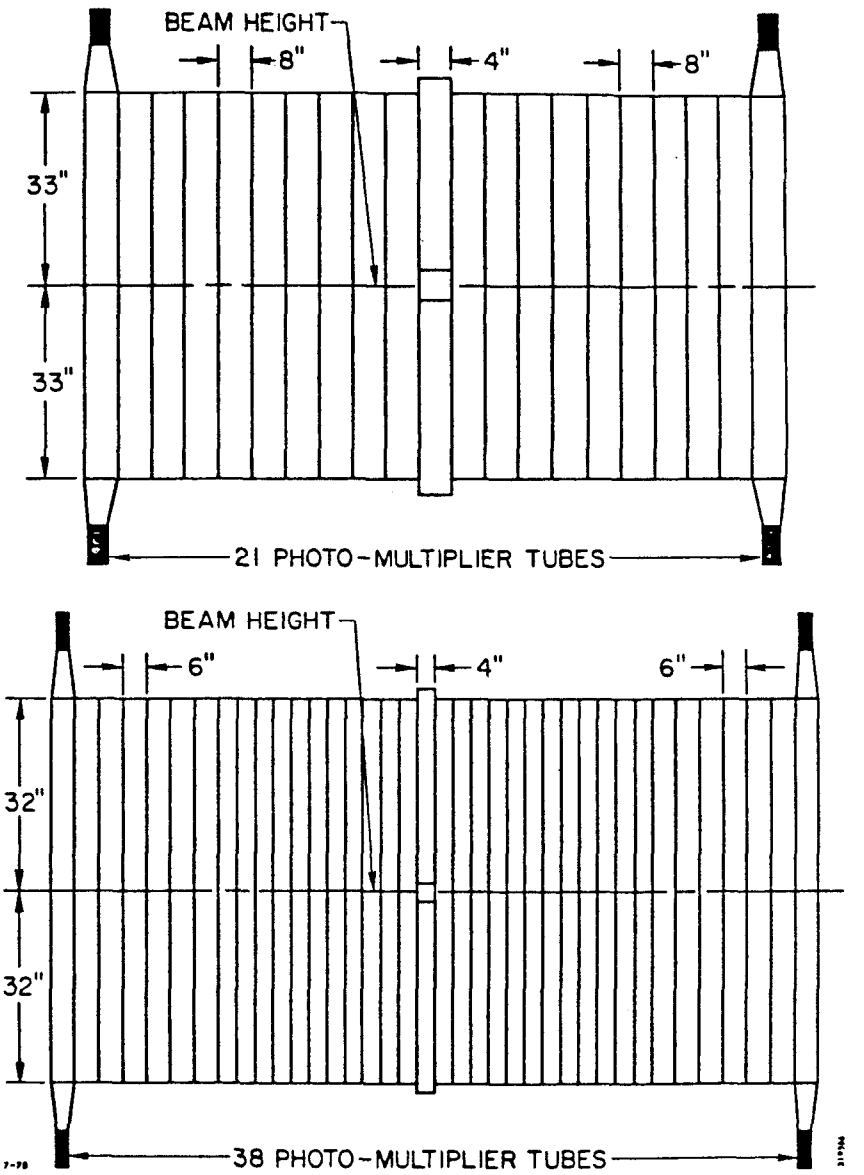

Figure 2.12. The HA and HB counters.

in the HA and HB counters. It is used in anti-coincidence in the event trigger to ensure that the incoming beam particle interacts in the target.

2.5.5 *The $\check{C}_2$ Čerenkov Counter*

The most downstream element of the LASS spectrometer is the $\check{C}_2$ counter. It is a threshold Čerenkov counter optically segmented into eight cells whose purpose is to provide K/π separation for particles passing through the dipole magnet with momenta above 3.5 GeV/c.

The counter consists of a box filled with Freon 12 (CCl_2F_2) that acts as a Čerenkov radiator. Particles enter the box through a 2 mm thick aluminum window and pass through a minimum of 1.75 m of gas. The Čerenkov photons radiated by the particle strike one or more of the eight mirrors located at the back of the counter. Light striking a particular mirror is reflected into one of eight light-collecting "horns" that focus the light onto the photocathode of a photomultiplier tube. Four of the horns and photomultipliers are located at the top of the counter and the remaining four are located at the bottom. The mirrors are organized into two rows of four mirrors each, with each row inclined approximately 10° degrees from the vertical.

The pulse height from the photomultiplier tubes is proportional to the amount of Čerenkov light striking a particular mirror. For this choice of radiator gas, π's and K's have momentum thresholds for producing Čerenkov light of 2.9 and 10.3 GeV/c. The effective momentum threshold of each cell is higher than this radiation threshold because of the geometry and location of the counter relative to the dipole magnet. With the magnet operating at full power, these effective thresholds range from 3.0 to 3.5 GeV/c.

3. The Event Trigger, Data Acquisition and Calibration

3.1 The Trigger Logic

The event trigger for experiment E-135 requires that the incident beam particle interact in the target and produce at least two charged secondaries. The spectrometer, in effect, triggers with high efficiency on the entire K^-p cross section for charged particle production. In addition to this physics trigger, the spectrometer also triggers on particular subsets of events that are used for monitoring and diagnostic purposes.

The implementation of the trigger is a logic circuit that consists of two separate components. The first is the beam trigger logic that identifies good beam candidates that enter the target. The second is the cluster logic that has the responsibility of deciding when two or more charged secondaries have been produced in the target.

3.1.1 The Beam Trigger

An interacting beam particle is defined by requiring that: (1) an incoming beam particle is identified as a kaon; (2) the particle enters the target; and (3) no more than one particle enters the target within the trigger time resolution. Figure 3.1 is a schematic drawing of the beam trigger logic circuit.

A beam particle is unambiguously identified as a K through the use of the upstream Čerenkov counters, $\check{C}_\pi$ and $\check{C}_K$. Since $\check{C}_\pi$ is set to count only π's while $\check{C}_K$ counts both π's and K's, no signal in $\check{C}_\pi$ and a signal in $\check{C}_K$ unambiguously identifies the beam particle as a K. This is written as $\check{C}_K \wedge \overline{\check{C}_\pi}$.

The RING (R) and SY counters determine if the beam particle enters the target. Requiring that there is a signal in SY and no signal in R ensures that the incoming particle goes into the target and is not accompanied by additional "halo." A signal from the SE counter is also required. These requirements are schematically expressed as $SE \wedge SY \wedge \overline{R}$.

The $\Theta\Phi$ counter is used to ensure that the incoming particle enters the target at least 20 nsec before and after any other beam particle. Briefly, the signals from this counter are ORed together to create the logic signals $\Theta \geq 1$ or $\Phi \geq 1$ ($\Theta\Phi \geq 1$), and $\Theta \geq 2$ or $\Phi \geq 2$ ($\Theta\Phi \geq 2$). A beam particle candidate will generate a $\Theta\Phi \geq 1$ signal.

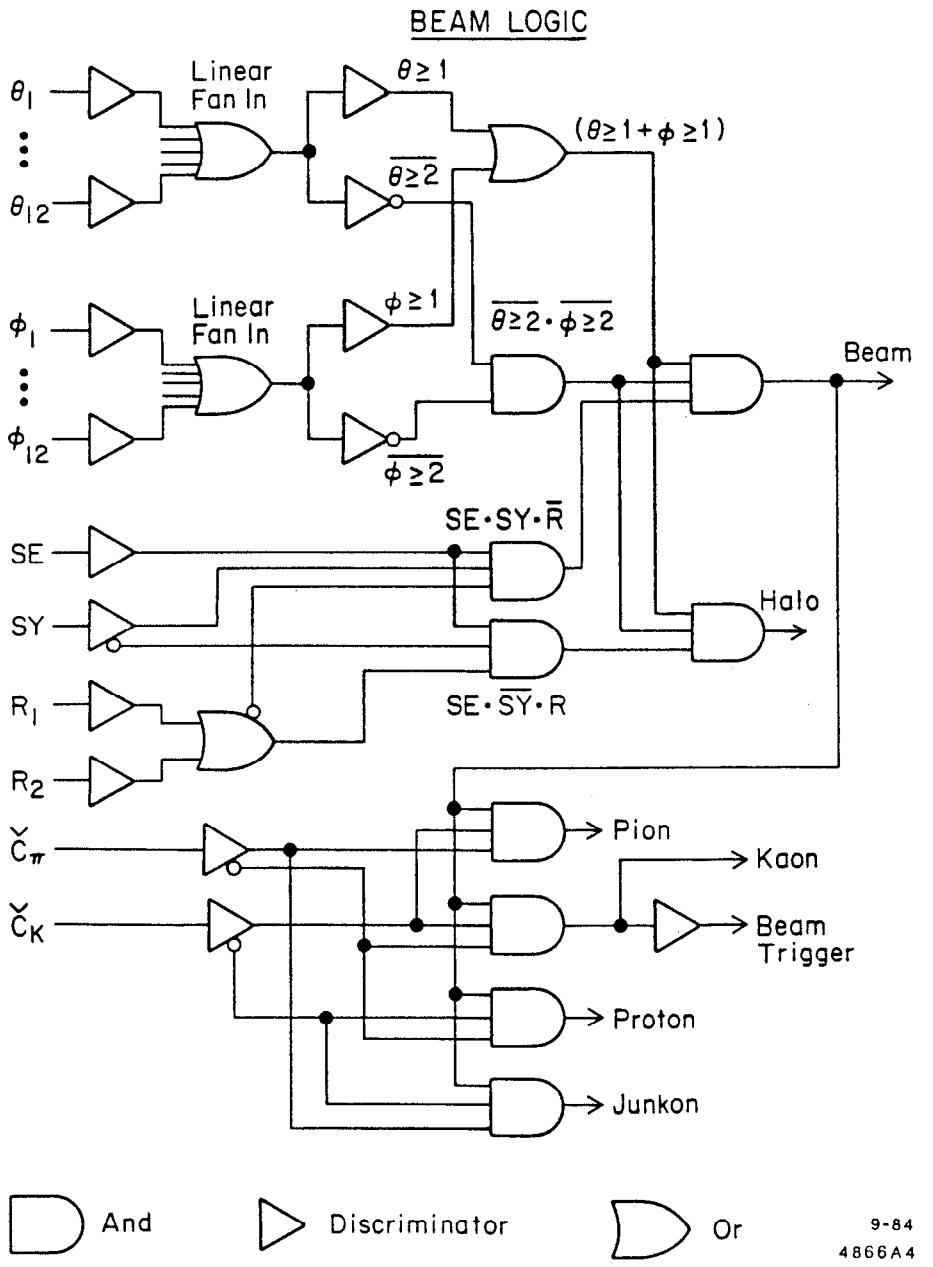

Figure 3.1. The beam trigger logic.

Another particle striking this counter within $\sim$ 20 nsec before or after this candidate will generate a $\Theta\Phi \geq 2$ signal that vetoes the candidate beam. This ensures that when more than one beam particle enters the spectrometer during a beam spill, the two particles are widely enough separated in time so that the PWC's and scintillator devices in the spectrometer can discriminate between the two interactions in the event that both beam particles interact in the target. The time window of $\pm$20 nsec is determined by the SE counter's capability of resolving the signals generated by two successive beam particles. Schematically this requirement is written as $\Theta\Phi \geq 1 \wedge \overline{\Theta\Phi \geq 2}$.

The complete beam trigger (BT) requirement is:

$$BT = \Theta\Phi \geq 1 \wedge \overline{\Theta\Phi \geq 2} \wedge SE \wedge SY \wedge \overline{R} \wedge \check{C}_K \wedge \overline{\check{C}_\pi}. \tag{3.1}$$

3.1.2 The Cluster Logic

The purpose of the cluster logic is to determine when two or more charged particles exit the region surrounding the target. This is accomplished by counting the number of hits in the two inner cylindrical PWC's and in the first two plug chambers. These four devices conceptually form two concentric cylinders that wrap around the target and that are closed at the downstream end. The anode electronics of these devices determine the number of anode clusters ("hits") detected on each plane.

The number of clusters in each anode plane is used to form the logic signals listed in Table 3.1. To ensure that a second beam track does not count in the cluster logic, the central 32 wires of the plug 1 anode planes are not included in the cluster logic. The remaining wires are ORed together to form the cluster multiplicities employed in Table 3.1. In plug 2, only the central wires in each plane (the central 64 wires for the y and e planes and the central 80 wires for the x plane) are connected to the cluster logic. The "hole" in plug 1 deadens the trigger for events that have tracks produced entirely in the very forward direction; the "anti-hole" in plug 2 ensures that it is still possible to detect when at least one particle is

Table 3.1. The cluster logic signals. CYL_i denotes the number of clusters in the ith cylindrical PWC.

Signal	Definition
$PLG_1 \geq 1$	at least 2 plug 1 planes have ≥ 1 hit
$PLG_1 \geq 2$	at least 2 plug 1 planes have ≥ 2 hits
$PLG_2 \geq 1$	at least 2 plug 2 planes have ≥ 1 hit
$PLGS \geq 1$	$PLG_1 \geq 1 \wedge PLG_2 \geq 1$
$CYL \geq 2$	$CYL_2 \geq 1 \wedge (CYL_1 \geq 2 \vee CYL_2 \geq 2)$
$CYL \geq 3$	$CYL_2 \geq 1 \wedge (CYL_1 \geq 3 \vee CYL_2 \geq 3)$
$\overline{CYL \geq 3}$	$\overline{CYL_1 \geq 3 \wedge CYL_2 \geq 3}$
$CYL = 2$	$CYL_2 \geq 2 \wedge \overline{CYL \geq 3}$
$CYL = 1$ *or* 2	$CYL_2 \geq 1 \wedge \overline{CYL \geq 3}$

very forward. Each logic signal formed from the cylinder cluster logic includes the requirement that $CYL_2 \geq 1$. This reflects the difference in noise levels between the two inner cylindrical PWCs; being located farther from the beam axis, cylinder 2 has a substantially lower rate of accidental hits.

3.1.3 The Event Trigger Definition

The complete event trigger is formed from the logical OR of four separate physics triggers, labelled $T0(i)$, $i = 1$ to 4, and four monitoring triggers labelled $T1$, $T2$, $T3$, and $T4$. The latter four triggers are "scaled-down," *i.e.* only a fraction of the events that trigger on these trigger types are recorded. For this reason they are known as the minority triggers. The event trigger logic uses the beam trigger (BT), the cluster logic signals and the number of hits in the TOF, HA, and HB counters in the trigger decision. The four physics triggers are defined as:

$$
\begin{aligned}
T0(1) &= BT \wedge \overline{LP} \wedge TOF \geq 1 \wedge ((PLG_1 \geq 1 \wedge CYL \geq 2) \vee CYL \geq 3) \\
T0(2) &= BT \wedge \overline{LP} \wedge \overline{HA \geq 1 \wedge HB \geq 1} \wedge CYL = 2 \\
T0(3) &= BT \wedge \overline{LP} \wedge TOF \geq 1 \wedge \\
&\qquad (PLGS \geq 1 \wedge CYL = 1 \textit{ or } 2 \wedge HA \geq 1 \wedge HB \geq 1) \\
T0(4) &= BT \wedge \overline{LP} \wedge TOF \geq 2 \wedge PLG_1 \geq 2
\end{aligned}
\tag{3.2}
$$

$T0(1)$ is designed to trigger on events with three or more charged secondaries, at least two of which pass through the cylinders. $T0(2)$ triggers on events where only two particles are produced transverse to the beam and are detected in the cylinders; this trigger excludes events were at least one particle is produced forward enough to pass through the dipole. $T0(3)$ triggers on events where one or more particles are forward and where one or two particles are produced transverse to the beam. This trigger relies on the "anti-hole" in plug 2 to detect the very forward particle(s). $T0(4)$ triggers primarily on events where two or more particles are produced in the forward region.

Two modifications were made to the trigger over the course of the E-135 data taking. The first change was to loosen the $PLG_1 \geq 2$ requirement to demand only one of the three plug 1 planes to have 2 or more hits. This made the $T0(4)$ trigger less sensitive to any inefficiency of plug 1. The second change was the removal of the $HA \geq 1 \wedge HB \geq 1$ requirement in $T0(3)$. The effect of this was to include events that contain forward-produced particles that do not pass through the dipole.

The trigger efficiency for the $\bar{K}^\circ \pi^+\pi^- n$ final state is insensitive to either of these changes. For that reason, the analysis of this final state requires the accepted events to satisfy the tighter (*i.e.* the original) trigger definitions. Figure 3.2 shows the acceptance of this physics trigger for the $\bar{K}^\circ \pi^+\pi^- n$ final state. The acceptance is plotted as a function of three-body invariant mass for two different four-momentum transfer squared ($t' \equiv t - t_{min}$) intervals. The fall-off in acceptance at low $\bar{K}^\circ \pi^+\pi^-$ masses is due to the effect of the plug 1 hole in the cluster logic. At higher t', this effect is less pronounced as the charged particles are produced in general at larger angles with respect to the beam axis.

The definitions of the minority triggers are:

$$\begin{aligned} T1 &= BT \wedge \overline{LP} \wedge TOF \geq 1 \wedge HA \geq 2 \wedge HB \geq 2 \\ T2 &= BT \wedge \overline{LP} \wedge TOF \geq 1 \wedge HA \geq 1 \wedge HB \geq 1 \wedge \overline{HA \geq 2 \vee HB \geq 2} \\ T3 &= BT \\ T4 &= BT \wedge \overline{LP} \wedge TOF \geq 1 \end{aligned} \tag{3.3}$$

Each minority trigger includes a particular class of events used to monitor or calibrate the spectrometer. $T1$ is designed to be sensitive to events in which

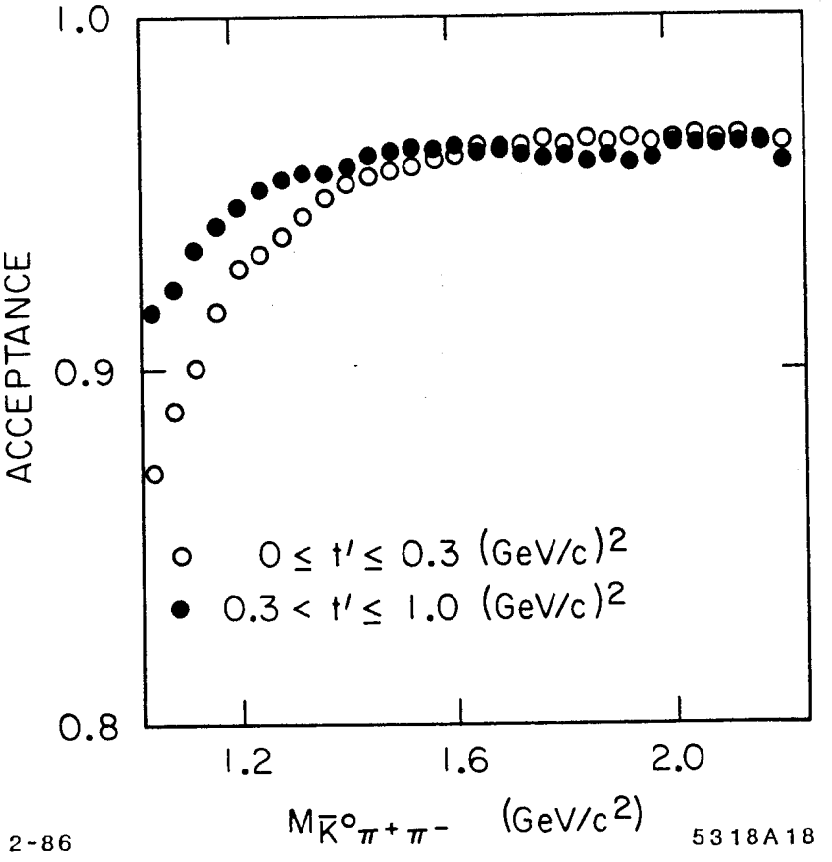

Figure 3.2. The trigger acceptance for the $\bar{K}^0\pi^+\pi^-n$ final state. The acceptance is calculated for three-body final states that decay isotropically in the three-body rest frame as a function of $\bar{K}^0\pi^+\pi^-$ invariant mass. The acceptance for two four-momentum transfer squared intervals is shown.

Table 3.2. The minority trigger rate scale factors.

Trigger Type	Scale Factor
$T1$	10
$T2$	100
$T3$	1000
$T4$	50

the beam particle weakly decays into a three-charged-prong final state. These τ-decay events are used to monitor the relative calibration of the P-hodoscope and the dipole magnet. The $T2$ trigger accepts K^-p elastic scattering events. These elastic scatters are used to monitor the momentum calibration and to perform various checks of the performance of the reconstruction algorithm in the dipole spectrometer. The $T3$ trigger yields a random sample of beam tracks and thus provides a direct measurement of the beam phase space. The $T4$ trigger provides a random sample of "interacting" events where the only requirement is that the event have a good beam track that interacts (or decays) in the spectrometer.

The raw minority trigger rates are substantially higher than the physics trigger rate. For this reason, each minority trigger is counted down using a specially designed NIM module called the trigger rate equalizer.[33] The modules scale down the raw minority trigger rates by the factors shown in Table 3.2.

The deadtime associated with an event trigger is dictated by the time needed to clear out the ionization in the spark chamber gaps ($\sim$ 15 msec), but for large events can increase due to the time needed to complete the readout of the PWC system. The livetime of the detector was $\sim$ 60% under typical running conditions.

3.2 The Data Acquisition System

The LASS data acquisition system consists of:

1. five device controllers, each one coordinating the acquisition of data from a separate data branch;
2. a DEC PDP-11/04 minicomputer that collects the data from the device controllers;
3. an IBM System 7 computer that accepts the data from the PDP-11 and sends

it to the SLAC central computer system; and

4. the SLAC TRIPLEX computer system that performs the task of logging the data onto magnetic tape.

The coordination of this data acquisition network, along with the online monitoring of the experiment, is performed using the SLAC REALTIME program[34] running in the SLAC TRIPLEX. Figure 3.3 is a schematic showing the layout of the data acquisition network.

3.2.1 The Device Controllers

The function of each device controller is to temporarily store the data from a particular group of devices until the data can be transferred to the PDP-11 minicomputer. The device controllers are either CAMAC-based or pseudo-CAMAC in design, and most of them do some preprocessing of the data. The architecture of the data acquisition system is shown in Fig. 3.4.

There are five separate data branches from the spectrometer into the memory of the PDP-11, though only four of these paths are used when an event is read out. (the fifth one is used for some online monitoring purposes and is used to read out the voltage settings (DVM's) of various devices). Each path consists of several devices that obtain and store the raw event information, and a device controller coupled with a DMA (direct memory access) unit[35] that handles the transfer of the data into the PDP-11 memory.

The first of the data branches is a series of conventional CAMAC modules that handle the signal processing of the hodoscope devices, the TDC and ADC information for the TOF and Čerenkov counters, and the signals from the instruments on the beam line. Each of the CAMAC crates is controlled with a SLAC Type U crate controller,[36] the crate controllers being daisy-chained together to form a serial data path. The data from each crate are serially passed to the DMA unit that handles the data transfer into the PDP-11 memory.

The signals from the PWC anode devices are amplified and stored in a shift register memory. The time of arrival of each anode signal relative to the event trigger is stored in the form of a 6-bit time-slot mask along with the corresponding anode wire number. The bits in the time-slot masks are set to indicate the 25 nsec

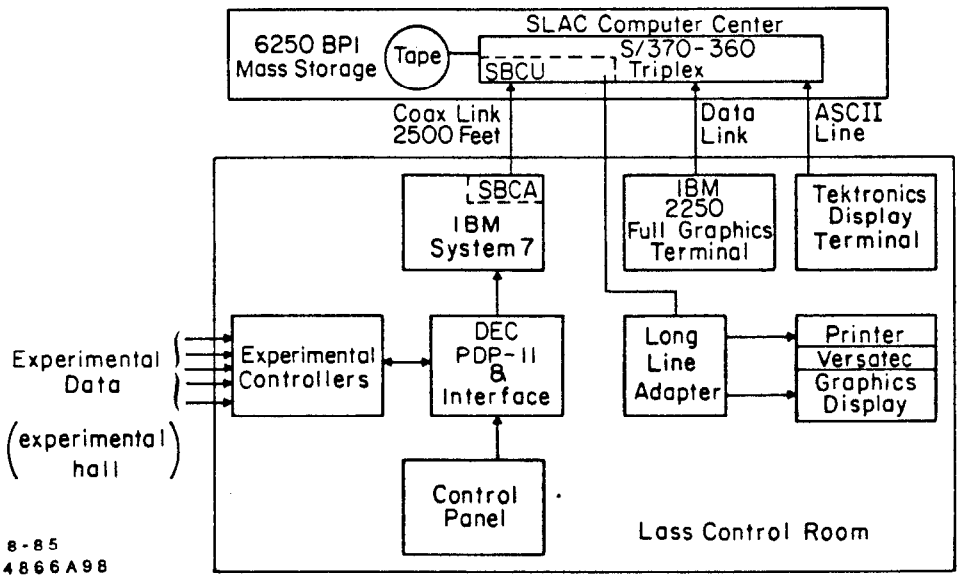

Figure 3.3. The LASS data acquisition network.

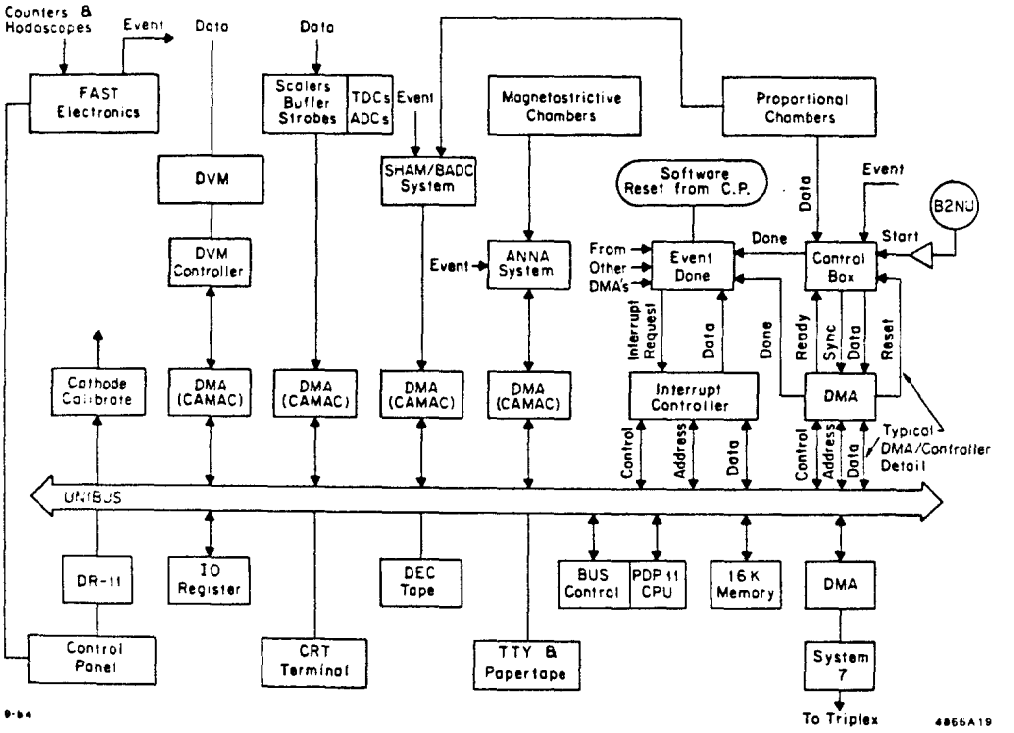

Figure 3.4. A detailed view of the data acquisition system. The data acquisition network consists of five "branches," with each branch having access to the PDP-11 memory via a DMA.

time bucket during which the signal on the anode is detected (relative to the time the beam trigger occurs). There are 16 channels of anode readout packaged on a PC board, with 16 boards filling a specially-designed crate. The entire PWC readout system is contained in 64 crates. When an event trigger occurs, a PWC crate controller (shown in Fig. 3.4) serially reads out the data in the crates, compresses the data into a list of hit wire numbers and their corresponding time-slot masks, and passes the data via the corresponding DMA into the PDP-11 memory.

The signals from the cathode foil strips are first amplified and then passed into a SHAM-IV module, a fast charge integrator that integrates the signal and stores the result in a capacitor. Each SHAM module consists of 32 individual channels. The output of each SHAM is presented to a BADC module, a 12-bit ADC multiplexor.[37] The BADC multiplexes the output of up to 20 SHAM modules, or a total of 640 channels. It digitizes the input signals and executes a micro-coded algorithm that performs a zero-suppression. There are six BADC's used in the cathode chamber readout, and they in turn are controlled by one SLAC crate controller. The DMA for this system transfers the processed data in the BADC's to the PDP-11.

The ANNA modules store all of the information from the MS system.[32] This information consists of the time of arrival of up to 15 magnetostrictive pulses on each wand. The ANNA module digitizes the time information using a 20 MHz clock and stores them in a fast TTL memory. These modules, being CAMAC based, are read out via the DMA using a standard CAMAC protocol.

In addition to these four device controllers there is a facility to read out the voltage settings of various counters as well as the contents of several scalers that accumulate data from the beginning of the current run. After every 256 events, the scaler information is automatically read out and written onto the raw data tapes.

3.2.2 The PDP-11 Minicomputer

The PDP-11/04 serves as the front-end for the data acquisition system. The information from each data branch passes directly into the PDP-11 memory through the corresponding DMA branch driver. Prior to an event trigger, the PDP-11 allocates an event buffer and partitions the buffer into four blocks. Each DMA unit is "primed" with the start address and length of one of the data blocks. When an

event trigger occurs, each DMA branch driver begins to transfer the data from the corresponding device controller. The device controller passes a data word to the DMA unit, the DMA requests control of the PDP-11 Unibus, transfers the data word into the block of memory and updates the memory address for the next word. The DMA then relinquishes control of the Unibus and waits for the next data word from the device controller. The four DMA units operate in parallel.

The data transfer through a DMA is completed when all the data have been transferred or when the allocated block in the PDP-11 memory has been filled. The completion of all the DMA's is detected by a control circuit that then sends an interrupt to the PDP-11. The PDP-11 formats the event buffer and initiates another DMA process, the transfer of the formatted event buffer to the System 7 computer.

There is room for three event buffers in the PDP-11 memory. Normally, one buffer is receiving data from the device controller DMA's, the second is being reformatted by the PDP-11, and the third is being transferred to the System 7.

3.2.3 The System 7 Computer

The purpose of the IBM System 7 is to provide the data link between the PDP-11 computer and the SLAC Triplex computer system located $\sim 1/2$ km from the detector. The System 7 reads the raw event buffer from the PDP-11 memory via a separate DMA channel, and passes the data buffer to the Triplex via a coaxial cable. The System 7 is responsible for the communications protocol on the link to the Triplex.

3.2.4 The REALTIME Operating System

The spooling of the raw data onto tape and the online monitoring of the spectrometer is performed by several "tasks" resident in the REALTIME operating system running on the Triplex computer. The SPOOLER task is responsible for receiving the data from the System 7 and writing it onto magnetic tape. It has the highest priority of all the tasks as the PDP-11 cannot enable the spectrometer for another event if the SPOOLER task is unable to process the previous event buffer. The ANALYSIS task samples the data being written to tape and processes

as many events as possible. The online processing consists of unpacking the data and performing track reconstruction using a crude form of the event processing software. The ANALYSIS task also monitors various aspects of the spectrometer, such as coordinate multiplicities and efficiencies of chambers.

The experimenter communicates with the REALTIME system and the various tasks executing under the system via an IBM 2250 Graphics Display terminal located in the experiment control room next to the spectrometer. For example, results from the ANALYSIS task such as histograms and single-event displays can be presented on the 2250 scope, and histograms can be defined or deleted in the ANALYSIS task by issuing commands to the task using the REALTIME system.

3.3 The Data Sample

The data set for experiment E-135 was acquired in three separate running periods over the course of two years. A check-out run was performed over a period of two weeks in November and December, 1980. The subsequent data-taking runs took place during:

- February 4, 1981 through March 3, 1981;
- May 9, 1981 through June 29, 1981; and
- March 27, 1982 through May 27, 1982.

In all three cycles, data were taken with K^- and K^+ beams. The K^- data constitute approximately 80% of the recorded events.

The K^-p data set is divided into $\sim$ 2200 runs. Each run consists of $\sim$ 55 000 events and fills a single 6250 bpi (bytes/inch) tape volume. A run was stopped when the raw data tape reached 97% capacity although occasionally it was terminated prematurely when the data acquisition process had to be interrupted.

Besides the two minor trigger changes described earlier, the only other change in running conditions occurred after the second data-taking cycle, when the dipole magnet was reduced to half-power. This effectively breaks the K^- data sample into two separate data sets. This difference, although accounted for properly in the subsequent analysis, has little affect on the reconstruction efficiency or resolution of the $\bar{K}^\circ \pi^+\pi^- n$ final state.

3.4 The Alignment and Calibration Procedures

3.4.1 Chamber Alignment

The absolute alignment of the entire LASS spectrometer is an enormous undertaking because of the large number of discrete components in the system. A systematic method is followed to ensure that all the chambers are aligned correctly with respect to an absolute reference frame.

The absolute reference point is defined by the gap chambers as they are amenable to direct survey. The wire-by-wire spacing of the anodes on each gap chamber plane is known from a survey performed prior to the installation of the chambers, and the z-locations of these planes are obtained from absolute survey measurements. The cathode foil alignment is determined in two steps. Firstly, a correction is made for the distortion of the cathode foils when they are stretched over the chamber frames. This distortion is measured after the foils are stretched, the measurements are fitted to a fifth-order polynomial function that parametrizes the local displacement of the cathode strip with respect to its nominal position as a function of the x–y position on the cathode plane, and this function is then used to correct the local coordinate values obtained from the pulse height data. In the second step, single wire anode coordinates are matched to the corresponding x values calculated using pairs of cathode coordinates. For a large ensemble of such matchpoints, a χ^2 function defined by

$$\chi^2 = \sum \left(\frac{x_{meas} - x_{calc}}{\delta x_{calc}} \right)^2$$

is minimized by allowing a small anode plane translation (~20–50 μ) and a rotation of each cathode foil about its center (the largest rotation is ~0.4 mrad). The coordinate system is then defined on the basis of gap 1 and gap 3.

The other chambers in both the solenoid and dipole spectrometer are then localized relative to the two gap chambers using events collected with both magnets turned off so that all particles produced in the target follow straight-line trajectories. In this procedure, the straight-line track segments are reconstructed using only the two gap chambers. The residuals of the measured and predicted track positions in

the other planes are collected for a large number of tracks and shifts are determined that would bring each plane into alignment with the gap chambers. These shifts include both translations in the x–y plane and small rotations of the entire plane about any of the coordinate axes. The procedure is repeated with the anode planes in the shifted locations and a new set of corrections are determined. The process converges in a few iterations to a set of anode plane positions that are consistent with the gap chamber positions. (In particular, gap 2 required a very small ($\sim$0.2 cm) translation in x and y in order that it be aligned with gaps 1 and 3.)

The cylindrical PWC devices require special handling because of the need to measure both the position of the chambers and the departure of each chamber from cylindrical symmetry. This alignment is performed after all the planar chambers are aligned as described above. The alignment procedure requires the use of helical tracks so that the radii of each cylinder can be determined unambiguously. Tracks are reconstructed in the planar chambers and are projected into the cylindrical devices. The residuals of the measured and predicted track positions are accumulated and are converted into shifts of each cylindrical chamber in both position and orientation. This procedure is iterated until the inner four cylinders are aligned relative to the planar chambers. The outer 2 cylinders are then aligned relative to the inner four.

The beam chambers are aligned using special data runs in which the event trigger is modified to only require a good beam track. In these runs, the non-interacting beam tracks are reconstructed in the plug and full-bore chambers and are projected into the beam chambers. The residuals of the beam chamber coordinates and track positions are accumulated and the beam chamber positions are adjusted until they are in alignment with the plug and full-bore chambers.

The alignment of the chambers in the dipole spectrometer is determined with the magnet-off data by extrapolating tracks found in the solenoid chambers into the twixt region and accumulating the coordinate residuals of the tracks in all of the devices. The alignment of the MS chambers is performed under the assumption that the wands are linear in behavior, *i.e.* the speed of propagation of magnetostrictive pulses along each wand is constant. The devices in the downstream region are aligned in a similar manner.

To correct for the non-linearities in the wands, a subsequent alignment procedure is performed independently in the twixt and downstream MS chambers. Lines are found in each region and the coordinate residuals are accumulated as a function of the coordinate position along the wand. These residuals are then used to form a look-up table that is used to correct the reconstructed MS coordinates. This alignment procedure is repeated until the corrections converge.

The alignment of the anode planes in the spectrometer was constant over the course of the experiment, except for a few occasions when the plug-gap chamber assemblies were withdrawn for repair and subsequently re-installed. Each time the charge of the beam was reversed, the downstream MS chambers and the HA and HB hodoscopes were shifted to take into account the reversed bend of the beam particle as it passes through the dipole magnet. At each such change, alignment data were taken in order to determine the revised positions of these devices.

The MS chamber alignment varied substantially over periods as short as a few hours, an affect attributed to instabilities in the magnetostrictive wands. This variation was monitored offline so that whenever the alignment degraded significantly, a new internal MS alignment was performed. This re-alignment was performed $\sim$ 50 times over the course of the experiment.

3.4.2 Electronics Calibration

The ADC readouts for the Čerenkov, TOF, and cathode strip devices are the only parts of the data acquisition electronics that demonstrate significant run-to-run variation over the course of the experiment. In the case of the Čerenkov and TOF systems, this variation takes the form of pedestal fluctuations. These fluctuations are taken into account offline by determining the pedestal values at the beginning of each run using a sample of 100 events and using these values for the entire run.

The cathode readout electronics, employing the SHAM-BADC modules, present a more complex situation. For these devices, it was necessary to monitor both the pedestal and the gain of each channel. For this purpose, a special calibration circuit inserts a fixed amount of charge at the front end of each of the amplifier circuits. The resulting ADC values are recorded on the event data tape and subsequently used to determine the relative gain of each channel as a function

of time. The data runs are divided into 42 blocks defined by changes in the gain of a set of channels (normally caused by the replacement of one or more SHAM modules). A set of calibration constants is determined for each block using these calibration data stored on the raw event tapes.

The possibility of short-term pedestal fluctuations in the cathode readout was addressed in the last running period using an automated procedure to determine the pedestal values. The pedestals for each channel were continuously updated during the data acquisition and the most current values were written to tape periodically through each run. This information was used during the event processing to virtually eliminate any pedestal fluctuations. However the overall improvement in the performance of the cathode devices was small, reflecting the rarity of significant short-term pedestal fluctuations.

3.4.3 Time of Flight Calibration

The time of flight system is calibrated offline using processed data. The conversion of measured TDC counts in a paddle into particle flight time takes into account the following affects:

- "time walk" of the TOF discriminators due to variations in light pulse;
- "time walk" of the SE start pulse;
- the light transit time in the scintillator;
- the timing offset between the SE start pulse and the TDC module;
- the distortion in the light pulse at the photomultiplier end of the scintillator due to the wedge-shaped geometry of the paddles; and
- run-by-run variations in the behavior of one or more of the above effects.

The parametrization used to convert the observed TDC value in a counter into measured time t_{meas} in nanoseconds is given by

$$t_{meas} = \alpha_1 TDC - \alpha_2 - \frac{\alpha_3}{\sqrt{ADC_{SE}}} - \frac{l}{v} - \frac{\alpha_4 + \alpha_5 l}{\sqrt{ADC_{TOF}}} - \alpha_6 l^2 - \alpha_7 l^3. \qquad (3.4)$$

The variables in Eqn. 3.4 are defined in Table 3.3. The data runs in the experiment are grouped into 13 blocks, delimited by changes in the running conditions or modifications to one of the TOF system components. A set of constants is

Table 3.3. The variables in the TOF correction formula.

Measurements	Definition
l	measured light path in scintillator
TDC	measured TDC of TOF counter
ADC_{SE}	measured SE ADC
ADC_{TOF}	measured TOF ADC
Constant	**Definition**
v	speed of light in scintillator
α_1	conversion from TDC counts to nanoseconds
α_2	timing offset of TOF module and SE counter
α_3	constant for SE time walk correction
α_4	constant for TOF time walk correction
α_5	correlation between light path length in paddle and pulse height because of paddle geometry
α_6, α_7	higher order corrections to v due to paddle geometry

determined for each TOF channel in every block by fitting the calibration constants to a sample of $\beta \equiv v/c = 1$ ($p \geq 3$ GeV/c) negatively-charged tracks obtained from a subset of the runs in the block.

The timing offset α_2 is the only calibration constant that has significant run-to-run variations within a block. To correct for this, the average raw TDC count for fast particles was accumulated on a run-by-run basis during event processing. The variation in this average TDC over the block of runs is used to remove any remaining variation of the timing offset. This calibration procedure resulted in TOF measurements that are stable over the course of the entire experiment.

3.4.4 *Momentum Calibration*

The momentum calibration of the spectrometer is performed by determining the absolute momentum calibration for the dipole spectrometer, and then ensuring that the solenoid spectrometer and beam P-hodoscope agree with the dipole spectrometer in the cases where two or more devices provide overlapping momentum information.

Although the dipole magnetic field was measured prior to the experiment, it is still necessary to check this measurement by performing an absolute calibration of the dipole spectrometer. This calibration is performed by reconstructing K° decays in which at least one of the daughter particles passes through the dipole spectrometer. The shift in the measured $\pi^+\pi^-$ invariant mass of the K° parent from the expected value is converted into a scale factor that is applied to the dipole magnetic field map. This scale factor is 1.007 for the dipole at full-field and approximately 1.004 for the dipole operated at half-field.

K^-p elastic-scatter events and fully reconstructed τ-decays of the beam particle provide two independent ways of calibrating the dipole magnet and P-hodoscope. Fully reconstructed elastic events in which the final state K^- is reconstructed in the dipole are used to directly measure the relative calibration of the P-hodoscope and the dipole for 11 GeV/c particles. The final state of a τ-decay event consists of three particles, each having an average momentum of $\sim$ 3.6 GeV/c. The cases where all three daughters are measured with the dipole spectrometer provide another check of the dipole-beam calibration, in which the dipole is now measuring substantially slower particles.

On a run-by-run basis, it is possible to measure $\Delta_{p_z} \equiv p_{final} - p_{beam}$ for both the elastic and τ final states. If the momentum calibration of the P-hodoscope or dipole is systematically drifting, then the same trend should be seen in Δ_{p_z} from the elastic and τ-decay events. On the other hand, if the dipole momentum was systematically changing because of a misalignment of the twixt or downstream chambers, the effect on the elastic and τ-decay events would be different since the τ-decays involve particles that have dipole bend angles $\sim$ 3 times larger than an elastic event, *i.e.* the effect of a position measurement systematic on the τ-decay Δ_{p_z} would be on average three times smaller than on the elastic Δ_{p_z}.

Figure 3.5 shows the measured Δ_{p_z} for both classes of events as a function of run number for most of the E-135 data runs. From the plot it is possible to group the runs into several blocks. The block boundaries happen to fall at points where the beam charge is changed and the downstream chambers in the dipole are shifted to take into account the reversed beam trajectory through the aperture of the dipole magnet. The detailed structure in the plots between beam changes

is very similar, suggesting that either the P-hodoscope or dipole scale factor is drifting systematically over those periods. However there are discontinuities in Δ_{p_z} at block boundaries, especially for the elastic events. Because no discernible change was noted in the reconstructed $\pi^+\pi^-$ invariant mass for K° decays measured using the dipole, the variation in Δ_{p_z} from the τ-decays is assumed to reflect variation in the P-hodoscope calibration, most likely due to short term changes in the secondary beam line optics.

The relative variations in Δ_{p_z} for the τ-decays and elastic scattering events can be understood as coming from variations in the alignment of the dipole spectrometer. To remove this effect, an additional correction in the form of an overall angle offset between the twixt and downstream chambers of the dipole spectrometer is employed to adjust the dipole momentum calibration. The largest fluctuations implied by the differences in Fig. 3.5(a) and 3.5(b) are on the order of 0.5 mrad, which corresponds to a systematic shift of approximately one σ in the downstream MS coordinate measurements. The magnitude of this effect is consistent with the uncertainty inherent in the procedure used to align the dipole spectrometer.

3.4.5 Calibration of the dE/dx System

To use the pulse height information from the cylindrical cathode chambers as ionization measurements, the response of each cylinder to particles traversing its gas gap has to be known. The observed pulse height in a cylinder chamber PH is path-length corrected to relate it to the particle's mean ionization per unit gas length I by

$$I = f_\theta(\theta) PH \tag{3.5}$$

where θ is the angle defined by the particle's trajectory through the cylinder and the vector normal to the surface of the cylinder, and $f_\theta(\theta)$ is the path length correction. With this definition, $\cos\theta$ is inversely proportional to the path length of the particle in the proportional chamber gas. Hence one would expect that $f_\theta(\theta) \propto \cos\theta$. However the observed pulse height still shows a path length dependence after correction by $\cos\theta$. The additional path length correction is shown in Fig. 3.6(a).

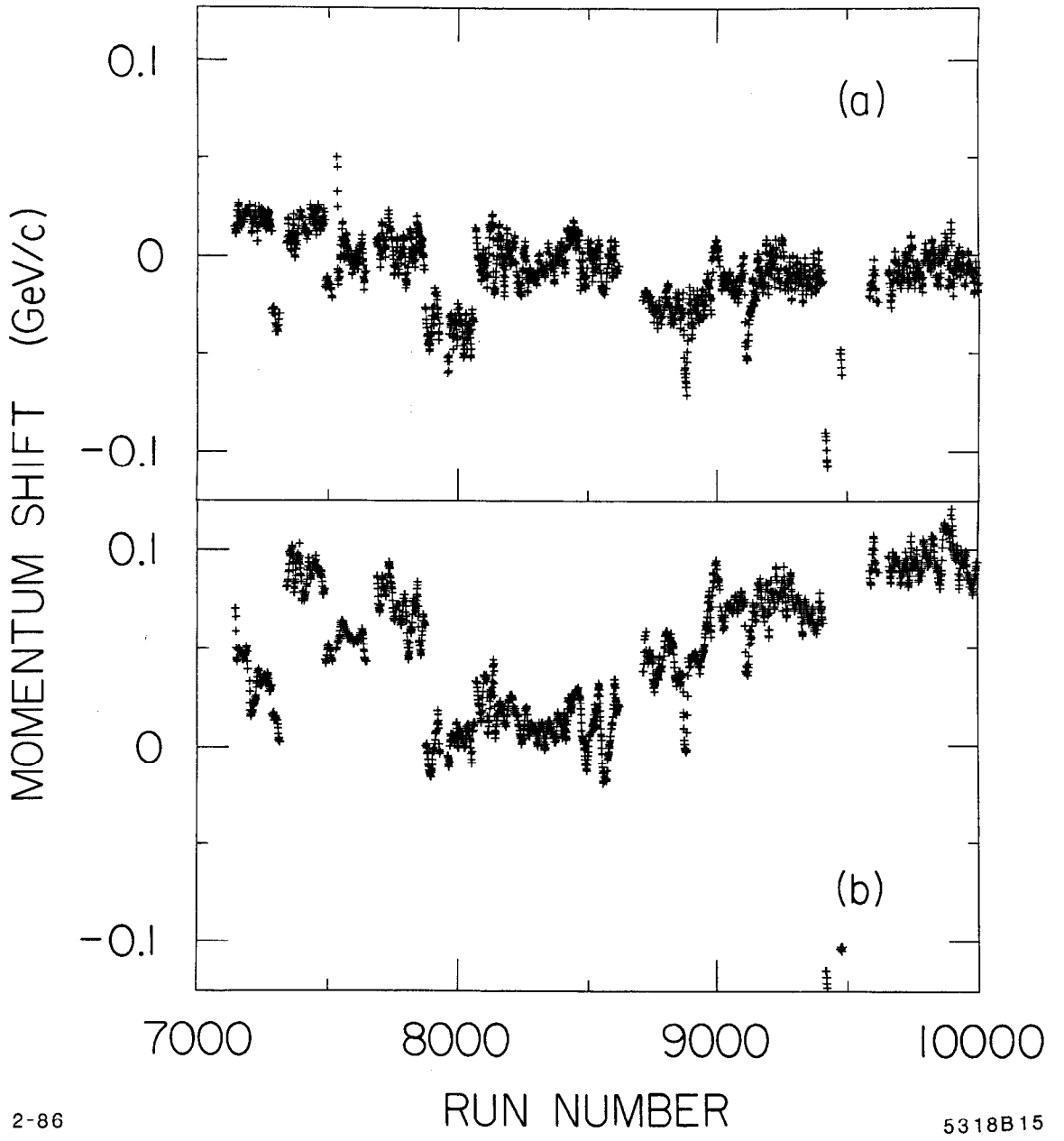

Figure 3.5. The dependence of Δ_{p_z} on run number. The measured $\Delta_{p_z} \equiv p_{final} - p_{beam}$ for τ-decay events (a) and elastic events (b) is plotted as a function of run number.

Although the exact mechanism causing the remaining path length dependence is not well understood, it probably arises from saturation effects in the gas. This remaining path length dependence is removed empirically by parametrizing the data in Fig. 3.6(a) with a polynomial quadratic in $\cos\theta$.

The path length correction is run-dependent due to gain variations in the chamber gas from run-to-run. Therefore, an offline calibration procedure empirically determines this correction for each cylinder and each run using relativistic ($\beta \geq 0.9$) negatively-charged particles that intersect one or more of the cylindrical chambers. The observed pulse heights are multiplied by $\cos\theta$ and the mean pulse height for each cylinder as a function of $\cos\theta$ is determined (this is how Fig. 3.6(a) was obtained). These data are then fit to a quadratic polynomial forced to 1 at $\cos\theta = 1$.

After the path-length correction is determined for a run, the β-dependence of the path-length corrected pulse heights is determined for each cylinder using a sample of protons from K^-p elastic scattering events. The observed pulse height of a proton's cylinder coordinate is first corrected to remove any path-length dependence. The ionization loss for protons at a fixed velocity is well-known to be Landau-distributed and this behavior should be reflected in the path-length corrected pulse height measurements. However, the distribution of the variable $(f_\theta PH)^{0.3}$ is found to be approximately Gaussian in nature, and so this feature is used to simplify the description of the pulse-height information. The mean and σ of this distribution as a function of β is determined from the proton sample. This dependence is shown in Fig. 3.6(b), where $(f_\theta PH)^{0.3}$ is plotted versus β for a typical run and cylinder. The typical width of this distribution is 1 and the variation in the mean between $\beta = 0.1$ and $\beta = 1.0$ is 2-3. The β-dependence of the mean is parametrized by a quadratic function.

From the known path-length and β-dependence we can form a likelihood function that, given a number of observed pulse heights on a cylinder track, gives the likelihoods that the particle is a π or a p. In practice, the observed pulse heights are path-length corrected and then compared with the predicted distribution to determine the probabilities that the observed pulse heights were generated by a proton or a π. A likelihood ratio is formed from these two probabilities and the

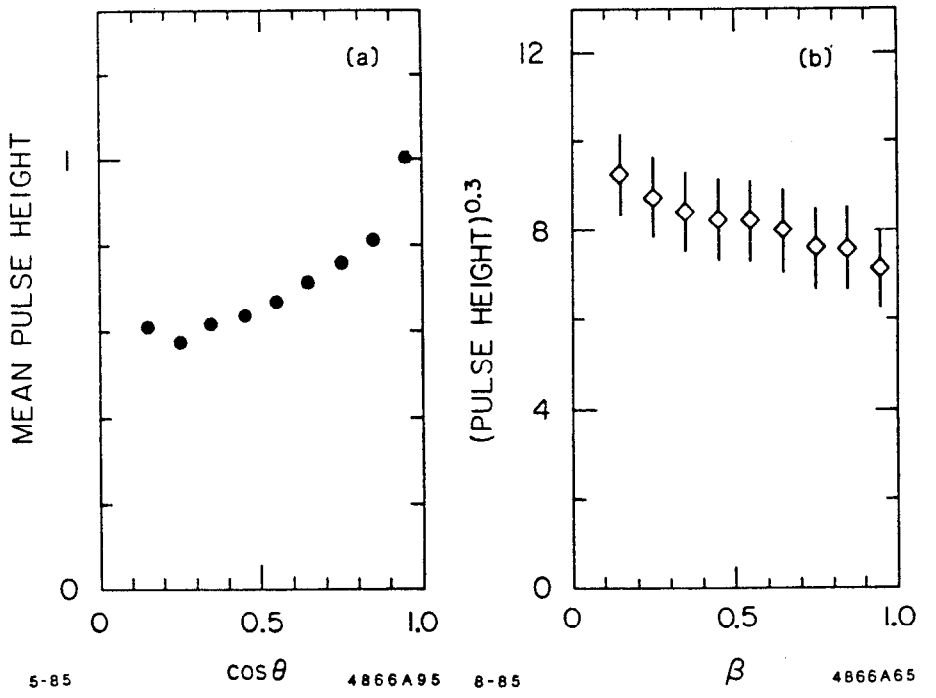

Figure 3.6. The behavior of the cylinder pulse heights. The residual path length correction for a typical cylinder and run is shown in (a) as a function of $\cos\theta$. The correction is normalized to unity at $\theta = 0$ (normal incidence). The β-dependence of $(PHf_\theta)^{0.3}$ is shown in (b).

ratios obtained from all the cylinder coordinates associated with the particle are multiplied together. The resulting ratio is the quantity used to select one or other of the particle hypotheses. An illustration of the type of separation that is possible with this method is given below in the description of the $\bar{K}^{\circ}\,\pi^{+}\pi^{-}n$ event selection.

4. Event Reconstruction and Simulation

4.1 OVERVIEW

Prior to the physics studies of the E-135 data sample, the raw data obtained during the data acquisition process have to be processed. The processing is performed by a computer program that determines the trajectories of the charged particles passing through the spectrometer. These trajectories are used to locate the interaction point of the beam track (the primary vertex) and the decay vertices (secondary vertices) of any particles produced in the primary interaction that subsequently decay weakly. The result of this reconstruction algorithm is a list of the tracks with their associated track parameters and coordinates, and a description of the topology of the entire event, *i.e.* the locations of the primary and secondary vertices and the tracks associated with each vertex. The first section of this chapter describes the structure of this program and the various algorithms used to perform the event reconstruction.

The E-135 event sample consists of 140 000 000 triggers, of which $\sim$ 85% are physics data events. Since the event reconstruction algorithm requires $\sim$ 0.55 sec/event on an IBM 3081K computer, the CPU time needed to process the entire data sample is $\sim$ 2.4 CPU-years (IBM 3081K equivalents). To meet this need, a computer known as the 168/E was designed and built. This processor is described in the second section of this chapter.

For any particular K^-p interaction, the distribution of events detected by the spectrometer must be corrected for acceptance losses in order to reveal the characteristics of the underlying physics distributions. The traditional approach (and the one followed here) is to have a model of the spectrometer that incorporates all the effects relevant to the triggering, reconstruction and selection of an event sample. We then generate a distribution of events and determine how the events are perturbed by the presence of the spectrometer and how many of the generated events are "detected" as a function of the parameters describing the event. This procedure is implemented with a computer program called the Monte Carlo, and the latter part of this chapter is devoted to a description of this program.

4.2 Event Reconstruction

The event reconstruction program is broken into several steps:

1. the transformation and decoding of the raw data;
2. the pattern recognition algorithm that reconstructs the particle trajectories;
3. the topology recognition algorithm that determines the location of the primary and secondary vertices; and
4. the packing of the resulting information into a concise data record that is stored away for subsequent event selection.

4.2.1 Raw Data Unpacking

The first step in the event reconstruction is the unpacking of the raw data. The raw data record is organized into a fixed length header, followed by up to four separate blocks, labelled Blocks 2, 3, 4, and 7.

Block 2 has the information from the buffer strobe modules, the Čerenkov counter ADC's, the TOF counter TDC's and ADC's, and some information taken from the online scalars such as the number of K's since the last trigger, and the time since the last beam track.

Block 3 contains the data from the PWC anode planes. This consists of a list of the PWC anodes that had hits and the 6-bit time-slot mask for each wire. The time-slot information is used to determine whether the hit on the wire came from an event-associated particle or one produced sometime before or after the event trigger. A particle can turn on a cluster of anode wires, so one part of the unpacking algorithm consists of merging adjacent anode wires into a single anode cluster. The anode clusters are translated into absolute coordinates in space using the known chamber location and the position of the cluster within the chamber. The uncertainty σ assigned to each coordinate is the standard deviation associated with a "top-hat" distribution whose width w corresponds to the size of the anode cluster (*i.e.* $\sigma = w/\sqrt{12}$).

Block 4 contains the pulse height information from the cathode strips in the gap and cylindrical chambers. The raw data consist of a list of fired cathode strips and the ADC count for each strip, the latter being proportional to the integrated charge detected on the strip. The ADC information is adjusted by pedestal, gain,

and cross-talk corrections to remove strip-to-strip variations in the response of the cathodes and the electronic readout.

The fired strips on each foil are grouped into "clusters" that are delimited by an inactive strip. The pulse height information on adjacent strips is then used to locate cathode "peaks", one or more adjacent cathode strips that can be associated with a single image charge induced by an anode avalanche. The pulse height profile of the strips within the peak region determines where the centroid of charge is located along the direction perpendicular to the direction of the strips. The uncertainty in the centroid position is inferred from the shape of the pulse height profile of the strips in the peak region. The peak position resolutions are given in Table 2.1.

Block 7 forms the last block in the event record and carries all the raw data from the MS chambers. These data consist of the time of arrival of the magnetostrictive pulses at the end of the wands of each MS chamber. The first and last clock count on each wand are the pulses generated by the two fiducial wires at each end of the wand. The fiducial locations in the absolute coordinate system of the LASS spectrometer are used to convert the time of arrival of each pulse into a space coordinate, with correction for the nonlinearity of the wand. The uncertainty in a spark coordinate is a function of the wand on which the spark was detected. These wand uncertainties are listed in Table 2.5.

Several checks are made on the integrity of the raw data buffer to ensure that the data are sound. The only significant source of bad event records is the limitation of 6 kB (kilobytes) on the record length. For an event exceeding this length limit, the last block (Block 7) is usually truncated, compromising any track reconstruction in the dipole spectrometer. Such events, which are considered fatal failures and are discarded, constitute $\sim$3% of the data sample.

4.2.2 Beam Track Finding

The incoming beam particle position and direction are measured by the beam chamber package. Since a good beam candidate is often accompanied by one or more secondary beam tracks that are also detected in the beam chambers, it is necessary to use a pattern recognition algorithm to convert the anode information from the beam chambers into the beam track parameters.

The beam package is physically divided into the upstream package of anode planes (with wire orientations y, x, p, and e) and a downstream package (with wire orientations y, x, y', x', e, and p). Coordinates are defined from the list of live anode wires by first clustering adjacent anodes together and converting the central wire number into a space coordinate. An anode cluster is divided into separate coordinates if the time-slot information for the anodes in the cluster are not consistent. Such clusters are usually adjacent hits from two beam particles.

The pattern recognition algorithm begins by forming separate lists of two-way, three-way, and four-way matchpoints in the upstream and downstream packages. An n-way matchpoint is n anode coordinates, each one from a separate anode plane, that are consistent with a single point in the plane perpendicular to the z-axis. In this process, coordinates in the separate planes are made into a matchpoint only if their time information is internally consistent, *i.e.* the time-slot bit patterns for the coordinates overlap by at least one bit. All possible four-way matchpoints are first constructed, followed by all possible three-way matchpoints where each three-way matchpoint is allowed to be included in one and only one four-way matchpoint. Two-way matchpoints are made from the remaining unused anodes that have overlapping time-slot bit patterns.

Beam track candidates are formed from a pair of matchpoints with consistent time-slot patterns, one each from the upstream and downstream packages. The beam track candidates are then judged on the basis of their overall timing consistency, the total number of coordinates associated with the beam track and how the candidate agrees with the allowed beam phase space. The beam track candidates that satisfy these criteria are kept as legitimate beam tracks in the event.

An in-time beam track is selected by corroborating each beam track in the $\Theta\Phi$ hodoscope and requiring that it also pass through the SY counter. The other reconstructed beam tracks are usually due to beam particles that pass through the detector without interacting in the target. To reduce the confusion created by these secondary beams, each secondary beam track is extrapolated through the solenoid and twixt region. If at least 18 of the 24 PWC planes have coordinates that corroborate the extrapolated beam track, these coordinates are poisoned out and

are not used to define matchpoints in the subsequent solenoid track finding (they are, however, used for track corroboration).

On average, there are approx 1.5 beam tracks per event trigger in the E-135 data set. Somewhat less than half of all events have one beam track candidate. In ~2% of events, the beam track defining the beam trigger decayed upstream of the beam chambers and a suitable beam track candidate is not found. Events with more than three beam tracks are immediately discarded because of the resulting confusion in the solenoid detector. This afflicts ~3% of all event triggers.

4.2.3 Solenoid Track Finding

The uniform magnetic field in the solenoid vertex detector causes charged particles to execute helical trajectories as they pass through the instrumented region of the solenoid bore. Since there are on average five charged tracks per event trigger it is necessary to employ a pattern recognition algorithm to reconstruct the track helices from the raw coordinate information.

The helix track-finding algorithm is based on the use of very precise matchpoint information derived from the individual PWC devices in the solenoid. Three matchpoints are chosen, each from a separate device, that are consistent with a helix oriented along the z-axis. This helix candidate is extrapolated to the other devices in the solenoid to define a window in the active area of the device. The size of the window is determined from the errors on the initial three matchpoints. A coordinate found within this window is considered a corroborating coordinate. Once all devices have been searched in this manner, the track candidate is judged on the basis of how many corroborating coordinates were found relative to how many were expected to lie on the track; a candidate with an excessive number of missing coordinates is immediately discarded. A χ^2 fit to a helix is performed on the coordinates of the candidate. If the resulting fit is satisfactory, the track is accepted and included in the list of solenoid tracks.

The description I gave above is a crude overview of the algorithm. I will now amplify on some of the salient details. It is important to emphasize that the success of the algorithm depends crucially on the quality of the raw coordinate information. In particular the gap chambers play a significant role in the structure

of the algorithm, as the list of matchpoints from these chambers is almost completely free of spurious combinations (due to the inherent precision of the coordinates as well as the use of the cathode pulse-height matching criterion). For this reason, the algorithm first uses matchpoints from the three gap chambers to define the candidate helices before matchpoints from the PWC devices are employed.

On the surface, the speed of the algorithm would appear to be driven by the combinatorial process of examining triplets of matchpoints to determine whether they are consistent with a helical trajectory. However, this is not the case for several reasons.

Firstly, the knowledge of the precision of the coordinates is employed at each stage to reject helix candidates. For example, the uncertainties of the initial matchpoints are extrapolated along with the predicted helix location so that the smallest possible corroboration windows can be defined consistent with high corroboration efficiency. This allows the efficient use of coordinate information of varying accuracy.

Secondly, once a successful track candidate has been found, a procedure known as "poisoning" is invoked. The track is first judged to determine if it is of high quality on the basis of the number of missing coordinates and the quality of the helix fit. The coordinates on high quality tracks are poisoned, *i.e.* they are flagged as being used and removed from any remaining unused matchpoint; when such a matchpoint has less than two unpoisoned coordinates left, it is eliminated from the list of possible matchpoints. Since the devices in the solenoid have inherently little noise, this dramatically reduces the list of matchpoints. The speed of the track-finding algorithm increases with the number of tracks found until there are no more unused coordinates available from which matchpoints could be manufactured.

Thirdly, a special method of defining helix candidates is employed early in the track-finding algorithm after all triplets of matchpoints in the gap chambers have been used up. A trial helix is defined using two matchpoints and the position of the beam in the center of the target. Since most particles are produced at the primary vertex, this procedure enhances the track finding. In particular it adds additional redundancy for finding the wide-angle tracks that hit the solenoid magnet before traversing all the chambers.

The process of cycling over triplets of matchpoints drawn from three devices is known as a "call." The number of possible calls is large, but in practice it suffices to use only 34 calls in the track finding in the planar devices. This ensures that the helix track finding is highly redundant and does not depend strongly on the behavior of any one plane or device in the solenoid.

The fit of the helix to the track coordinates takes into account the multiple scattering experienced by the particle. Two simplifying assumptions are made; (a) all particles are π's, and (b) the multiple scattering errors are uncorrelated. Both assumptions are only approximately correct but are adequate for the relatively small amount of scattering experienced by a particle in the solenoid region. If the helix χ^2 fit is of poor quality, the coordinate with the largest contribution to the χ^2 is identified and dropped from the fit if its χ^2 contribution exceeds 12. This coordinate removal is repeated until the resulting fit is satisfactory or too many coordinates have been dropped, in which case the track candidate is rejected. As a final requirement, all fitted tracks must have confidence levels $> 10^{-4}$.

The track-finding algorithm places specific requirements on the geometry of the helix candidates. Tracks found using matchpoints from the planar chambers are required to turn no more than 2π radians within the z-range of the three matchpoints. This places a lower limit of ~ 0.080 GeV/c on the p_t of planar found tracks, but avoids the problems associated with dealing with helices that turn very rapidly as they pass through the solenoid.

This requirement is not imposed on tracks that are found using matchpoints in the cylinder chambers. However, helix candidates defined with cylinder matchpoints are required to turn no more than π radians within the z-range of their matchpoints. Tracks that turn more than π radians passing through the cylinder package are found in multiple segments but are subsequently identified as one track in the topology recognition algorithm. This restriction effectively deals with the problem of reconstructing multiply-looping tracks (*e.g.*, slow tracks produced perpendicular to the beam axis that tend to curl up as they lose energy and are therefore not amenable to a simple helix fit).

The resulting track-finding efficiency for a track that does not decay and does not suffer a nuclear interaction in the solenoid is in excess of 99%, a figure arrived

at by a scan of several hundred events and from Monte Carlo studies. The average time spent in the track-finding algorithm is approx 240 msec/event on the IBM 3081K computer, which corresponds to $\sim$ 45% of the total average time spent in event reconstruction.

4.2.4 Dipole Track Finding

Reconstructing particle trajectories in the dipole spectrometer involves four distinct steps:

1. Finding line segments in the region downstream of the dipole magnet.
2. Finding lines in the region between the solenoid and dipole magnets (the "twixt" region).
3. Crossing each downstream line segment through the dipole magnet aperture to the corresponding twixt line segment.
4. Joining the entire dipole track (*i.e.* the crossed downstream and twixt line segment) to the corresponding helix exiting the downstream aperture of the solenoid magnet.

The line segments in the downstream and twixt regions are found using the same pattern recognition algorithm. The method takes advantage of the relatively good coordinate resolution in the MS chambers and the relatively large z-separation of the spark gaps inside each MS chamber.

Consider, for example, the line finding in the downstream region. Two similar coordinate planes are chosen (*e.g.* MSD1 x and MSD4 x). A pair of x-coordinates, one from each plane, define a projection in the x–z plane. This plane defines two new x-values in the adjacent spark gaps of each chamber (in this case MSD1 e–p and MSD4 e–p). Pairs of e–p coordinates in each of these two spark gaps are examined to determine whether any one pair defines an x-position that agrees with the predicted x-value. If a pair of coordinates consistent with the predicted x-value is found in each adjacent gap, the six coordinates taken together define a candidate line segment. This candidate line segment is extrapolated to all the other chambers in the region and any coordinate consistent with the extrapolated line is flagged. The number of expected coordinates on the candidate line segment is determined along with the number actually found; if there are too many missing coordinates

the line candidate is rejected. If the level of corroboration is acceptable, all the coordinates are included in a least-squares fit to a common line. If the confidence level from the fit is $< 10^{-4}$, the line candidate is rejected.

Having obtained a well-corroborated line segment, a final check is made to see whether the line candidate is corroborated in the devices with the best in-time resolution. If the line candidate fails to be corroborated in the proportional wire chambers or scintillator hodoscopes it is considered an out-of-time track. All in-time and out-of-time tracks are then classified according to how well they fit, how many coordinates they have and how many coordinates are missing on the track. If the line candidate is of excellent quality according to these criteria it is considered "poisonable". The coordinates on such poisonable lines are flagged and are not used in subsequent candidate line finding (although they are allowed to be used in the corroboration of other line candidates). This poisoning strategy substantially improves the speed of the line-finding algorithm without compromising its efficiency. All acceptable in-time line segments are stored away; the out-of-time line segments are discarded.

The line finding in the twixt region incorporates the plug 4 and plug 5 chambers to enhance the pattern recognition efficiency for tracks very close to the beam axis that pass through the deadened regions of the MS chambers. The twixt MS chambers are substantially more inefficient than the downstream chambers and so in cases were a twixt partner to a downstream line is not found, the twixt line finding incorporates information about the downstream lines. This involves estimating the direction of the twixt line by using the angle of the downstream line in the non-bending plane (the y–z plane) and the position of the downstream line in the center of the dipole aperture. Although this augments the track finding in the twixt region, the resulting twixt line-finding efficiency is only 95%.

The downstream and twixt lines are crossed through the dipole aperture to form a complete dipole track by taking each downstream line and extrapolating it to the center of the dipole aperture. All uncrossed twixt tracks are also extrapolated to the dipole center and the twixt track that provides the best match to the downstream line is identified with that downstream line. An estimate of the dipole track momentum is made from the total bend of the track in the $x - z$ plane. This

estimate is used to swim the downstream track through the dipole magnetic field into the twixt region; the discrepancy between the angle of the swum track and the twixt track provides a correction to the initial momentum estimate. This procedure is iterated until the angles of the swum track and twixt track agree. The error in the momentum estimate is determined from the uncertainty in the downstream and twixt lines, taking into account the multiple scattering of the particle as it passes through the dipole spectrometer.

The final step in the dipole track reconstruction is the joining of the dipole track to the corresponding solenoid helix track. This procedure involves determining the solenoid track that matches the dipole track and then refitting the solenoid helix to the coordinates measured in the solenoid with the additional constraint that the total helix momentum agree with the measured dipole track momentum. Each dipole track is swum from the twixt region back into the solenoid up to the gap 3 chamber. The solenoid track that matches the swum dipole track in position and direction at this chamber is identified with the dipole track. The solenoid helix is refitted with an additional term added to the χ^2 of the fit that constrains the momentum of the helix to agree, within the dipole momentum uncertainty, with the dipole momentum. Provided this fit is successful, the unconstrained fit of the helix is replaced with the results of the new fit. The success rate of the refitting procedure is above 95% and Monte Carlo studies have shown that the failures are primarily the result of the track decaying or suffering a large-angle scatter in the dipole spectrometer.

4.2.5 Topology Recognition

In most cases it is not possible to unambiguously ascribe an event to one particular topological configuration without making specific assumptions about the final state. Because of this, the topology recognition algorithm determines the topological interpretations the track information can support in a way that avoids biasing the topology recognition toward any one specific primary and secondary vertex configuration.

There are eight event topologies that are considered in this procedure. Usually the tracks in the event can be arranged into several different vertex configurations.

Occasionally the number of configurations is such that the event is consistent with all eight possible topological interpretations. In cases where there are multiple choices of event topology, the resolution of the ambiguities is left to the subsequent analysis of the data. The eight topologies are:

1. All charged helices are associated with the primary vertex.
2. A number of charged helices and a neutral track are associated with the primary vertex, where the neutral track decays subsequently into a pair of charged prongs and is consistent with a K° interpretation.
3. As in 2 above, but where the neutral track is a Λ or $\bar{\Lambda}$ candidate.
4. As in 2 above, but where the neutral track is a candidate for a γ conversion into e^+e^-.
5. A number of charged helices associated with the primary vertex, with an additional charged prong that is a Ξ^- or an Ω^- candidate. This V^- candidate decays into an observed charged track and a neutral track that in turn decays into a pair of charged prongs. The neutral track is consistent with a Λ or a $\bar{\Lambda}$ candidate, and the V^- $\Lambda\pi^-$ (ΛK^-) invariant mass must be consistent with a Ξ^- (Ω^-).
6. A primary vertex with two associated neutral tracks decaying into pairs of charged tracks, with any number of additional charged primary tracks.
7. A primary vertex with an associated V^- and a V° track, along with any number of additional primary charged tracks.
8. A primary vertex with three associated V°'s, with any number of additional charged primary tracks.

The topology recognition algorithm also identifies pairs of same-sign charge tracks that meet in space and are consistent with arising from the decay or scatter of a single track (*i.e.* a "kink"). This algorithm also identifies sets of tracks that arise from one particle executing several revolutions inside the spectrometer. Such trajectories, which typically arise from tracks produced with low p_l and relatively high p_t, are separated by the helix pattern recognition algorithm into several half-π loops. The "daughter" tracks in these track pairings are identified and are removed from further consideration in the topology recognition algorithm.

Most of the $\bar{K}^\circ\pi^+\pi^-n$ events are reconstructed as V°+2 prong's and are

classified as Topology 2 events. Of the remaining events that are not classified as having a Topology 2 hypothesis, most of them have K°'s that decay too close to the primary vertex.

A search is first made for the possible K° candidates. The topology reconstruction algorithm looks for pairs of oppositely signed tracks that pass within 1 cm of each other. The points of closest approach on each track are determined by an iterative least squares fit. The track vectors at these points are evaluated and the $\pi^+\pi^-$ invariant mass of the two track combination is computed. The K° selection requires that this invariant mass be between 0.436 and 0.557 GeV/c^2.

The momentum sum of the K° daughters is used to determine the neutral track direction. This neutral connector and the remaining charged tracks in the event are the candidates for primary vertex tracks. A preliminary estimate of the primary vertex location is made by averaging the distance of closest approach of the remaining tracks with the beam track. A least squares fit is then performed to determine the point of closest approach of all primary tracks to a common vertex position. The fit minimizes

$$\sum d_i^2 \tag{4.1}$$

where d_i is the distance of closest approach of the ith track to the primary vertex. If the fit to this common vertex is of poor quality, the track with the largest d_i is removed and the fit is repeated. This procedure is iterated until an acceptable fit is achieved.

A minimum decay length is required of the K° candidate as a final requirement of the Topology 2 hypothesis. The minimum length varies as a function of the K° polar angle θ as

$$d_{min} = \sqrt{1 + \cos\theta} \text{ cm.} \tag{4.2}$$

This cut is necessary to achieve a reasonable K° signal-to-noise ratio in the events assigned to Topology 2. As discussed in the following description of the $\bar{K}^\circ \pi^+\pi^- n$ event selection, the events that fail this cut are recovered; however they are eventually removed by a decay length cut stronger than that in Eqn. 4.2 in order to achieve a clean $\bar{K}^\circ \pi^+\pi^- n$ sample.

4.2.6 DST Formatting

The processed event information is written onto magnetic tape in the form of a data summary tape (DST) event record. Because of the large number of events, this information is heavily compressed to yield the smallest event record while still retaining all the relevant event information that could be needed in later event analysis and selection. The format of the DST event record allows for the addition or removal of blocks of information; this ability to modify the DST record structure is used in several stages of the event analysis.

The DST record format consists of several banks, each bank being a separate block of information in the record. The pointer bank is the first bank on the record and contains a list of the other banks along with their locations (pointers). This structure provides an easy framework in which to add or delete banks. When an event record is read from the DST, the unpacking of the record can be controlled so only the banks the user requires in his analysis need be decoded. This is an important consideration when it is necessary to read through a large number of events efficiently.

Two other record types are produced in parallel with the DST record. The first is a "super-stripped tape" (SST) record that duplicates the most relevant information carried on the DST record in a much smaller record size. The SST record only carries the parameters of the found charged tracks, the topology information, and the data from the particle identification devices. The size of an SST record is approximately one-sixth of the corresponding DST record. It is designed for preliminary studies of the data, especially in cases where the events of interest are relatively rare.

The second record type is known as a DEDX calibration record. A DEDX record is written for an event where at least one track has a number of cylinder matchpoints, or where the event is tagged as being a fully reconstructed K^-p elastic scatter. It carries the track momentum, angle of impact through each cylinder, and the observed pulse height of the track's cathode foil coordinates. This information is used to calibrate the relative response of the cylindrical cathode chambers to the ionization induced by protons and pions as a function of angle and velocity, which

is required for the DEDX particle identification.

4.3 THE 168/E EMULATOR

The event reconstruction of the E-135 data sample was performed at a computer center located at Nagoya University, and at SLAC using a "farm" of emulators known as the 168/E's. These processors emulate the instruction set of an IBM 370 generation computer and are designed to provide large amounts of computing power to cpu-intensive event-oriented applications such as the processing of High Energy physics data. Each processor provides the equivalent throughput of $\sim \frac{1}{9}$ of an IBM 3081K computer. Details of the design and operation of the 168/E processors can be found in Ref. 38.

The processor consists of: (a) an execution unit that fetches instructions from a special program memory and reads and writes to a separate data memory; (b) a program memory of 176 kB; and (c) a data memory of 176 kB. A set of processors is attached directly to a Unibus controlled by a PDP-11/04 minicomputer, which manages all the I/O of the processors. The PDP-11 writes the input data buffer into the processor's data memory, downloads the program into its program memory, and subsequently reads the output data buffer after the program's execution.

Because of the relatively small size of a processor's program memory, it is usually necessary to overlay the executing program. To convert a **FORTRAN** application to run on the processor, the user code is divided into overlays and the compiled **TEXT** code for each overlay is cross-compiled into the 168/E microcode. This translation process also involves determining the location of the **FORTRAN** common blocks in the processor data memory and mapping the common block structure from one overlay to the next. The E-135 event reconstruction program is broken down into nine overlays.

The processor farm at SLAC consists of nine processors linked to the PDP-11, the PDP-11 in turn being linked to the SLAC main computer center. A program running on one of the center's computers reads the input raw data tape, passes events to the PDP-11 and in turn writes out the processed events. The PDP-11 employs a specially designed interface known as the Bermuda Triangle[39] to communicate with each of the nine processors. Typically 7–8 168/E's were operating

at any one time; one processor was chronically ill and never ran reliably for more than 2 weeks.

The performance of each processor was monitored daily by executing the same set of events in each processor and ensuring that the results were correct and in agreement between the processors. The farm was run continuously over a period of 16 months and in that time it processed $\sim$ 40% of the E-135 data sample, the remainder being processed concurrently in Nagoya. After the event reconstruction was completed, the E-135 Monte Carlo program was implemented on the farm and the facility was turned over to the generation of Monte Carlo events.

4.4 The Monte Carlo Simulation

One goal of the $\bar{K}^\circ \pi^+\pi^- n$ analysis is to understand how the events are produced in $K^- p$ interactions. Since we only observe a subset of these events because of effects such as nuclear absorption, weak decays, inefficiencies in the spectrometer, software reconstruction inefficiencies, and sample selection requirements, it is necessary to have a method of extracting the produced data distribution from the observed one.

One can view this process in the following way: A $\bar{K}^\circ \pi^+\pi^- n$ event is specified by an eight-dimensional vector $\vec{\tau}$ ($\vec{\tau}$ can be chosen to be $m(\bar{K}^\circ \pi^+\pi^-)$, t', $m(\pi^+\pi^-)$, and five angles). Assuming that the efficiency of detecting events is finite in a particular small volume $d^8\vec{\tau}$ in this eight-dimensional space, it is only necessary to know the total efficiency $\varepsilon(\vec{\tau})$ for observing a $\bar{K}^\circ \pi^+\pi^- n$ event as a function of $\vec{\tau}$; from the observed event population in $d^8\vec{\tau}$ we can then determine the produced population in this volume element. The problem of extrapolating from the observed to the produced distributions then reduces to the determination of $\varepsilon(\vec{\tau})$.

However, ε does not have a convenient analytic representation. We determine $\varepsilon(\vec{\tau})$ by a Monte Carlo technique in which events are generated in this eight-dimensional vector space and the generated particles are tracked through a model of the spectrometer. The response of the spectrometer is simulated and the resulting "raw data" event information is presented to the reconstruction program described in the previous section. The reconstructed events are written to tape along with the generated event information and are subsequently processed in a manner identical

to the handling of the data events, *i.e.* the generated events are put through the data selection process to model the effects of the selection requirements on $\varepsilon(\vec{\tau})$.

The algorithms that comprise this Monte Carlo procedure are described in the following subsections.

4.4.1 Track Generation

The distribution of the generated event sample is dictated by the requirements of the analysis performed on each specific final state. For the $\bar{K}^\circ \pi^+\pi^- n$ analysis, the Monte Carlo data must be organized in $m(\bar{K}^\circ \pi^+\pi^-)$ and t' bins with the events distributed uniformly over the allowed phase space in each bin. The generated MC event distribution is described in detail in Section 6.2.4. In this subsection, I will briefly describe how an event is generated .

The generated event information consists of the location of the primary interaction vertex in the target and the 4-vectors for the K^- beam, the three final-state mesons, and the neutron recoil. Since the phase space of the incoming beam depends on the steering of the primary and secondary beamlines, approx 50 000 events satisfying the T3 trigger were selected at random from the E-135 raw data sample. The primary beam tracks reconstructed from these events are used for the generated beam track position and momentum at the interaction vertex. The measured primary beam track vector is crudely extrapolated into the target and its interaction point is determined randomly, accounting for the nuclear absorption length of the target material. The measured beam track vector at the primary vertex is taken as the generated track vector. This vector is then propagated backwards out of the target with the multiple scattering and energy-loss effects properly incorporated to define the generated beam track vector in the beam chambers. This vector and position is smeared according to the measurement errors of the beam chamber package and the smeared vector is taken as the measured primary beam track. This method accurately reproduces the produced beam phase space as the smearing of the beam track over its allowed phase space due to measurement errors is relatively small.

The secondary beam tracks in the T3 events are also used in the MC event generation. They are propagated forward through the spectrometer and allowed to

generate coordinates in the plug and full-bore chambers. These secondary beam tracks, smeared by the beam chamber measurement errors, are then stored away as the measured secondary beams in the list of beam tracks. The algorithm in the event reconstruction program for poisoning the coordinates produced by these secondary beam tracks is subsequently used. In this way the effects of the secondary beam tracks on the helix-track reconstruction are properly incorporated.

The manner in which the $|t'|$ and the meson four-momenta are generated for an event is described in Section 6.2.4.

4.4.2 Particle Tracking in the Monte Carlo

The effects experienced by particles traversing the spectrometer are simulated in the Monte Carlo as the generated particles are projected out from their production vertex. These effects include:

1. multiple Coulomb scattering;
2. energy loss in the material inside the spectrometer;
3. nuclear absorption of particles in the material inside the spectrometer;
4. weak decays of charged and neutral particles; and
5. variations in magnetic field strengths.

A comprehensive model of the spectrometer is employed to incorporate these effects in the generated particle tracking. Detailed geometrical descriptions of the target, the particle detectors in the solenoid and dipole spectrometer, and the various particle identification devices are used to ensure that all effects experienced by a particle passing through the spectrometer are simulated. For this purpose, the spectrometer is viewed as being composed of volumes (such as chamber frames, air, and steel) and of active detectors that respond to the passage of a particle.

Each generated particle is integrated through the magnetic field of the spectrometer. The integration, or swimming, is performed by a fourth-order Runge-Kutta algorithm with a nominal step size of 30 cm (decreasing when necessary to ensure the accuracy of the resulting trajectory). At each detector interface encountered by the particle, the swimming algorithm determines the position and momentum of the particle. The swimming terminates when the particle enters iron, decays, ranges out, or exits the spectrometer.

The stepping program accumulates a volume history of the particle from the point an active detector is exited until the next active detector is encountered, at which time this history is used to calculate a perturbation to the particle's position and trajectory at the active detector due to multiple scattering experienced since the last detector. This multiple scattering perturbation takes into account the effect of both the continuous scattering and any thin-plane scattering experienced by the particle.

The energy-loss of the tracked particle is computed at each step by converting the amount of material traversed into an effective decrease in the range of the particle. The range of the particle at the end of the step is then determined and converted back to an energy for the particle. In cases where the particle is minimum ionizing the energy-loss calculation is done with a linear approximation using the energy-loss constants tabulated in Ref. 40. The "effective" magnetic field used in the integration of the particle's orbit over a step is scaled so as to take into account the effect of energy-loss on the trajectory of the particle over the step.

To take into account the effect of nuclear absorption, each generated particle is assigned a random number that is converted into the number of collision lengths λ the particle will traverse before experiencing a nuclear interaction. As the particle is tracked, the amount of material traversed at each step is converted into the corresponding number of collision lengths. This conversion takes into account the differences in nuclear absorption cross sections for the various particle species as well as the variation in the cross section as a function of particle energy.[41–43] When the particle's accumulated number of collision lengths reaches λ, the particle is considered to have suffered a nuclear interaction. The absorption process is modeled simply; the particle stops in the material and no secondary particles are generated.

Particles with weak decay modes are allowed to decay according to the branching ratios and lifetimes listed in Ref. 44. The algorithm used is similar to the one that incorporates the effect of nuclear absorption; the proper time interval between a particle's generation and decay is determined prior to swimming. During the swimming, the proper time of the particle is integrated until the assigned proper time interval has elapsed. The particle then decays, with the decay mode chosen at

random from the list of possible decay modes for the particle (the frequency of each decay mode is determined by the known branching ratios). The daughter particles are added to the list of generated tracks and are tracked separately through the rest of the spectrometer. The angular distributions of the daughter tracks in the parent particle rest frame are uniform with one exception: the decay $K^{\pm} \rightarrow \pi^{\pm}\pi^{+}\pi^{-}$ is generated according to the known final state distribution over the three-π Dalitz plot.[44]

The swimming of the particle's trajectory takes into account the variation in the magnetic field as a function of position. The magnetic field in the spectrometer from the target region to just beyond the dipole magnet is known from measurements of the three field components over an $x - y$ grid taken at 2.54 cm intervals in z. The variation of each field component as a function of x and y for a given value of z is parametrized by a 7th-order polynomial. The set of polynomial coefficients is the field map used to determine the forces on a charged particle during the swimming procedure.

4.4.3 Coordinate Simulation and Detector Response

As each charged particle is stepped through the spectrometer the particle passes through a number of detectors that in principle respond to the particle's passage. The detectors are either PWC's, MS chambers, Čerenkov counters, or scintillators. The efficiencies of the detectors were stable over the course of the experiment with a few notable exceptions: (a) the 3.5y and the plug 5y planes were not functional for most of the latter half of the experiment; (b) the plug 5e plane efficiency varied significantly in the first half of the experiment; and (c) the efficiency of the MST2 x–y spark gap was down by $\sim$ 15% in the first quarter of the experiment. These variations in efficiency are taken into account in the Monte Carlo program.

The simulation of the PWC anode coordinates is performed by first digitizing the position of the particle to the nearest anode wire. A particle creates a hit in the anode plane that consists of one or more clustered wires. The expected cluster size of a coordinate depends on the angle of the track in the plane orthogonal to the direction of the anodes, and this correlation is explicitly coded in the coordinate generation algorithm for the PWC devices. The efficiency of the device is taken into

Table 4.1. The planar chamber efficiencies. These efficiencies are averages over each plane. For some devices, the efficiencies vary internal to the device (*e.g.* wire-by-wire in the case of the plug chambers).

Solenoid Devices					
Plane	Efficiency	Plane	Efficiency	Plane	Efficiency
Plug 1x	0.990	Plug 2x	0.892	Plug 3x	0.995
Plug 1y	0.990	Plug 2y	0.990	Plug 3y	0.990
Plug 1e	0.995	Plug 2e	0.980	Plug 3e	0.995
Gap 1x	0.975	Gap 2x	0.985	Gap 3x	0.985
Gap 1y	0.959	Gap 2y	0.976	Gap 3y	0.974
TA	0.950	TB	0.950	TC	0.950
1.5x	0.975	2.5x	0.975	3.5x	0.970
1.5y	0.980	2.5y	0.975	3.5y	0.815
1.5e	0.990	2.5e	0.975	3.5e	0.970
Dipole Devices					
Plug 4x	0.980	Plug 5x	0.945	JHUP	0.955
Plug 4y	0.960	Plug 5y	0.880	JHX	0.940
Plug 4e	0.955	Plug 5e	0.945	JHY	0.490
				JHDN	0.965

account by using the measured wire-by-wire efficiency for the specific plane. The inefficiency in the regions around the support wires in the full-bore chambers and the support rings in the cylindrical chambers is also modeled. The average efficiencies of the planar PWC devices are given in Table 4.1. The average efficiencies of the cylindrical PWC devices are listed in Table 4.2.

The probability of detecting the induced pulse from an anode avalanche on a cathode foil is $\sim$ 100%. However the cathode coordinate reconstruction (*i.e.* the peak-finding algorithm) introduces inefficiencies due to the overlap of the pulse height profiles of two or more coordinates. The simulation of this software effect can be performed in one of two ways. One algorithm generates the pulse heights that would be observed on the opposing cathode foil strips for each anode avalanche and then lets the cathode peak reconstruction algorithm in the event processing program find the separate peak positions. The second method generates the cathode

Table 4.2. The cylindrical chamber efficiencies. The efficiency shown is averaged over the entire device.

Coordinate	Efficiency	Coordinate	Efficiency
Cyl 1ϕ	0.987	Cyl 4ϕ	0.990
Cyl 1z	0.946	Cyl 4z	0.980
Cyl 2ϕ	0.992	Cyl 5ϕ	0.958
Cyl 2z	0.982	Cyl 5z	0.946
Cyl 3ϕ	0.977	Cyl 6ϕ	0.967
Cyl 3z	0.958	Cyl 6z	0.955

coordinate smeared by the known cathode resolution and simulates the effect of the overlap of multiple cathode peaks. The results of the two algorithms only begin to differ for events with large numbers of cylindrical tracks, a situation that does not occur in the $\bar{K}^\circ \pi^+\pi^- n$ final state. Therefore, the second method is used in the generation of the $\bar{K}^\circ \pi^+\pi^- n$ Monte Carlo data as it is somewhat simpler and the resulting program is substantially smaller. (The size criterion is relevant because the Monte Carlo program is executed in the $168/\mathrm{E}$ emulators that place specific limitations on the size of a program.)

The coordinate resolutions of the MS chambers are known from the alignment studies and are listed in Table 2.5. These resolutions are wand-dependent and so this effect is incorporated in the coordinate simulation. Since the wand readout merges two coordinates that are less than 0.45 cm apart, this is also performed in the MS coordinate generation. The efficiencies of the four planes in a chamber are correlated, *i.e.* the probability of observing a coordinate in one plane depends on which coordinates are observed in the other three planes. To take this effect into account the correlation has been measured using reconstructed data. These correlations are then used when determining if the coordinates on a particular track are observed.

In order to accurately determine the efficiencies of the devices in the twixt region, the inefficiency in the twixt track finding had to be taken into account. This tracking inefficiency results in measured coordinate efficiencies that are

Table 4.3. The MS chamber efficiencies. The efficiencies are averaged over the plane-to-plane correlations that are simulated in the Monte Carlo.

Plane	Efficiency		Plane	Efficiency	
	Wand 1	Wand 2		Wand 1	Wand 2
MST1 x	0.76	0.70	MSD1 x	0.96	
MST1 y	0.76		MSD1 y	0.97	
MST1 e	0.66	0.64	MSD1 e	0.95	
MST1 p	0.72	0.68	MSD1 p	0.96	
MST2 x	0.82	0.83	MSD2 x	0.95	
MST2 y	0.83		MSD2 y	0.97	
MST2 e	0.87	0.78	MSD2 e	0.94	
MST2 p	0.87	0.73	MSD2 p	0.96	
MST3 x	0.82	0.83	MSD3 x	0.92	0.91
MST3 y	0.84		MSD3 y	0.92	
MST3 e	0.82	0.77	MSD3 e	0.92	0.80
MST3 p	0.83	0.78	MSD3 p	0.93	0.79
			MSD4 x	0.90	0.84
			MSD4 y	0.92	
			MSD4 e	0.95	0.96
			MSD4 p	0.94	0.95

systematically higher than the actual efficiencies, as the tracks with the fewest generated coordinates are never reconstructed. To determine the true efficiencies, the efficiency measurements were incorporated into the MC coordinate algorithm and a large sample of MC data in the twixt region was generated. (The generated distribution of the tracks in these data was obtained using the directions and positions of measured solenoid tracks at the TOF counter.) The efficiencies measured from this sample showed how much the efficiencies in the coordinate simulation had to be decreased to match the measured efficiencies in the data. This process was then repeated to ensure that the resulting measured efficiencies from the MC events and real data agree. The overall reduction in efficiency for the twixt chambers is 0.94. The resulting MS efficiencies, averaged over the plane-to-plane correlations, are listed in Table 4.3.

The simulation of the Čerenkov counters is performed by swimming the charged

Table 4.4. The scintillator hodoscope efficiencies.

Counter	Efficiency
TOF	0.999
Quad	0.981
HA	0.994
HB	0.990

particles through the counter and determining how many Čerenkov photons are given off by the particle inside each cell. This number is determined from studies of the light detection efficiency of each ring of cells for π's as a function of π momentum. The number of Čerenkov photons detected by the photomultiplier is determined by scaling the number of produced photons by the light collection efficiency, which varies with track position within the optical cell. The detected number of photons is converted into an ADC count using the width of the observed single photo-electron peak in the ADC distributions of each counter. In $\check{C}_2$, the light-collection optics are a critical aspect of the counter and so the Čerenkov photons are ray-traced to determine if they reach the phototube.

The efficiencies of the scintillator hodoscopes are listed in Table 4.4. The active surfaces of the TOF, Quad, HA, and HB counters have been mapped using a large sample of real data and the resulting geometric information (*e.g.* cracks) is implemented in the Monte Carlo algorithm.

4.4.4 Monte Carlo and Detector Performance

In this section I will describe some of the checks of the Monte Carlo program that have been made. Besides requiring agreement in the observed performance of the individual detectors, a number of specific final states from the E-135 data sample have been studied and their properties have been compared with the those predicted by the Monte Carlo.

To confirm that the individual detectors are simulated correctly, a large sample of very clean n-prong events were chosen from the E-135 data set. The efficiencies and resolutions of the detectors were measured using the tracks in this sample.

The particle vectors from each data event were then used to define a Monte Carlo generated event; these events were processed through the Monte Carlo and the efficiencies of the chambers were measured using the reconstructed Monte Carlo data. A similar procedure was performed using reconstructed twixt and downstream lines from the data. The resulting comparison of efficiencies confirmed that the Monte Carlo correctly reproduces the individual device efficiencies and resolutions. (This approach avoids the problem of knowing how to generate a Monte Carlo sample that is commensurate with the distribution of real events observed in the spectrometer. The assumption in this procedure is that the acceptance of the detector is uniform and high over the allowed phase space of the observed events. This assumption is validated, *a posteriori*, by the acceptance measured using the generated Monte Carlo sample.)

Additional checks on the simulation have been made using specific final states. Elastic scattering events ($K^- p \rightarrow K^- p$) provide a means of measuring the track reconstruction efficiency for the fast K^- scatters because these events can be cleanly tagged with only the proton recoil. This channel, having a well known differential cross section, also provides a means of checking the overall event reconstruction efficiency and normalization for the experiment. In addition, it also provides a way of comparing the momentum resolution for the beam and fast dipole tracks in the real data and Monte Carlo. Events from τ-decays of the beam ($K^- \rightarrow \pi^-\pi^+\pi^-$) provide another means of comparing the resolution of the reconstructed final state in the real data and the Monte Carlo data. The comparison of the MC and data event distributions for these two reactions indicates that the Monte Carlo correctly simulates the kinematic resolution and reconstruction efficiency of the spectrometer.

The $\bar{K}^\circ \pi^+\pi^- n$ channel was also used to check the Monte Carlo simulation. However a detailed discussion of the results of this study are deferred to Section 5.6.

5. Selection of the $\bar{K}^\circ \pi^+\pi^- n$ Sample

The $\bar{K}^\circ \pi^+\pi^- n$ event selection is performed in several stages or "strips." The first stages in the data selection focus on reducing the data sample to a more manageable size, while the goal of the subsequent stages is the isolation of the $\bar{K}^\circ \pi^+\pi^- n$ sample.

The strips that perform this reduction are:

- the "Meson" strip, a rather coarse selection that isolates all the low-multiplicity events produced with a small missing momentum;
- the "V°+2 prong" topology strip that requires the events to be topologically consistent with a V°+2 prong hypothesis;
- the "MVFIT" strip that takes all events with relatively low $\bar{K}^\circ \pi^+\pi^-$ invariant mass and fits them with the fitting program **MVFIT**; and
- the "V°" strip that places more stringent cuts on the topological definition of the V° candidate.

The input to the final event selection is the V° strip.

In this chapter, I will describe these four strips and the final event selection. This description will be followed by a discussion of the obvious features of the $\bar{K}^\circ \pi^+\pi^- n$ data sample that in turn will be followed by a discussion of the $\bar{K}^\circ \pi^+\pi^- n$ kinematic resolution, normalization, and data sample sensitivity.

5.1 The Meson and Topology Strips

The primary goal of the meson strip is to produce a data set one-third the size of the entire data sample that contains a number of final states characterized by a forward-produced multi-particle system accompanied by a seen or unseen recoil state. To achieve this goal, events with between 2 and 9 charged tracks are selected with the additional requirement that

$$p_{beam} - \sum p_z < 2.0 \quad \text{GeV/c}, \tag{5.1}$$

where p_{beam} is the beam momentum and the sum is over all the charged tracks reconstructed in the event. This selection achieves a condensation of 3-to-1 from the DST tapes and succeeds in retaining all of the events where most of the momentum

in the event is carried away by the charged tracks. It includes such final states as $K^-\pi^+n$, $K^-\pi^+\pi^-p$, $\bar{K}^\circ\pi^-p$, and $\bar{K}^\circ\,\pi^+\pi^-n$.

The next stage of the event selection is the V°+2 prong topology strip, that selects events with at least 4 charged tracks that can be topologically interpreted as having two charged prongs at a primary vertex, with two additional tracks forming a V° associated with the primary vertex. The V° is required to be consistent with the decay of a K° produced at the primary vertex.

The topology recognition program **VRHUNT** used in the offline event reconstruction demands that the V° flight path be greater than 1.0 to 1.4 cm (see Eqn. 4.2) for such topologies. The primary motivation for this cut is to reduce the number of background events resulting from 4-prong final states where a pair of tracks make up a fake V°. However, since at this point in the selection it is not clear whether this cut is necessary for the $\bar{K}^\circ\,\pi^+\pi^-n$ event selection, the flight path requirement is removed from the topology selection for the V°+2 prong strip.

The cost of this decision is that the topology strip results in a substantially larger event sample. Although it was not germane to the $\bar{K}^\circ\,\pi^+\pi^-n$ analysis, this topology strip also includes V°+1-prong events; since the strip also selects the final state $\bar{K}^\circ\,\pi^-p$, keeping the 1-prong events ensures that $\bar{K}^\circ\,\pi^-p$ events where the proton has been absorbed in the target are also included.

This topology strip achieves a condensation of 6-to-1 from the meson strip tapes, so that the resulting data sample fills 58 magnetic tape reels and contains 4 426 000 events.

5.2 THE MVFIT AND V° STRIPS

The third stage in the event selection process involves the geometrical and kinematic fitting of the V°+2 prong events. Three cuts are applied prior to the fitting process to further reduce the data sample. The first cut demands that the p_z balance requirement defined in Equation 5.1 be satisfied when the sum over the final state charged tracks is performed over the four tracks comprising the V°+2 prong topology. In addition, the two charged prongs at the primary vertex are required to be of opposite charge. Finally, since this analysis is interested in studying the meson states with masses below approximately 2.3 GeV/c^2, the invariant $\bar{K}^\circ\,\pi^+\pi^-$

mass of the V°+2 prong system is required to be less than 3.0 GeV/c^2.

Events passing these requirements are geometrically and kinematically fit using the fitting program **MVFIT**, a multi-vertex least-squares fitting program described in Appendix A. The coordinates on each track are fit to a helix with the helices from the same vertex being constrained to pass through a common point in space. The V° momentum reconstructed from the two helices describing the decay daughters is also constrained to point at the primary vertex. To determine the helix and vertex parameters that best describe the event, **MVFIT** minimizes a χ^2 determined from these parameters and the measured track coordinates.

The fit that imposes these constraints is performed on every event and is called the "geometry" fit. Each event is also fit to two additional hypotheses. A "K°" mass-constrained fit is performed where the invariant $\pi^+\pi^-$ mass of the V° is constrained to equal the K° mass (in addition to the V° pointing constraint). The third fit is a kinematical fit requiring 4-momentum conservation at the primary vertex with a missing neutron, a K° mass-constraint and the V° pointing requirement. This last fit is called the "1C-fit," although the number of actual constraints on the event is four due to the additional V° pointing and mass constraints.

Two additional fits are done to particular subsets of events. A Λ mass-constrained fit is performed when the invariant $p\pi^-$ mass for the V° is roughly consistent with a Λ mass. This criterion is satisfied by $\sim$ 15% of the events. The other optional fit is a kinematical fit that is performed on events consistent with the $\bar{K}^\circ\,\pi^- p$ interpretation on the basis of the missing-mass-squared assuming a $\bar{K}^\circ\,\pi^- p$ final state ($mm^2(\bar{K}^\circ\,\pi^- p)$). This fit requires 4-momentum conservation at the primary vertex assuming a $\bar{K}^\circ\,\pi^- p$ final state and no missing particles. This "4C-fit" is performed on $\sim$ 10% of all events.

These fit results are appended to each event record. This strip is CPU intensive as the time required to fit each event is approx 400 msec on the IBM 3081K processor. For this reason, the majority of the fitting was performed on an IBM emulator called a 3081/E.[45] The results of the **MVFIT** strip are written on 25 magnetic tapes.

The next stage, called the V° strip, is the last step before the final event

selection. Its purpose, as its name implies, is to further reduce the data sample by placing more stringent requirements on the definition of an acceptable V° candidate. The selection criteria are:

1. The event has a converged geometry fit.
2. The charges of the helices must not have changed during the geometry fit. This removes a small number of events, all of which have at least one badly or incorrectly measured track.
3. The decay length of the V° has to be greater than 0.5 cm. This cut removes most of the 4-prong events from the sample with little loss of real K°+2-prong signal. Figure 5.1 shows the event distribution as a function of the V° invariant $\pi^+\pi^-$ mass and decay length. The highest row of bins in this histogram is from events with decay lengths less than 0.5 cm, corresponding to the events removed by the decay length cut. This figure illustrates the poor K° signal-to-noise ratio for these events.
4. Events with $mm^2(\bar{K}^\circ\,\pi^+\pi^-) > 2.0$ $(\mathrm{GeV/c^2})^2$ are rejected. This cut eliminates events that are either inconsistent with $\bar{K}^\circ\,\pi^+\pi^-n$ or are very poorly measured.

The resulting condensation factor is approximately 2.5-to-1, yielding a data set of approximately 900 000 events on 13 tapes. These data are the input to the final selection program.

5.3 The Final Event Selection

Up to this stage, rather loose cuts have been applied to the data sample to avoid compromising the efficiency of detecting $\bar{K}^\circ\,\pi^+\pi^-n$ events. However a number of serious backgrounds in the data sample have to be eliminated at some cost to the overall event acceptance.

5.3.1 Background Removal

The largest backgrounds that are topologically identical to the $\bar{K}^\circ\,\pi^+\pi^-n$ final state result from the $\bar{K}^\circ\,\pi^-p$ and $\bar{K}^\circ\,\pi^-p\,\pi^\circ$ channels. Most of these background events are removed by identifying the proton on the basis of its ionization in the cylindrical PWC chambers or by measuring its mass using the TOF system.

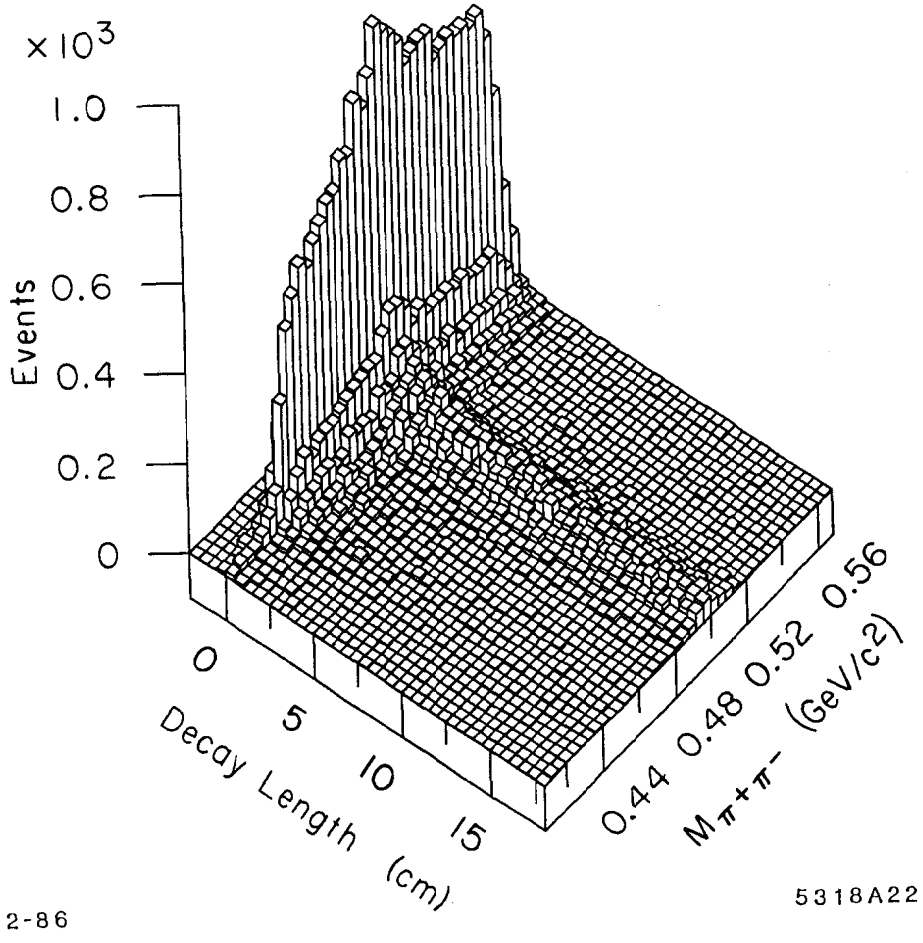

Figure 5.1. The event distribution versus $m(\pi^+\pi^-)$ and V° decay length. The bins are 0.001 GeV/c^2 and 0.5 cm wide in mass and decay length, respectively.

If the positive primary track has coordinates in the cylinders, the cylinder pulse height measurements are used to determine the ratio of the probability that the particle is a proton generating the observed pulse heights (η_p), to the probability that it is a π^+ (η_π). This distribution is shown in Fig. 5.2 plotted against the momentum of the positive particle. The particle is considered a proton if, below a momentum of 0.6 GeV/c, $\ln(\eta_p/\eta_\pi) > 1.0$, and for a momentum between 0.6 and 0.8 GeV/c, $\ln(\eta_p/\eta_\pi)$ is between 1.0 and 4.0, as shown in Fig. 5.2.

A particle hitting the TOF is identified by using the differences between the measured and expected times of flight for a proton and a π^+ hypothesis. A particle is called a proton when this time difference for the proton hypothesis is less than 3.0 σ while the time residual for the π^+ hypothesis is greater than 3.0 σ. In the rare cases where the particle is identified both in the cylinders and TOF and there is a conflict in the identification (*i.e.* one device labels the particle a proton and the other a π^+) the TOF's determination is used. This part of the selection removes $\sim$ 28% of the data events. The effect of this cut on the $\bar{K}^\circ\,\pi^- p$ contamination is illustrated in Fig. 5.3 where the $mm^2(\bar{K}^\circ\,\pi^- p)$ event distribution is shown before and after the events with tagged protons are removed. The residual $\bar{K}^\circ\,\pi^- p$ events are removed in the subsequent event selection; they survive this cut because the proton momentum is too high, or the proton failed to hit enough cylinders to be successfully identified using the dE/dx method.

The location of the primary interaction vertex is required to be inside the H_2 target. An event with a primary vertex z outside of $[14.0, 101.0]$ cm is removed. Approximately 0.9% of the events fail this cut.

At this stage it is possible to tighten up on the V° decay length cut to further reduce the remaining 4-prong background. A cut removing events with decay lengths less than 1.5 cm is imposed, which removes $\sim$21% of the data events.

A small background to the $\bar{K}^\circ\,\pi^+\pi^- n$ channel is

$$K^- p \rightarrow K^\circ \phi X \rightarrow K^\circ K^+ K^- X.$$

This background has a unique signature as the ϕ is quite visible in the K^+K^- invariant mass distribution of the two primary charged tracks. It is eliminated

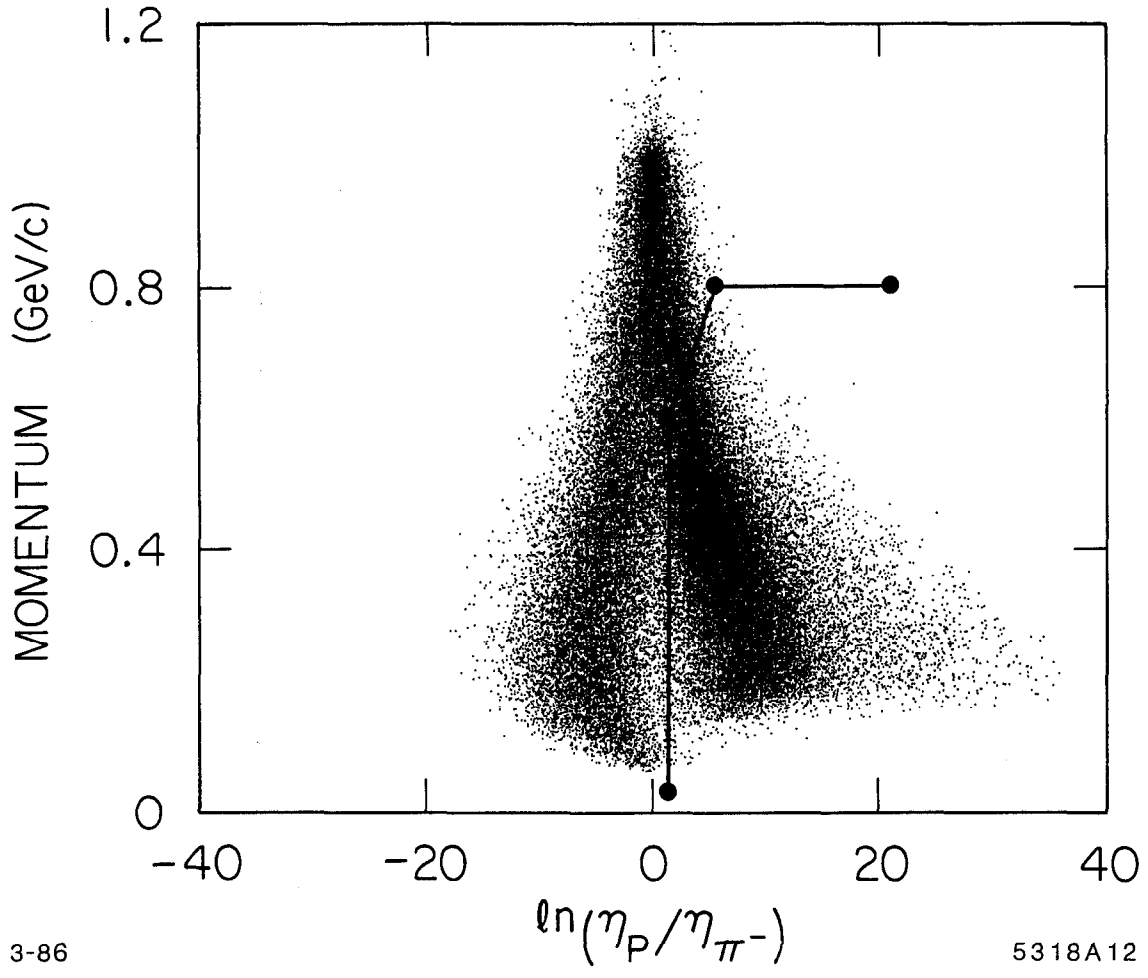

Figure 5.2. Particle momentum versus $\ln(\eta_p/\eta_\pi)$. The two bands show the clear separation of protons and π's below a momenta of ~ 0.8 GeV/c. The lines indicate the cut used to define the protons.

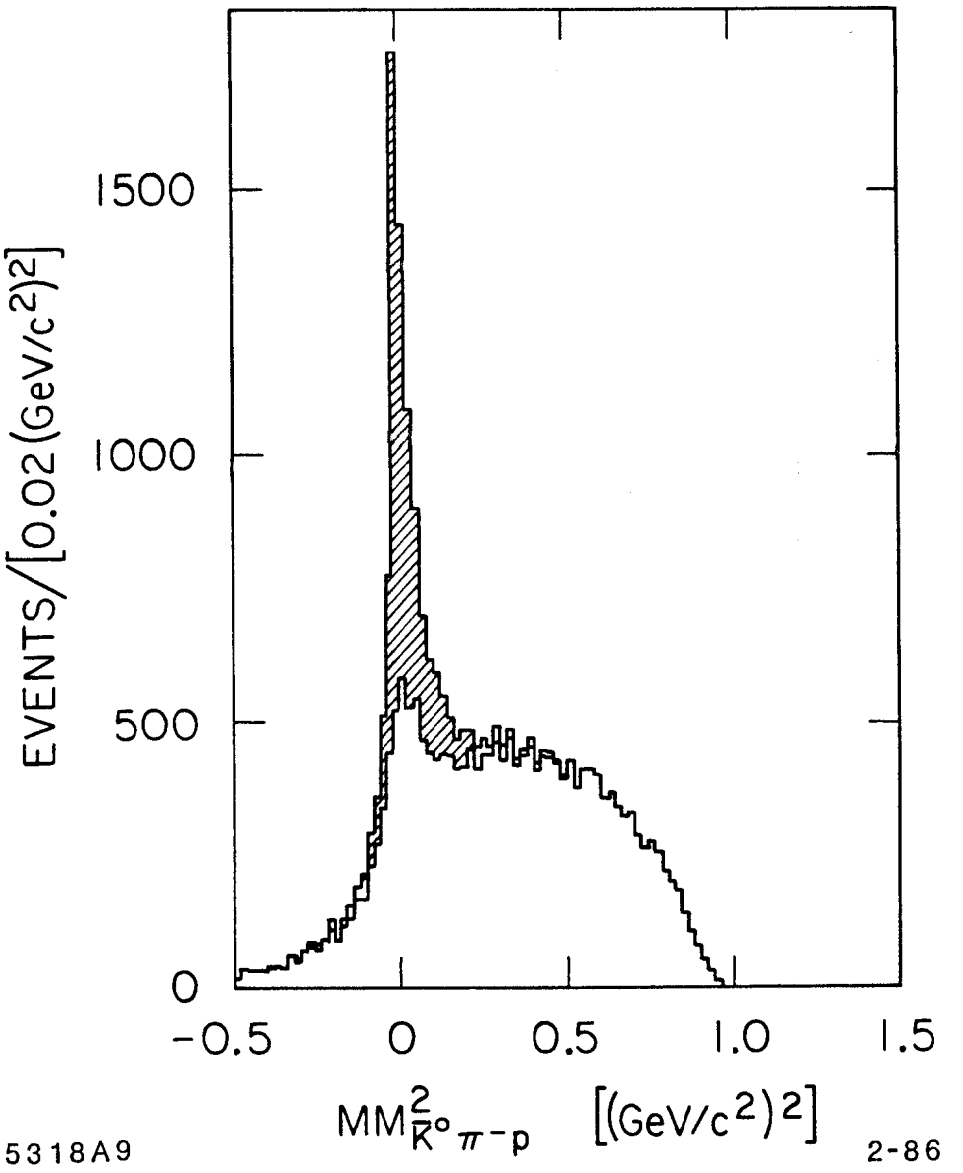

Figure 5.3. The $mm^2(\bar{K}^\circ \pi^- p)$ distribution before and after the proton cut. The histograms show the $mm^2(\bar{K}^\circ \pi^- p)$ distribution before and after the events with tagged protons are removed.

by removing events that have $m(K^+K^-) \leq 1.035$ GeV/c^2, where at least one of the charged prongs is identified as a kaon using the Čerenkov counters and the identification of the other charged prong is at least consistent with a K hypothesis. For a π identification, the particle must pass through a cell in one of the Cerenkov counters in which light has been detected. For a positive kaon identification, the cell traversed by the particle must be devoid of light and that region of the cell must have a measured efficiency in excess of 75% for detecting light if the particle were a π. Figure 5.4 shows the results of this cut on the invariant K^+K^- mass spectrum. The remaining hint of a ϕ signal comes from events where neither of the charged prongs could be identified as a kaon because they decayed in flight, they passed through an inefficient region of the counter, or they did not fall within the acceptance of the counter. About 2.7% of the events fail this cut.

Final states such as $\bar{K}^\circ K^+K^-X$ in which the K^+K^- is not from the decay of a ϕ are not explicitly removed from the event sample. This background and the one arising from the final state $K^\circ K^\pm\pi^\mp\Lambda$ with the Λ undetected are such that when the charged K's are called π's, the computed $mm^2(\bar{K}^\circ\,\pi^+\pi^-)$ is significantly above the neutron mass squared. Since a rather tight $mm^2(\bar{K}^\circ\,\pi^+\pi^-)$ is placed on the final data sample, both of these backgrounds (and indeed the one arising from the $\bar{K}^\circ\phi$ final state) are suppressed in the final $\bar{K}^\circ\,\pi^+\pi^-n$ event sample. The residual background from these sources is relatively harmless as long as it is not concentrated in one part of phase space. This is the motivation for explicitly removing the $\bar{K}^\circ\phi$ contamination; they occupy a small corner of three-body phase space and therefore could affect the subsequent analysis if only the $mm^2(\bar{K}^\circ\,\pi^+\pi^-)$ cut were used to anti-select them.

Because of the relatively high incidence of multi-beam events, there is a small background from events where one or more of the reconstructed solenoid tracks is a second beam track that was not poisoned out in the course of the beam track finding. Such tracks are characterized by very low p_t and are found along the beam axis in the solenoid. Consequently events having an unjoined solenoid track with $p_t \leq 0.008$ GeV/c whose trajectory in the solenoid does not extend beyond 10.0 cm from the solenoid axis are removed; this cut removes $\sim 1.3\%$ of the events.

A small number of "fake" V°'s remain in the data sample that can be recognized

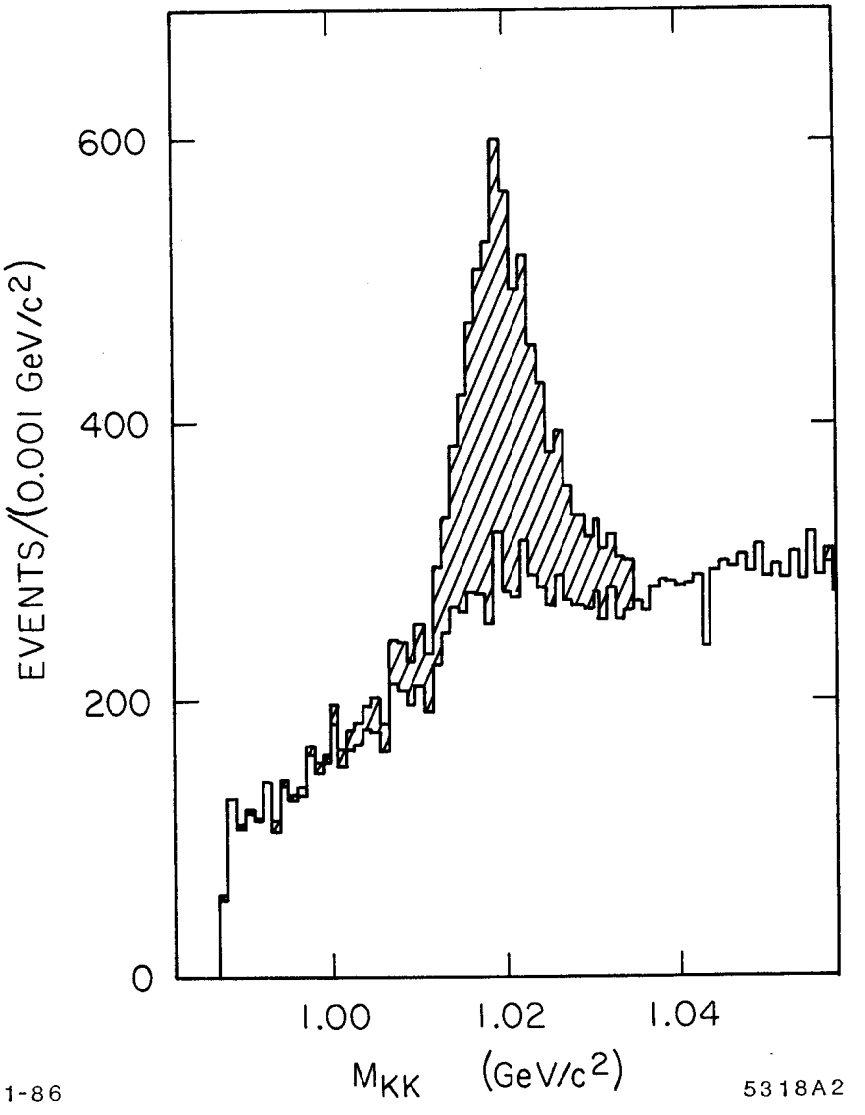

Figure 5.4. The effect of the ϕ cut. The outer histogram is the distribution for all events before the ϕ cut. The shaded portion shows the events removed by the cut.

by examining the distribution of found coordinates on their decay daughters. These fake V°'s are prone to having charged daughters with coordinates upstream of the fitted V° decay vertex. It is reasonable to occasionally find a few coordinates upstream of the decay vertex, *e.g.* there is a small probability for a real K° daughter to pick up a couple of spurious upstream coordinates in the coordinate corroboration algorithm (this is particularly true of forward V°'s decaying downstream of plug 1). However finding four or more coordinates upstream of the decay vertex is highly improbable for a real V° so events with such V°'s are removed. The fraction of events eliminated by this cut is minuscule ($< 0.1\%$).

The V°+2 prong topology selection does not place a requirement on the number of reconstructed solenoid tracks in the event. The only multiplicity requirement has been that the event have less than 10 helices (this is from the meson strip cuts). There are a significant number of events that have extra tracks, often for legitimate reasons. However a subset of these events are from different final states that have higher charged multiplicities. These background events are removed by rejecting any event that has an alternate topological hypothesis using more than six solenoid helices. In practice this cut has little effect; only $\sim 0.9\%$ of the remaining events are rejected by it.

The V°'s in the event sample are not all K°'s. A relatively small fraction of these V°'s arise from the charged decay of a Λ°. Because of the different Lorentz boost for a proton and π^+, such events can be removed with a cut on the angle of the positive decay daughter in the K° rest frame. Defining θ_{hel} to be this helicity angle in the $\pi^+\pi^-$ rest frame, events with $\cos\theta_{hel} > 0.78$ are removed from the data sample. Figure 5.5 and Fig. 5.6 show the $\cos\theta_{hel}$ versus $m(\pi^+\pi^-)$ distribution prior to placing the cut and the projection of this scatterplot onto the $\cos\theta_{hel}$ axis, respectively. The cut unequivocally removes all of the Λ° contamination; about 23% of the events are removed by it.

An alternative approach to removing the Λ°'s involves using the difference in the K° and Λ° mass-constrained fit confidence levels to identify Λ° candidate events. Although this cut retains more of the K° signal, it is also more difficult to model reliably in the Monte Carlo as it requires a detailed understanding of all of the coordinate errors, etc. Since it is a cut on the measured probability

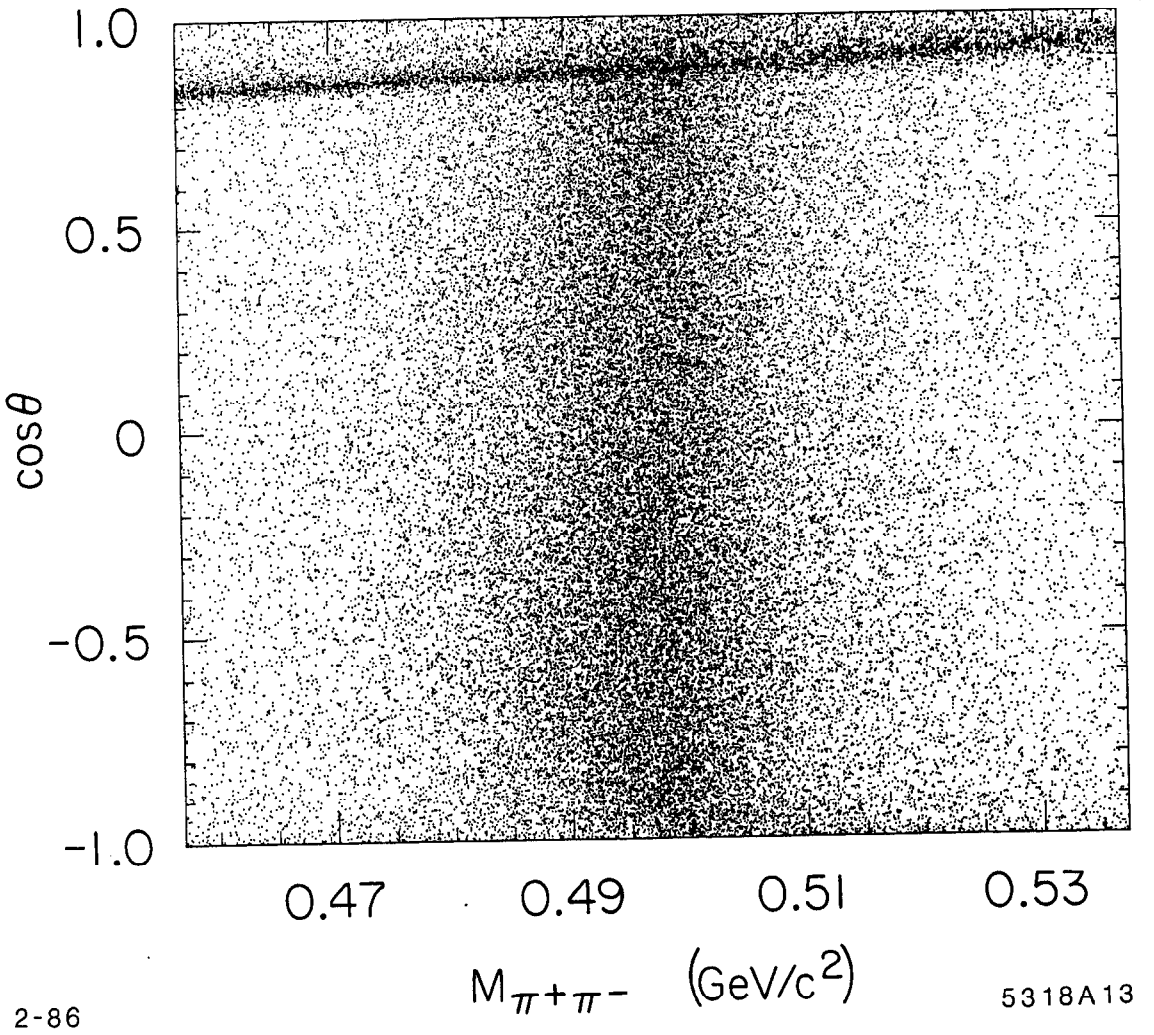

Figure 5.5. The scatterplot of $\cos\theta_{hel}$ versus $m(\pi^+\pi^-)$. The scatterplot shows $\cos\theta_{hel}$ of the π^+ in the $\pi^+\pi^-$ rest frame versus $m(\pi^+\pi^-)$ for all events prior to the Λ° cut.

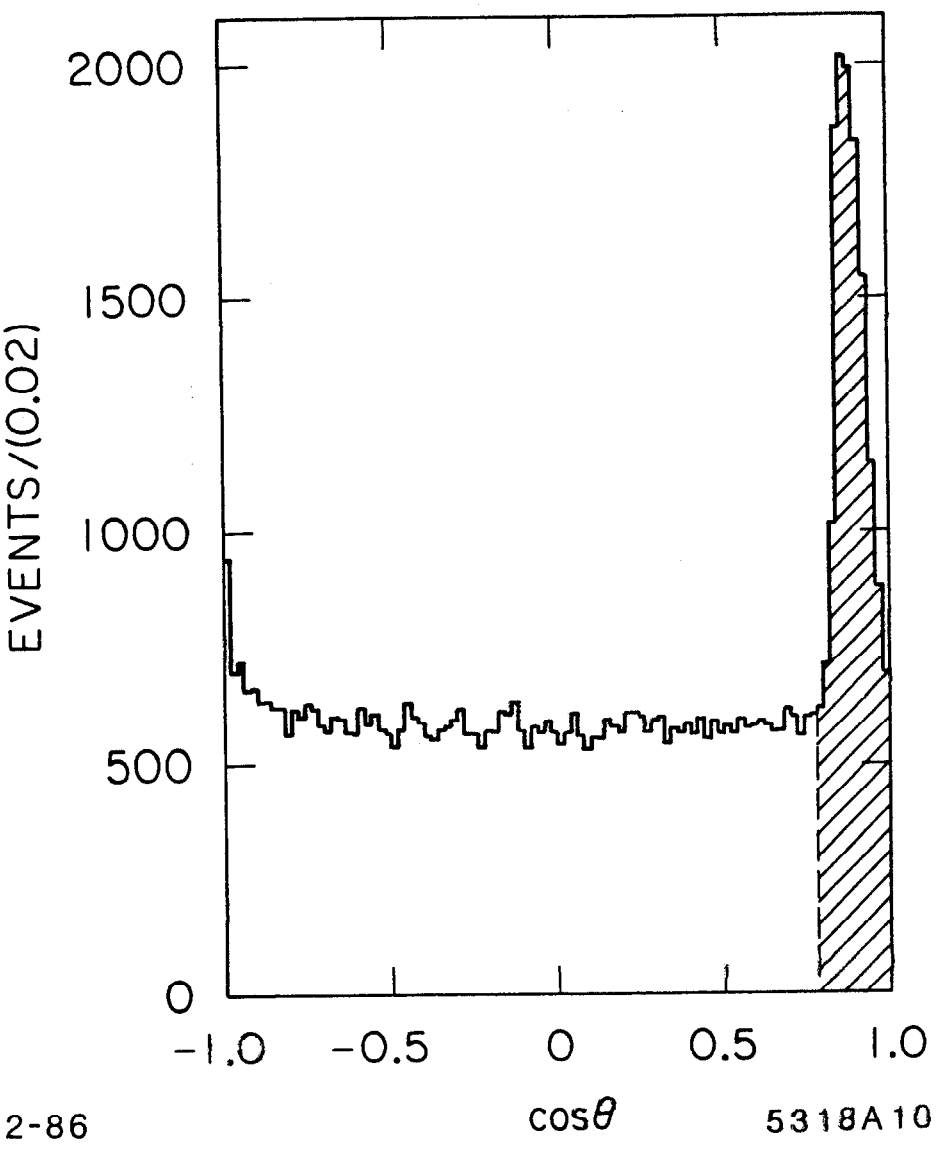

Figure 5.6. The $\cos\theta_{hel}$ distribution prior to the helicity cut. The shaded area shows the cut used to remove the Λ^0's. The peak in the backward direction comes from other sources of background that are removed in the subsequent selection.

for two different hypothesis, the cut also has to be able to account for changes in the relative populations of Λ° and K° events across phase space. This adds further complications, making the cut substantially more difficult to simulate correctly. For this reason the more straightforward $\cos\theta_{hel}$ cut is employed.

5.3.2 Resolution Cuts

Figure 5.7 shows the $mm^2(\bar{K}^\circ\,\pi^+\pi^-)$ distributions as a function of the number of dipole-joined tracks in the event. In the case where there are no dipole-joined tracks, the amount of neutron signal becomes very hard to evaluate because of the inherently poor resolution associated with these events. In particular, it is difficult to measure how much non-neutron background remains after any sort of mm^2 cut.

Since the PWA requires a rather "clean" data sample, the events are required to be well measured. This requirement is imposed by estimating the momentum uncertainty for the most poorly measured track in an event and rejecting the event if this uncertainty is excessively large. Different estimates of the momentum uncertainty can be derived for each event, perhaps the best being the variance on the fitted momentum derived from the geometry fit. However when performing a Monte Carlo simulation of the data it is hard to verify that this quantity is reproduced correctly. For that reason an alternative means of estimating the momentum uncertainty for a track is used.

The most poorly measured tracks in the spectrometer are those with relatively low polar angle that are not linked to dipole tracks. For such tracks the momentum uncertainty is dominated by the uncertainty in measuring the sagitta of the helical trajectory, and takes the form

$$\sigma_p^{est} = 36\frac{pp_l}{(\Delta z)^2\tan\theta}, \tag{5.2}$$

where p and p_l are the momentum and longitudinal momentum of the track, Δz is the z separation between the first and last coordinate on the track, and θ is the polar angle of the track. The factor of 36 is determined from a direct comparison of σ_p^{est} and the momentum uncertainty from the geometry-constrained fit. Figure 5.8 shows σ_p from **MVFIT** (σ_p^{MV}) plotted versus σ_p^{est} for unjoined solenoid tracks

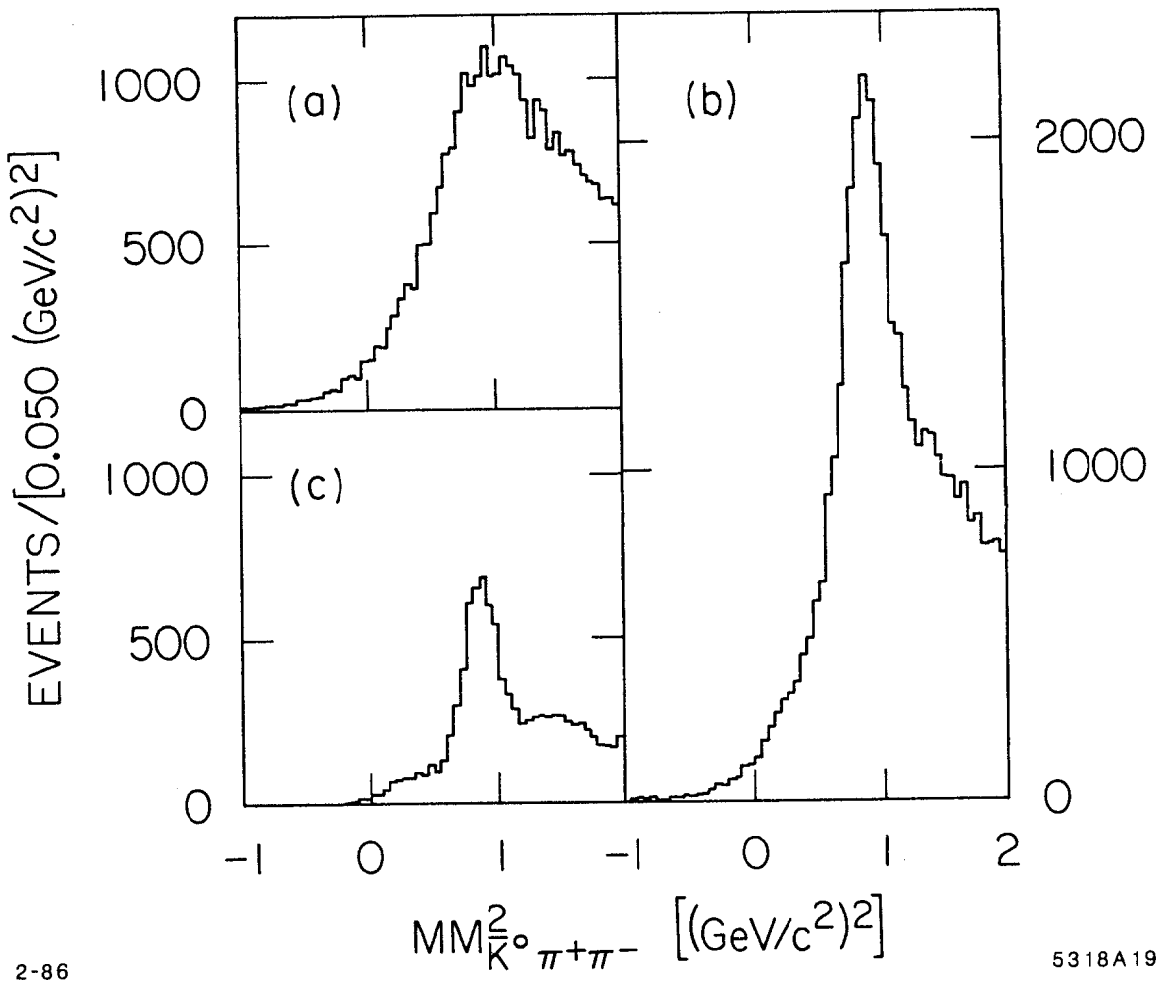

Figure 5.7. The $mm^2(\bar{K}^\circ \pi^+\pi^-)$ versus the number of dipole tracks. The mm^2 distributions are shown for events with: (a) no dipole-joined tracks; (b) one dipole track; and (c) two or more dipole tracks.

with momentum above 3.0 GeV/c. The resolution cut is implemented by requiring every fast track ($p > 3.0$ GeV/c) to either be linked to a dipole track or to have $\sigma_p^{est} < 0.360$ GeV/c. Figure 5.9 shows the effect of this cut on the neutron signal. The advantage of using σ_p^{est} (as opposed to σ_p^{MV}) is that it is a purely geometric quantity whereas σ_p^{MV} is determined by a sophisticated fit; to the extent that it is easier to model such geometric cuts, the cut as implemented is safer.

5.3.3 Trigger Requirement

The event trigger of the LASS spectrometer has an efficiency between 90 and 100% for successfully triggering on $\bar{K}^\circ \pi^+\pi^- n$ final states (see Fig. 3.2). In real data events there is the possibility that a $\bar{K}^\circ \pi^+\pi^- n$ event that does not satisfy the trigger is recorded, *e.g.* because of electronics noise in the event trigger logic. To ensure that the effect of the event trigger is consistently treated in both data and Monte Carlo events, a strict trigger requirement is placed on the events. All events are required to satisfy the physics triggers when only the four charged tracks comprising the $\bar{K}^\circ \pi^+\pi^-$ system are considered. This ensures that any "noise" in the detector does not cause an event to be included in the analysis that otherwise could not have triggered the detector. This trigger check simulates the hardware T0 logic completely (including anode clustering in the cylinders and plug chambers).

During the E135 data taking, two significant trigger changes occurred; the T0(4) plug 1 multiplicity requirement was relaxed during the middle of the 1981 data taking, and the T0(3) HA and HB requirement was removed before the start of the 1982 data taking. Since neither of these changes has a significant effect on the acceptance for the $\bar{K}^\circ \pi^+\pi^- n$ final state, the tight versions of both triggers are used in making up the software trigger.

The effect of the trigger cut is modest; approx 5% of Monte Carlo events with $\bar{K}^\circ \pi^+\pi^-$ invariant masses around 1.4 GeV/c^2 fail this cut, and on average a similar proportion of the data fail. The typical cause for a failure in both Monte Carlo and data events is that the T0(4) trigger is not satisfied when the trigger check is restricted to the four found tracks. This tends to occur in cases where the $\bar{K}^\circ$ has decayed downstream of plug 1 and the track corroboration failed to find all of the plug 1 coordinates for the two primary prongs.

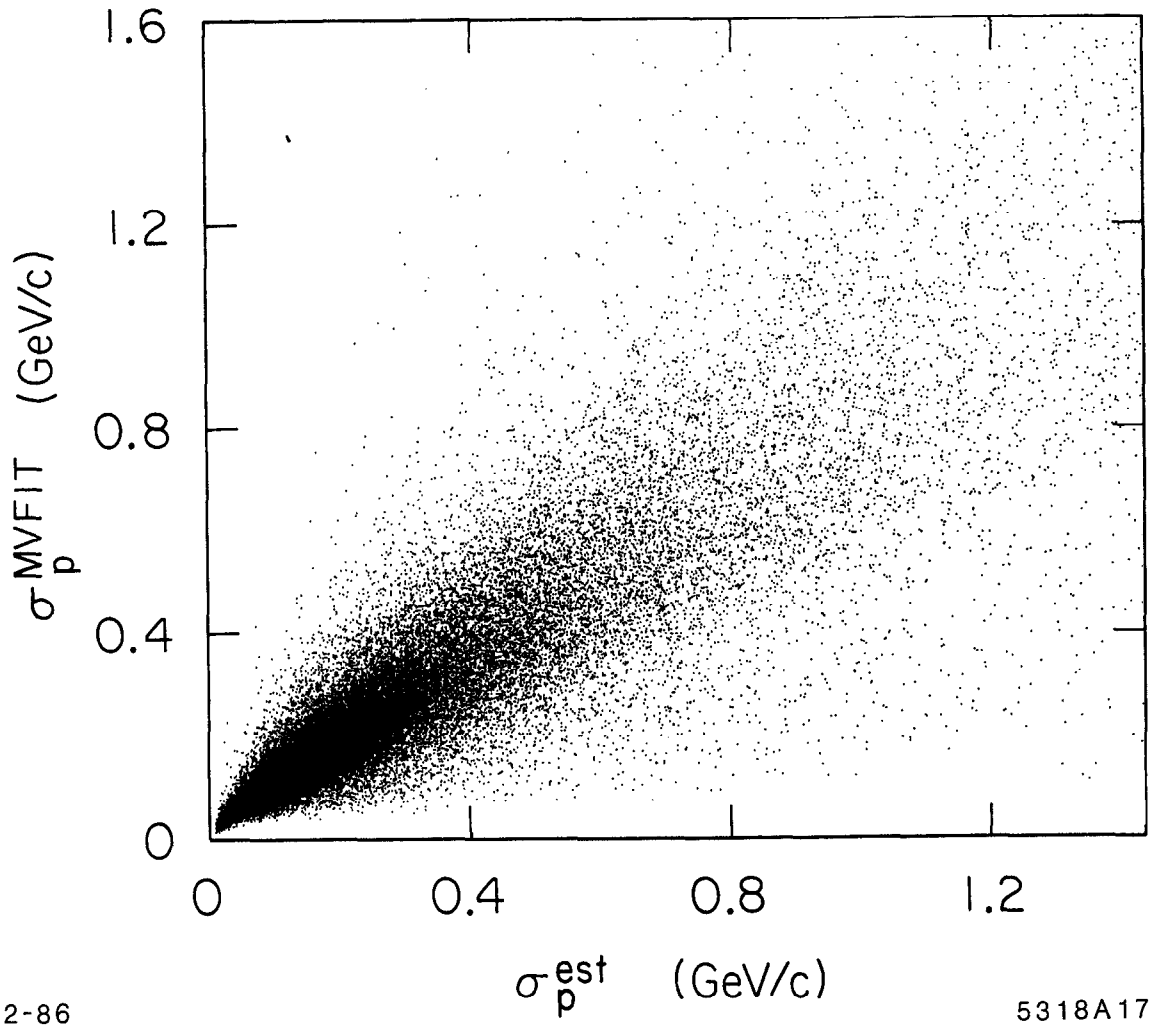

Figure 5.8. A comparison of σ_p from MVFIT and σ_p^{est}. The two estimates of σ_p are compared for all unjoined tracks with $p > 3$ GeV/c.

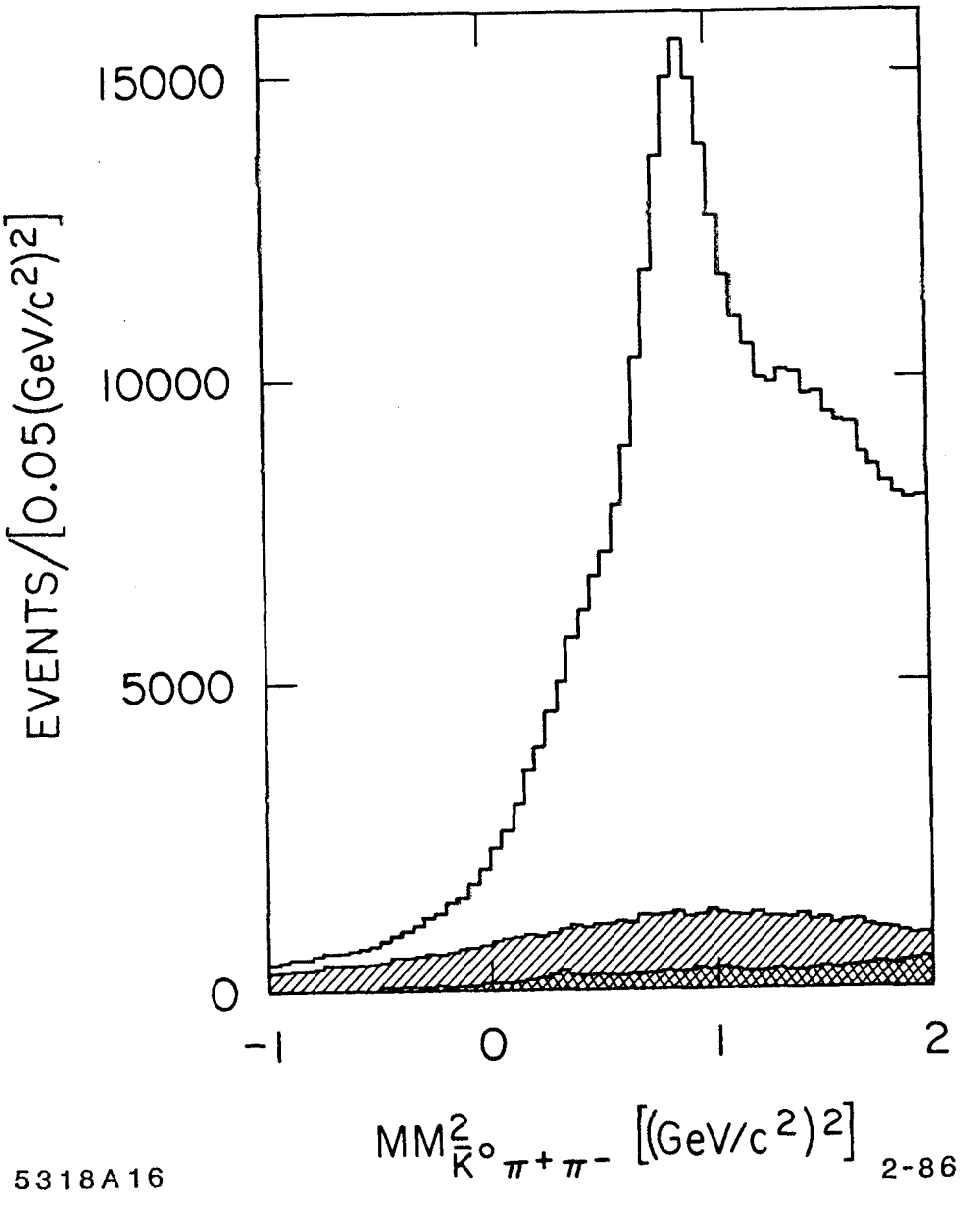

Figure 5.9. The effect of the σ_p cut and the 1C-fit requirement. The $mm^2(\bar{K}^\circ \pi^+\pi^-)$ is plotted for events passing the Λ cut (outer histogram), for events failing the resolution cut (singly-hatched histogram), and for events with a failed 1C-fit (cross-hatched histogram).

5.3.4 *Final $\bar{K}^\circ$ and Neutron Cuts*

The remaining cuts on the event sample are the $\bar{K}^\circ$ and neutron selection requirements. The residual background under the $\bar{K}^\circ$ comes mostly from n-prong channels such as $K^-\pi^+\pi^-p$ where one of the opposite signed pairs of particles has been interpreted as a V°. Such background events are typified by short decay lengths and at least one K in the final state.

Cutting hard on either the decay length (*e.g.* requiring a decay length $\geq$ 3–4 cm) or using the Čerenkov to positively identify kaon candidates removes a significant amount of the background, but also adversely affects the $\bar{K}^\circ\pi^+\pi^-n$ acceptance. Hence a less-stringent cut combining both criteria is applied; an event having a decay length $<$ 2.0 cm, or having a decay length $<$ 4.0 cm and at least one Čerenkov identified kaon is removed. Figure 5.10 shows the effect of this cut on the $\bar{K}^\circ$ signal. The Čerenkov identification requires that there be no light associated with the particle and that the particle's measured identification efficiency is in excess of 75%. (This cut also removes the backward peak in the helicity angle distribution shown in Fig. 5.6.) A $\pi^+\pi^-$ mass cut from 0.4777 to 0.5177 GeV/c^2 is placed on the V° candidate to complete the $\bar{K}^\circ$ selection.

At this stage in the selection, the only **MVFIT** requirement has been that each event have a converged geometry-only fit. An additional requirement that the event have a converged 1C-fit is imposed. The effect of this cut on the data sample is shown in Fig. 5.9 where the $mm^2(\bar{K}^\circ\pi^+\pi^-)$ distribution for the events removed by this cut is plotted. As one would expect, this cut preferentially removes background with little loss of real neutron.

The final neutron selection is a cut on the $mm^2(\bar{K}^\circ\pi^+\pi^-)$ keeping only events in the range $[0.3, 1.1]$ $(\mathrm{GeV/c^2})^2$. The lower limit for this cut is chosen to retain as much real neutron as possible but still remove some of the residual $\bar{K}^\circ\pi^-p$ and $\bar{K}^\circ\pi^-p\pi^\circ$ events. The upper limit is chosen to avoid including $\bar{K}^\circ\pi^+\pi^-\Delta$ events that "smear" under the neutron signal. Fig. 5.11 shows the mm^2 distribution for the events with $t' \leq 0.3$ $(\mathrm{GeV/c})^2$. Fig. 5.12 shows the V° invariant mass distribution after the neutron cut has been imposed (for this plot, the V° invariant mass cut was removed).

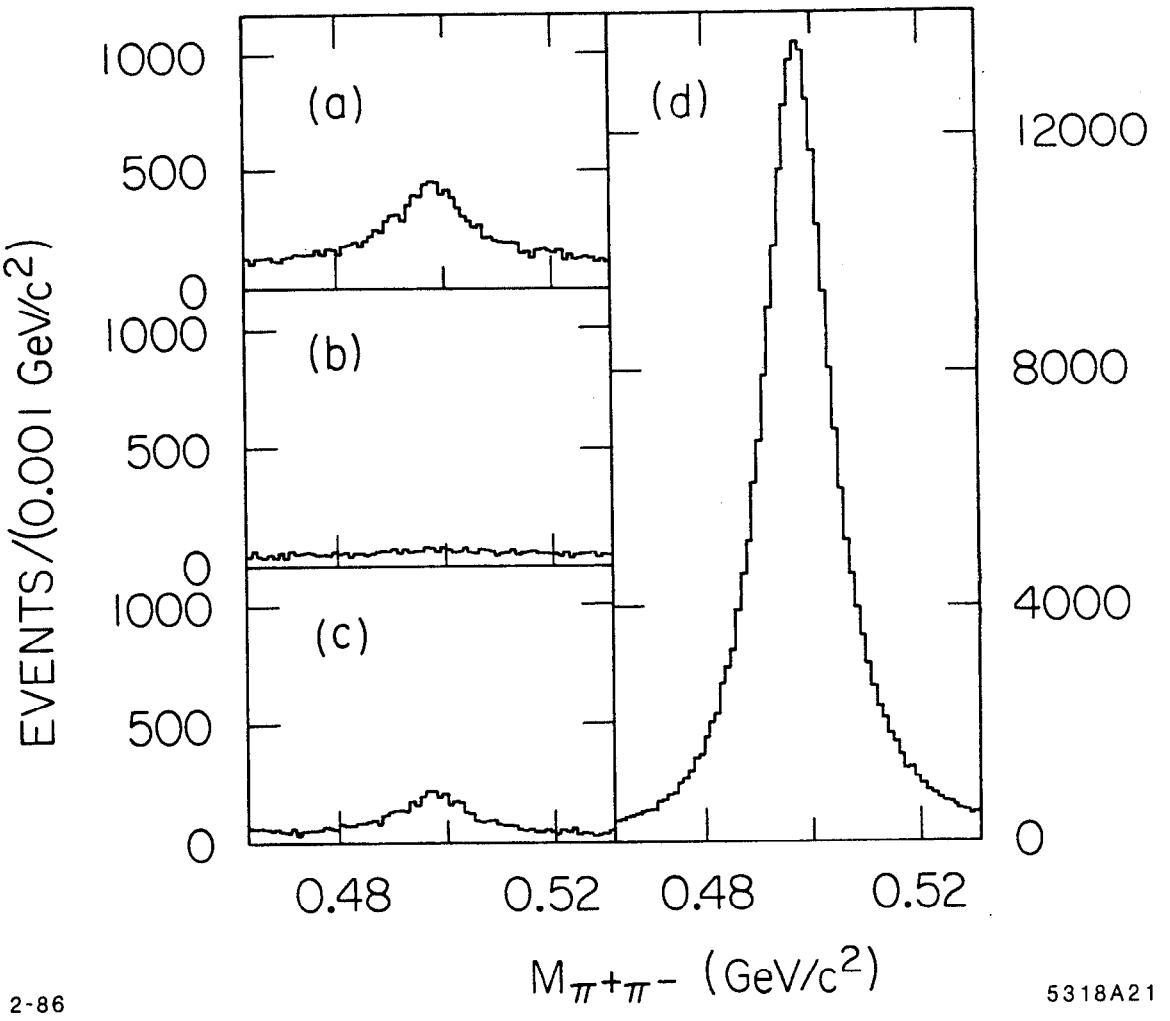

Figure 5.10. The effect of the Čerenkov and decay length cut. The V° $m(\pi^+\pi^-)$ distribution is shown for: (a) events failing the 2 cm decay length cut; (b) events removed because a V° daughter is tagged as a K; (c) events removed because a primary track is tagged as a K; and (d) the remaining event sample.

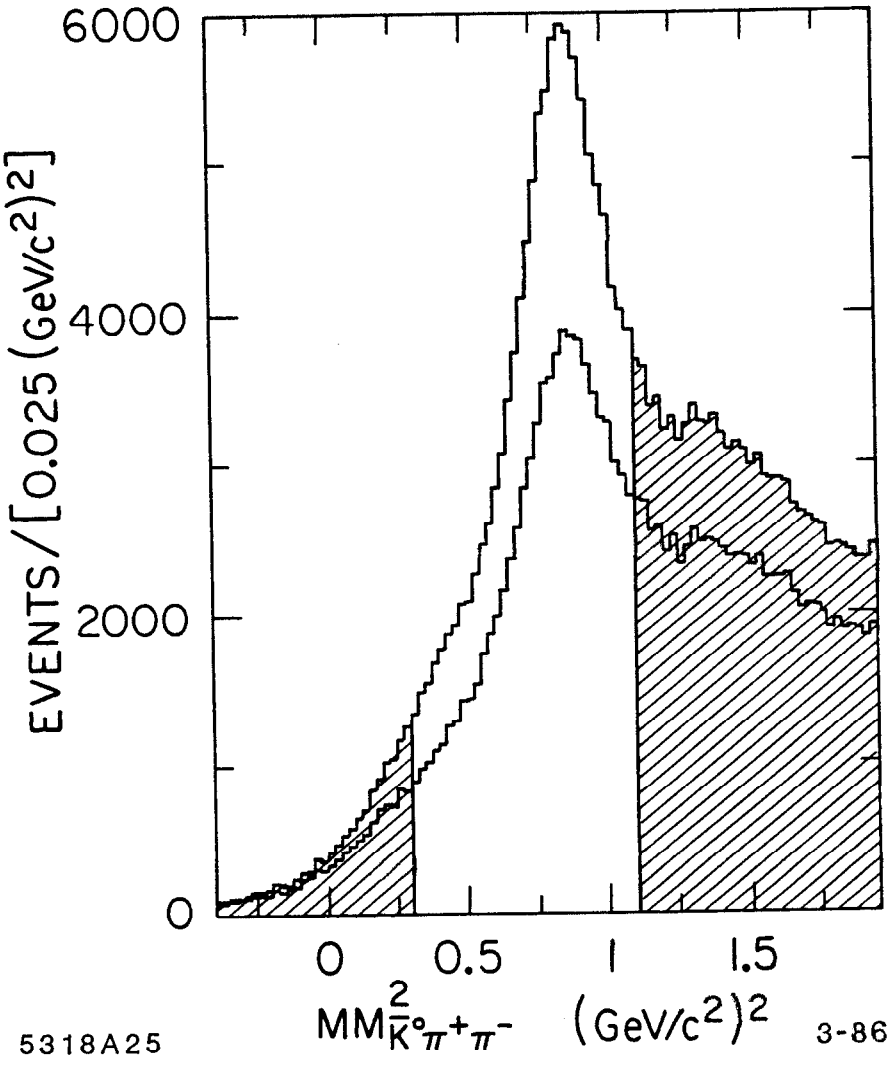

Figure 5.11. $mm^2(\bar{K}^\circ \pi^+\pi^-)$ for events with $t' < 0.3$ $(\mathrm{GeV/c})^2$. The outer histogram is for all events with $m(\bar{K}^\circ \pi^+\pi^-) < 2.4$ $\mathrm{GeV/c^2}$. The inner histogram is for all events surviving the N^*/Δ cut described in the text.

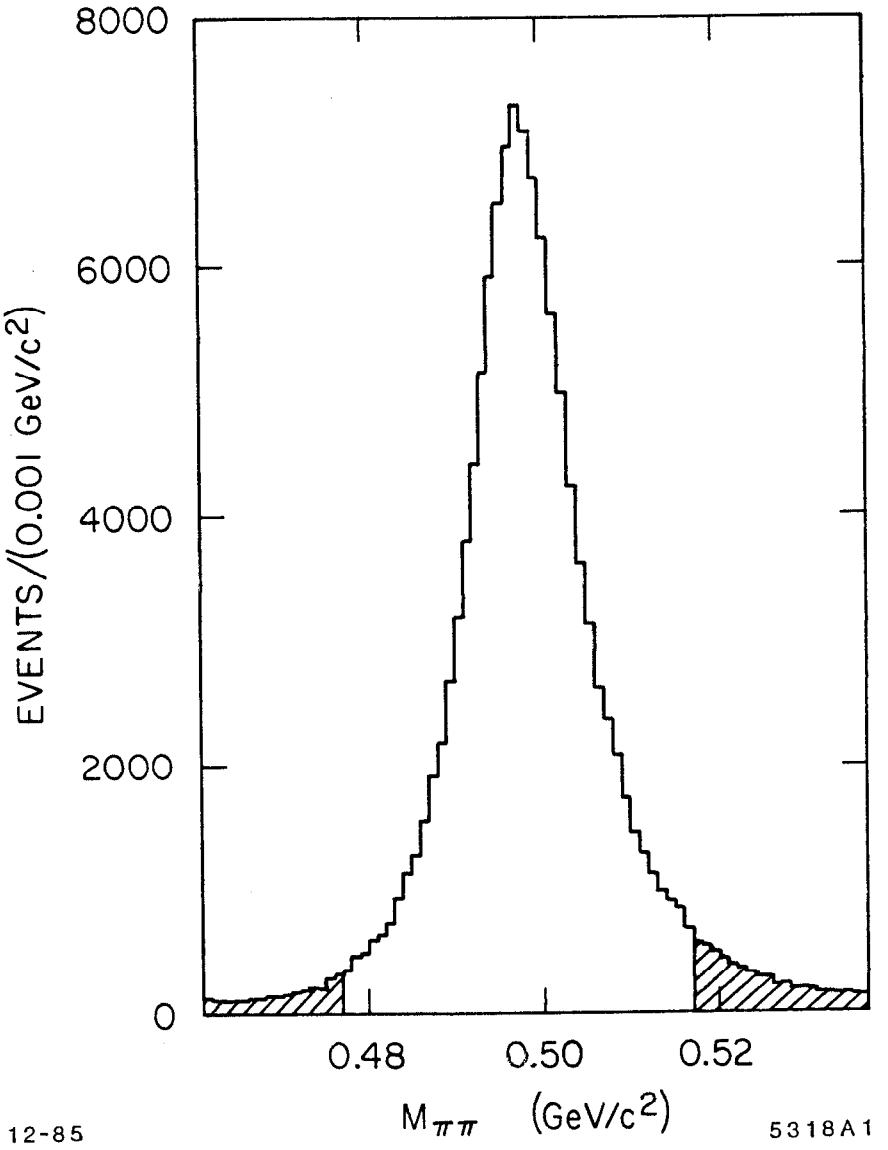

Figure 5.12. The $m(\pi^+\pi^-)$ distribution of the V° for the final sample. The shaded region shows the limits of the $m(\pi^+\pi^-)$ mass cut.

5.4 THE N^*/Δ PROBLEM

In previous $\bar{K}^\circ\,\pi^+\pi^- n$ studies, the processes

$$K^- p \rightarrow \bar{K}^\circ \pi^- (N^*/\Delta) \tag{5.3}$$

have not been clearly distinguished from the overwhelming $\bar{K}^\circ\,\pi^- p$ and $\bar{K}^\circ\,\pi^- p\,\pi^\circ$ backgrounds that overlap with the diffractively produced N^*/Δ final states at modest $\bar{K}^\circ\,\pi^+\pi^-$ invariant masses. With the ability to remove most of the proton events using the ionization measured in the cylindrical chambers, it proves possible to separate these distinct channels in the data selection and examine each one separately.

Figure 5.13 shows the scatterplot of the squared 4-momentum transfer from the beam to the $\bar{K}^\circ\pi^-$ system ($t'_{K-K^\circ\pi^-}$) versus $m^2(n\pi^+)$ for all events with $m(\bar{K}^\circ\,\pi^+\pi^-) < 2.4$ GeV/c^2. Figure 5.14 shows the projection of the data onto the $m^2(n\pi^+)$ axis. There are clear enhancements for m^2 ~1.5, ~2.2, and ~2.8 (GeV/c^2)^2. The lower mass enhancement can be associated with the $\Delta(1232)$ and the higher mass bumps indicate the production of a number of different N^* states. These resonances, which create legitimate $\bar{K}^\circ\,\pi^+\pi^- n$ final states, are undesirable as they do not correspond to the production of the three-body meson system recoiling against a neutron. In addition, they sit on a large bump that is largely from the reflection of the residual proton contamination from the $\bar{K}^\circ\,\pi^- p$ and $\bar{K}^\circ\,\pi^- p\,\pi^\circ$ channels.

These N^* events are eliminated by removing the low mass $n\pi^+$ events produced with small $t'_{K-K^\circ\pi^-}$. Events in an approximately trapezoidal region in the $m^2(n\pi^+)$–$t'_{K-K^\circ\pi^-}$ plane are excluded from the data sample. Because the amount of contamination grows with increasing $m(\bar{K}^\circ\,\pi^+\pi^-)$, the region excluded by this cut also varies with mass as described in Table 5.1. The inner histogram in Fig. 5.14 shows the effect of this cut on the data.

At this point, it is worth noting the amount of remaining $\bar{K}^\circ\,\pi^- p$ and $\bar{K}^\circ\,\pi^- p\,\pi^\circ$ contamination in the data sample. Fig. 5.15 shows the distribution of events in $mm^2(\bar{K}^\circ\,\pi^- p)$ for a number of different $m(\bar{K}^\circ\,\pi^+\pi^-)$ bins. Most of

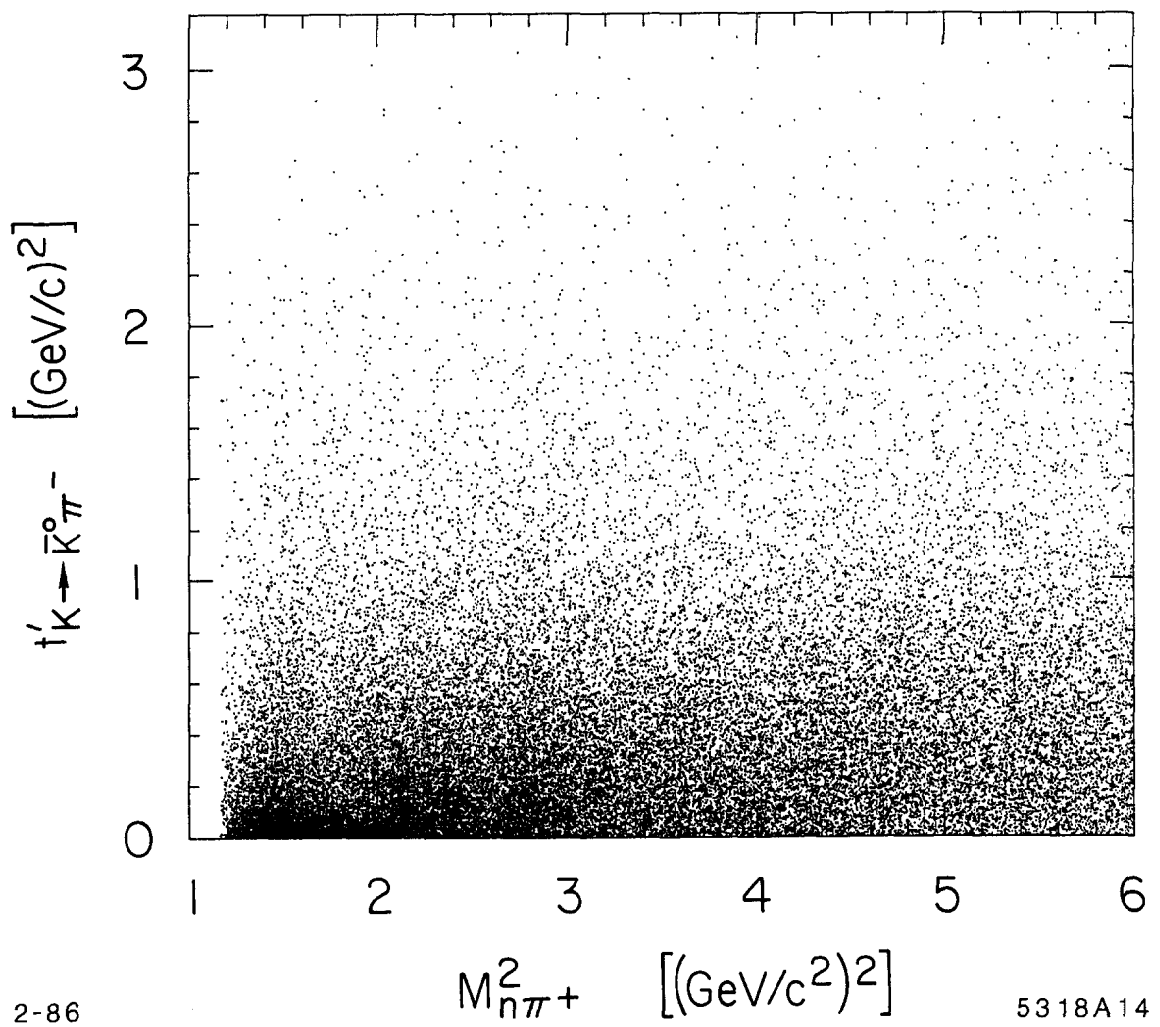

Figure 5.13. The scatterplot of $t'_{K-K^\circ\pi^-}$ versus $m^2(n\pi^+)$. The effective mass squared is computed using the fitted vectors from the 1C-fit.

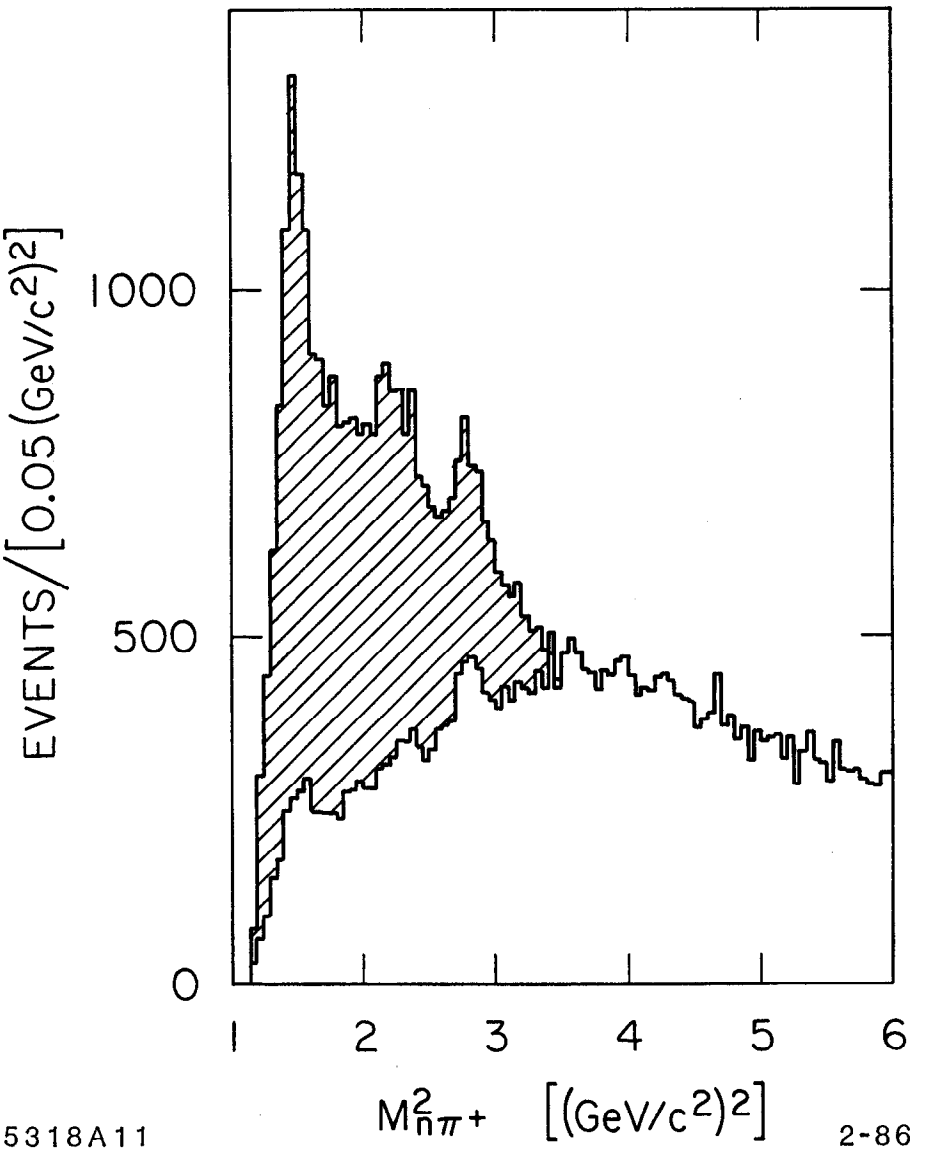

Figure 5.14. The $m^2(n\pi^+)$ distribution. The outer histogram is for all events, while the inner histogram shows the distribution for events passing the N^* cut.

Table 5.1. The parametrization of the N^* cut. The cut boundaries vary as a function of $M_3 = m(\bar{K}^\circ \pi^+\pi^-)$. For a given M_3 and $m^2(n\pi^+)$, a minimum $t'_{K-K^\circ\pi^-}$ $(\mathcal{T})$ is required of each event: For events with $m^2(n\pi^+) \leq 2.25$ $(\mathrm{GeV/c^2})^2$, $\mathcal{T}$ is independent of $m^2(n\pi^+)$; for events with $2.25 < m^2(n\pi^+) \leq 3.0$ $(\mathrm{GeV/c^2})^2$, $\mathcal{T}$ decreases linearly with m^2 from its value at $m^2 = 2.25$ to its value at $m^2 = 3.0$ $(\mathrm{GeV/c^2})^2$ shown in the table; and for events with $3.0 \leq m^2(n\pi^+) < 3.5$ $(\mathrm{GeV/c^2})^2$, $\mathcal{T}$ decreases linearly with m^2 to 0.0 from its value at $m^2(n\pi^+) = 3.0$ $(\mathrm{GeV/c^2})^2$.

M_3 Range GeV/c^2	$\mathcal{T}$ $(\mathrm{GeV/c})^2$	
	$m^2(n\pi^+) \leq 2.25$ $(\mathrm{GeV/c^2})^2$	Value at $m^2(n\pi^+) = 3.0$ $(\mathrm{GeV/c^2})^2$
$M_3 \leq 1.50$	0.1	0.1
$1.50 < M_3 \leq 1.63$	$0.1 + (M_3 - 1.50)0.3$	0.1
$1.63 < M_3 \leq 2.10$	$0.133 + (M_3 - 1.63)0.6$	$0.1 + (M_3 - 1.63)0.3$
$2.10 < M_3 \leq 2.20$	$0.42 + (M_3 - 2.10)0.3$	0.24
$2.20 < M_3$	0.45	0.24

the residual $\bar{K}^\circ \pi^- p$ contamination comes in at high $\bar{K}^\circ \pi^+\pi^-$ masses so that below a three body mass of 2.3 GeV/c^2 there is only weak evidence for proton events.

5.5 Properties of the $\bar{K}^\circ \pi^+\pi^- n$ Sample

Figure 5.16 shows the three-body mass distribution ($M_3 \equiv m(\bar{K}^\circ \pi^+\pi^-)$) of the $\bar{K}^\circ \pi^+\pi^- n$ event sample for all events and for events with $|t'| \leq 0.3$ $(\mathrm{GeV/c})^2$. The prominent structures are two peaks at approx $M_3 = 1.45$ and 1.80 GeV/c^2. With the high statistics, we can also discern a shoulder around $M_3 = 2.0$ GeV/c^2. All of this structure sits on top of a large continuum of events.

The scatterplot of t' versus M_3 is displayed in Fig. 5.17. The two prominent peaks appear as dark bands at low t' and diminish in strength relative to the underlying event distribution at higher t' values. On the other hand, at $\bar{K}^\circ \pi^+\pi^-$ masses around 1.3 GeV/c^2 a shoulder extending to higher t' is evident in the scatterplot. At $\bar{K}^\circ \pi^+\pi^-$ masses above 2 GeV/c^2 the distribution varies more slowly with t' so there are more events at quite large values of t'. This behavior is confirmed by the t' distributions in Fig. 5.18(a)-5.18(b) where the data have

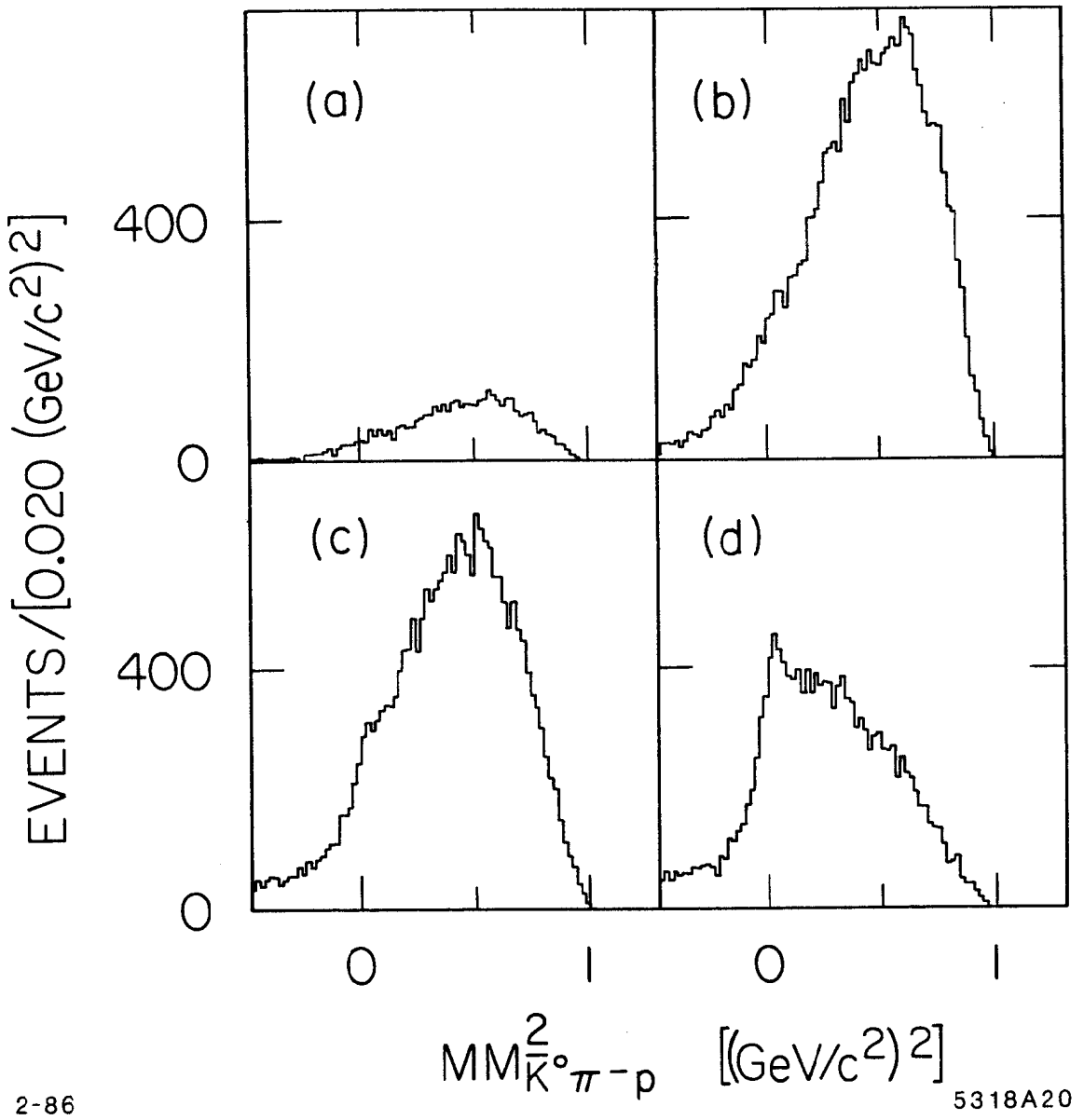

Figure 5.15. The $mm^2(\bar{K}^\circ \pi^- p)$ distribution for different $m(\bar{K}^\circ \pi^+ \pi^-)$ intervals. The $m(\bar{K}^\circ \pi^+ \pi^-)$ intervals are (a) 0.8-1.3 GeV/c^2, (b) 1.3-1.8 GeV/c^2, (c) 1.8-2.3 GeV/c^2, and (d) 2.3-2.8 GeV/c^2.

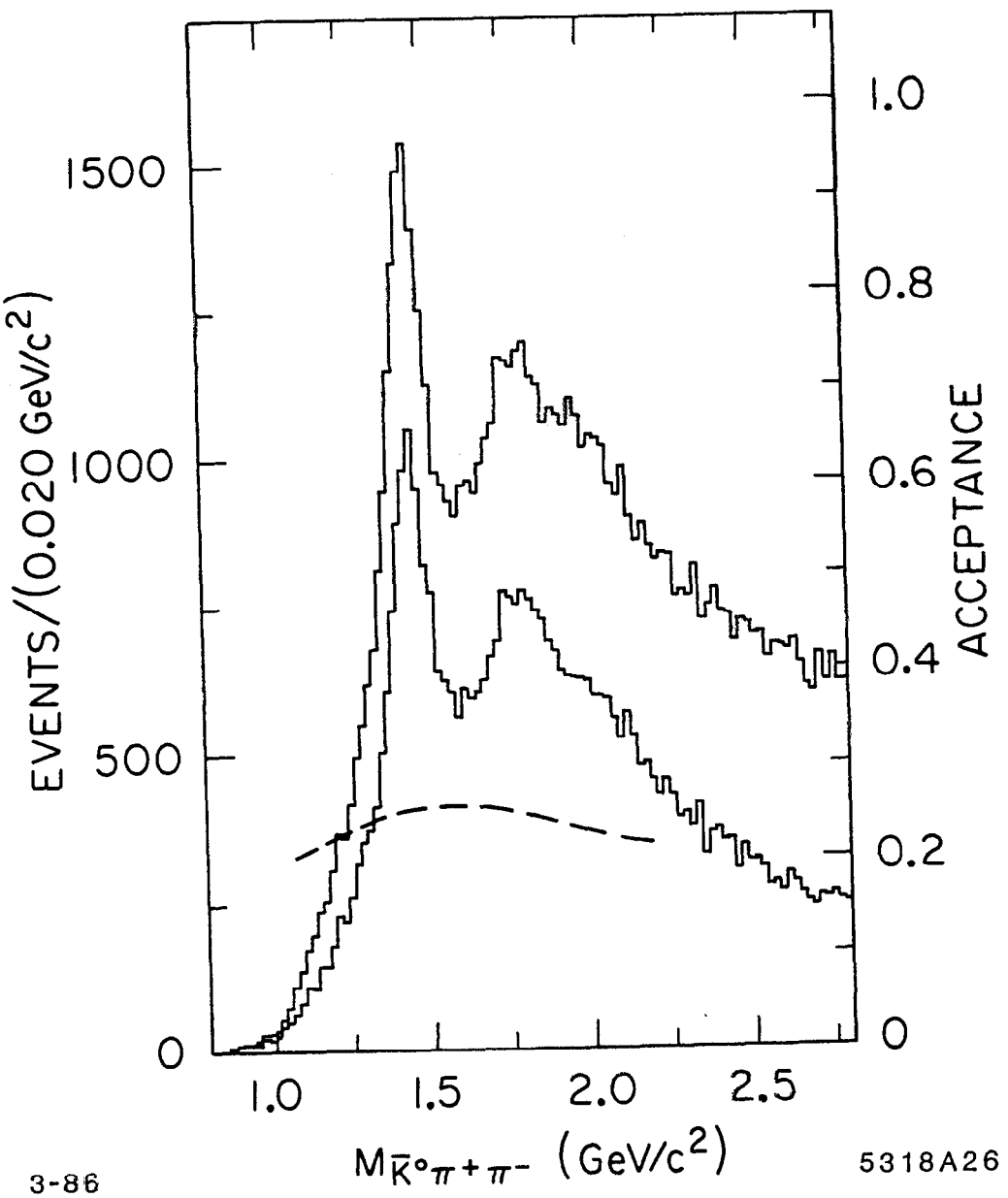

Figure 5.16. The $\bar{K}^\circ \pi^+\pi^-$ invariant mass distribution. The outer histogram is the $m(\bar{K}^\circ \pi^+\pi^-)$ distribution for the entire data sample. The inner histogram shows the same distribution for events with $|t'| \leq 0.3$ $(\mathrm{GeV/c})^2$. The dashed line shows the acceptance for the final event selection as a function of $m(\bar{K}^\circ \pi^+\pi^-)$.

been divided into three $\bar{K}^\circ \pi^+\pi^-$ mass bins. These distributions are not pure exponentials; however they can be described conveniently by one exponential distribution (with slope b_1) for $|t'| \leq 0.3$ (GeV/c)^2 and a second exponential (with slope b_2) for $0.3 < |t'| \leq 1.0$ (GeV/c)^2. The lines shown in Fig. 5.18 show the results of a fit of such a function to the distributions. The slope parameters resulting from the fit are listed in Table 5.2.

A closer look at the data reveals that there are substantial two-body interactions in the three-meson final state. To illustrate the behavior of these interactions as a function of M_3, the Dalitz plots for $1.3 \leq M_3 < 1.5$ GeV/c^2, for $1.5 \leq M_3 < 1.7$ GeV/c^2, for $1.7 \leq M_3 < 1.9$ GeV/c^2, and for $1.9 \leq M_3 < 2.3$ GeV/c^2 are shown in Fig. 5.19, Fig. 5.20, Fig. 5.21, and Fig. 5.22, respectively. In the lowest mass region, the Dalitz plot is dominated by $K^*(892)$ production with a relatively small amount of $\rho(770)$. It is clear from the location of the Dalitz plot boundary at $M_3 = 1.3$ GeV/c^2 that the $K\rho$ production is severely affected by the allowed phase space with the ρ lineshape being truncated just above the peak of the resonance. Figure 5.20 shows clear $K^*(892)$ and $\rho(770)$ bands but no hint of other structure; K^* production is still the dominant feature in the final state. In Fig. 5.21, which corresponds to events with $1.7 \leq M_3 < 1.9$ GeV/c^2, the $K^*(892)$ and $\rho(770)$ bands are still prominent, and there is now indication of $K^*(1430)$ production, although it is hard to discern a clear $K^*(1430)$ band. It appears as a slight enhancement in the projection of the scatterplot on the $m^2(\bar{K}^\circ\pi^-)$ axis. The Dalitz plot for the very highest mass bin, Fig. 5.22, shows clear $K^*(892)$, $\rho(770)$, and $K^*(1430)$ bands, with some indication of $f(1270)$ production. The evidence for the latter is the shoulder at a mass of ~ 1.25 GeV/c^2 in the projection of the Dalitz plot onto the $m^2(\pi^+\pi^-)$ axis.

From these plots it is clear that the $\bar{K}^\circ \pi^+\pi^-$ final state results largely from isobar production, *i.e.* the final state is the result of the production of a quasi-two body system in which one of the particles decays strongly. However there are a number of other points that can be made about the Dalitz plot distributions. Firstly, the event distributions outside the resonance bands are fairly uniform across the Dalitz plot. This is easily seen in the Dalitz plot for the very highest $\bar{K}^\circ \pi^+\pi^-$ invariant masses, Fig. 5.22. The event distribution within the inner contour is quite

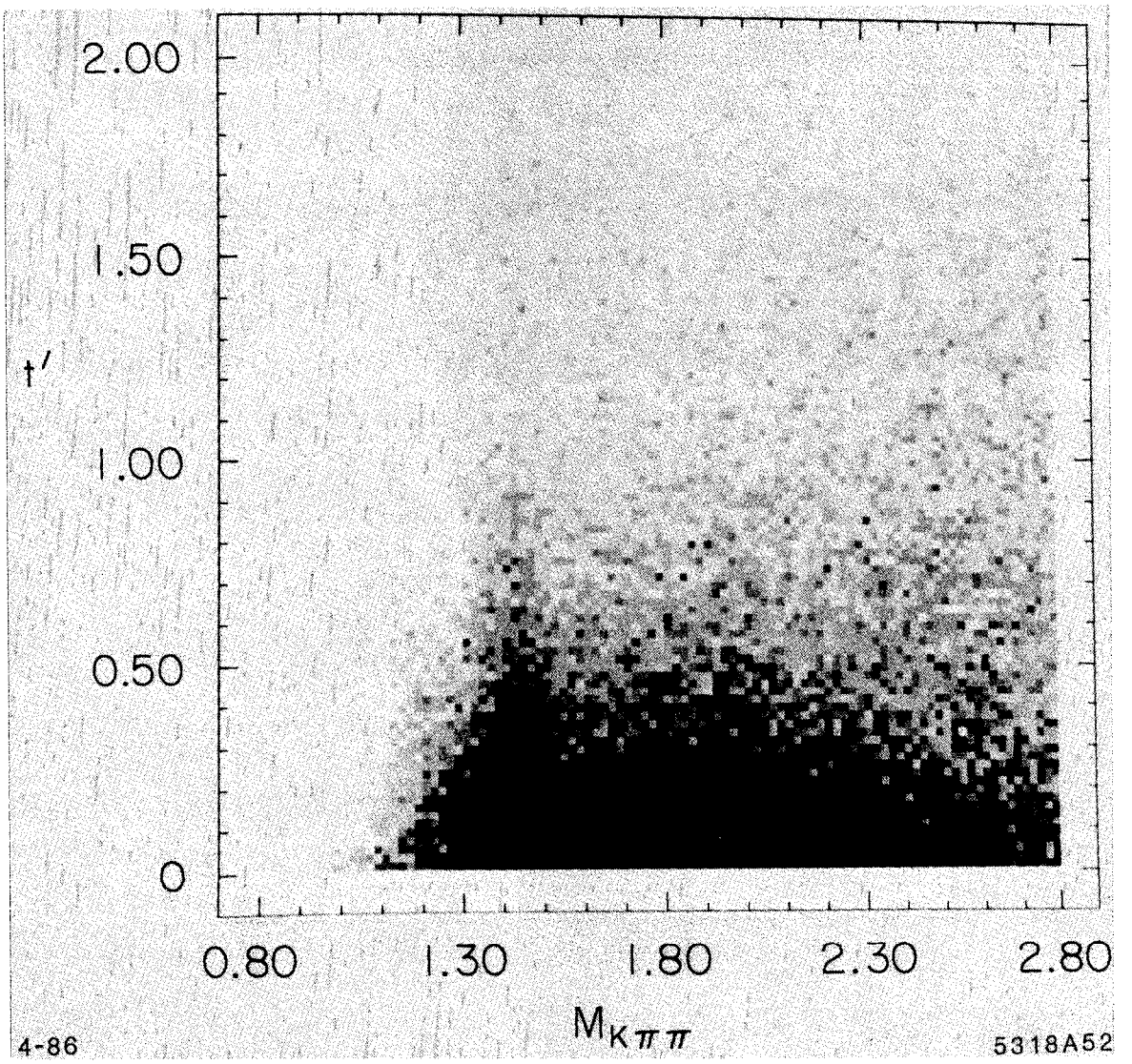

Figure 5.17. The scatterplot of t' versus $m(\bar{K}^\circ \pi^+\pi^-)$.

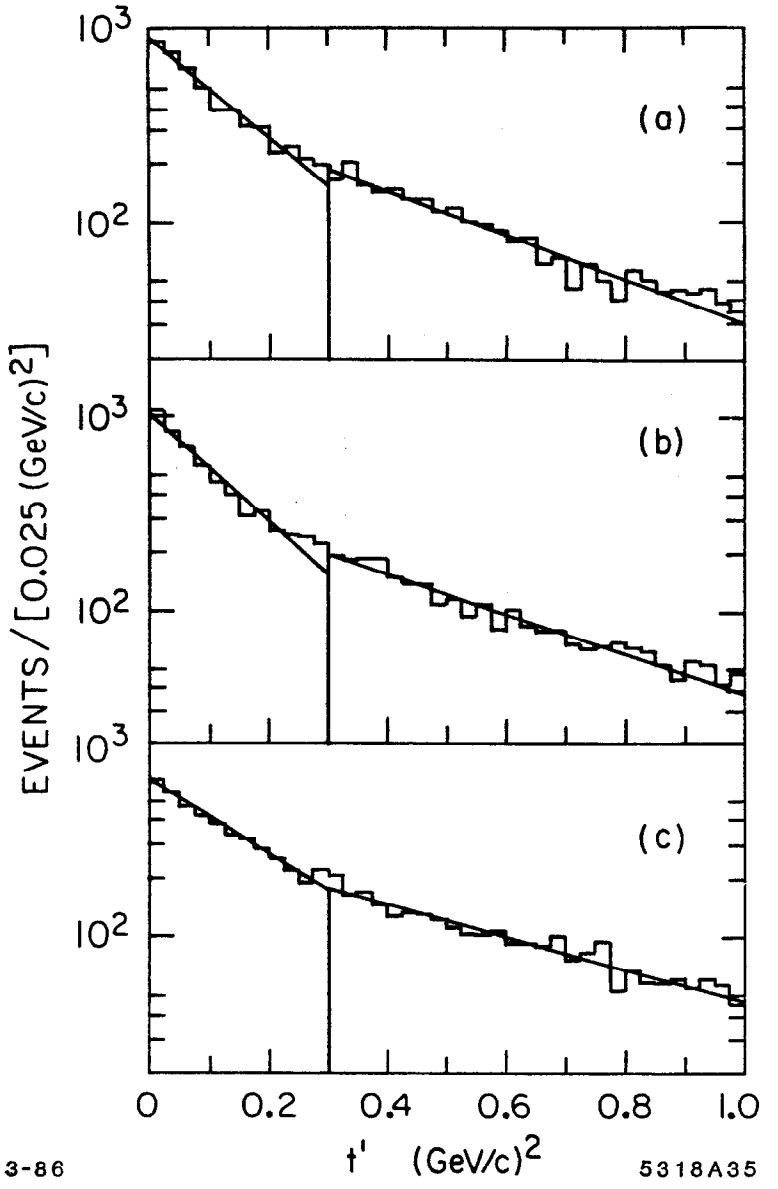

Figure 5.18. The t' distribution for three mass regions. The three histograms show the t' distributions for (a) events with $\bar{K}^\circ \pi^+\pi^-$ masses < 1.6 GeV/c^2, (b) events with $1.6 < M_3 \leq 2.0$ GeV/c^2, and (c) events with $\bar{K}^\circ \pi^+\pi^-$ masses > 2.0 GeV/c^2. The lines are the results of the fits described in the text.

Table 5.2. The slopes of the exponential $|t'|$ distributions.

$m(\bar{K}^\circ \pi^+\pi^-)$ Range (GeV/c^2)	b_1 ((GeV/c)$^{-2}$)	b_2 (invGeVc)
$M_3 < 1.6$	-5.8 ± 0.2	-2.6 ± 0.1
$1.6 \leq M_3 < 2.0$	-6.4 ± 0.2	-2.3 ± 0.1
$2.0 \leq M_3$	-4.4 ± 0.2	-1.9 ± 0.1

uniform outside the $K^*(892)$, $\rho(770)$, and $K^*(1430)$ bands. This would indicate that the underlying event distribution either: (a) does not arise through a quasi-two body state; or (b) derives from a two-body state in which the strongly-decaying resonance is very broad.

Secondly, the structure in the overlap regions of the resonance bands changes as a function of $\bar{K}^\circ \pi^+\pi^-$ invariant mass. This is most apparent in the overlap region of the $K^*(892)$ and $\rho(770)$. For example, in the mass bin $1.5 \leq M_3 < 1.7$ GeV/c^2 (Fig. 5.20), this overlap region is enhanced relative to the rest of the $K^*(892)$ band. In the next higher mass bin, this enhancement is no longer evident and in the very highest mass bin (Fig. 5.22), the $K^*(892)$ band appears to be the weakest in the region where it overlaps with the $\rho(770)$. Such changes in interference are expected; they would arise naturally if the quantum amplitudes of the two quasi-two body states were coherent.

There are a number of approaches that can be taken to understand the details of the production of the $\bar{K}^\circ \pi^+\pi^-$ system. In the context of trying to model the data, it is clear that the final state interactions must be taken into account properly. In addition such a model must also be able to incorporate the interference effects in the final state, some of which are already evident in the Dalitz plots. Finally, we would want to use as much of the information content in the event distribution as possible. This implies that maximum use should be made of the information contained in the angular distribution of the $\bar{K}^\circ \pi^+\pi^-$ final state. All these requirements are satisfied by the three-body isobar model, and so the next step in this study will be a partial wave analysis (PWA) of the three-meson system employing this model.

The description of the partial wave analysis formalism and methodology will

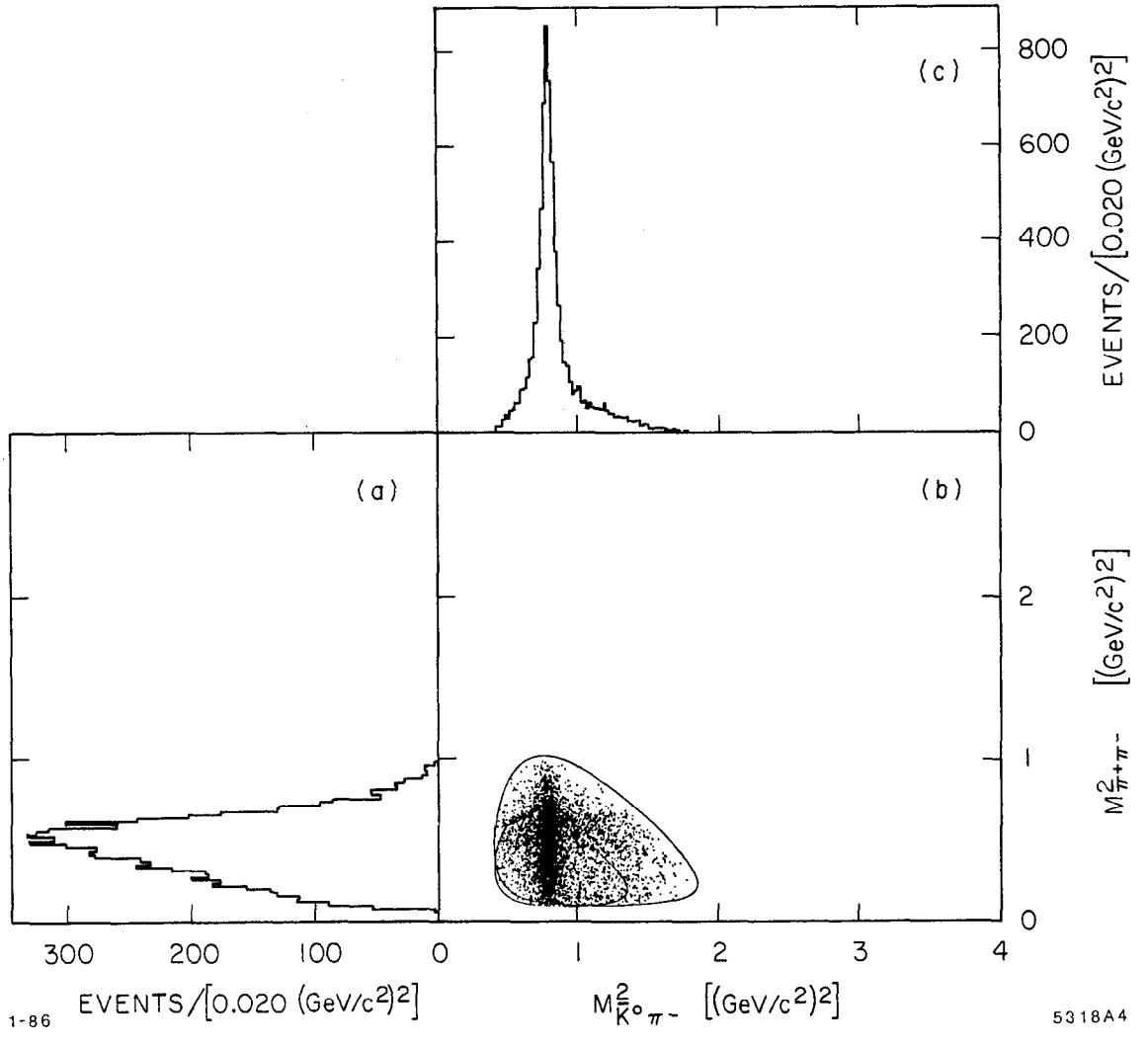

Figure 5.19. The Dalitz plot for $1.3 \leq M_3 < 1.5$ GeV/c^2. The contours show the boundaries of the Dalitz plot for the low and high mass limits.

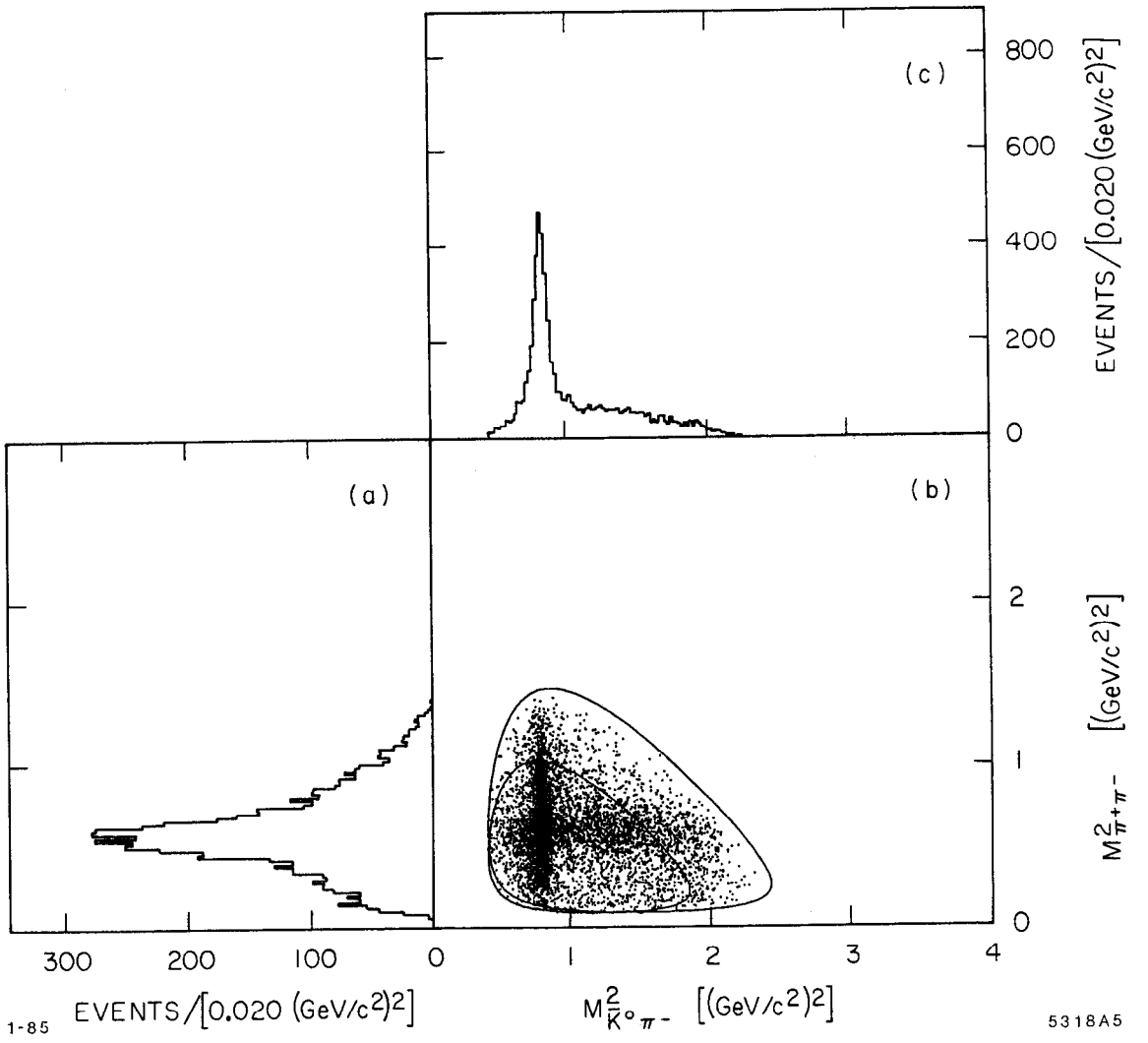

Figure 5.20. The Dalitz plot for $1.5 \leq M_3 < 1.7$ GeV/c^2. The contours show the boundaries of the Dalitz plot for the low and high mass limits.

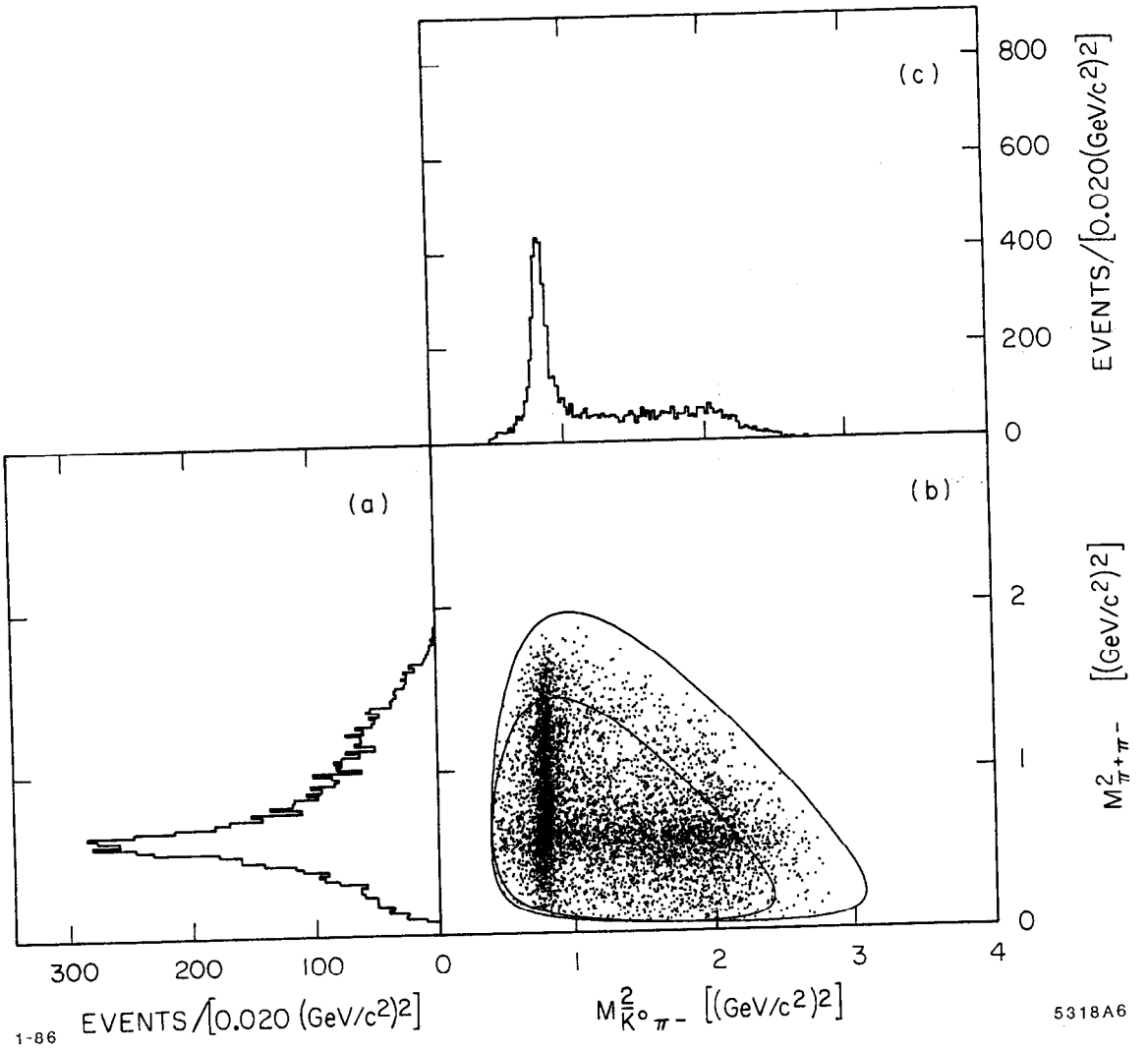

Figure 5.21. The Dalitz plot for $1.7 \leq M_3 < 1.9$ GeV/c^2. The contours show the boundaries of the Dalitz plot for the low and high mass limits.

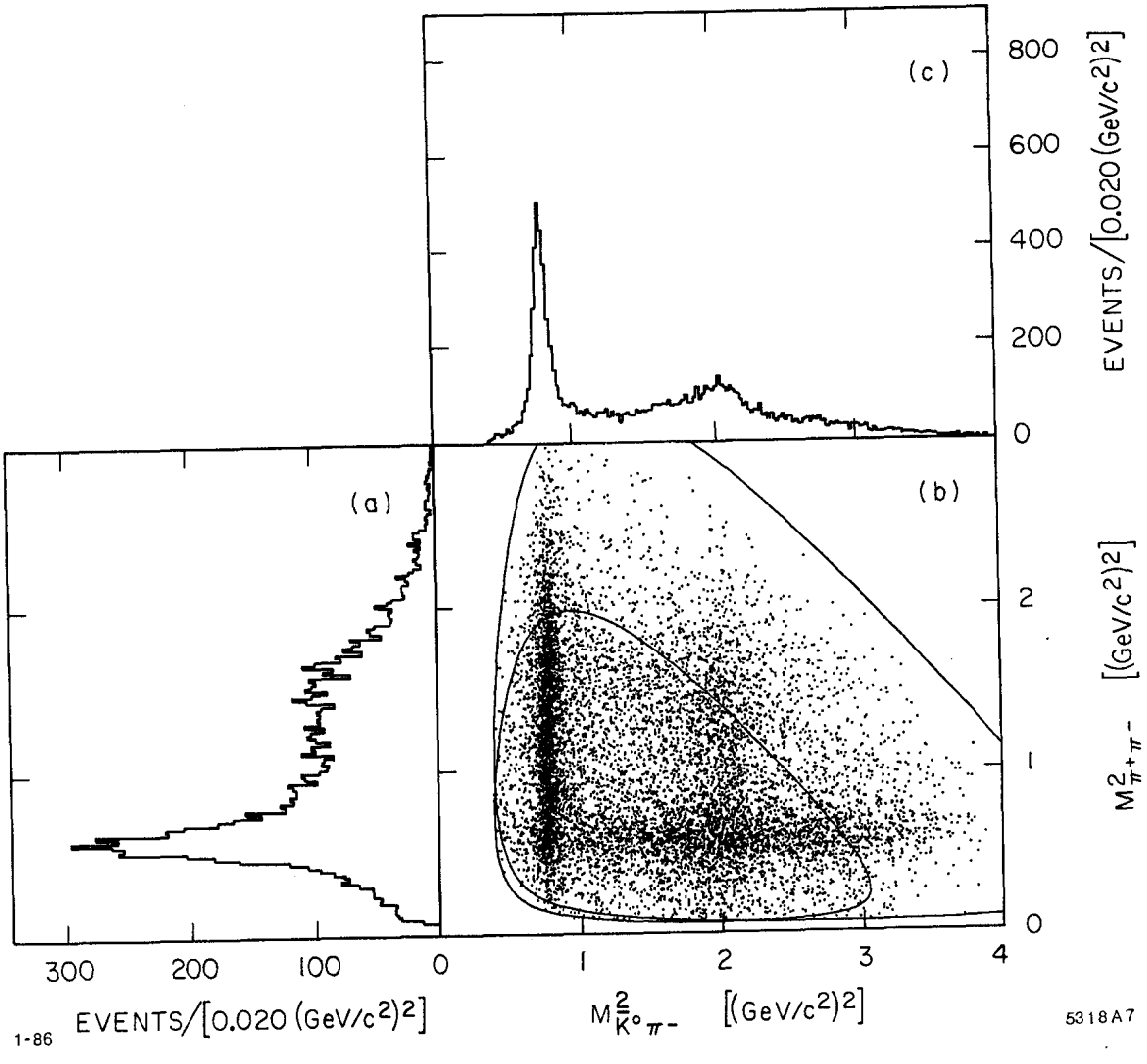

Figure 5.22. The Dalitz plot for $1.9 \leq M_3 < 2.3$ GeV/c^2. The contours show the boundaries of the Dalitz plot for the low and high mass limits.

be the subject of the next chapter. To finish the description of the data sample, the remainder of this chapter will discuss the performance of the spectrometer and the sensitivity of the experiment.

5.6 Spectrometer Resolution and Acceptance

The resolution of the LASS spectrometer depends strongly on the characteristics of the events in the data sample. The angular resolution of individual particle trajectories is dominated by the measurement of the track inside the solenoid, and so is constant for forward-produced particles and decreases only slightly for particles produced at high angles and measured only in the cylindrical chambers. On the other hand, the momentum resolution for single particles is non-uniform and shows a strong variation as a function of the particle's production angle θ. For most tracks, the momentum resolution is good, with $\sigma_p/p \sim 0.002 - 0.010$ for tracks with moderate momenta ($p \lesssim 2$ GeV/c) and production angles ($\theta \gtrsim 0.150$). The momentum resolution is uniformly the highest ($\sigma_p/p \sim 0.005$) in the very forward region ($\theta \lesssim 0.050$ rad) where the particles are measured in the dipole. It is lowest (σ_p/p ~0.1–0.2) for particles with $p \gtrsim$2–3 GeV/c and θ ~0.050–0.150 rad; such particles, which are not within the dipole acceptance, have momentum uncertainties given approximately by Eqn. 5.2.

Because of these large variations in momentum uncertainty, the kinematic resolution of a specific final state depends on the distribution of the produced events. The invariant mass resolution of the detector is demonstrated by the $\pi^+\pi^-$ invariant mass distribution for the $\bar{K}^\circ$ candidates in the final $\bar{K}^\circ \pi^+\pi^- n$ event sample. This distribution is shown in Fig. 5.23 for events with $t' \leq 0.3$ (GeV/c)^2 in two $\bar{K}^\circ \pi^+\pi^-$ invariant mass bins: $1.38 \leq m(\bar{K}^\circ \pi^+\pi^-) < 1.58$ GeV/c^2, and $1.74 \leq m(\bar{K}^\circ \pi^+\pi^-) < 1.94$ GeV/c^2. The full-width at half-maximum is ~ 0.013 GeV/c^2. This mass resolution depends strongly on the number of K° daughters that are reconstructed in the dipole. The relative number of $\bar{K}^\circ$ candidates with neither daughter, one daughter, and two daughters reconstructed in the dipole are listed in Table 5.3 for events in the lower $\bar{K}^\circ \pi^+\pi^-$ mass bin.

The reliability of the Monte Carlo (MC) simulation on the $\bar{K}^\circ \pi^+\pi^- n$ final state can be checked by comparing the reconstructed $\bar{K}^\circ$ mass distributions for

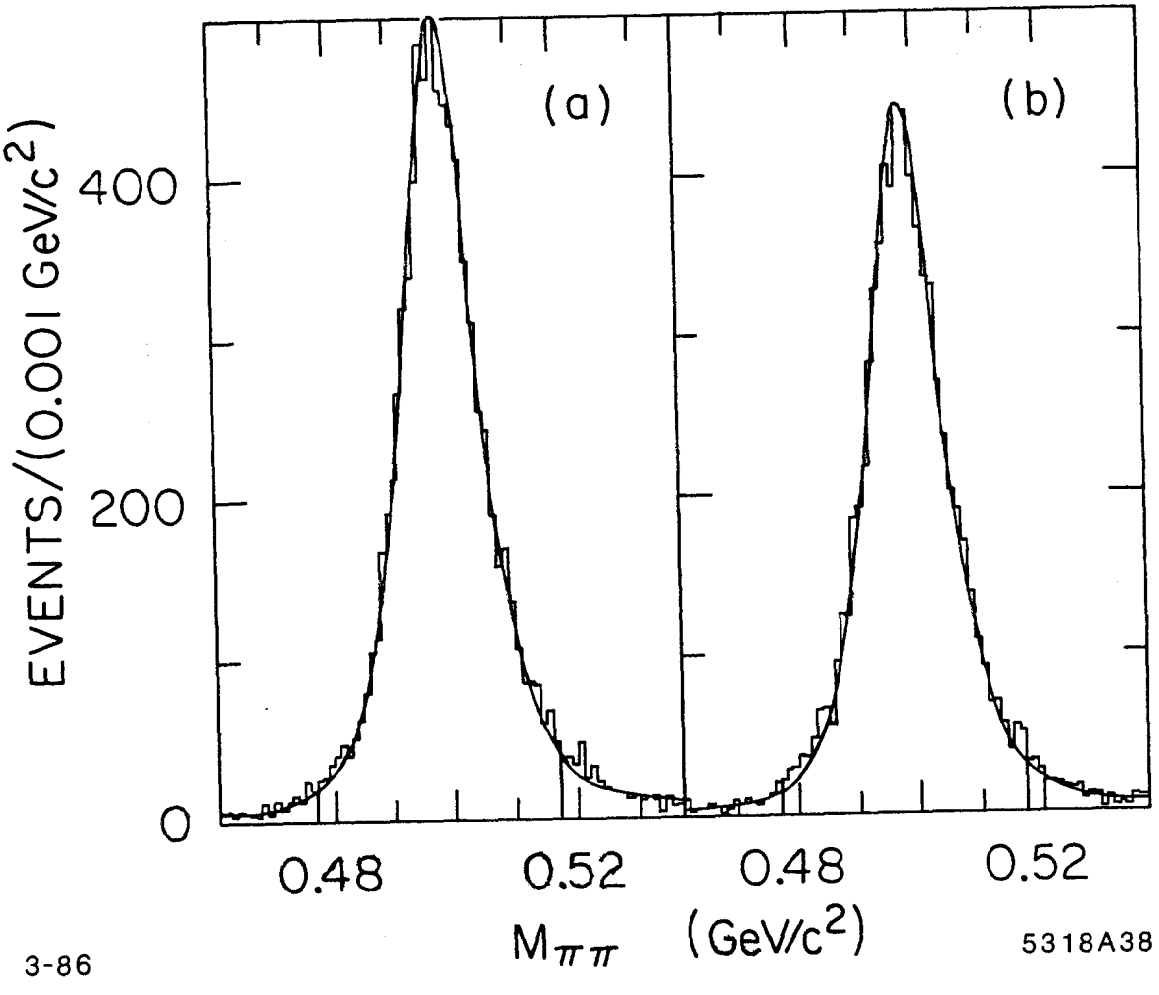

Figure 5.23. The $\bar{K}^\circ$ invariant mass for data and MC events. The histogram shows the $\pi^+\pi^-$ invariant mass distribution for data events with $m(\bar{K}^\circ\pi^+\pi^-) \sim 1.48$ GeV/c^2 (a) and $m(\bar{K}^\circ\pi^+\pi^-) \sim 1.84$ GeV/c^2 (b). The curves are fits to the MC lineshapes with a linear background.

Table 5.3. The number of dipole-reconstructed $\bar{K}^\circ$ candidates. The table lists the fractions of $\bar{K}^\circ$ candidates with different dipole track configurations. The full-width at half-maximum (FWHM) of the $\pi^+\pi^-$ invariant mass distribution for each type of $\bar{K}^\circ$ is listed, along with the population fractions predicted by the Monte Carlo.

Number of Dipole-joined Daughter Tracks	Fraction Observed	Fraction Predicted by MC	FWHM GeV/c^2
0	0.541 ± 0.010	0.52	0.017
1	0.412 ± 0.008	0.44	0.011
2	0.047 ± 0.002	0.04	0.007

Table 5.4. The results of the fit to the $\bar{K}^\circ$ lineshape. The background is parametrized as $\alpha + \beta(m(\pi\pi) - m_{\bar{K}^\circ})$ where $m^\circ_{\bar{K}}$ is the fitted mass of the $\bar{K}^\circ$.

Quantity	Value	
	$m(\bar{K}^\circ\,\pi^+\pi^-) \sim 1.48$ GeV/c^2	$m(\bar{K}^\circ\,\pi^+\pi^-) \sim 1.84$ GeV/c^2
K° mass	0.4973 ± 0.0007	0.4972 ± 0.0007
Peak Height	512 ± 6	473 ± 5
Background (α)	7.7 ± 0.5	5.7 ± 0.4
Background Slope (β)	701 ± 16	340 ± 13
χ^2/DOF	99/76	132/75
Contamination	0.038	0.032

data and MC events. This is done in Fig. 5.23 where the MC prediction for the $\bar{K}^\circ$ lineshape is superimposed on the data distribution. The MC lineshape comes from a fit of the data to the observed MC mass distribution allowing for a shift in the nominal $\bar{K}^\circ$ mass and a background term (linear in invariant $\pi^+\pi^-$ mass). A similar comparison and fit was performed to MC and data events satisfying $1.84 \leq m(\bar{K}^\circ\,\pi^+\pi^-) < 1.94$ GeV/c^2. The results of these two fits are summarized in Table 5.4.

To obtain a faithful representation of the data , it is necessary to distribute the

MC events in the same manner as the produced data events. This is achieved by using the results of the partial wave analysis described in the next chapter to weight the Monte Carlo events with their production probability, as determined from the PWA. This procedure creates a *weighted* MC event sample with the same Dalitz plot and angular variable correlations as exist in the data.

The offset in the nominal $\bar{K}^\circ$ mass indicates that there is a systematic shift of $\sim 0.11\%$ in the measured momentum for data events. This is consistent with the accuracy of the absolute momentum calibration of the spectrometer. The estimates of the $\bar{K}^\circ$ "contamination" quoted in the table are the fraction of background events within the invariant mass window ($0.4777 \leq m(\pi^+\pi^-) < 0.5177$) that is used to define the $\bar{K}^\circ$ sample. These estimate depend on the tails of the $\bar{K}^\circ$ distribution that in turn are sensitive to the weighting of the Monte Carlo data. In this situation, where the MC data have been weighted using the results of the fit to the events within the $\bar{K}^\circ$ mass window, the resulting weights for the events in the wings of the distribution are extrapolations and cannot be expected to reliably reproduce the observed data distributions. For example, the $\bar{K}^\circ$ mass distributions for MC events uniformly distributed in phase space have wings that are approximately twice as large as those in the weighted distributions, and the estimates of the contamination using the unweighted distributions are half those listed in Table 5.4. This would therefore indicate that the quoted $\bar{K}^\circ$ contamination is a conservative estimate.

The $\bar{K}^\circ\,\pi^+\pi^-$ invariant mass resolution is illustrated in Fig. 5.24 where the residual of the measured and generated three-body mass is histogrammed for Monte Carlo events that have passed through the event selection procedure. The generated mass of the $\bar{K}^\circ\,\pi^+\pi^-$ system is ~ 1.4 GeV/c^2 for this MC sample. The distribution is not well represented by a single gaussian distribution but a model with two gaussian distributions with widths of ~ 0.009 and ~ 0.019 GeV/c^2 in approximately equal proportions gives a reasonable fit to the peak. The full-width at half-maximum (FWHM) of this distribution is ~ 0.032 GeV/c^2, corresponding to a mean resolution of ~ 0.014 GeV/c^2. This resolution improves only slightly as the mass of the $\bar{K}^\circ\,\pi^+\pi^-$ system is increased.

The $mm^2(\bar{K}^\circ\,\pi^+\pi^-)$ resolution of the LASS spectrometer is a complex function of the event parameters. Figure 5.25 shows the data mm^2 distributions for

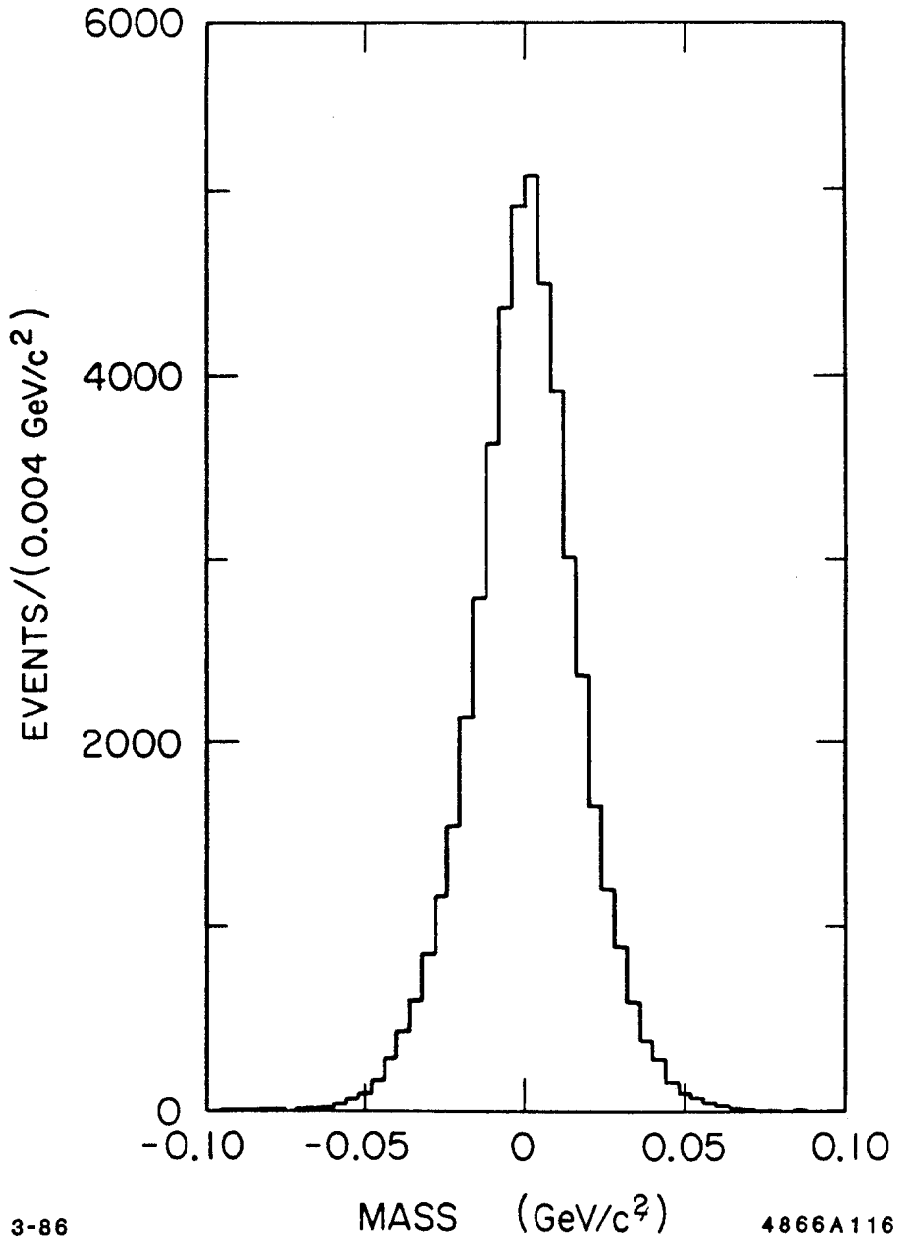

Figure 5.24. The $\bar{K}^{\circ}\pi^{+}\pi^{-}$ invariant mass resolution. The histogram shows the invariant mass resolution determined by Monte Carlo events for $m(\bar{K}^{\circ}\pi^{+}\pi^{-}) \sim 1.4$ GeV/c^2.

$m(\bar{K}^\circ \pi^+\pi^-) \sim 1.48$ and $m(\bar{K}^\circ \pi^+\pi^-) \sim 1.84$ GeV/c^2. The distributions show a clear neutron signal with an additional bump at $mm^2 \sim 1.5$ (GeV/c^2)^2 that comes from the reaction

$$K^- p \rightarrow \bar{K}^\circ \pi^+\pi^-\Delta(1232), \tag{5.4}$$

where the Δ is not detected. The solid curves superimposed on the data histograms are the results of fits using the predicted Monte Carlo mm^2 distributions for the neutron lineshape. Several background terms are included in the fit, and the dashed curves in Fig. 5.25 represent the sum total of these background contributions.

The shape of the Monte Carlo neutron lineshape is used in the fit to represent the data mm^2 resolution. However, an acceptable fit to the data is not possible without adding a stretch factor to the MC lineshape. This stretch factor, when treated as a free fit parameter, is sensitive to the details of the background parametrizations. For this reason, it is set to 1.15 for the fits described below, as fitted values between 1.10 and 1.25 can be obtained with different background assumptions. In addition to the stretch factor, an offset has to be added to the MC neutron lineshape to account for the apparent shift in the neutron peak. This shift is probably due to a relative offset in the measured beam and final state momenta that has not been removed by the momentum calibration. The magnitude of the mm^2 shift indicates that this offset is 0.015 ± 0.007 GeV/c, a figure that is consistent with the uncertainty in the momentum calibration.

There are several non-neutron background contributions to the mm^2 distribution: Firstly, there is the effect of the $\Delta(1232)$, which smears under the neutron. This is modeled by convoluting a Δ resonance with the MC lineshape predicted for the neutron. The unsmeared Δ lineshape is a p wave Breit-Wigner having a mass and width of 1.232 and 0.110 GeV/c^2, respectively,[11] and a linear background forced to start above $n\pi$ threshold representing the non-resonant part of the p wave amplitude under the $\Delta(1232)$.

Secondly, there is a contribution from the channel

$$K^- p \rightarrow K^\circ K^\pm \pi^\mp \Lambda, \tag{5.5}$$

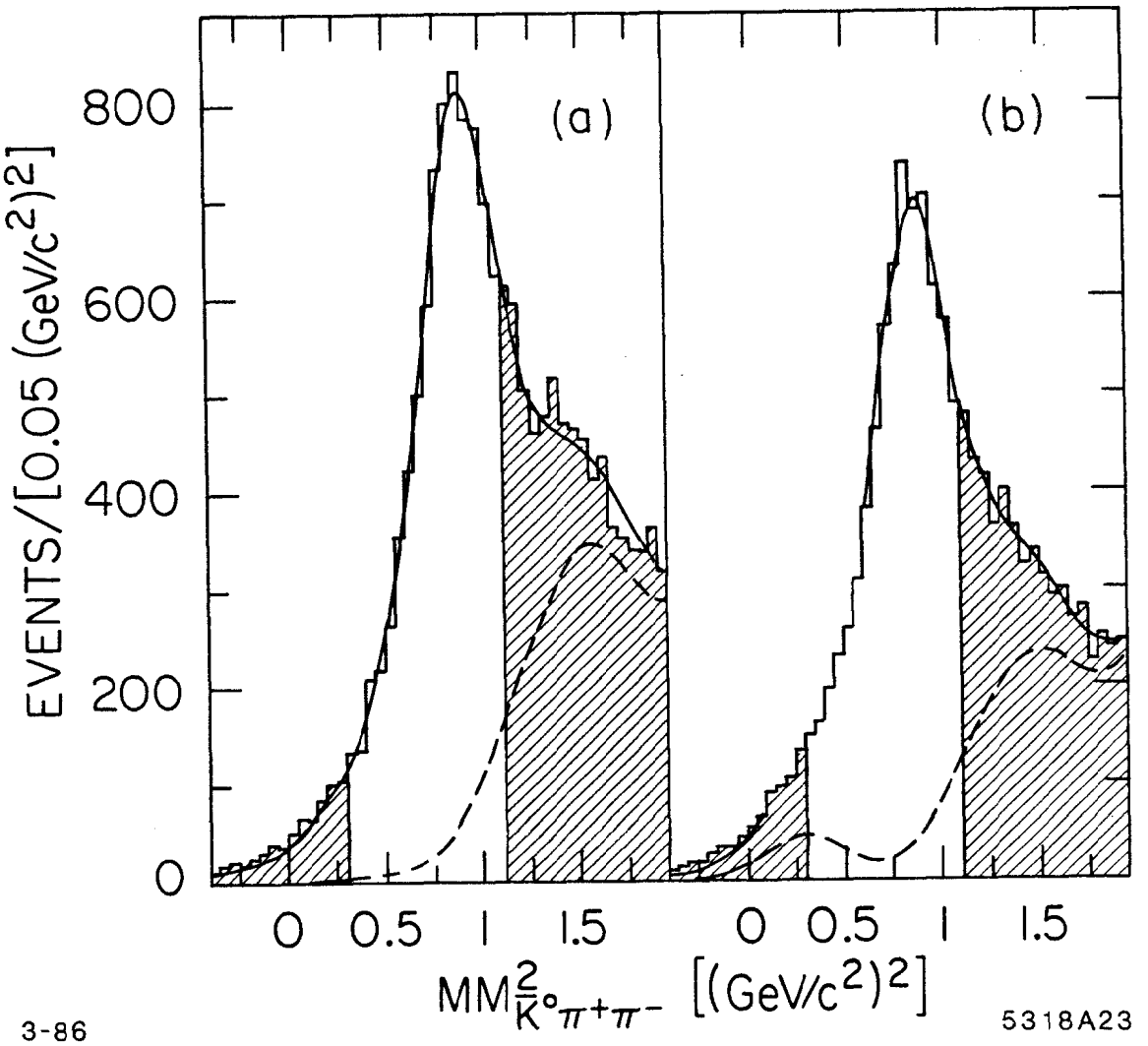

Figure 5.25. The $mm^2(\bar{K}^\circ\pi^+\pi^-)$ distributions for two $\bar{K}^\circ\pi^+\pi^-$ mass bins. The mm^2 distribution is shown for the two data bins $1.38 \leq m(\bar{K}^\circ\pi^+\pi^-) < 1.58$ and $1.74 \leq m(\bar{K}^\circ\pi^+\pi^-) < 1.94$ GeV/c^2 in (a) and (b), respectively. The curves are the results of the fits described in the text.

Table 5.5. The results of the fits to the mm^2 distributions. The contamination is the fraction of non-neutron events within the mm^2 interval of 0.3 and 1.1 $(\mathrm{GeV/c^2})^2$ used to define the $\bar{K}^\circ\pi^+\pi^-n$ data sample.

Quantity	Fitted Value	
	$m(\bar{K}^\circ\pi^+\pi^-) \sim 1.48$ GeV/c^2	$m(\bar{K}^\circ\pi^+\pi^-) \sim 1.84$ GeV/c^2
Neutron Mass^2	0.857 ± 0.003	0.856 ± 0.005
Peak Height	787 ± 8	679 ± 11
χ^2/DOF	74/51	64/52
Contamination	0.085 ± 0.010	0.100 ± 0.010

where the Λ has not been detected. Although this is a small background, the reflection of this final state in the mm^2 distribution is a shoulder around 1.2 $(\mathrm{GeV/c^2})^2$ with a width comparable to the neutron resolution. This shoulder is quite pronounced in the mm^2 distribution for the low mass bin and is still evident at high mass, though substantially smaller. It is parametrized by a gaussian lineshape whose mass, width, and normalization are determined by the fit to the data in the 1.48 GeV/c^2 mass bin. In the high $\bar{K}^\circ\pi^+\pi^-$ mass bin, the mm^2 and width of the Λ reflection are fixed at the values determined from the fit to the neutron in the lower mass bin.

In the high mass bin, a background contribution due to the reflection of the residual $\bar{K}^\circ\pi^-p$ and $\bar{K}^\circ\pi^-p\pi^\circ$ events is required. This contamination comes in the form of a bump at $mm^2 \sim 0.3$ $(\mathrm{GeV/c^2})^2$ with a width of ~ 0.2 $(\mathrm{GeV/c^2})^2$. A gaussian with this center and width are put into the fit with the height of the bump allowed to be a fitted parameter.

These fits describe the data very well in both mass regions, and although there is a significant amount of modeling that has gone into the predicted lineshapes, the estimate of the background under the neutron within the mm^2 cut of 0.3 and 1.1 $(\mathrm{GeV/c^2})^2$ is insensitive to most of these details. Table 5.5 lists the fit results.

The contamination in the neutron sample is estimated from the fit to be $9.25 \pm 1.0\%$, the majority of the background coming from events with a $\Delta(1232)$

recoil. Another way of estimating the background under the neutron is to assume that the leading edge of the mm^2 distribution represents the neutron lineshape, and to fold it about the center of the distribution to predict the trailing edge of the neutron lineshape. Because of the reflection of the residual protons in the higher $\bar{K}^\circ \pi^+\pi^-$ mass bin, this procedure is only possible for the mm^2 distribution in the lower $\bar{K}^\circ \pi^+\pi^-$ mass bin. This approach results in a background estimate of $6.8 \pm 0.6\%$ when 0.857 $(\mathrm{GeV/c^2})^2$ is used for the measured neutron mass squared, the uncertainty in this estimate arising from its sensitivity to the point chosen as the peak of the neutron. The value taken for the neutron contamination is the average of these two estimates

$$8.0 \pm 1.0 \pm 1.2\% \tag{5.6}$$

where the systematic error has been chosen to encompass the two values.

The acceptance of the $\bar{K}^\circ \pi^+\pi^-$ final state cannot be easily characterized as it depends on the way the events are produced. However, one way to quantify the acceptance is to use events distributed uniformly in phase space. This has been done for two Monte Carlo event samples with different $\bar{K}^\circ \pi^+\pi^-$ masses; the acceptance losses due to the various data selection requirements are listed in Table 5.6 for these event samples.

The most significant cuts are the requirement of a correct topology and the neutron mm^2 cut. The topological acceptance for the $\bar{K}^\circ \pi^+\pi^-$ final state is determined by the size of the spectrometer and the amount of material encountered by each particle; there is an $\sim$7% probability for *each* of the charged particles in the $\bar{K}^\circ \pi^+\pi^-$ system to either decay or be absorbed early enough in the spectrometer to become unfindable in the subsequent event reconstruction. The mm^2 cut is severe because of the significant background from $\bar{K}^\circ \pi^+\pi^-$ final states produced against a $\Delta(1232)$. Relaxing this cut would create an unacceptable background in the final $\bar{K}^\circ \pi^+\pi^- n$ sample.

The fact that the Monte Carlo does not accurately reproduce the data $mm^2(\bar{K}^\circ \pi^+\pi^-)$ distribution implies that the effect of the mm^2 cut on the event acceptance is not correctly simulated. The scaling and mass shift needed to make

Table 5.6. The effect of the event selection on the acceptance. The table lists the effect of the selection criteria on the $\bar{K}^\circ \pi^+\pi^- n$ phase space acceptance for $\bar{K}^\circ \pi^+\pi^-$ masses around 1.48 and 2.20 GeV/c^2. The cuts are described in the preceding section. The category of miscellaneous cuts refer to the secondary beam cut, the cut to remove fake V°'s, and the cut to remove events with better alternative topological interpretations.

	$m(\bar{K}^\circ \pi^+\pi^-) \sim 1.48$ GeV/c^2		$m(\bar{K}^\circ \pi^+\pi^-) \sim 2.20$ GeV/c^2	
Selection Requirement	Fraction Cut	Accumulative Acceptance	Fraction Cut	Accumulative Acceptance
Event Trigger	0.955	0.955	0.957	0.957
Correct Topology	0.709	0.677	0.732	0.700
Good Geometry fit	0.992	0.672	0.994	0.696
Decay length > 0.5 cm	0.964	0.647	0.962	0.670
$mm^2 < 2.0$ (GeV/c^2)^2	0.962	0.622	0.975	0.653
Protons tagged	1.000	0.622	1.000	0.653
Vertex in Target	1.000	0.622	1.000	0.653
Decay Length > 1.5 cm	0.965	0.600	0.948	0.620
Miscellaneous Cuts	0.999	0.599	0.999	0.619
Λ° Removal	0.894	0.534	0.892	0.552
Resolution Cut	0.894	0.479	0.882	0.487
ϕ Cut	0.999	0.479	1.000	0.487
Good 1C-fit	0.998	0.478	0.998	0.486
Identified $K^\pm$	0.994	0.475	0.995	0.484
Decay Length > 2.0 cm	0.978	0.464	0.973	0.471
$m(\pi\pi)$ Cut	0.897	0.417	0.912	0.429
$mm^2(\bar{K}^\circ \pi^+\pi^-)$ Cut	0.657	0.274	0.696	0.298
Software trigger	0.940	0.257	0.979	0.292
N^*/Δ cut	0.903	0.232	0.838	0.245

the Monte Carlo and data mm^2 distributions agree is such that it introduces an overall acceptance reduction of 0.901 in addition to the acceptance derived using the Monte Carlo. This additional reduction is taken into account in the analysis, and is already included in the effect of the mm^2 cut listed in Table 5.6.

5.7 NORMALIZATION

The production cross section for the $\bar{K}^\circ \pi^+\pi^- n$ final state is derived from the total number of beam particles incident on the target, the number of observed events, and the acceptance of the $\bar{K}^\circ \pi^+\pi^- n$ final state as determined by the Monte

Carlo. The observed number of events N_{obs} is related to the production cross section σ by

$$N_{obs} = \varepsilon \sigma N_{beam} \rho_p L, \tag{5.7}$$

where ε is the acceptance of the detector, N_{beam} is the effective number of beam particles incident on the target, ρ_p is the number of protons/cm^3 and L is the length of the target. The quantity $N_{beam}\rho_p L$ is the sensitivity of the experiment and has units of nb^{-1}.

The acceptance factor ε is determined with the Monte Carlo program. The factor N_{beam} is determined by summing the number of beam particles incident on the target over the course of the experiment and correcting this raw beam flux for several losses. The raw, uncorrected beam flux is $1.469 \times 10^9 \pm 0.3\%$, the effect of the spectrometer deadtime and various small data processing losses for the K^- data sample having been already taken into account. This raw flux count also reflects a small additional loss introduced by the selection process for the $\bar{K}^\circ \pi^+\pi^- n$ reaction. The uncertainty in it comes from estimating the raw flux for the subset of runs for which the measured beam flux is unavailable or is considered unreliable for normalization purposes. A number of corrections have to be made to this value:

1. The decay of the beam particle from the point where it creates a genuine beam trigger and is reconstructed properly to the point where it enters the target, a distance of $\sim$ 145 cm.
2. The attenuation of the beam in the target due to proton interactions and decay.
3. Inefficiencies and deadtime in the hardware trigger logic (distinct from the deadtime loss due to the time interval required to read out the event).
4. Failures that are detected during the course of the event processing, such as bad event buffers due to random failures in the data acquisition system, too many beam track candidates, and beam reconstruction failures due to beam decays that occur well upstream of the spectrometer ($z \lesssim -130$ cm).

The size of these corrections, along with their associated uncertainties, are given in Table 5.7. The uncertainty in the beam decay loss arises from the estimate of the upstream point at which a beam particle could decay and still be counted

Table 5.7. The corrections to the raw beam flux.

Type of Correction	Size of Correction
Beam decay before entering target	0.983 ± 0.002
Beam interaction/decay in target	0.954 ± 0.002
Electronics and trigger deadtime	0.996 ± 0.010
Event processing losses	0.822 ± 0.020
Total corrections	0.768 ± 0.026

as a genuine beam trigger. The uncertainty in the absorption loss comes mostly from the measured total cross section for $K^- p$ at 11 GeV/c, 23.3 ± 0.8 mb.[42] The uncertainty in the deadtime loss is estimated by considering various mechanisms that could cause such an inefficiency in the timing coincidences in the trigger logic. The event processing losses are known precisely; however, there is some uncertainty in deciding which losses are truly random and do not vary with the choice of final state. For example, one such loss arises from event buffers that are too large and could be correlated with large events (although there are indications that this is not so). In correcting for these processing losses, it has been assumed that they are random. The uncertainty this introduces has been estimated by summing the losses that could conceivably be event-dependent and using half of this total as the systematic error. With these corrections, $N_{beam} = 1.128 \times 10^9 \pm 2.6\%$.

The target proton density ρ_p, averaged over the course of the experiment, is $4.728 \times 10^{22} \pm 0.5\%$ cm^{-3}. The uncertainty in this value comes from the systematic error in the average liquid H_2 density in the target. The target length L is known precisely at room temperature but the shrinkage of the target when cooled to liquid H_2 temperature has to be taken into account. The value used for the effective target length is 84.6 ± 0.2 cm, which is consistent with an estimate of the shrinkage and a direct measurement of the primary vertex z distribution of $\bar{K}^\circ \pi^+ \pi^- n$ events.

With these corrections, the sensitivity of the experiment is

$$4.082 \pm 2.7\% \text{ events/nb.} \tag{5.8}$$

With this nominal sensitivity, the experiment is approximately four times more

sensitive than any previous study of this channel.

6. The Partial Wave Analysis

6.1 The Three-Body Isobar Model

6.1.1 Introduction

The three-body isobar model was introduced in the early 1970's, its first application being to the study of the three-π system.[46,47] Subsequently it was used in the early studies of the $K\pi\pi$ final state[14–16] and the $N\pi\pi$ system.[48] By the mid-1970's, it had become an accepted and proven tool for studying the complex dynamics of three-body systems. The model is used to obtain a description of the three-body system in the form of a partial wave decomposition, and so the methodology followed to implement it is commonly known as a three-body partial wave analysis (PWA).

Although the model itself is relatively straight-forward, it has two practical limitations. Firstly, the analysis requires a large sample of events as the data have to be fit to a model employing many parameters. Secondly, the analysis is rather sensitive to acceptance effects. If large parts of the final state phase space are excluded because of instrumental effects in the detector or biases in the data selection, the robustness of the analysis can be compromised. As a corollary to this, a detailed description of the final state acceptance (including the effects of any data selection requirements) has to be available. Historically, these limitations were overcome with the advent of the very large bubble chamber exposures, and the large scale electronic detectors optimized to give uniform phase space acceptance and yield high-statistics data samples.

The three-body isobar model had been in use for several years before the first thorough exposition of its theoretical formalism was published by Hansen and his colleagues in 1974.[49] Since then, a number of papers describing various details of the model have been published.[50,51] It is safe to say that the theoretical underpinnings and assumptions of the model are fairly well understood.

Two implementations of the three-body PWA have been discussed in the literature. The original algorithm, designed by Ascoli and colleagues[46,47] and known as the Illinois program, faithfully implements the formalism described in Ref. 49. An alternative implementation has been formulated by Herndon et al.,[52] and is known

as the SLAC-LBL program. The two programs differ in the way the data are fit: the Illinois program chooses to fit the density matrix elements that describe the production of the final state, whereas the SLAC-LBL program fits the three-body partial wave amplitudes from which the density matrix elements can be derived. The density matrix approach suffers from having to make assumptions in order to reduce the number of free parameters in the fitting procedure as well as to satisfy the rank conditions on the density matrix. The amplitude approach parametrizes the fit so that the number of parameters is kept to a minimum and the density matrix rank condition is always satisfied. However it is not clear that the rank condition should be enforced as background effects in the data sample may invalidate it. This issue is discussed in detail in Ref. 53 and Ref. 54. The SLAC-LBL model is employed in this analysis.

My goal in this section is to provide a heuristic description of the salient components of the PWA, and is *not* to embark on a detailed exposition of its derivation and theoretical justification. In particular, I will emphasize the various assumptions and approximations made by the model. This description will draw heavily from a previous work[54]; the interested reader should refer to it for further details of the analysis and methodology.

6.1.2 The Partial Wave Amplitudes

In the context of the isobar model, the $\bar{K}^{\circ}\pi^{+}\pi^{-}$ final state is considered to be produced through one of several intermediate two-body states, each comprising an isobar and a bachelor meson. The isobar subsequently decays into the two other mesons observed in the final state, *independently* of the initial isobar-bachelor system. This is illustrated in Fig. 6.1 where a set of quantum numbers specifying the final state is introduced: (a) the total spin and parity J^P of the isobar-bachelor state; (b) the absolute value M of the projection of J onto a quantization axis; (c) the variable η known as the "naturality" of the exchanged system producing the isobar-bachelor system; (d) the orbital angular momentum L of the isobar and bachelor; and (e) the spin l of the isobar. These quantum numbers, along with the identity of the isobar, define a specific partial wave. In this notation a partial wave

is uniquely specified by:

$$\eta J \equiv \{J^P M^\eta \text{isobar } L\}. \tag{6.1}$$

In Fig. 6.1, $A_{s\eta J}$ represents the complex-valued partial wave amplitude that governs the production of an isobar-bachelor system in the quantum state specified by ηJ; $X_{\eta J}$ is the complex-valued decay amplitude that describes the angular correlations of the isobar-bachelor system and the decay of the isobar into its two daughter mesons.

An explicit assumption in the model is that $A_{s\eta J}$ depends only on the three-body invariant mass M_3, the squared 4-momentum transfer to the proton $t \equiv |p_{\text{in}} - p_{\text{out}}|^2$ (we use $t' \equiv t - t_{min}$ where t_{min} is the minimum t for the given value of M_3), and the two relative helicity states of the incoming and outgoing spin-$\frac{1}{2}$ nucleons. This assumption implies that $X_{\eta J}$ must describe the behavior of the isobar-bachelor system and the decay of the isobar. With this, we write the probability of observing a $\bar{K}^\circ \pi^+\pi^- n$ event as

$$P = \frac{d^8\sigma}{d\omega^8} = \sum_{\substack{s=+,-\\ \eta=+,-}} \left| \sum_J A_{s\eta J} X_{\eta J} \right|^2. \tag{6.2}$$

The variable s represents the two possible relative helicity states of the nucleons: $s = +$ for the initial and final nucleons to be aligned ("non-flip"), and $s = -$ for the initial and final nucleon helicities to be opposite ("flip"). In principle, the partial wave amplitudes for the two helicity states are independent though in most of what follows we will assume that the ratio of flip to non-flip amplitudes is the same for all partial waves (this is equivalent to ignoring the s dependence[54]). The infinitesimal $d\omega^8$ represents the eight variables required to specify a $\bar{K}^\circ \pi^+\pi^- n$ final state. One of these is a trivial angle of rotation about the beam direction, two are taken as the three body invariant mass M_3 and squared four-momentum transfer t', and the remaining five are normally a two-body invariant mass and four angles.

The expression in Eqn. 6.2 consists of an incoherent sum of four terms, each term being a coherent sum of amplitudes over a set of partial waves. The four terms reflect the fact that final states due to different η or s are incoherent and do not interfere. The incoherence of states produced with different helicities is an

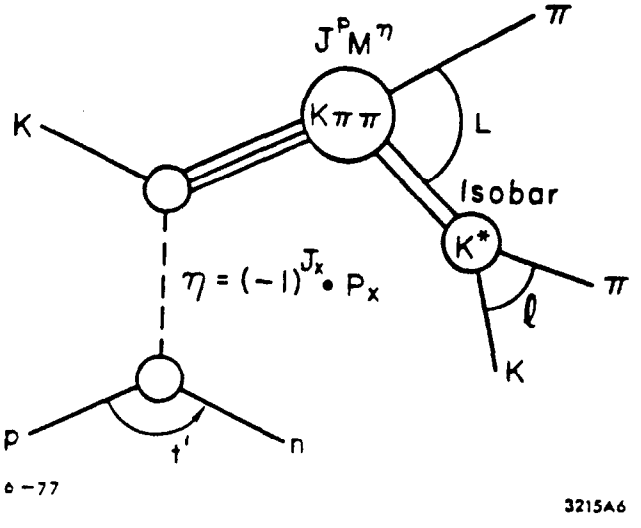

Figure 6.1. The production of the three-meson final state. The final state is produced via an intermediate isobar-bachelor system, *e.g.* $K^*\pi$ as shown here. The variables in the figure are described in the text.

elementary result of quantum mechanics. The incoherence of states with opposite naturality arises from the parity constraints on two-body scattering. In effect, a transformation of basis is made from the states specified by J and $M_z^J = -J, \ldots, J$ to those specified by J, $\eta = \pm$ and $M = 0, \ldots, J$ where for $M = 0$ only one value of η is allowed, namely

$$\eta = (-1)^{J+L+l}. \tag{6.3}$$

In a model where the final state is being produced through an exchange mechanism, η is related to the spin-parity of the exchanged particle, as illustrated in Fig. 6.1. This interpretation is exact for $M = 0$ final states; for $M \neq 0$ partial waves this holds to order ${s_{cm}}^{-1}$ where s_{cm} is the squared center-of-mass energy.

The goal of the PWA is to determine the partial waves present in the data and to extract their intensity and relative phase dependence on M_3 and t'. Since we know the behavior of the decay amplitudes $X_{\eta J}$ from angular momentum theory and the experimental measurements of two-body interactions, we can use this knowledge to determine the $A_{s\eta J}$ in the context of a maximum likelihood fit employing the probability density of Eqn. 6.2. We now turn to a discussion of the exact form of the $X_{\eta J}$, followed by a description of the maximum likelihood fit procedure.

6.1.3 The Decay Amplitudes

The $X_{\eta J}$ are defined in a coordinate system in which the angular momentum states for the isobar-bachelor and the isobar state are most readily expressed. For consistency of notation, we will cyclically label the three mesons $\{i, j, k\}$. An isobar of type i will refer to one whose final state is composed of mesons jk. For convenience, we will write the decay amplitude as

$$X_{\eta J} = C_J \, G_{\eta J} \, B_J. \tag{6.4}$$

The quantity C_J is a product of two Clebsch-Gordan coefficients representing the isospin projection of the final $\bar{K}^\circ \pi^+ \pi^-$ state on the initial three-meson system with isospin $|T, T^z\rangle$:

$$C_J = C(\tau_i t_i T;\, \tau_i^z t_i^z T^z)\, C(\tau_j \tau_k t_i;\, \tau_j^z \tau_k^z t_i^z). \tag{6.5}$$

The variables τ_i and τ_i^z are the isospin of the ith meson, and t_i and t_i^z are the isospin of the isobar. The C_J term is for convenience; its usefulness is apparent only when data from different charged modes of the same final state are being analyzed. The factor $G_{\eta J}$ carries the information about the angular momentum and spin of the wave, while B_J represents the dynamics of the isobar system. Their meaning will be discussed below.

The explicit form of the $G_{\eta J}$ is

$$G_{\eta J} = \begin{bmatrix} \eta = +1 \; Re \\ \eta = -1 \; Im \end{bmatrix} \sqrt{\frac{(2L_i+1)(2l_i+1)}{4\pi}} \sum_{\lambda_i=-l_i}^{+l_i} C(L_i l_i J;\, 0\lambda_i\lambda_i)\, D^J_{\lambda_i M}(\alpha_i\beta_i\gamma_i)\, d^{l_i}_{\lambda_i 0}(\theta_i). \tag{6.6}$$

The D^J_{mn} and d^l_{mn} are the familiar rotation matrices of angular momentum theory (*e.g.*, see Ref. 55). Although the form of $G_{\eta J}$ is somewhat formidable, its derivation is a straightforward exercise (see Ref. 52 or Ref. 54 for two alternative approaches). The four angles θ_i, α_i, β_i, and γ_i are defined for each isobar type and are illustrated in Fig. 6.2. The angle θ_i is the helicity angle of the isobar and so is related to its intrinsic spin (this is why the θ_i dependence of $G_{\eta J}$ is of the form $d^{l_i}_{\lambda 0}(\theta_i)$). The angles β_i and γ_i are the polar and azimuthal angles of the bachelor meson in the t channel production coordinate frame shown in Fig. 6.2(b). This coordinate system is defined in the $\bar{K}^\circ\pi^+\pi^-$ rest frame with the direction of the beam as the z-axis and the normal to the production plane, $\vec{p}_{\text{proton}} \wedge \vec{p}_{\text{neutron}}$, as the y-axis. In other words, β_i and γ_i are the Jackson and Trieman-Yang angles of the isobar-bachelor system. As such, they are the coordinates in which the angular distribution of a $\bar{K}^\circ\pi^+\pi^-$ state of a particular spin can be conveniently represented by the rotation matrices. The remaining angle α_i relates the orientations of the decay frame shown in Fig. 6.2(c) and the t channel production frame. To make the definitions of the α_i, β_i, and γ_i explicit, let $\hat{x}$, $\hat{y}$, and $\hat{z}$ represent the coordinate axes in the t channel production frame, and let $\hat{x}_i$, $\hat{y}_i$, and $\hat{z}_i$ represent the coordinate axes in the decay

frame. Then:

$$\begin{aligned}\alpha_i &= \arctan(\frac{\hat{z}\cdot\hat{y}_i}{\hat{z}\cdot\hat{x}_i});\\ \beta_i &= \arccos(\hat{z}\cdot\hat{z}_i);\\ \gamma_i &= \arctan(\frac{\hat{y}\cdot\hat{z}_i}{\hat{x}\cdot\hat{z}_i}).\end{aligned} \tag{6.7}$$

The power of the three body PWA comes from the use of the angular correlations, represented by $G_{\eta J}$, and the Dalitz plot information contained in B_J. The event distribution in the four-dimensional angle space (θ_i, α_i, β_i, γ_i) has very specific forms for different partial waves. A number of explicit forms for $|G_{\eta J}|^2$ are:

$$\begin{aligned}|G_{1^+0^+K^*S}|^2 &= (\sin\theta\cos\alpha\sin\beta+\cos\theta\cos\beta)^2\\ |G_{2^+0^-K^*D}|^2 &= \frac{3}{2}\sin^2\theta\sin^2\alpha\sin^2 2\beta\\ |G_{2^+1^+K^*D}|^2 &= \left\{\frac{\sin\theta}{2}\left[2\cos\alpha\cos^2\beta\sin\gamma-\sin\alpha\,(\cos\beta-1)\cos\gamma\right]\right\}^2.\end{aligned} \tag{6.8}$$

The behavior of $|G_{2^+1^+K^*D}|^2$ is illustrated in Fig. 6.3 where the distributions of the four angles for Monte Carlo events weighted by $|G_{2^+1^+K^*D}|^2$ are presented. It is apparent that there is a substantial loss of information when the angular correlations are not taken into account. An extreme example of this is the $1^+0^+K^*S$ wave; the projection of the probability density onto the θ, β, or γ axis yields a flat distribution that is independent of the remaining angle!

Traditionally, the factor B_J has been written as[54]

$$B_J = \frac{Q_i^{L_i}}{\sqrt{Q_i^{2L_i}+\ldots+constant}} f_J(M_3,t')W(m_i,l_i). \tag{6.9}$$

The variable Q_i is the momentum of the isobar and bachelor meson in the $\bar{K}^\circ\pi^+\pi^-$ CMS (center-of-mass), and m_i is the invariant mass of the isobar system. The first factor in Eqn. 6.9 is known as the barrier factor for two particles with orbital angular

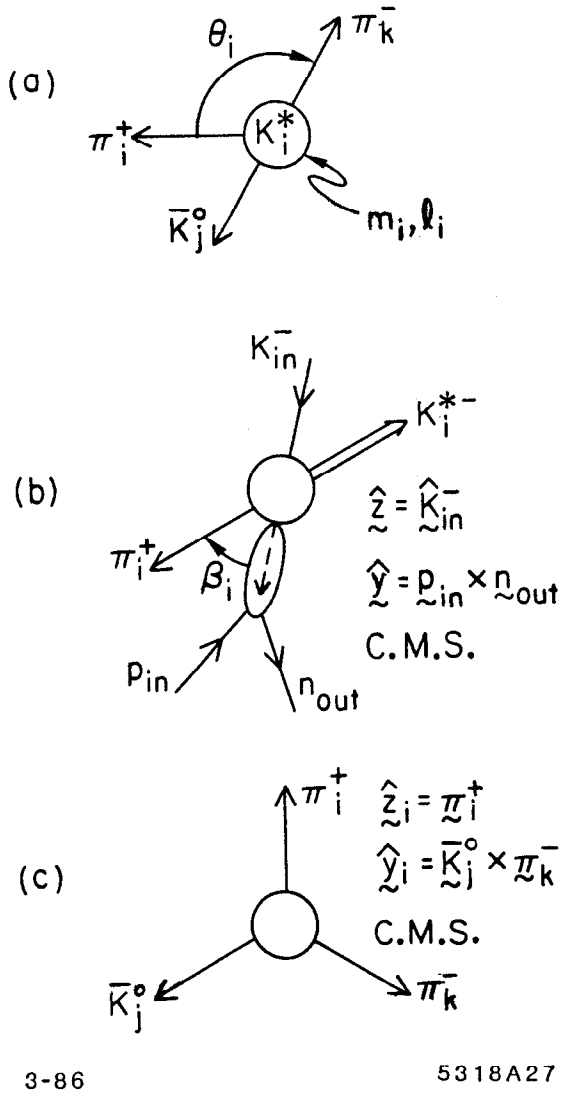

Figure 6.2. The angles describing the three-meson system. The angle θ_i is defined in the isobar rest frame (a). The angles β_i and γ_i are defined in the three-meson rest frame (b). The angle α_i relates the coordinate frame in (b) to the $\bar{K}^\circ \pi^+ \pi^-$ decay coordinate system in (c).

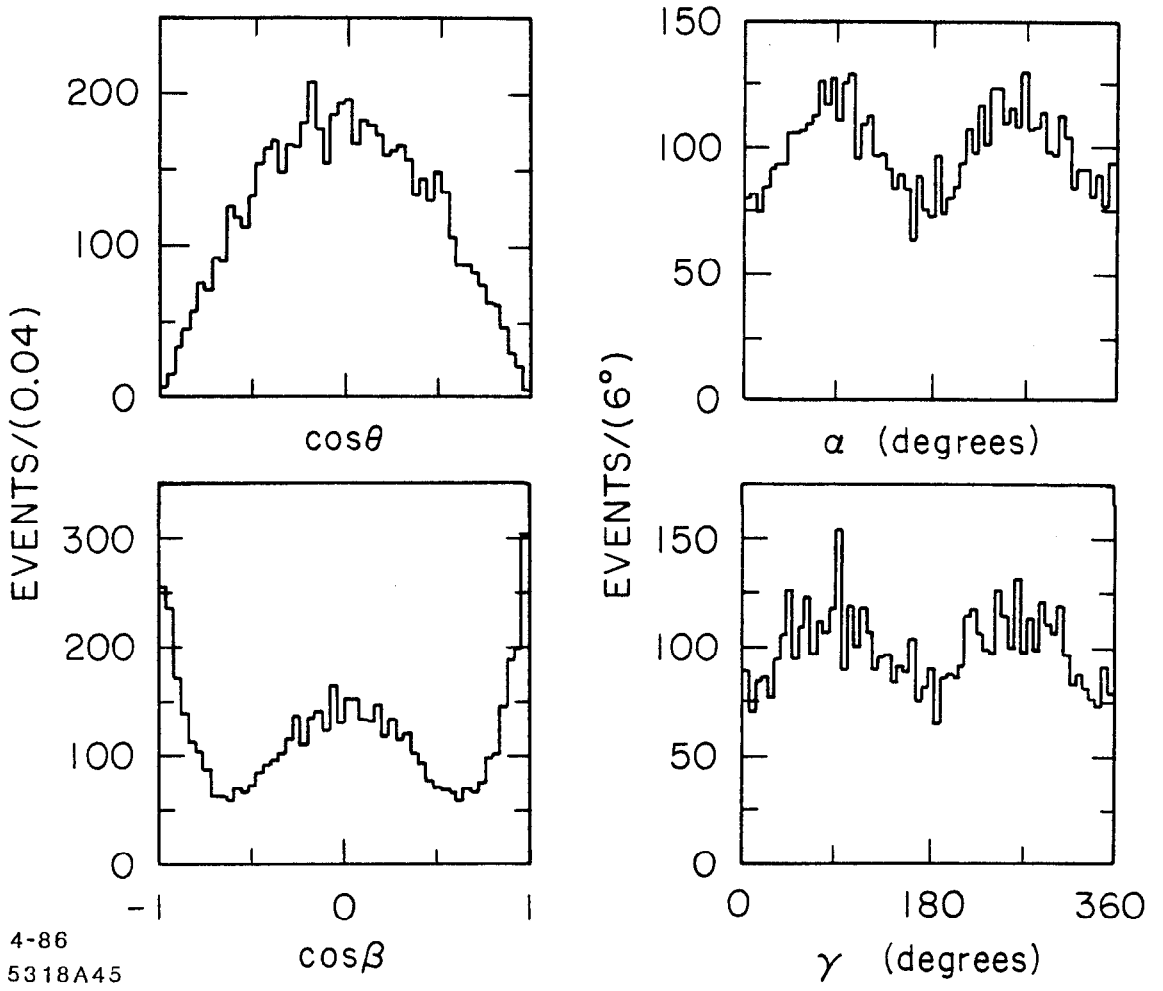

Figure 6.3. The projections of $|G_{2+1+K^*D}|^2$. The distributions of Monte Carlo events weighted by $|G_{2+1+K^*D}|^2$ are shown for the four angles in the K^* frame. In each case, the probability density has been integrated over the other three angles.

momentum L. The explicit forms for $L = 1$, 2, and 3 are[56]

$$\begin{cases} \sqrt{\dfrac{(QR)^2}{(QR)^2+1}} & \text{for} \quad L=1, \\ \sqrt{\dfrac{(QR)^4}{(QR)^4+3(QR)^2+9}} & \text{for} \quad L=2, \text{ and} \\ \sqrt{\dfrac{(QR)^6}{(QR)^6+6(QR)^4+45(QR)^2+225}} & \text{for} \quad L=3. \end{cases} \tag{6.10}$$

They are normalized to approach unity as $QR \to \infty$. The interaction radius R is set to 1 fermi. The factor $f_J(M_3, t')$ allows the inclusion of *a priori* knowledge of the M_3 or t' dependence of the particular partial wave. In the absence of such information, it is set to unity. The final term $W(m_i, l_i)$ is the Watson final state interaction factor, which is obtained from experimental studies of $\pi\pi$ and $K\pi$ scattering. Its precise definition will be deferred until the following section where we make the connection between it and the $A_{s\eta J}$.

6.1.4 *The Interpretation of the $A_{s\eta J}$*

To understand the $A_{s\eta J}$'s it is useful to derive the form of Eqn. 6.2 in the case where the three-body system is being produced resonantly. This exercise also shows how various kinematic factors such as three-body phase space are accounted for.

Consider the case where we have the processes

$$K^- p \to \mathcal{R} n \to a_j\ b_j n, \tag{6.11}$$

where $\mathcal{R}$ is a resonant state that has k two-body decay modes $a_j b_j$, for $j = 1$ to k. The mass and total width of $\mathcal{R}$ are denoted by M_0 and Γ^{tot} and the partial widths of the k decay modes of $\mathcal{R}$ are given by Γ^j, $j = 1$ to k. The differential cross section for Eqn. 6.11 can be written as[57]

$$d\sigma_R^j = F \left[\frac{\sqrt{M_0 \Gamma^j}}{{M_0}^2 - M^2 - i M_0 \Gamma^{tot}} \right]^2 M dM. \tag{6.12}$$

Here, M is the invariant mass of the $a_j b_j$ system. I will ignore the first term F as it should only depend on the exchange mechanism and phase space of the produced state; the former is assumed to be a function of t' while the latter depends only weakly upon M. I will also ignore the angular correlations in the final states as they are not relevant in the following discussion.

By definition, Eqn. 6.12 has the phase space dependence of the final state subsumed in the partial width Γ^j. Although the exact definition of the partial width is subject to debate, it is generally agreed that it should include both the final state phase space as well as the angular momentum barrier factor. The form of Γ^j used in this analysis is

$$\Gamma^j = \frac{\left(\gamma^j\right)^2 BF_{L_j}(Q_j)}{M_0}\left(\frac{Q_j}{M}\right). \tag{6.13}$$

Here, Q_j is the 3-momentum of a_j (or b_j) in the rest frame of $\mathcal{R}$, and γ^j is called the reduced coupling[58] and is a constant independent of M and Q_j (this definition of γ^j differs trivially from that given in Ref. 58 due to the form of the barrier factor). With this definition, γ^j has units of energy. Note that the last factor in Eqn. 6.13 accounts for the M and Q_j dependence of the $a_j b_j$ phase space. The total width Γ^{tot} of $\mathcal{R}$ is defined as

$$\begin{aligned}\Gamma^{tot} &= \sum_{j=1}^{k} \Gamma^j \\ &= \sum_{j=1}^{k} \frac{\left(\gamma^j\right)^2 BF_{L_j}(Q_j)}{M_0}\left(\frac{Q_j}{M}\right).\end{aligned} \tag{6.14}$$

In the isobar model, we picture the decay of $\mathcal{R}$ into the final three-body system as taking place first into $a_j b_j$, and then a_j decaying into the two other mesons. In this context, M is the invariant three-meson mass M_3. Using Eqn. 6.12 to write

down the probability for this decay chain, the differential cross section becomes

$$\begin{aligned} d\sigma &= F\left[\sqrt{\frac{Q_j q_j}{m}}\left(\frac{\gamma^j\sqrt{BF_{L_j}(Q_j)}}{{M_0}^2 - M^2 - iM_0\Gamma^{tot}}\right)\left(\frac{\gamma_j^{iso}\sqrt{BF_{l_j}(q_j)}}{m_j^2 - m^2 - im_j\Gamma_j^{iso}}\right)\right]^2 dMd^5\omega \\ &= \left[\left(\frac{\sqrt{F}\gamma^j}{{M_0}^2 - M^2 - iM_0\Gamma^{tot}}\right)\left(\sqrt{\frac{Q_j q_j}{m}}\frac{\gamma_j^{iso}\sqrt{BF_{L_j}(Q_j)BF_{l_j}(q_j)}}{m_j^2 - m^2 - im_j\Gamma_j^{iso}}\right)\right]^2 dMd^5\omega \\ &= \left(A_{s\eta J}B_J\right)^2 dMd^5\omega, \end{aligned} \tag{6.15}$$

where m_0 and Γ_j^{iso} are the central mass and width of a_j, m is its two-body invariant mass, and q_j is the 3-momentum of one of the daughters of a_j in the a_j rest frame. The infinitesimal $d\omega^5$ is $dm^2 d\cos\theta d\alpha d\cos\beta d\gamma$, the Euler angles being defined for the a_j isobar. With this, we can identify

$$\begin{aligned} A_{s\eta J} &= \frac{\sqrt{F}\gamma^j}{{M_0}^2 - M^2 - iM_0\Gamma^{tot}} \\ B_J &= \sqrt{\frac{Q_j q_j}{m}}\frac{\gamma_j^{iso}\sqrt{BF_{L_j}(Q_j)BF_{l_j}(q_j)}}{m_j^2 - m^2 - im_j\Gamma_j^{iso}}. \end{aligned} \tag{6.16}$$

The identification of $A_{s\eta J}$ and B_J made in Eqn. 6.16 is arbitrary in the sense that the various quantities could be absorbed in either term. However, to measure the $A_{s\eta J}$, the data are binned in $M \equiv M_3$ and t' and the $A_{s\eta J}$ are determined assuming that they are constant across the bin. In this resonant decay model, the choice of B_J in Eqn. 6.16 ensures that the $A_{s\eta J}$ are as mass-independent as possible and are not functions of any of the other variables (such as q_j).

This also shows the required form of the Watson factor $W(m,l)$ introduced in Eqn. 6.9 in the case where the phase shift information is parametrized as a Breit-Wigner. Another result of this derivation is that we have a form for the effect of a resonance on the mass behavior of a partial wave amplitude $A_{s\eta J}$.

For completeness, I will describe the specific forms used for the isobar phase shifts (a relativistic Breit-Wigner refers to the parametrization introduced above):

1. The $\kappa(1350)$ is a K-matrix parametrization of the $K\pi$ s wave amplitude.[20]

2. The $\epsilon(1250)$ is a K-matrix parametrization of the $\pi\pi$ s wave amplitude.[59]
3. The $K^*(892)$ is modelled as a p wave Breit-Wigner resonance with a mass and width of 0.8921 and 0.0513 GeV/c^2, respectively.[11]
4. The $\rho(770)$ is a parametrization of the $\pi^+\pi^-$ p wave.[60]
5. The $\omega(783)$ is defined as a p wave Breit-Wigner resonance with a mass and width of 0.7826 and 0.0099 GeV/c^2, respectively.[11]
6. The $K^*(1430)$ is a d wave Breit-Wigner resonance with mass and width of 1.430 and 0.100 GeV/c^2.[11]
7. The $f(1270)$ is a d wave Breit-Wigner resonance with mass and width of 1.274 and 0.178 GeV/c^2, respectively.[11]

To distinguish between the $K^*(892)$ and $K^*(1430)$ isobars in the partial wave labeling, "K^*" will refer to the $K^*(892)$ while "K^{**}" will refer to the $K^*(1430)$.

The guiding principle in the selection of these specific parametrizations has been that they should embody an accurate description of the two-body dynamics. For this reason, the $\rho(770)$ parametrization is complicated as this state is poorly represented with a conventional resonance line-shape. The descriptions of the ϵ and κ are particularly problematic as there are conflicting interpretations of the s wave behavior observed in the $\pi\pi$ and $K\pi$ scattering experiments. The choice of parametrization for these isobars has been made solely on the basis of how well the models represent the available data and *not* on the preference of one interpretation of the s wave over another. In this sense, the terms "ϵ" and "κ" refer to the two-body s waves and not to a specific resonance interpretations even though the parametrizations for these isobars are motivated by resonance pole interpretations.

Figure 6.4 shows the behavior of the $\pi^+\pi^-$ isobars as a function of $\pi^+\pi^-$ invariant mass and three-body mass. The intensity increases with increasing M_3 because of the phase space terms. The plots are for isobar-bachelor states with $L = 0$. Figure 6.5 shows the lineshapes for the $\bar{K}^\circ\pi^-$ isobars.

6.1.5 The Assumptions of the Model

The three-body isobar model is an approximation to the physical process under study. The validity of these approximations has been discussed in exhaustive detail by a number of authors[49–61] and so I will only briefly review them here.

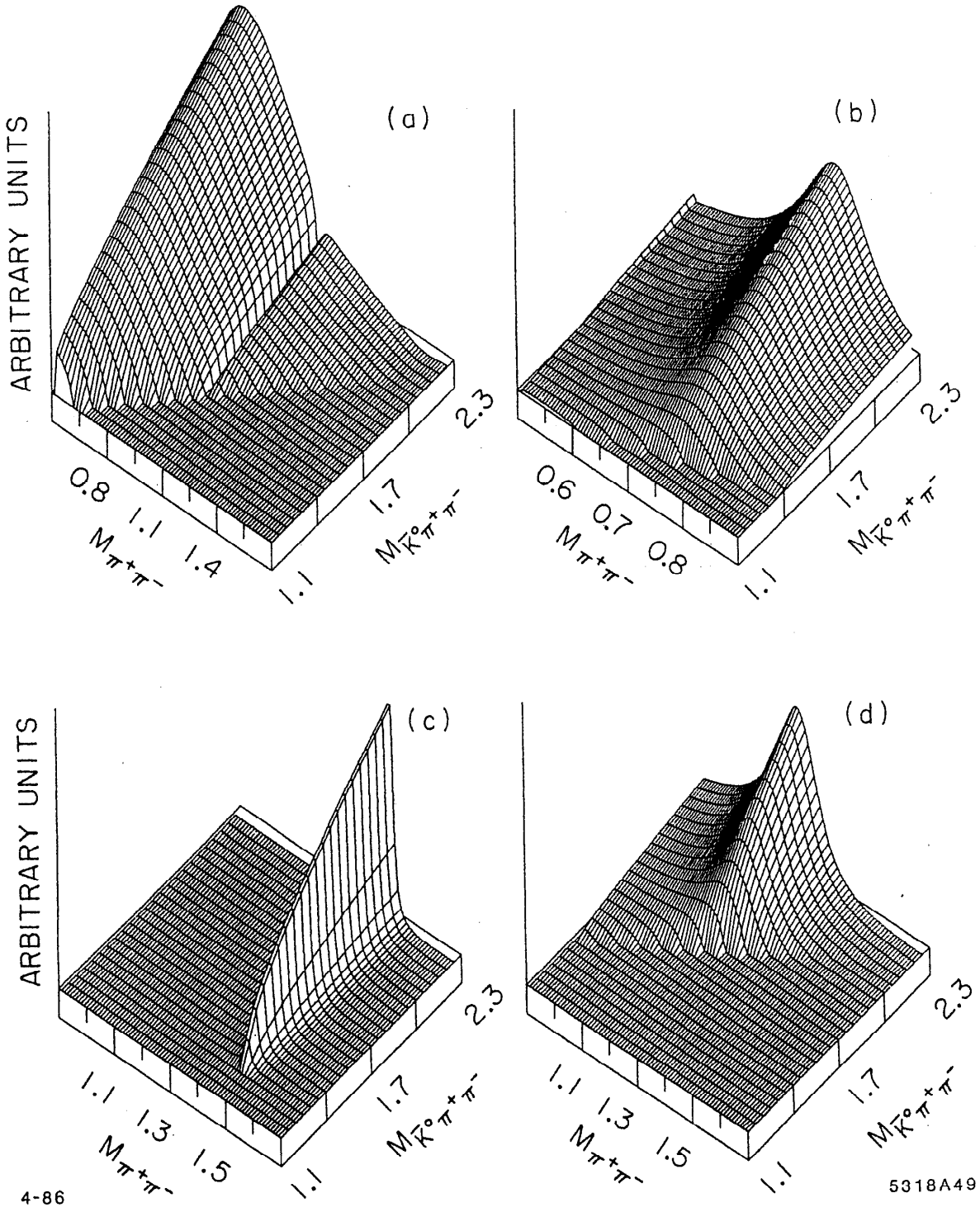

Figure 6.4. The $\pi^+\pi^-$ isobar parametrizations. The intensity (amplitude squared) of the ϵ (a), the $\rho(770)$ (b), the $\omega(783)$ (c), and the $f(1270)$ (d) isobars are plotted versus $\pi^+\pi^-$ invariant mass and three-body invariant mass.

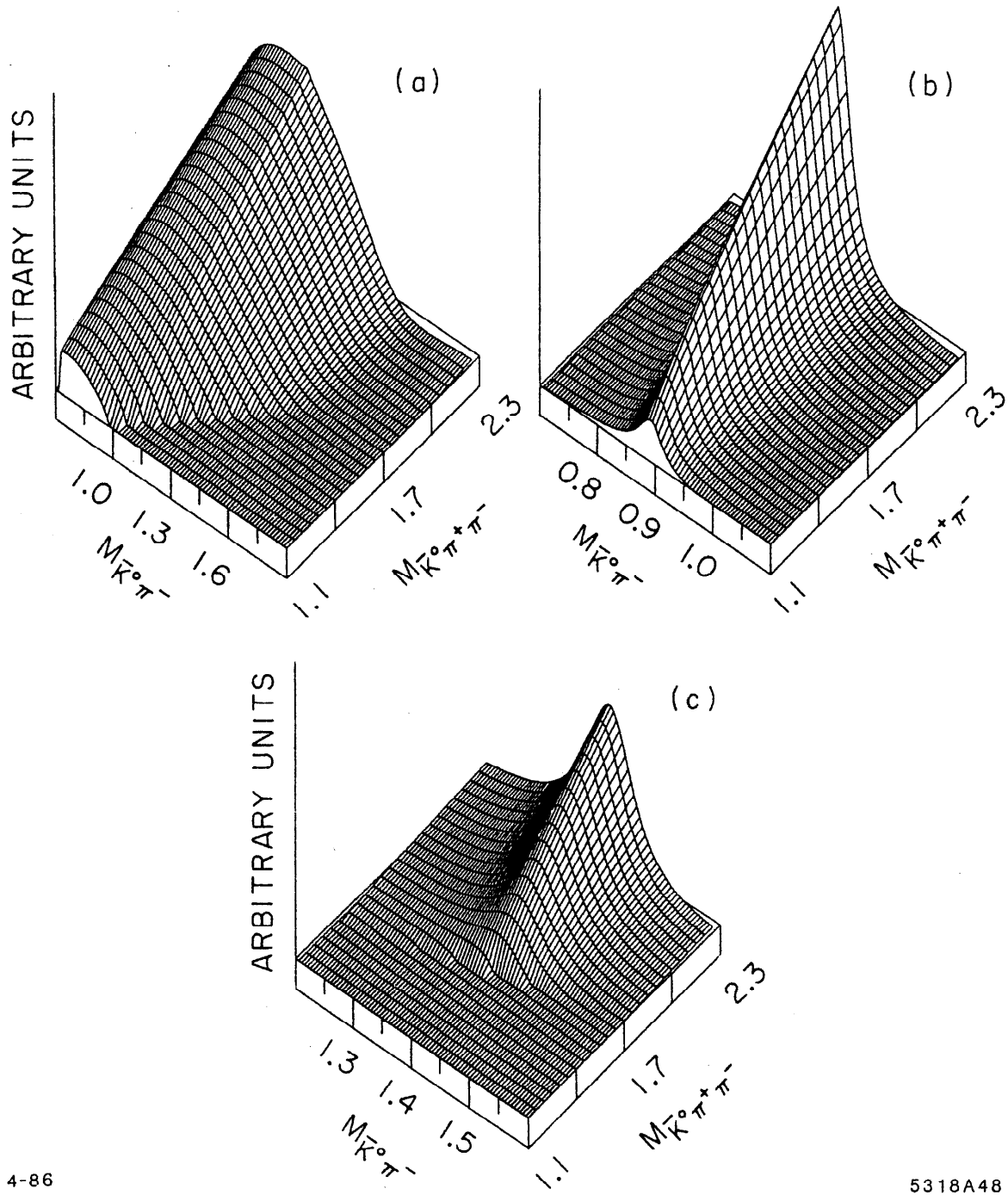

Figure 6.5. The $\bar{K}^{\circ}\pi^{-}$ isobar parametrizations. The intensity (amplitude squared) of the κ (a), the $K^{*}(892)$ (b), and the $K^{*}(1430)$ (c) isobars are plotted versus $\bar{K}^{\circ}\pi^{-}$ invariant mass and three-body invariant mass.

The most serious criticism levelled at the isobar model is that it does not explicitly obey unitarity. By writing the energy-dependence of the decay amplitude in the form of a Watson factor, it is assumed that the isobar can only be produced by the direct breakup of the initial state into the isobar and bachelor mesons. However, other processes can contribute to the amplitude for an isobar-meson system of type i besides this direct contribution. The most problematic of these is the initial state decaying via an isobar of type $j \neq i$, with that isobar decaying and one of the decay daughters interacting with the bachelor meson to produce the type i isobar. This rescattering process would change the energy-dependence of the decay amplitude. In effect, the isobar model ignores this possibility and assumes that in the regions of the Dalitz plot where isobars of two different types overlap, this rescattering process can be ignored.

This criticism has been addressed by attempting to incorporate these unitary constraints into the definition of the decay amplitudes. Several authors have attempted this[62–64] and although no definitive conclusion could be drawn, the consensus has been that the addition of these unitary effects does not significantly affect the results of the analysis and hence does not warrant the considerable effort required.

Another assumption of the model is that the overlap of isobars of different types is relatively small. This arises from the belief that by including the lowest angular momentum eigenstates for isobars from different representations the description of the final state is complete. The possibility of there being an amplitude that is not factorable in the way we have assumed is not allowed. In a two-body PWA, this problem does not arise since the angular momentum eigenstates are mutually orthogonal and two competing descriptions of a process are not introduced. In the three-body PWA, the same angular momentum eigenstates are in the fit for two or more isobars. These eigenstates are not orthogonal and so the efficacy of the analysis cannot be established.

For example, in the $\bar{K}^0\pi^+\pi^-$ final state for masses around 1.4 GeV/c^2, the $K^*(892)\pi$ and $K\rho(770)$ final states overlap almost totally on the Dalitz plot. These isobars have the potential to interact substantially, leaving open the question of whether the results of the PWA can be trusted. In practice, this has not appeared

to create serious problems as the results of the analysis are sensible even in this overlap region.

In the case of the diffractive $K\pi\pi$ and 3π analyses,[17–19,47,65] the results are often criticized because of the uncertainties arising from the use of a "Deck" process to model some of the partial wave contributions.[66] It cannot be emphasized too strongly that these critiques are not of the three-body isobar model *per se*, but rather of how the partial wave amplitude behavior in these specific channels is to be interpreted. In fact, there is little controversy over the application of the three-body formalism in these cases.

6.2 The Mechanics of the PWA

6.2.1 Overview

Having defined the elements of the PWA, I will now describe how the partial wave amplitudes $A_{s\eta J}$ are estimated from the data.

The extended maximum likelihood method[67,68] is used to estimate the values of the partial wave amplitudes. The decay amplitudes for the data events are calculated and are used to define a likelihood function $\mathcal{L}$ derived from the probability density given in Eqn. 6.2. This likelihood function is maximized to determine the best estimates of the $A_{s\eta J}$'s. In addition to the calculation of decay amplitudes for the data events, this method requires the computation of a set of integrals over phase space, known as the "acceptance" and "normalization" integrals. This integration is performed using Monte Carlo events that have been subjected to the same analysis and selection criteria as the data events. The data sample is then subdivided into several small M_3 and t' bins and within each bin the partial wave amplitudes are estimated using the maximum likelihood fit. The M_3 and t' dependence of the partial wave amplitudes is extracted from these solutions.

Figure 6.6 shows a flowchart that depicts these stages in the analysis; each step will be described in detail below.

6.2.2 The Initial Wave Set

At the outset of the analysis, a "wave set" is chosen that includes all of the partial waves that might be important in the description of the data. The size of this

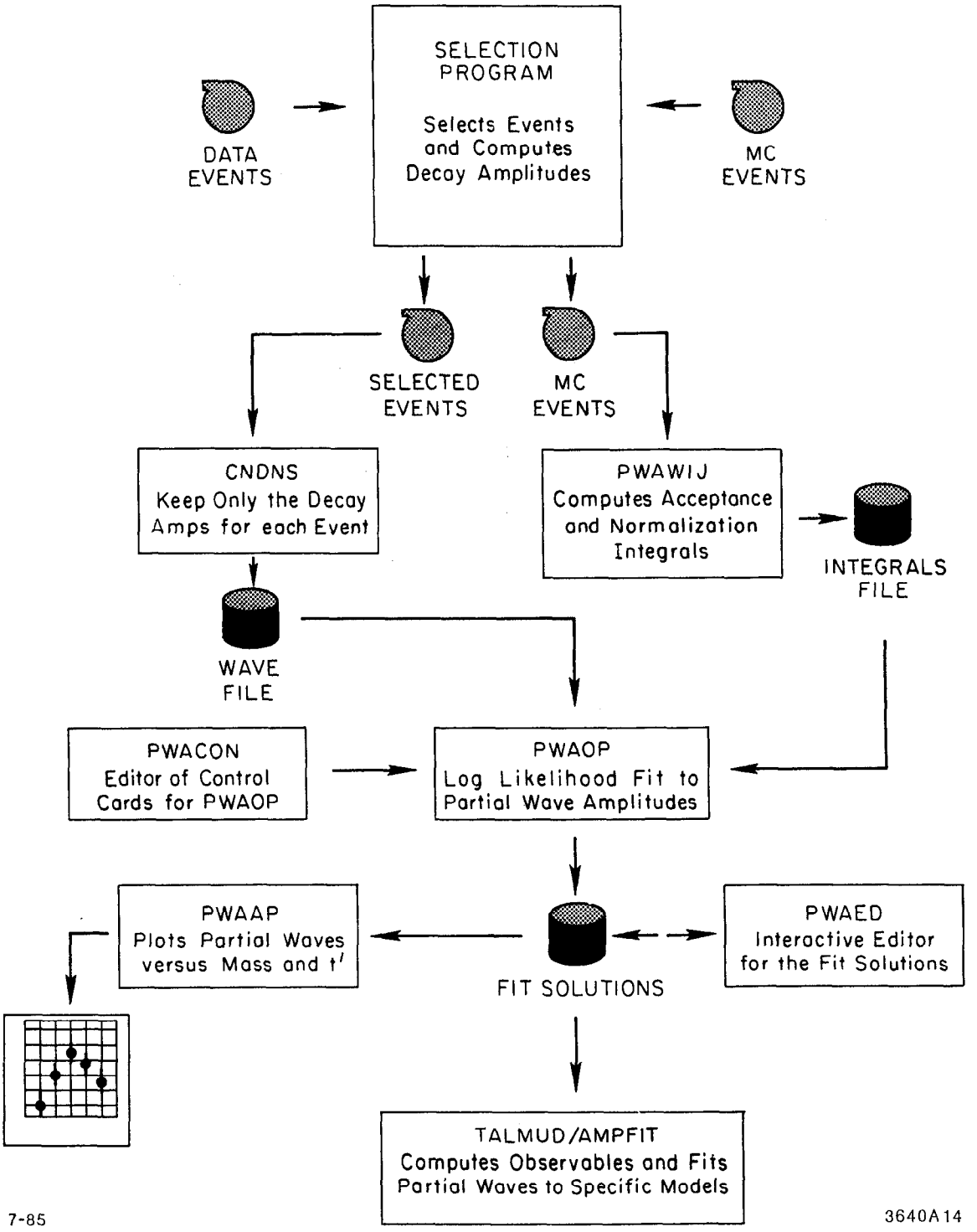

Figure 6.6. The stages in the partial wave analysis. Each box represents a software package that performs the specified function. The arrows represent the flow of data and information through these programs.

wave set is constrained by practical considerations such as the amount of storage needed for the Monte Carlo data (this grows linearly with the size of the wave set), and the computer time required to calculate the acceptance and normalization integrals (this is a quadratic function of the number of waves). Up to 200 waves can be handled by the current implementation of the fitting program.

The wave set for the $\bar{K}^\circ \pi^+\pi^-$ PWA has been chosen using the following general guidelines:

1. Include all partial waves with total spin $J \leq 4$ and relative orbital angular momentum in the isobar-bachelor meson system $L \leq 2$. For high spin waves ($J > 2$), higher orbital angular momenta are necessary.
2. Include all magnetic substates $M \leq 2$. The exceptions to this are waves with an ω isobar and the $J^P = 4^-$ waves with the κ and ϵ isobars, for which only the $M = 0$ waves are included.
3. Include the $K^*(892)$, $\rho(770)$, $\omega(783)$, $\kappa(1350)$, $\epsilon(1300)$, $K^*(1430)$ and the $f(1270)$ isobars.

These criteria can be viewed as *a priori* assumptions about the partial waves that are expected to be significant in the production of the $\bar{K}^\circ \pi^+\pi^- n$ final state.

The requirement of $J \leq 4$ is justified from the results of previous analyses of two-body and three-body final states that have shown no evidence for amplitudes with $J > 4$ below invariant masses of 2.3 GeV/c^2.

The second requirement is justified on two grounds: Firstly, a wave with $M \neq 0$ has a unique signature—it generates an event distribution that has structure in the γ angle of the particular isobar, this structure having a periodicity related to the absolute value of M. An examination of the event distribution shows no evidence for $M > 1$ waves and indicates that the data are dominantly produced via $M = 0$ waves. Secondly, a previous analysis[22] of this channel examined waves with $M \leq 3$ and found no significant waves with $M > 1$ for the same range of three-body invariant masses.

The last requirement requires little additional justification as it is based on the observed Dalitz plots. The $\omega(783)$ isobar has been added because previous studies of the diffractive $K^-\pi^+\pi^-p$ channel[19] and this channel[22] have indicated that the

$\pi^+\pi^-$ lineshape just above the peak of the $\rho(770)$ may be distorted due to $\rho-\omega$ interference effects.[69,70] In this case, the ω isobar would not be observed directly because of its small coupling to $\pi^+\pi^-$ but would be observed only as an interference effect in the $\pi^+\pi^-$ lineshape.

A three-body phase space term is not normally included in the isobar model formalism since all production is assumed to occur through isobar formation and decay. However in the course of the PWA, it was discovered that the data required such a term to properly describe the distribution of events over the Dalitz plot. This term is represented by the decay amplitude $X_{PS} = 1$.

With these criteria the resulting wave set consists of 99 $\eta+$ and 85 $\eta-$ partial waves. This wave set is listed in Appendix B.

6.2.3 The Likelihood Fit

The extended maximum likelihood method is based on an *a priori* knowledge of the form of the probability density governing the event distribution. In this case, the events are distributed over the five-dimensional space describing the three-meson system at a fixed mass M_3 and t'. The unnormalized probability distribution for the ith event in the data sample is written as

$$P_{obs}^{(i)} = P^{(i)}\epsilon^{(i)}. \tag{6.17}$$

The quantity $P^{(i)}$ is the theoretical probability that the ith event be produced; it is given by Eqn. 6.2, where the decay amplitudes $X_{\eta J}$ are computed from the parameters of the event. The acceptance $\epsilon^{(i)}$ is the probability that the produced event be detected in the spectrometer and find its way into the data sample.

Suppose we have a sample of N observed events in a mass and t' bin $\Delta M_3 \Delta t'$. Then the likelihood function for this sample of events is

$$\mathcal{L} = \left(\prod_{i=1}^{N} \frac{P_{obs}^{(i)}}{\overline{N}} \right) \frac{(\overline{N})^N}{N!} e^{-\overline{N}} \tag{6.18}$$

where the normalization of $P_{obs}^{(i)}$ is defined by

$$\overline{N} \equiv \int P_{obs}(\omega) d\omega^5. \tag{6.19}$$

The integral in Eqn. 6.19 is performed over the entire five-dimensional phase space ω of the three-meson system. The replacement of $P_{obs}^{(i)}$ with the expression in Eqn. 6.17 makes $\mathcal{L}$ a function of the $A_{s\eta J}$'s; the principle of extended maximum likelihood maintains that the best estimate of the $A_{s\eta J}$'s is the one that maximizes $\mathcal{L}$.

The problem is simplified by working with $\ln\mathcal{L}$ instead of $\mathcal{L}$. The expression for $\ln\mathcal{L}$ becomes,

$$\begin{aligned}\ln\mathcal{L} &= \sum_{i=1}^{N} \ln\epsilon^{(i)} + \sum_{i=1}^{N} \ln P^{(i)} \\ &\quad - \sum_{s\eta}\sum_{I}\sum_{J} A_{s\eta I} A_{s\eta J}^{*} \int \epsilon(\omega) X_{\eta I}(\omega) X_{\eta J}^{*}(\omega) d\omega^{5} \\ &\rightarrow \sum_{i=1}^{N} \ln P^{(i)} - \sum_{s\eta}\sum_{I}\sum_{J} A_{s\eta I} A_{s\eta J}^{*} W_{\eta IJ}^{Acc}\end{aligned} \tag{6.20}$$

where we have defined

$$\begin{aligned}W_{\eta IJ}^{Acc} &\equiv \int \epsilon(\omega) X_{\eta I}(\omega) X_{\eta J}^{*}(\omega) d\omega^{5} \\ &\approx \frac{\int d\omega^{5}}{N_t} \sum_{j=1}^{N_t} \epsilon^{(j)} X_{\eta I}(\omega_j) X_{\eta J}^{*}(\omega_j).\end{aligned} \tag{6.21}$$

In Eqn. 6.20 the terms that are independent of the $A_{s\eta J}$ have been dropped since they are irrelevant in maximizing $\ln\mathcal{L}$ with respect to these variables. The expression for $W_{\eta IJ}^{Acc}$ is the numerical evaluation of the integral, performed using N_t thrown Monte Carlo events in the $\Delta M_3 \Delta t'$ bin. The quantity ω_j is the five-dimensional vector representing the measured phase space location of the jth Monte Carlo event, and $\epsilon^{(j)}$ is either 1 or 0 depending on whether or not the Monte Carlo event was reconstructed and passed the selection criteria. The evaluation of this integral is described in the next subsection. The triple summation in Eqn. 6.20 yields the number of observed events $\overline{N}$ predicted by the fit.

A useful property of $\ln\mathcal{L}$ in Eqn. 6.20 is that the acceptance only enters into the likelihood function through the $W_{\eta IJ}^{Acc}$, which are independent of the $A_{s\eta J}$'s and can be computed prior to the $A_{s\eta J}$ fitting. Therefore, $\ln\mathcal{L}$ is a bilinear function of

the $A_{s\eta J}$ (recall the form of $P^{(i)}$ given in Eqn. 6.2) and in practice efficient methods are available for maximizing such functions.

6.2.4 *The Acceptance and Normalization Integrals*

As mentioned in the previous section, the number of observed events predicted by the likelihood function is given by

$$\begin{aligned} \overline{N} &\equiv \int P_{obs}(\omega) d\omega^5 \\ &= \sum_{s\eta} \sum_{I} \sum_{J} A_{s\eta I} A_{s\eta J}{}^* W^{Acc}_{\eta I J}. \end{aligned} \tag{6.22}$$

From this expression, we can see that the number of observed events attributed to a partial wave ηJ is given by

$$N^{obs}_{\eta J} = |A_{s\eta J}|^2 W^{Acc}_{\eta J J}.$$

A second set of integrals, used for normalization, are defined as

$$\begin{aligned} W^{Nor}_{\eta I J} &\equiv \int X_{\eta I}(\omega) X_{\eta J}{}^*(\omega) d\omega^5 \\ &\approx \frac{\int d\omega^5}{N_t} \sum_{j=1}^{N_t} X_{\eta I}(\omega_j) X^*_{\eta J}(\omega_j). \end{aligned} \tag{6.23}$$

This definition differs from that of the $W^{Acc}_{\eta I J}$ by the absence of the acceptance probability ϵ in the integration. In effect, the $W^{Nor}_{\eta I J}$ relate the fitted partial wave amplitudes to the number of events produced in the detector, *i.e.*

$$N^{pred}_{\eta J} = |A_{s\eta J}|^2 W^{Nor}_{\eta J J}.$$

The ratio of $W^{Acc}_{\eta J J}$ and $W^{Nor}_{\eta J J}$ is the "acceptance" for the partial wave with quantum numbers ηJ. Although the normalization integrals are not used when fitting the partial wave amplitudes, they are needed to convert the fitted partial wave intensities to acceptance-corrected cross sections.

It is necessary to calculate these integrals in bins that are commensurate with the data binning chosen for the PWA. Since it is not known *a priori* what the most suitable data binning will be, it is convenient to choose a fine Monte Carlo mass and t' binning when generating the Monte Carlo data and then to average the resulting integrals over the chosen data bins. A mass bin width of 0.020 GeV/c^2 was chosen, with the binning starting from the bin $1.030 \leq M_3 < 1.050$ GeV/c^2. Four $|t'|$ bins were defined as follows: 0.0–0.1 (GeV/c)^2; 0.1-0.3 (GeV/c)^2; 0.3-0.6 (GeV/c)^2; and 0.6–1.0 (GeV/c)^2.

The distribution of generated events in three-body invariant mass M_3 is uniform, whereas the distribution in $|t'|$ is exponential. The $|t'|$ distributions are

$$\exp(-5.5|t'|) \text{ for } |t'| \leq 0.3 \text{ (GeV/c)}^2$$

and

$$\exp(-2.5|t'|) \text{ for } 0.3 < |t'| \leq 1.0 \text{ (GeV/c)}^2,$$

the slopes having been chosen to agree with the data distribution (see Table 5.2). By throwing the Monte Carlo data with a particular t' distribution, the partial wave amplitudes are assumed to have the thrown t' dependence across the fitted t' bin. [The same effect could have been achieved by generating the Monte Carlo uniformly in t' and having $f_J(M_3, t') = \exp(-b|t'|/2)$ in Eqn. 6.9 for all waves ($b = 5.5$ and 2.5 for the low and high $|t'|$ region, respectively). However this would have been a more inefficient process and would have resulted in less accurate integrals. By preferentially distributing the Monte Carlo events in the regions where the data density is highest, the accuracy of the $W^{Acc}_{\eta IJ}$ and $W^{Nor}_{\eta IJ}$ scales with the statistical power of the data.] The assumption of a common t' dependence for all partial waves is an approximation, but was verified to be adequate for the PWA of the $\bar{K}^\circ \pi^+\pi^-$ data by performing two iterations of the analysis. This is described in more detail in the next subsection.

For a given mass and t', the generated vectors for the three mesons are thrown using a uniform phase space generation algorithm described in Ref. 71. However, this generated distribution is modified to enhance the MC event density for the $K^*(892)$ mass region in the Dalitz plot in order to obtain accurate integrals for the

$K^*(892)$ waves (since the $K^*(892)$ is relatively narrow, the numerical integration to obtain the $W^{Acc}_{\eta IJ}$ and $W^{Nor}_{\eta IJ}$ for this isobar suffers from "Monte Carlo inefficiency"). This enhancement is achieved by throwing three times more MC events for the region defined by $0.80 \leq m(\bar{K}^\circ\pi^-) < 0.98$ GeV/c^2 than elsewhere in the Dalitz plot. The events in this region are weighted by a factor of $\frac{1}{3}$ so that the weighted MC event sample remains uniformly distributed in phase space.

In each 0.020 GeV/c^2 mass bin, 44 000 Monte Carlo events were generated for $|t'| \leq 0.3$ (GeV/c)^2, and 19 000 events were generated for $|t'| > 0.3$ (GeV/c)^2; the sample size was such that the accepted Monte Carlo event sample was at least ten times larger than the corresponding data sample. The minimum value for the ratio of the number of accepted Monte Carlo events to the number of observed data events occurs around $M_3 = 1.45$ GeV/c^2 where it is ~ 13.

6.2.5 The Fitting Procedure

The mass dependences of the $A_{s\eta J}$ were first determined for the event sample with $|t'| \leq 0.3$ (GeV/c)^2. This sample was divided into fine M_3 mass bins and the values of the $A_{s\eta J}$'s were estimated in each of these bins using the fitting procedure described below. Subsequently the $A_{s\eta J}$ were determined as a function of t' by dividing the data into two broad M_3 bins and fitting the data within each mass bin in four narrower t' bins. The results of this latter analysis indicated that in the lower mass region $M_3 \leq 1.69$ GeV/c^2, the t' dependences of the larger partial waves are quite different.

Because of this disparity, a second iteration of the PWA was performed that included a more accurate t' dependence for each partial wave within the $|t'|$ interval 0.0—0.3 (GeV/c)^2. The decay amplitudes for the data and MC events were weighted by the measured t' dependences, the acceptance and normalization integrals were recalculated, and the $A_{s\eta J}$ refit as a function of M_3 with this improved model. A comparison of the mass dependences determined in the two iterations indicated that the results are only weakly dependent upon the input t' dependence.

The choice of data binning is a compromise between the conflicting criteria of: (a) having enough data within each bin to ensure that the fitting process is stable; and (b) choosing narrow bins so that rapid variations in the $A_{s\eta J}$ can be detected.

Table 6.1. The $\bar{K}^{\circ}\pi^{+}\pi^{-}$ mass binning used in the PWA. The table lists the number of events for $|t'| \leq 0.3$ (GeV/c)^2.

Bin Center GeV/c^2	Bin Width GeV/c^2	Number of Events
1.070	0.080	214
1.140	0.060	303
1.200	0.060	481
1.260	0.060	735
1.310	0.040	627
1.350	0.040	857
1.390	0.040	1326
1.430	0.040	1758
1.470	0.040	1628
1.510	0.040	1293
1.550	0.040	1071
1.600	0.060	1547
1.660	0.060	1624
1.720	0.060	1903
1.780	0.060	2003
1.850	0.080	2521
1.930	0.080	2241
2.010	0.080	2145
2.090	0.080	1960
2.170	0.080	1680
2.250	0.080	1487

The mass binning chosen for the analysis is shown in Table 6.1 and the t' binning is shown in Table 6.2.

The program **PWAOP**[54] is used to determine the $A_{s\eta J}$ in each of the data bins. For each fit, this program is provided with the following information: (a) the mass and t' bin limits; (b) the set of partial wave amplitudes that are to be included in the fit; (c) the reference waves in the fit; and (d) how the fit is to be initialized. **PWAOP** sets up the data and invokes a generalized fitting program known as **OPTIME**[72] that locates a *local* maximum of $\ln\mathcal{L}$ starting from the initial values of the partial wave amplitudes. Since $\ln\mathcal{L}$ typically has a number of local maxima, it is necessary to repeat the fits with different initial values for the $A_{s\eta J}$

Table 6.2. The t' binning used in the PWA. The event populations are shown for the two $\bar{K}^\circ \pi^+\pi^-$ mass bins in which the t' analysis was carried out.

Bin Center $(GeV/c)^2$	Bin Width $(GeV/c)^2$	Number of Events	
		$1.370 \leq M_3 < 1.470$	$1.730 \leq M_3 < 1.850$
0.05	0.10	2090	2234
0.20	0.20	1856	1762
0.45	0.30	1096	1119
0.80	0.40	511	595

to establish the values of $A_{s\eta J}$ at the global maximum of $\ln\mathcal{L}$.

In the fit, a reference amplitude has to be chosen for each set of coherent waves (*i.e.* waves with the same η and nucleon helicity) since it is only possible to measure relative phases. The choice of reference wave, which has its imaginary component set to zero, is arbitrary from the physics point of view and so is motivated solely by considerations such as fit stability and convenience. If a very small amplitude is chosen as a reference wave, the relative phase errors will be large and the real and imaginary components of the other waves in the fit will be highly correlated. Since large correlations between fit parameters are generally undesirable for such a likelihood fit, the reference wave should be large relative to the other waves in the particular coherent term. It is also inconvenient to switch reference waves frequently as the behavior of the relative phases is then less transparent.

It is impossible to include all partial waves in the fit for a given data bin, as the finite event statistics can only support a fit with a limited number of parameters. The partial waves that are required to model the data in each bin were determined in an iterative search through the entire set of 184 waves. Initially the partial waves in the fit (the "base" wave set) were those that had been found to be significant in earlier analyses of the $\bar{K}^\circ \pi^+\pi^- n$ data. A set of solutions with this wave set was obtained in several adjacent bins. Another partial wave was then added to the wave set and the fits repeated with this augmented wave set. If the added partial wave amplitude was significant and the quality of the fits increased over

the previous wave set, the new wave was adopted into the base wave set and the process repeated with another partial wave. This procedure continued until all partial waves had been tested in this fashion. To guard against the possibility of rejecting small waves whose significance might be enhanced by the inclusion of another small wave into the wave set, waves found to be marginal candidates were also fit simultaneously with other marginal waves and their combined significance judged.

Given a particular base wave set, there are usually a number of solutions for the $A_{s\eta J}$ in each mass bin, with each solution defining a local maximum of $\ln\mathcal{L}$. To determine these local maxima, the fit to a particular mass bin and base wave set is repeated several times (10—30), each fit being initialized randomly. The solutions with reasonable values of $\ln\mathcal{L}$'s are then used to initialize the fit in the adjacent mass bins, *i.e.* the solutions are "propagated" in mass or t'. This process normally resulted in 1—5 fit solutions for each bin.

The criterion of maximum $\ln\mathcal{L}$ is not sufficient to distinguish between solutions once their $\ln\mathcal{L}$ difference is only a few units. Therefore, in order to identify *the* solution for the $A_{s\eta J}$ two further criteria are used:

1. Only the solutions that have the highest $\ln\mathcal{L}$ are considered. Normally a cut is made rejecting solutions that have $\ln\mathcal{L}$ that are more than 20 units less than the maximum $\ln\mathcal{L}$ value observed in the bin.
2. The solutions are required to show smooth $A_{s\eta J}$ behavior across neighboring bins. This requirement of continuity is used to choose the correct solution in each mass bin from among the ones satisfying the criteria of maximum $\ln\mathcal{L}$.

The cut of 20 in $\ln\mathcal{L}$ difference was chosen to ensure that all possible solution candidates were given consideration. The additional requirement of continuity was sufficient in most cases to select a unique solution within a bin. Usually the $\ln\mathcal{L}$ value of this solution was either the maximum observed for the fits in that data bin or was within 5 units of the maximum value.

6.2.6 Comparisons of Fit Results to Data

It is possible to check the quality of a PWA fit by comparing the observed event distribution with that predicted by the fit solution. This comparison is

difficult to make quantitative as there are very few accurate statistical tests that can be employed to compare five dimensional distributions. However, it is possible to compare one and two dimensional projections of the predicted and observed distributions to check that they agree.

The predicted event distribution is generated from the fit solution using the fitted $A_{s\eta J}$, Eqn. 6.2 for the probability of observing a particular event, and the subset of the Monte Carlo event sample that passed all the selection requirements. This Monte Carlo event sample already has all the effects due to detector acceptance and event selection included. To obtain the predicted event distribution, it only remains to fold in the produced event distribution given by the fitted $A_{s\eta J}$ and the $X_{\eta J}$ calculated for each Monte Carlo event. Each accepted Monte Carlo event is weighted by its production probability computed using Eqn. 6.2 and this sample is then used to create one and two dimensional projections of the predicted event distribution, which may then be compared with the corresponding projections of the data distribution.

The predicted and observed distributions of the four angles θ, α, β, and γ, and $\bar{K}^{\circ}\pi^{-}$ and $\pi^{+}\pi^{-}$ invariant mass were compared for all of the mass bins. Several two dimensional distributions were also examined (*e.g.* the θ-γ and α-β distributions) to check that the correlations were being correctly reproduced by the solutions. These comparisons showed that the fits provided a good description of the data.

Figure 6.7 shows a comparison of the predicted and observed event distributions for the four angles defined in the $\bar{K}^{\circ}\pi^{-}$ system, and for the $\bar{K}^{\circ}\pi^{-}$ and $\pi^{+}\pi^{-}$ invariant masses in the 1.43 GeV/c^2 mass bin. Figure 6.8 shows similar distributions for the mass bin centered at 1.80 GeV/c^2; in this figure, the angles are defined in the $\pi^{+}\pi^{-}$ system.

6.3 The Results of the PWA

6.3.1 Observables and Errors

Although the parameters estimated by the fitting procedure are the $A_{s\eta J}$, they are expressed in arbitrary units that depend on the normalization of the decay amplitudes. Therefore, a partial wave amplitude is normally represented by its intensity σ_J and phase ϕ_J, the latter being measured relative to the appropriate

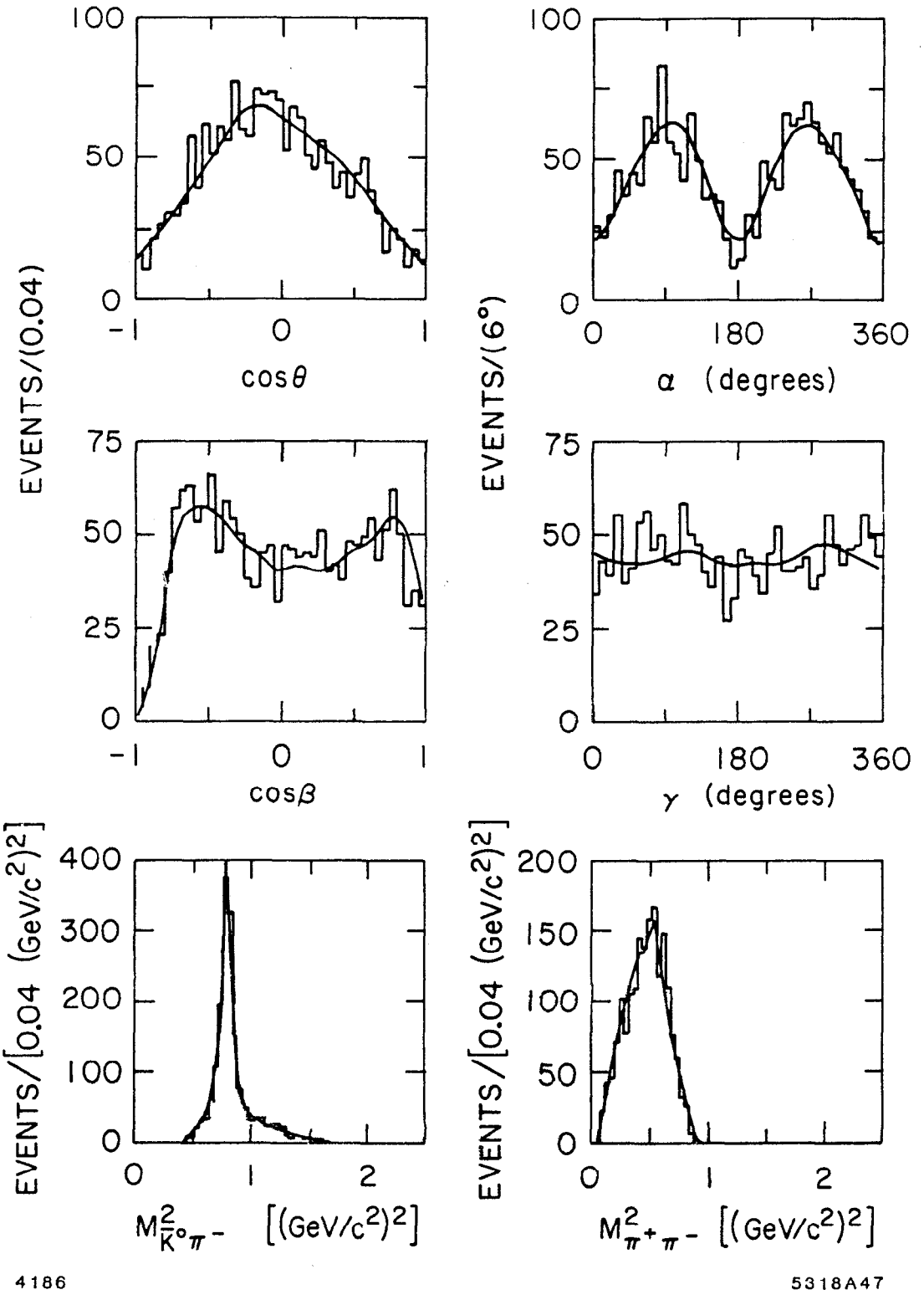

Figure 6.7. The comparison of the fit to the data for $M_3 = 1.43$ GeV/c^2. The predicted (solid curve) and the observed (histogram) distributions are shown for the mass bin centered at 1.43 GeV/c^2. The angles are defined for the $\bar{K}^0\pi^-$ system.

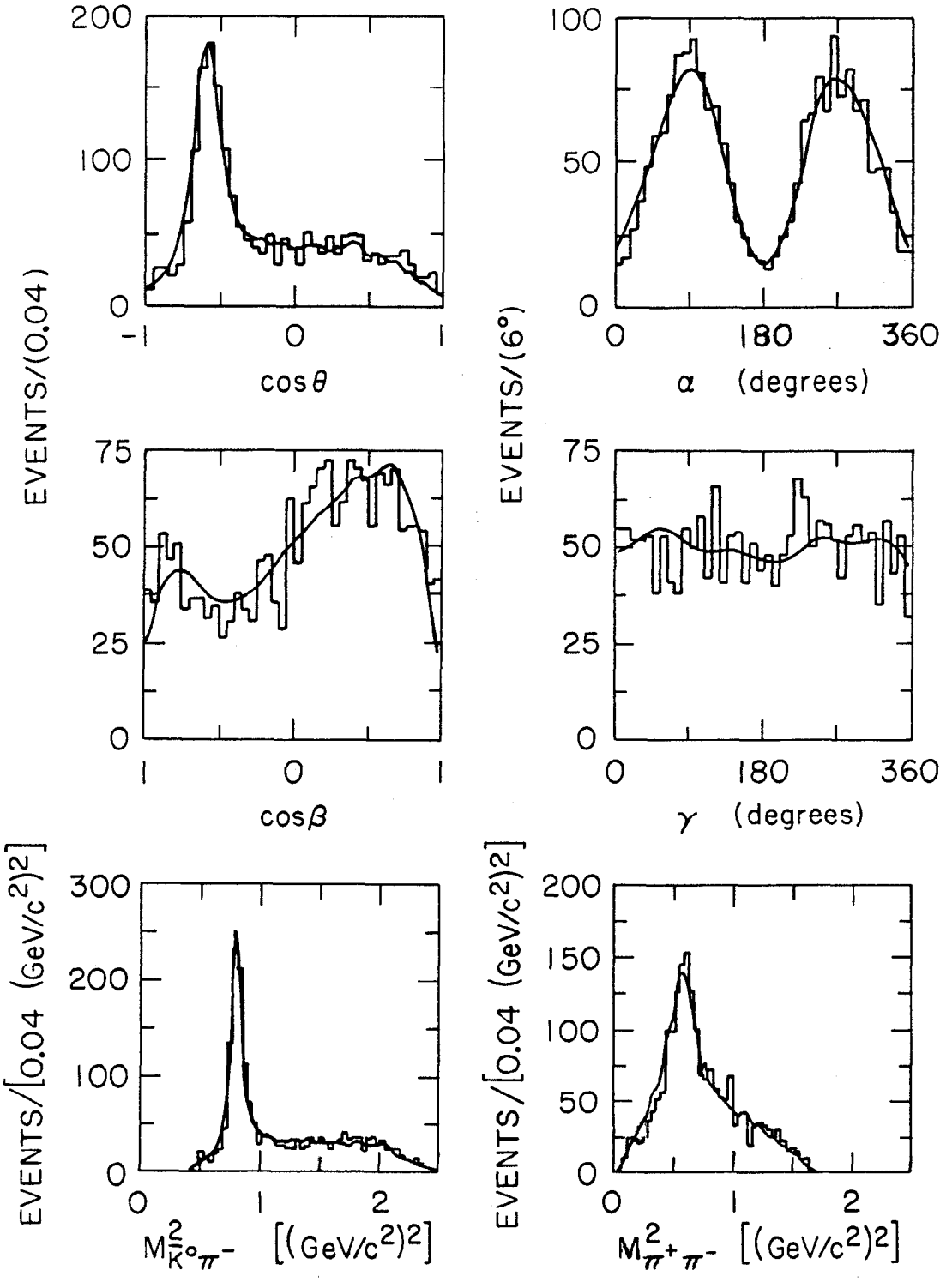

Figure 6.8. The comparison of the fit to the data for $M_3 = 1.80$ GeV/c^2. The predicted distributions (solid curves) and the observed distributions (histograms) are shown for the mass bin centered at 1.80 GeV/c^2. The angles are defined for the $\pi^+\pi^-$ system.

reference wave. If we let $a_J \equiv Re(A_{s\eta J})$ and $b_J \equiv Im(A_{s\eta J})$, then

$$\begin{aligned} \sigma_J &\equiv \frac{\sigma_0}{\Delta M_3 \Delta t'}(a_J^2 + b_J^2) W^{Nor}_{\eta JJ}, \text{ and} \\ \phi_J &\equiv \arctan\left(\frac{b_J}{a_J}\right). \end{aligned} \tag{6.24}$$

With this definition, σ_J is the differential cross section for the Jth wave in the fitted mass and t' bin, and ϕ_J its phase relative to the reference wave. Unless explicitly mentioned, σ_J will be expressed in units of $(0.02\ \text{GeV/c}^2)^{-1}$ and represents the differential cross section integrated over the t' bin from 0.0 to 0.3 $(\text{GeV/c})^2$ corrected for all acceptance effects (except the $\bar{K}^\circ$ visibility). This choice of units amounts to setting σ_0 to unity in Eqn. 6.24. The plotted σ_J can be converted from events into nanobarn units by dividing by the sensitivity determined in §5.7 (using the appropriate factor to scale the energy and momentum units).

The statistical errors on these quantities are determined from the fit error matrix V:

$$\begin{aligned} \sigma_{\sigma_J} &= 2\frac{\sigma_0}{\Delta M_3 \Delta t'} W^{Nor}_{\eta JJ} \sqrt{a_J^2 V_{a_J a_J} + 2a_J b_J V_{a_J b_J} + b_J^2 V_{b_J b_J}} \\ \sigma_{\phi_J} &= \frac{1}{a_J^2 + b_J^2} \sqrt{b_J^2 V_{a_J a_J} - 2a_J b_J V_{a_J b_J} + a_J^2 V_{b_J b_J}}. \end{aligned} \tag{6.25}$$

These are the uncertainties associated with σ_J and ϕ_J in the following plots, but they should be treated with some caution; they only express the statistical errors from the likelihood fit and do not represent the additional uncertainty from at least three other sources:

1. The fitted amplitudes can be affected by the addition of small partial waves that might be present, although they do not appear to be significant when added to the wave set. The procedure used to select the waves can unambiguously identify the largest ones required to fit the data, but it cannot be expected to determine the contributions (if any) from the very smallest waves.
2. For small partial waves, the uncertainty in ϕ_J is often dominated not by the statistical errors but by ambiguities due to multiple fit solutions for a

data bin. These ambiguities begin to be significant in the high mass region above a three-body mass of $\sim$ 1.9 GeV/c^2. In this mass region, the Dalitz plot is so large that the overlap of isobars of different type (such as $K^*(892)$ and $\rho(770)$) is small. Since the relative phases are defined primarily by the data distribution in these overlap regions, it is therefore understandable that the definition of these phases becomes increasingly difficult. These phase ambiguities also can effect small partial wave amplitudes.

3. There is the uncertainty due to the approximations of the isobar model.

Based on experience, the additional uncertainties are estimated to be of the order of $\sim$30 events/(0.02 GeV/c^2).

6.3.2 The Wave Set

The data were fit with the wave set listed in Fig. 6.9, where the dependence of the wave set on $\bar{K}^\circ\pi^+\pi^-$ mass is shown. The $J^P = 1^-$ and 2^+ waves are required over the entire mass region, whereas the other spin-parity waves tend to be large either at low or high $\bar{K}^\circ\pi^+\pi^-$ mass.

The wave set does not contain any waves with ϵ or κ isobars but does contain an incoherent three-body phase space wave. Since previous analyses of this channel have employed the scalar isobars, I will dwell for a moment on this feature of the analysis. The data distribution can be adequately represented by a combination of $J^P = 0^-$ and 1^+ κ or ϵ waves at low three-body mass, but as the mass of the $\bar{K}^\circ\pi^+\pi^-$ system increases, no combination of these scalar isobars can faithfully reproduce the data distributions. The reason for this is clear from the Dalitz plot distributions in Fig. 5.19–5.22: the event distributions outside the vector and tensor isobar bands are relatively uniform, showing little enhancement at low sub-masses as would be expected of an ϵ or κ isobar. That these isobars can represent the data at lower $\bar{K}^\circ\pi^+\pi^-$ mass is due to the small size of the Dalitz plot. The two-body mass dependences of both scalar isobars are weak enough that they differ little from a function that has no dependence on the Dalitz plot variables. In addition, because the angular distributions associated with a $0^-0^+\epsilon S$ and $0^-0^+\kappa S$ mimic a uniform phase space distribution, there is no additional information that would distinguish these partial waves from uniform phase space at low three body masses.

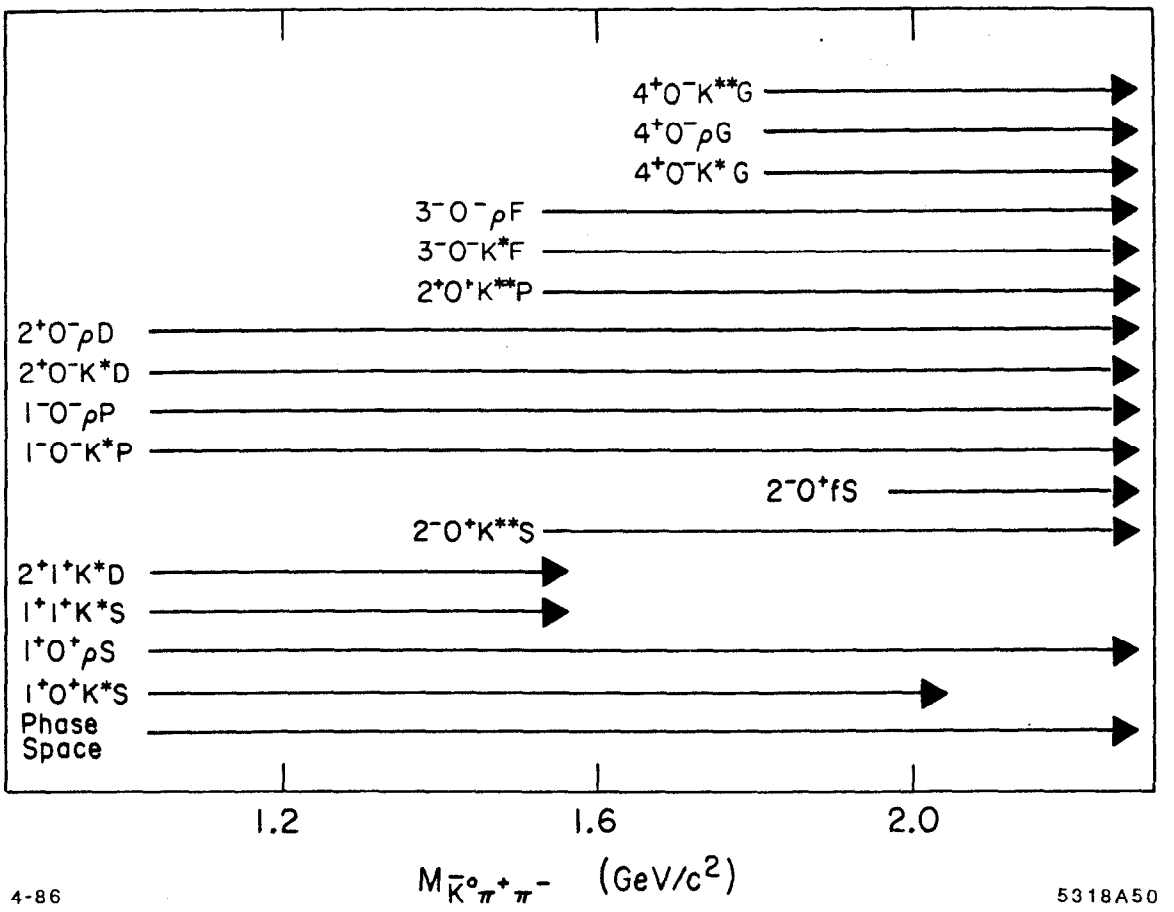

Figure 6.9. The partial waves required to fit the data. The arrows beside each partial wave indicate the range of masses within which the wave was found to be significant.

The difference between the phase space term and the waves with scalar isobars only becomes apparent at higher $\bar{K}^\circ \pi^+\pi^-$ mass.

With the three-body phase space amplitude removed, the fits demand a relatively large $J^P = 0^-$ κ or ϵ wave at low mass, and a significant 1^+ wave at higher masses. However the quality of the fits is degraded considerably, with $\ln\mathcal{L}$ decreases of between 20–60 when compared with the fits including only the incoherent phase space amplitude. A comparison of the observed and predicted event distributions when only the scalar isobars are included in the wave set confirms the fit's inability to reproduce the data. On the other hand, the presence of the phase space term in the fit eliminates any significant ϵ or κ intensity.

There is little change in the other partial wave amplitudes in the fit when the ϵ/κ waves are exchanged for the phase space term, with the possible exception of the $1^+0^+\rho S$ wave. The intensity of this wave below $\bar{K}^\circ \pi^+\pi^-$ masses of $\sim$ 1.6 GeV/c^2 can be made to vary by as much as a factor of two when different choices are made for these "background" amplitudes.

6.3.3 The Mass Dependences of the Partial Wave Amplitudes

The summed intensities of the natural and unnatural spin-parity waves (the J^P sums) are shown as a function of $\bar{K}^\circ \pi^+\pi^-$ mass in Fig. 6.10 and Fig. 6.11, respectively. The 1^- intensity shows a shoulder at $\sim$ 1.35 GeV/c^2 and a sharp peak at $\sim$ 1.8 GeV/c^2, followed by a rapid fall-off, so that at a mass of 2.25 GeV/c^2 the 1^- cross section has almost vanished. The 2^+ cross section shows a dramatic peak around 1.45 GeV/c^2 that is due to the production and decay of the 2^+ $K^*(1430)$. The peak appears to lie on very little background as the intensity falls to approximately one-sixth of the peak height about 0.2 GeV/c^2 above the enhancement. The 2^+ intensity shows a second, broader structure centered at $\sim$ 2.0 GeV/c^2, with the cross section falling off slowly above that mass. The 3^- J^P sum has a relatively broad bump around 1.75 GeV/c^2 arising from the production and decay of the 3^- $K^*(1780)$. The 4^+ intensity is significant only above $\sim$ 2 GeV/c^2; it shows a rise up to a mass of 2.1 GeV/c^2 with an indication of a drop above 2.2 GeV/c^2. Although this effect in the 4^+ cross section is relatively weak, it confirms a similar observation in this channel[22] and can be understood as arising from the g

wave $K^*(2060)$ resonance.[13,21]

The phase space intensity shown in Fig. 6.11 exhibits a linear rise from 1 GeV/c^2 to $\sim$ 1.5 GeV/c^2, whereupon it flattens off and remains constant up to about 2 GeV/c^2 in $\bar{K}^\circ\pi^+\pi^-$ mass. It then begins to roll off and is down to about 60% of its maximum at 2.25 GeV/c^2. The 1^+ cross section shows a large, broad peak centered at $\sim$ 1.4 GeV/c^2 sitting on a significant background. Above 1.6 GeV/c^2 it remains small and slowly falls so that it is almost negligible at the highest masses. The 2^- sum is only significant above 1.5 GeV/c^2 and shows no clear structure. The analysis found that no 3^+ waves were required by the data.

These J^P sums indicate that the production and decay of the $\bar{K}^\circ\pi^+\pi^-$ system is quite complicated. In particular, the two peaks in the $\bar{K}^\circ\pi^+\pi^-$ invariant mass distribution (Fig. 5.16) at $\sim$ 1.4 and $\sim$ 1.8 GeV/c^2 result from the superposition of several enhancements of different spin and parity; the lower mass peak is mostly 2^+ but has large 1^+ and 1^- contributions, whereas the higher mass peak is largely 1^- with some contribution from 3^-. These results contrast sharply with the naive expectation that the two structures result only from the leading 2^+ $K^*(1430)$ and 3^- $K^*(1780)$ states.

The further decomposition of the 1^+ sum into its separate contributions is shown in Fig. 6.12. The $1^+0^+K^*S$ intensity shows a broad bump centered around 1.4 GeV/c^2, which is the largest contribution to the total 1^+ cross section. This wave is the reference wave for the $\eta+$ amplitudes up to a mass of 1.63 GeV/c^2; the $2^-0^+K^{**}S$ then becomes the reference wave as it is the largest $\eta+$ wave in the higher mass region. The $1^+1^+K^*S$ intensity is small and shows no sharp structure over the mass region where it is significant. The $1^+0^+\rho S$ intensity rises through the region where the $1^+0^+K^*S$ peaks, and then falls off rapidly above a $\bar{K}^\circ\pi^+\pi^-$ mass of 1.5 GeV/c^2. The peak in the $1^+0^+K^*S$ cross section and the lack of a similar structure in the $1^+0^+\rho S$ is the signature expected from the axial-vector $Q(1400)$. This resonance, which is copiously produced in the diffractive reaction $K^-p \to K^-\pi^+\pi^-p$, decays almost entirely into $K^*\pi$ with very little $K\rho$ coupling. On the other hand, the $1^+0^+\rho S$ amplitude is probably not resonant, even though it shows a peak around 1.45 GeV/c^2. A resonance in this wave would require the

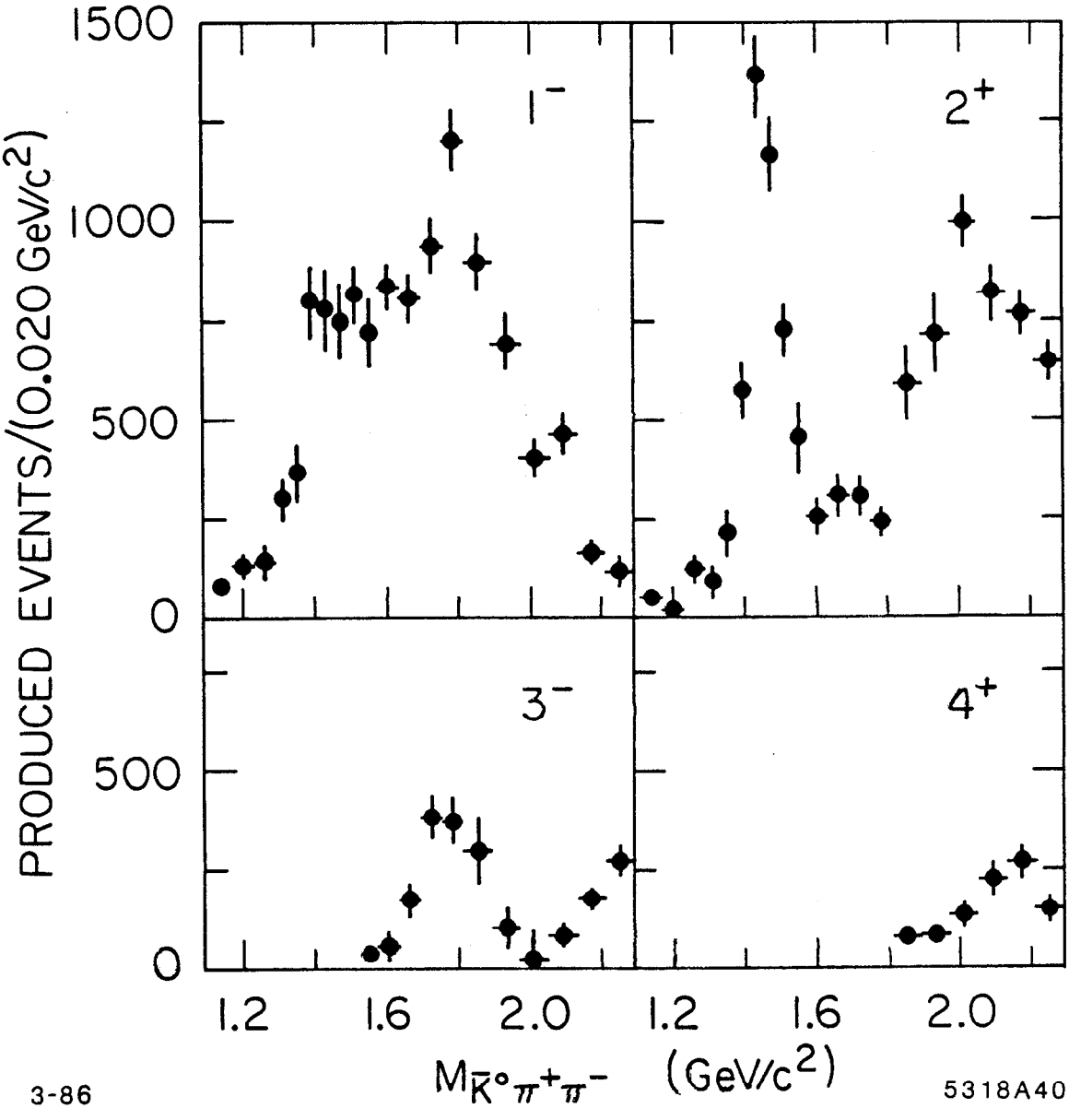

Figure 6.10. The natural spin-parity wave sums. The summed intensities of the natural spin-parity partial waves with the same J^P are plotted as a function of mass. The sums include the interference terms between coherent waves.

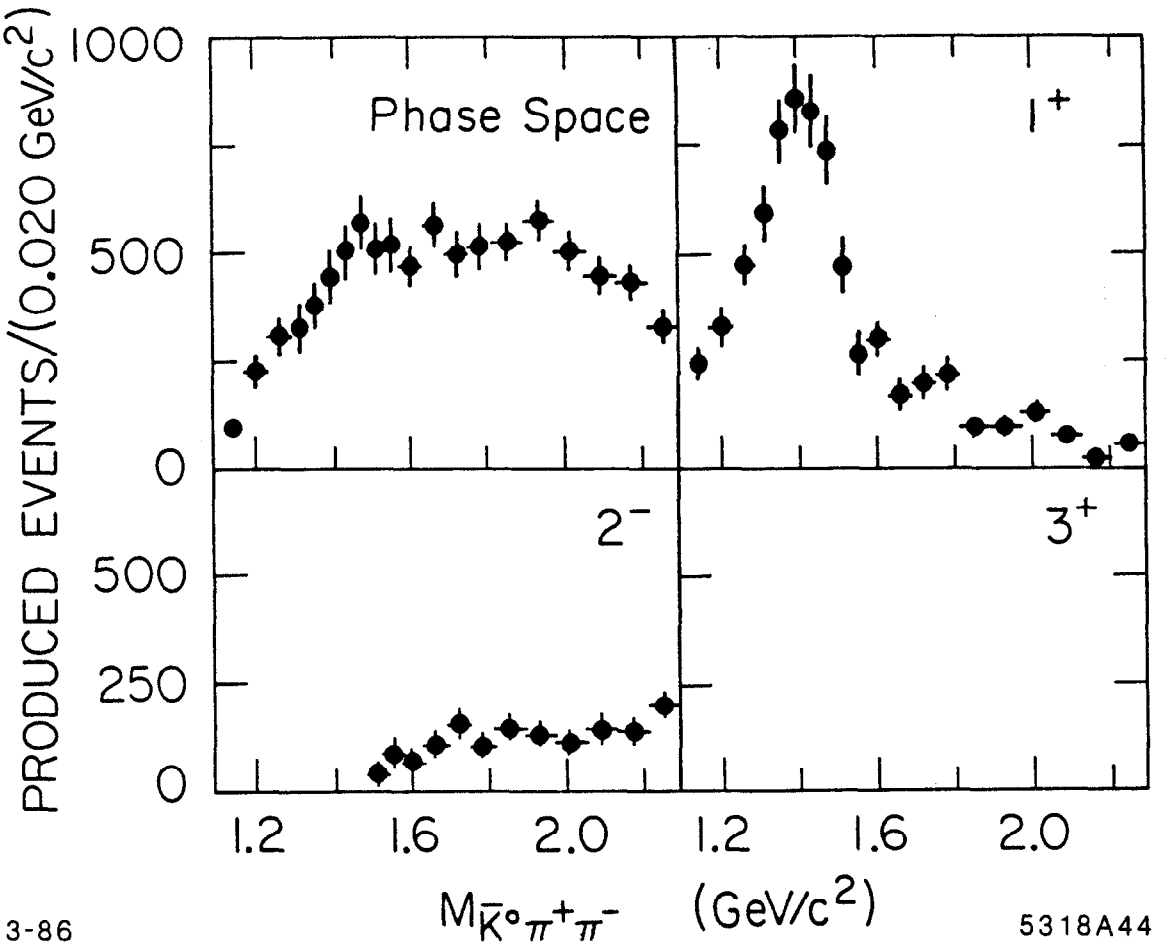

Figure 6.11. The phase space and unnatural spin-parity wave sums.

relative phase of the $1^+0^+\rho S$ to first decrease below $\sim$ 1.4 GeV/c^2 because of the effect of the $Q(1400)$ in the reference wave, and then to advance above this mass because of the absolute phase motion required of a resonance. The data contradict this expectation; the $1^+0^+\rho S$ phase measured relative to the $1^+0^+K^*S$ decreases continuously through the low mass region, so that tts behavior is consistent with a non-resonant interpretation. The $1^+1^+K^*S$ relative phase is constant through the $Q(1400)$ mass region, indicating that it also has a significant $Q(1400)$ component.

Figure 6.13 shows the mass dependence of the two 1^- partial waves, the $1^-0^-K^*P$ and the $1^-0^-\rho P$. The $1^-0^-K^*P$, being the consistently largest $\eta-$ wave over the entire mass region, is the reference wave for the other $\eta-$ waves. It shows a sharp peak at a mass of $\sim$ 1.4 GeV/c^2, then falls off quickly, reaching half its maximum intensity around 1.6 GeV/c^2. A smaller peak is evident at $\sim$1.8 GeV/c^2; at higher mass, it falls off and is relatively small by a mass of 2.25 GeV/c^2. The $1^-0^-\rho P$ intensity behaves quite differently; it is small in the 1.4 GeV/c^2 region, but rises smoothly to a broad peak around 1.8 GeV/c^2 and then falls off at higher mass. The phase of the $1^-0^-\rho P$ relative to the $1^-0^-K^*P$, measurable only above a mass of $\sim$ 1.4 GeV/c^2, decreases by $\sim 60^\circ$ up to a mass of 1.7 GeV/c^2 and remains approximately constant for the rest of the high mass region. A full discussion and interpretation of this phase motion is left until the 2^+ partial waves have been presented. The 1^- amplitudes in Fig. 6.13 also indicate a second set of ambiguous solutions in the 1.3–1.6 GeV/c^2 mass region. This ambiguity is discussed later in this section.

Figure 6.14 shows the mass dependences of the $J^P = 2^-$ partial waves, the $2^-0^-K^{**}S$ and the 2^-0^-fS. The $2^-0^-K^{**}S$ partial wave is used as the reference amplitude for the $\eta+$ waves above a mass of 1.63 GeV/c^2 as it is the largest of the $\eta+$ waves in this region. Its turns on around $K^*(1430)\pi$ threshold and is smooth and relatively featureless. It falls off slightly at masses above 2 GeV/c^2, and this creates the impression of a very broad bump centered at $\sim$ 1.8 GeV/c^2. The 2^-0^-fS is the only partial wave with an $f(1270)$ isobar. It is relatively small and becomes significant above a mass of 2.1 GeV/c^2, consistent with the amount of $f(1270)$ observed in the Dalitz plot distributions. It is worth noting that the

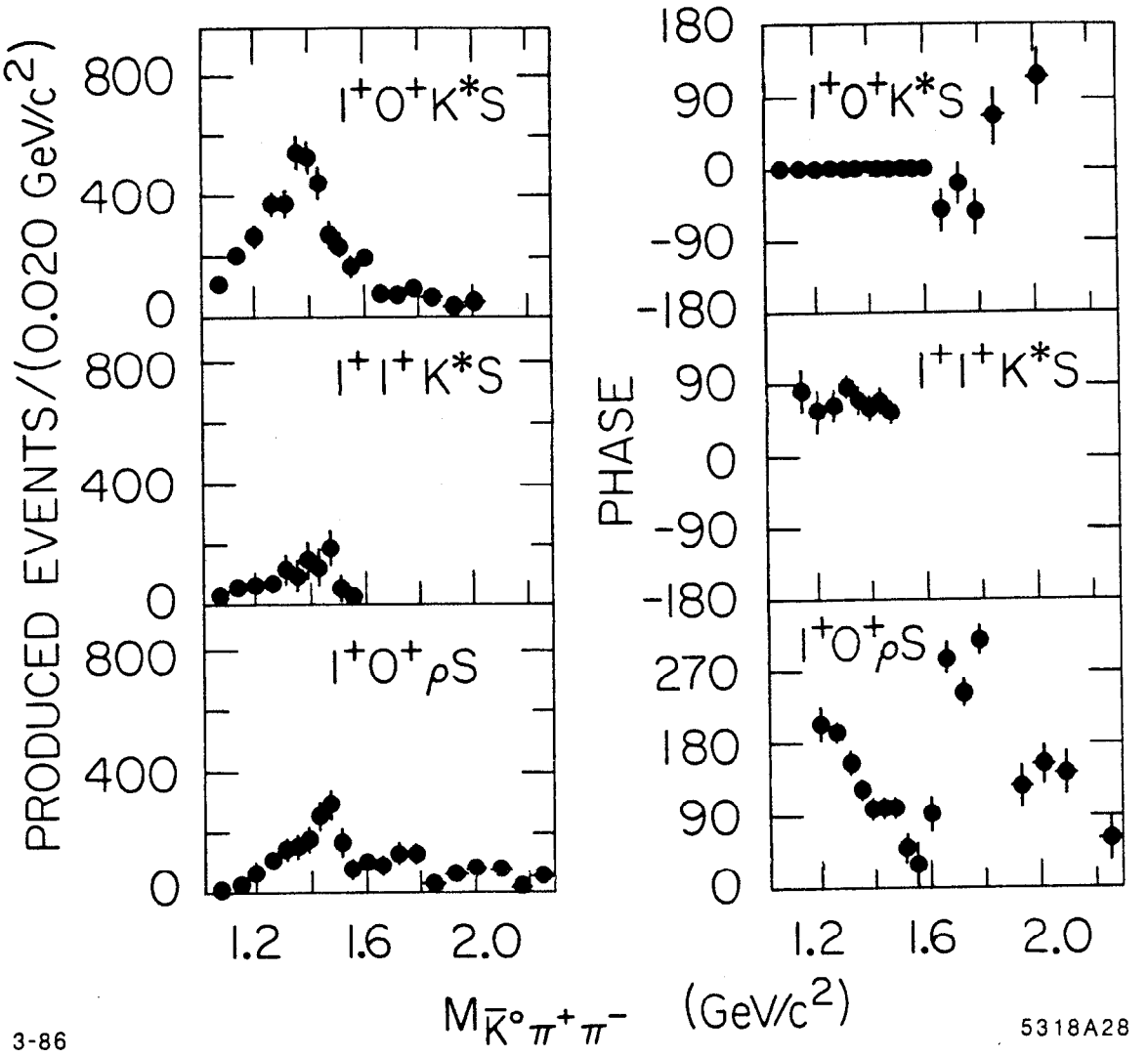

Figure 6.12. The intensities and phases of the $J^P = 1^+$ partial waves. The $1^+0^+K^*S$ is the reference wave for the $\eta+$ waves up to a mass of 1.63 GeV/c^2.

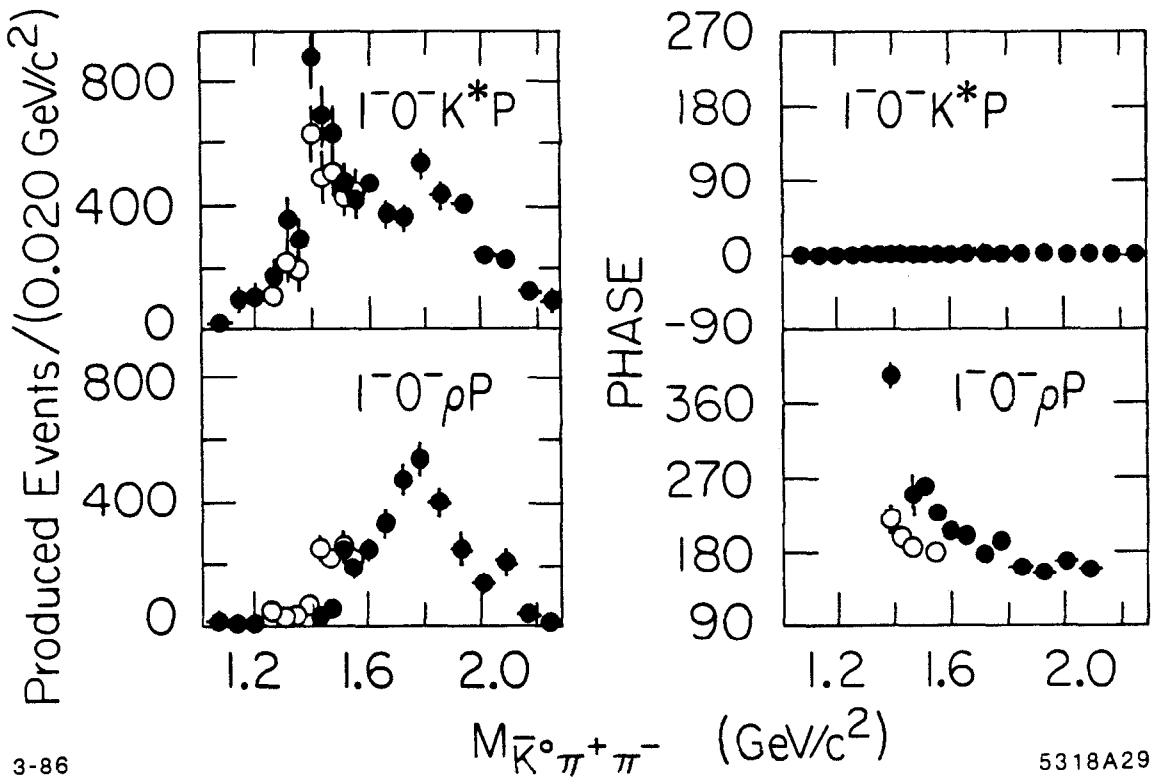

Figure 6.13. The mass dependences of the 1^- partial wave amplitudes. The $1^-0^-K^*P$ wave is the reference wave for the $\eta-$ waves.

two tensor isobars, the $K^*(1430)$ and the $f(1270)$, appear in the most favoured kinematical configuration, with the isobar-bachelor system in a relative s wave.

The mass dependences of the four 2^+ partial wave amplitudes are shown in Fig. 6.15 and Fig. 6.16. The $2^+0^-K^*D$, $2^+0^-\rho D$, and $2^+1^+K^*D$ intensities all have a peak around 1.43 GeV/c^2 that is naturally attributed to the production and decay of the $K^*(1430)$. In addition to this, the $2^+0^-K^*D$ and the $2^+0^-\rho D$ intensities show a second bump around a mass of 2 GeV/c^2. The $2^+0^-K^{**}P$ intensity becomes significant above 1.65 GeV/c^2 but doesn't have the pronounced structure at 2 GeV/c^2 seen in the other two 2^+ waves.

The phases of the $\eta-$ 2^+ waves are measured relative to the $1^-0^-K^*P$ amplitude. The $2^+0^-K^*D$ amplitude, which is very well determined around the 1.4 GeV/c^2 mass region, has a relative phase that is virtually constant up to $\sim$ 1.6 GeV/c^2 where it begins to move slowly backward. This implies that the absolute phase of the $1^-0^-K^*P$ partial wave is advancing in lockstep with the absolute phase of the resonant $2^+0^-K^*D$ amplitude. This phase behavior, together with the behavior of the $1^-0^-K^*P$ intensity that peaks in the same region as the $2^+0^-K^*D$ amplitude, gives the $1^-0^-K^*P$ wave the characteristics of a resonance amplitude centered around the mass of the $K^*(1430)$. The behavior of the $2^+0^-\rho D$ intensity mirrors that of the $2^+0^-K^*D$ around the 1.43 GeV/c^2 region. The phases of the $2^+0^-\rho D$ and $2^+0^-K^*D$ amplitudes are relatively real, a situation that is expected of the decay amplitudes of a single resonance. However this relationship does not hold off the peak of the $K^*(1430)$ resonance, an effect that may be due to a non-resonant component in the $2^+0^-\rho D$ amplitude. In the region of the enhancement at $\sim$2 GeV/c^2, the phases of the three 2^+ partial waves are relatively real.

The intensities and relative phases of the 3^- partial wave amplitudes are shown in Fig. 6.17. Both the $3^-0^-K^*F$ and the $3^-0^-\rho F$ intensities show clear bumps around 1.75–1.80 GeV/c^2 on top of very little background. These enhancements are interpreted as coming from the production and decay of the 3^- $K^*(1780)$, as the observed masses and widths agree with the known properties of this state. If this association is made, then the absolute phase of the 3^- partial waves should be advancing throughout the 1.65–1.95 GeV/c^2 mass region. The approximately constant phase of the two 3^- waves relative to the reference wave suggests that the

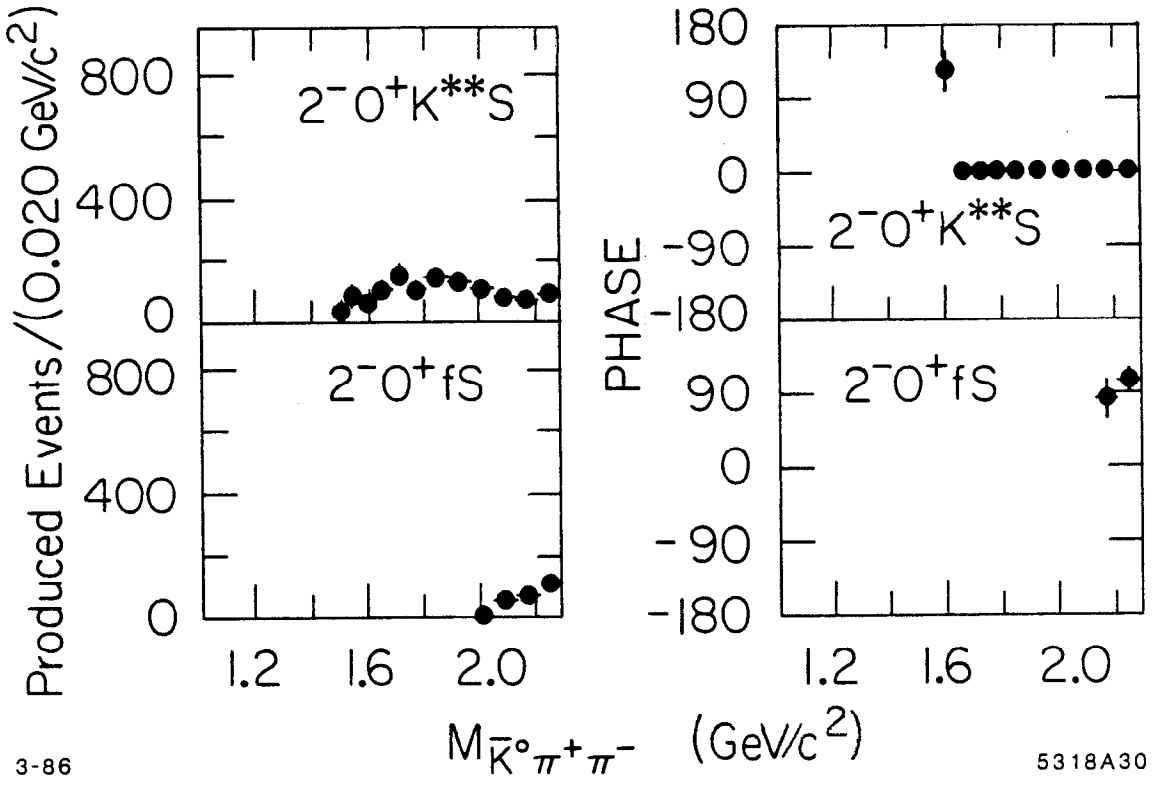

Figure 6.14. The 2^- partial wave amplitudes. The $2^-0^-K^{**}S$ amplitude is used as the reference wave for the $\eta+$ waves above a mass of 1.63 GeV/c^2.

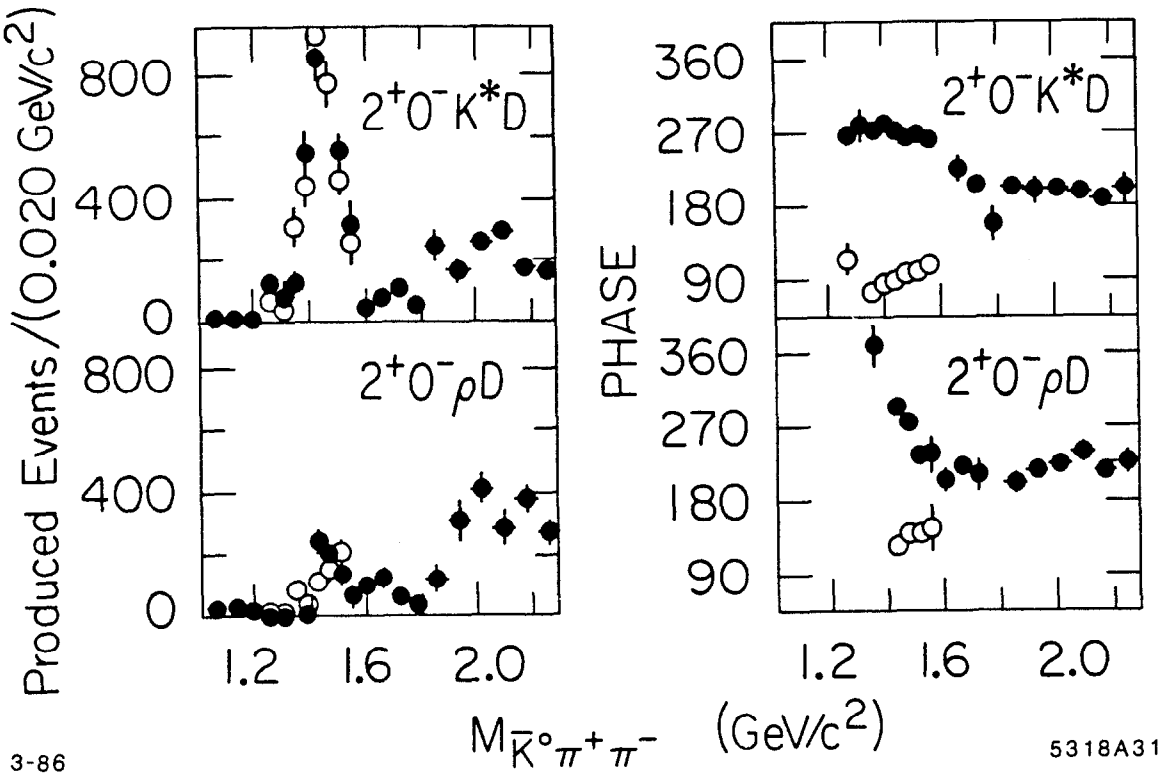

Figure 6.15. The mass dependences of the $2^+0^-K^*D$ and the $2^-0^-\rho D$ amplitudes. The open circles represent the behavior of the second set of solutions, known as Branch II. The reference wave is the $1^-0^-K^*P$ partial wave.

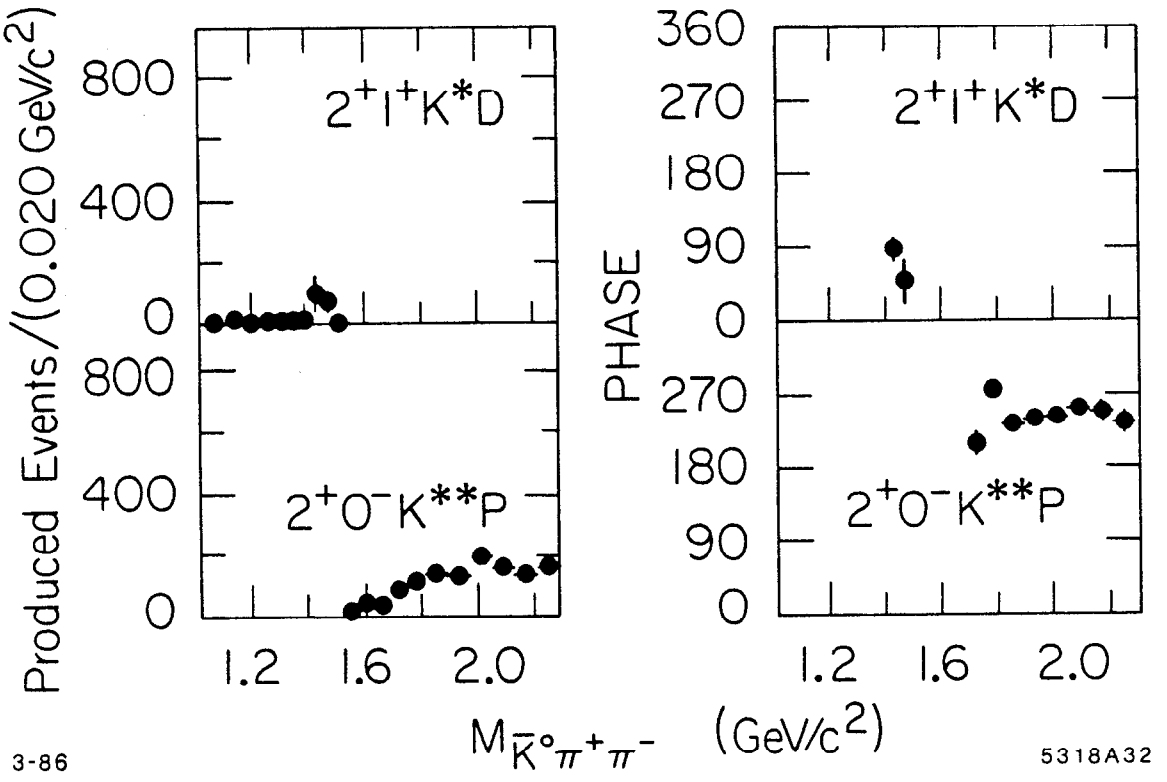

Figure 6.16. The $2^+1^+K^*D$ and the $2^-0^-K^{**}P$ amplitudes. The reference wave is the $1^-0^-K^*P$ partial wave.

absolute phase of the reference wave must be increasing. This would associate an advancing phase with both the reference $1^-0^-K^*P$ wave and the $1^-0^-\rho P$ wave, as the latter also shows an approximately constant phase relative to the $1^-0^-K^*P$. Hence, the higher mass structures in the two 1^- waves would appear to have resonant phase motion.

The mass dependence of the 4^+ waves is shown in Fig. 6.18. All three amplitudes show some structure around 2.1 GeV/c^2 but its significance is difficult to assess. In addition, their relative phase measurements are unreliable because of their small size and the lack of substantial overlap between different isobars on the Dalitz plot. The $4^+0^-K^*G$ shows a small enhancement around ~ 2.13 whereas the intensity of the $4^+0^-\rho G$ does not have such a clear structure. The $4^+0^-K^{**}F$ amplitude is the weakest of the 4^+ partial waves, and only has a significant intensity in the 2.09 GeV/c^2 mass bin.

There are two sets of ambiguous solutions in the 1.35–1.55 GeV/c^2 mass region, which differ in the mass dependence of the $1^-0^-K^*P$, $1^-0^-\rho P$, $2^+0^-K^*D$, and $2^+0^-\rho D$ amplitudes. This ambiguity is similar to one reported in a previous analysis of this channel.[22] The most significant differences between these two sets of solutions, labelled Branch I and Branch II, are in the relative phase behavior of the 2^+ waves and in the isobar decomposition of the 1^- cross section. The solutions in the two branches are equally good fits to the data, with Branch II having a slightly higher value of $\ln\mathcal{L}$ on average. For this reason, the ambiguity cannot be resolved on the basis of the $\ln\mathcal{L}$ differences between the two branches.

This ambiguity arises because of the predominance of $K^*(892)$ production in this mass region. Because of this, the production reaction is simply

$$K^-p \to K^*(892)\pi^+n,$$

i.e., the final state approximates a quasi-two-body system recoiling against the neutron. A partial wave analysis of such a two-body system has inherent phase ambiguities arising from the cosine dependence of the cross section on the relative phases of the amplitudes. The implication for the $\bar{K}^0\pi^+\pi^-$ PWA is that the two largest coherent waves in this mass region, the $1^-0^-K^*P$ and the $2^+0^-K^*D$, will

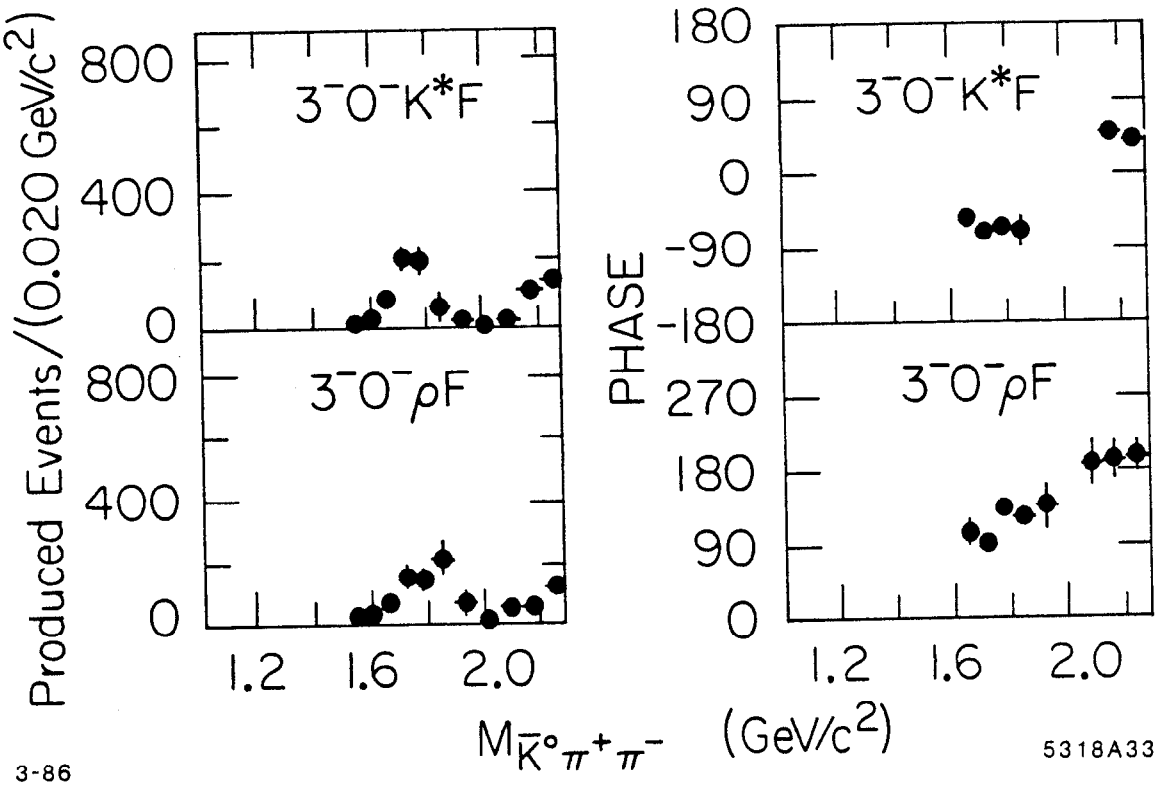

Figure 6.17. The 3^- partial wave amplitudes.

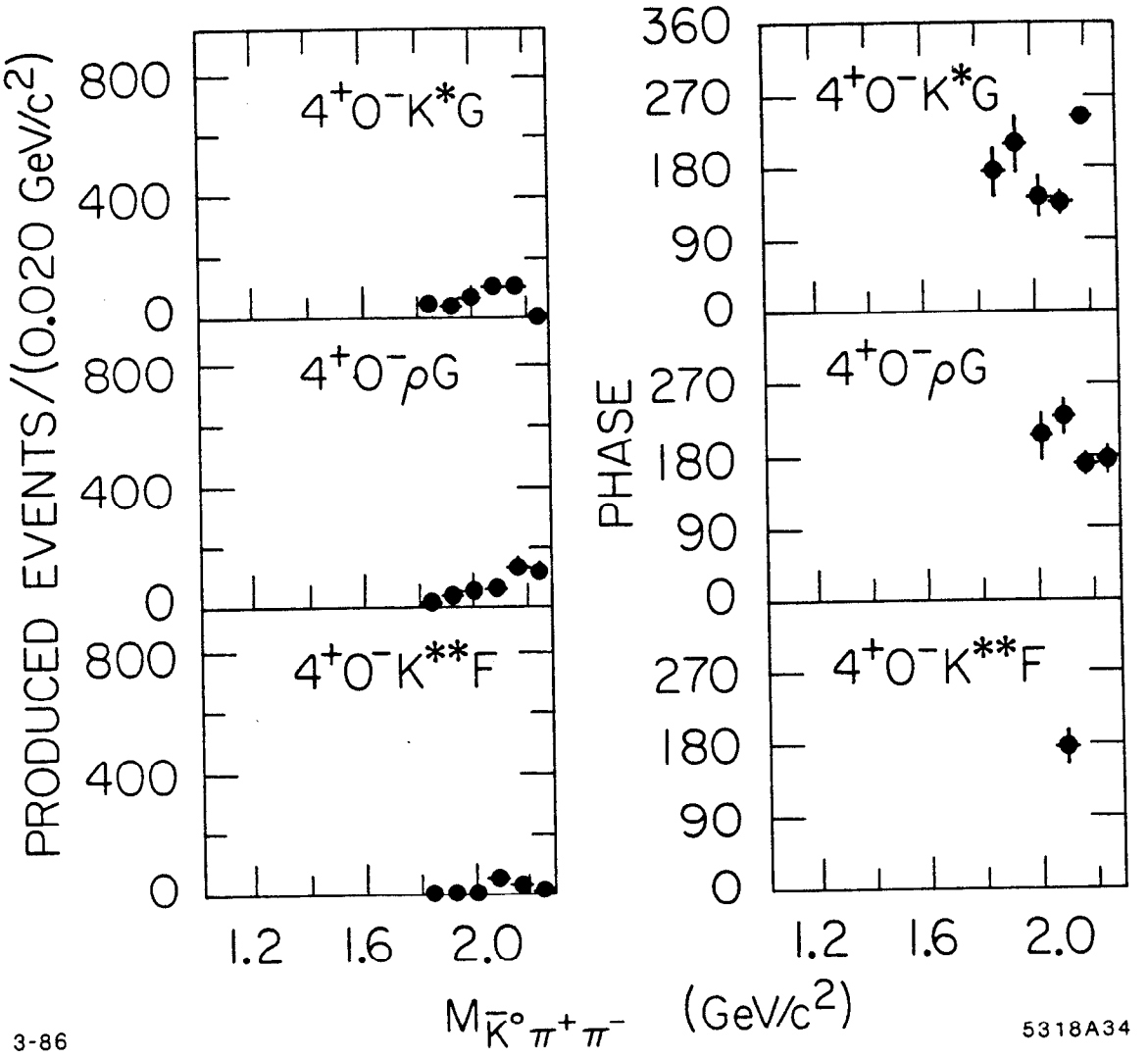

Figure 6.18. The $J^P = 4^+$ partial wave amplitudes.

show the classic phase ambiguity $\phi_J \iff -\phi_J$. The differences in behavior of the ρ amplitudes are driven by the change in their small interference terms with the much larger $K^*(892)$ waves.

Although it is not possible to argue away the existence of either solution branch in the 1.4 GeV/c^2 mass region, the discontinuous behavior of Branch II around 1.6 GeV/c^2 supports the contention that Branch I represents the physical solution. In the subsequent interpretation of the amplitude behavior, only Branch I will be considered. In any event, the largest distinction between solution branches is in the relative phase offsets between the $K^*(892)$ waves, which has no affect on the mass dependence of their relative phases or intensities. Because of this, the physics interpretation of the data is insensitive to the choice of solution branch.

6.3.4 The t' Dependences of the Partial Wave Amplitudes

The production angular distributions (*i.e.* the t' dependences) of the partial wave amplitudes reflect the nature of the mechanisms producing the resonant states. These t' dependences were measured in two relatively broad mass bins centered at 1.42 and 1.79 GeV/c^2. The data in these two bins are subdivided into four t' bins in the range $0.0 \leq |t'| < 1.0$ (GeV/c)^2, as described in §6.2.5, and the amplitudes in each t' bin are determined with the fitting program. The wave set established by the mass-dependent analysis is used in these fits.

The fitted intensities of the partial waves as a function of t' are shown in Fig. 6.19 for the largest $J^P = 1^+$ and 1^- waves. Figure 6.20 shows the t' dependences of the two largest 2^+ amplitudes in the 1.42 GeV/c^2 mass bin, the $2^+0^-K^*D$ and the $2^+0^-\rho D$ partial waves. The t' dependences of the 3^- amplitudes are shown in Fig. 6.21. The t' dependences of the smaller partial waves are not shown as these waves are not significant at large $|t'|$. The intensities of all the partial waves show approximate exponential dependences, but there are significant variations in slope among the intensities.

Since the majority of the partial wave intensities can be characterized by an exponential t' dependence, each intensity distribution was fit to such a function. The fitted distributions are shown in Fig. 6.19–6.21 as solid lines for the fits to the data in the low mass bin, and as dashed lines for the fits in the high mass bin.

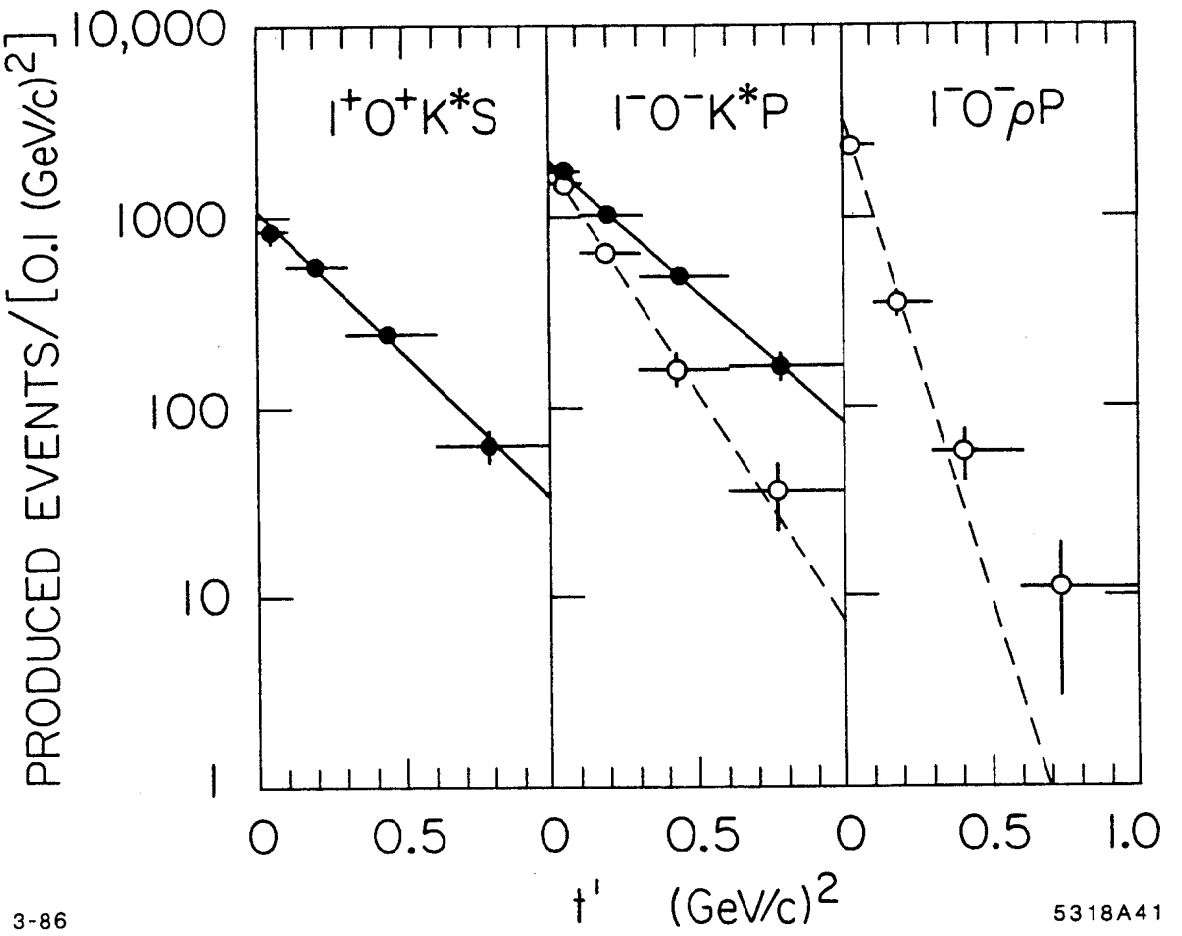

Figure 6.19. The t' dependences of the 1^+ and 1^- partial waves. The solid dots and lines represent the data in the 1.42 GeV/c^2 mass bin; the open dots and dashed lines are for the 1.79 GeV/c^2 mass bin. The lines are the results of the fits described in the text.

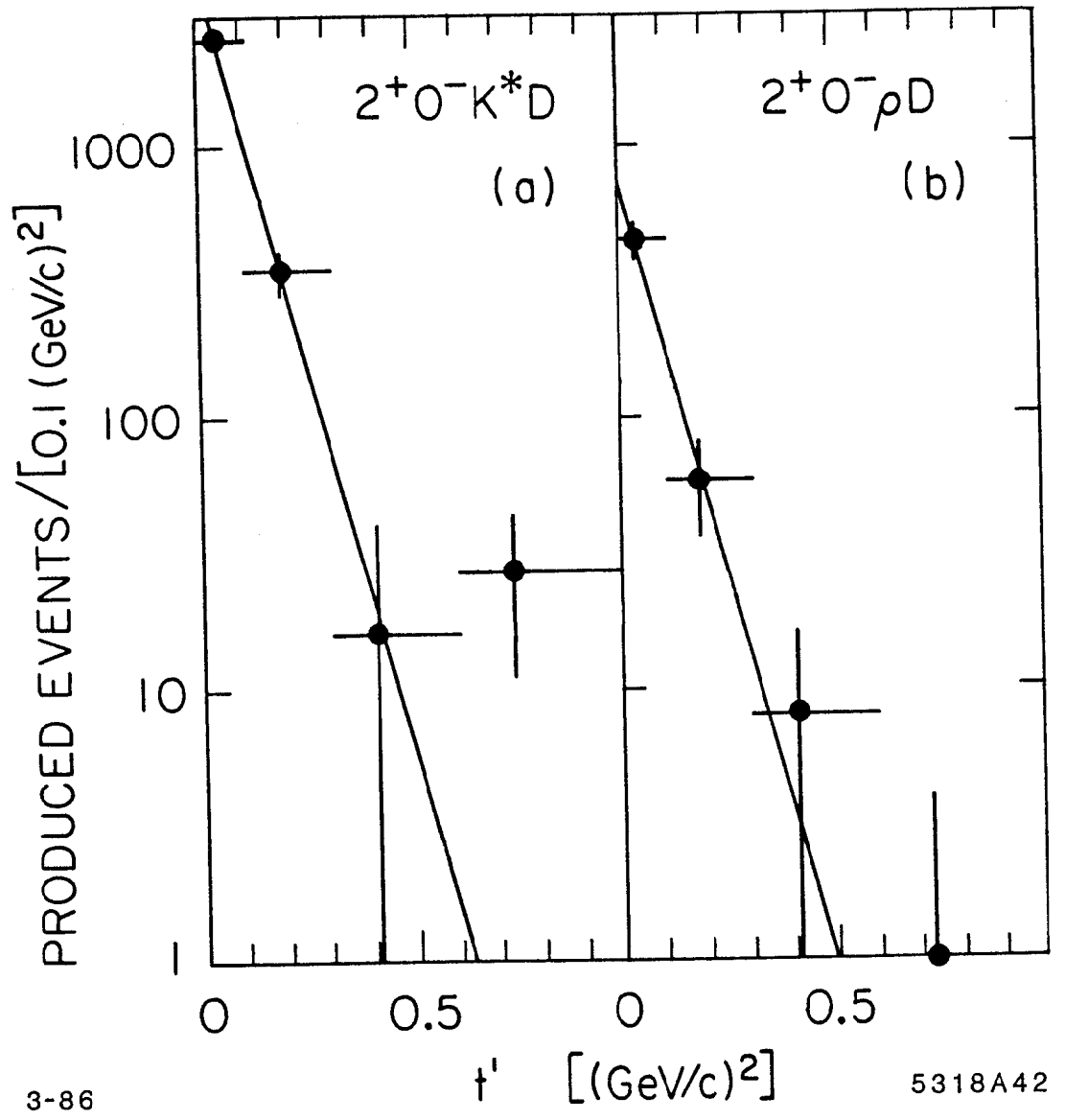

Figure 6.20. The t' dependences of the 2^+ waves at low $\bar{K}^\circ\pi^+\pi^-$ mass. The intensities as a function of t' are plotted for the $2^+0^-K^*D$ and the $2^+0^-\rho D$ partial waves in the 1.42 GeV/c^2 mass bin. The lines are the results of the fits described in the text.

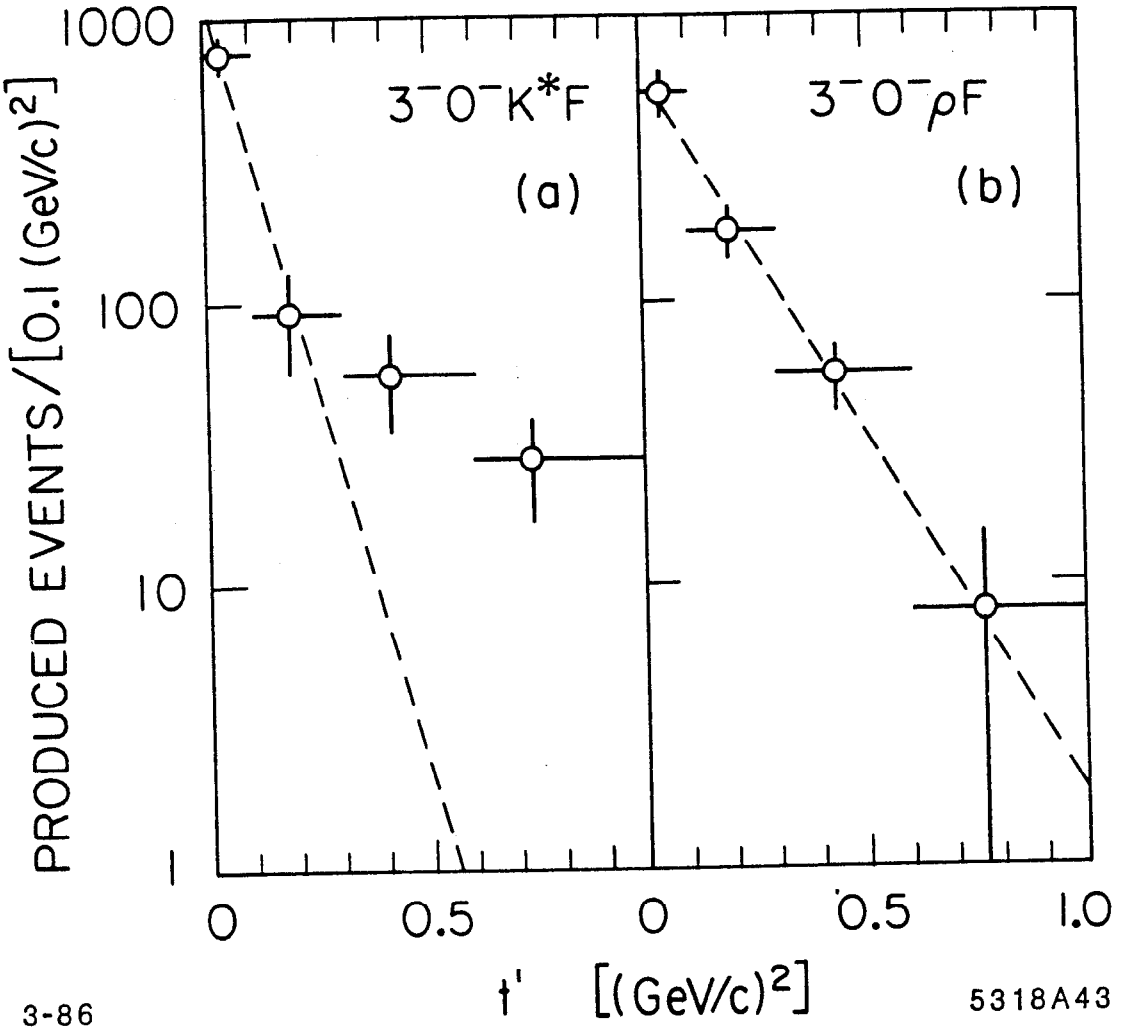

Figure 6.21. The t' dependences of the 3^- waves. The lines are the results of the fits described in the text.

Table 6.3. The parameters of the partial wave t' dependences. The partial wave intensities are modeled as $N_0 \exp(-b|t'|)$, which represents the number of events observed in the mass bin as a function of $|t'|$. The table lists the fitted values for N_0 and b.

	$1.37 \leq M_3 < 1.47$ GeV/c^2		$1.73 \leq M_3 < 1.85$ GeV/c^2	
Wave Name	N_0 Events/(0.1 (GeV/c)^2)	b (GeV/c)$^{-2}$	N_0 Events/(0.1 (GeV/c)^2)	b (GeV/c)$^{-2}$
$1^+0^+K^*S$	1001 ± 98	3.51 ± 0.26		
$1^-0^-K^*P$	1959 ± 151	3.19 ± 0.23	1884 ± 165	5.60 ± 0.44
$1^-0^-\rho P$			3358 ± 264	11.76 ± 0.95
$2^+0^-K^*D$	3543 ± 252	12.90 ± 1.15		
$2^+0^-\rho D$	655 ± 107	13.10 ± 2.60		
$3^-0^-K^*F$			1089 ± 201	12.60 ± 2.80
$3^-0^-\rho F$			624 ± 123	5.91 ± 0.88

The fitted normalizations and exponential slopes of these waves are presented in Table 6.3.

As is apparent from the distributions, both the $1^+0^+K^*S$ and the $1^-0^-K^*P$ have shallow t' slopes in the low mass region, while the 2^+ intensities show steep t' dependences. In the high mass region, the $1^-0^-\rho P$ and the $3^-0^-K^*F$ intensities also have large t' slopes, indicating that the production mechanisms for these amplitudes are similar to the mechanism producing the 2^+ amplitudes at lower mass. Such steep t' dependences are characteristic of π-exchange, which has successfully described $K\pi$ production data.[21,59] On the other hand, the shallow t' slopes of the $1^+0^+K^*S$ and $1^-0^-K^*P$ waves at low mass indicate that neither couples strongly to the $K\pi$ initial state. This coupling is forbidden by parity conservation for the $1^+0^+K^*S$ amplitude, but no such selection rule inhibits it for the $1^-0^-K^*P$ wave. Its lack of $K\pi$ coupling is probably due to the dynamics of the resonant state.

7. Spectroscopy

7.1 Resonance Parameters

7.1.1 Definitions and Methodology

The resonance contributions to the 1^-, 2^+, and 3^- partial waves can be extracted by performing simultaneous fits of Breit-Wigner lineshapes to the real and imaginary parts of the fitted partial wave amplitudes. The fits are performed by modeling the mass dependence of each amplitude by one or more resonant components, and in some cases a non-resonant background contribution.

The variables that parametrize each amplitude are estimated by fitting the predicted amplitude behavior to the measured partial wave intensities and relative phases. This fit minimizes a χ^2 function defined by the difference vector between the predicted and measured amplitudes and the error matrices of the PWA fit solutions in each mass bin. The full error matrix from **PWAOP** is employed so that the statistical correlations among the measured amplitudes are taken into account. For these χ^2 fits, an additional uncertainty corresponding to 30 events/(0.02 GeV/c^2) is added in quadrature to each partial wave amplitude error in an attempt to account for the other uncertainties of the PWA method. This additional error only affects the uncertainties for the smaller amplitudes as the statistical errors on the larger partial waves are typically of the order of 100 events/(0.02 GeV/c^2). None of the results presented below is sensitive to the magnitude of this additional error.

The program **MINUIT** is used to minimize the χ^2 function. In the results that follow, the quoted statistical errors are those determined by **MINUIT** and are based on the numerical evaluation of the second derivative of the χ^2 function at its minimum. In cases where an additional error is quoted, it is a systematic uncertainty that reflects the sensitivity of the result to various assumptions, such as the form of the background parametrizations.

The parametrization of the resonance lineshape is the one derived in §6.1.4. In cases where several coherent resonant amplitudes are fit simultaneously, the product of the production and decay phases of each resonance are also fit parameters. These phases are defined relative to the phase of one chosen resonance in the fit. The effect of phase space on the pure Breit-Wigner lineshape is explicitly taken into account

by the definition of the $A_{s\eta J}$. Such phase space effects are significant, and for a broad resonance can lead to a displacement of the resonant pole from the peak in the differential cross section by tens of MeV/c^2. When a branching fraction is quoted, it is defined as the ratio of the partial widths (to be consistent with the definition used by the Particle Data Group[73]). For most resonances, this differs from the ratio of total cross sections because of the difference in resonant lineshape for different decay modes (due primarily to the energy-dependence of the partial width). All differential and total cross sections will be quoted for the $|t'|$ bin 0.0–0.3 (GeV/c)^2, unless explicitly stated otherwise.

7.1.2 The Fit to the 1^+ $Q(1400)$

The $1^+0^+K^*S$ intensity shows a large bump around 1.4 GeV/c^2 that results from the production and decay of the axial-vector $Q(1400)$. The lack of a similar effect in the $1^+0^+\rho S$ intensity is consistent with this interpretation as the $Q(1400)$ is known to have a very small $K\rho$ coupling.[11]

The $1^+0^+K^*S$ intensity cannot be parametrized by a pure s wave Breit-Wigner as such a function cannot reproduce both the rapid fall-off of the cross section above 1.4 GeV/c^2 and the slight bulge in the intensity around 1.15 GeV/c^2. A background parametrization using a quadratic function with an arbitrary phase relative to the resonant lineshape gives a good representation of the $1^+0^+K^*S$ intensity for the mass region between 1.11 and 1.75 GeV/c^2. The 1.07 GeV/c^2 mass bin, which is strongly affected by phase space, was not used in the fit to determine the $Q(1400)$ parameters. Table 7.1 presents the results of the fit. The systematic errors reflect the sensitivity of the results to different background parametrizations. The differential cross section is quoted for the peak of the resonance, and has the effect of the $\bar{K}^0\,\pi^+\pi^-$ mass binning removed.

The lineshape predicted by the fit is shown in Fig. 7.1(a) and is an excellent description of the data. The values for the $Q(1400)$ mass and width are in good agreement with earlier observations of the Q in the diffractively produced three-body final states[17–19] and in $\bar{K}^0\,\pi^+\pi^-n$.[23]

Table 7.1. The 1^+ $Q(1400)$ parameters. The differential cross section is quoted at the peak of the resonance in events/(0.02 GeV/c^2), and is corrected for binning effects.

$Q(1400) \rightarrow 1^+0^+K^*S$	
Mass (GeV/c^2)	$1.373 \pm 0.014 \pm 0.018$
Width (GeV/c^2)	$0.188 \pm 0.054 \pm 0.060$
χ^2/DOF	7.4/7
$d\sigma/dM_3$	$545 \pm 48 \pm 18$

7.1.3 The Fits to the 2^+ Amplitude at Low Mass

The $2^+0^-K^*D$, $2^+1^+K^*D$, and $2^+0^-\rho D$ partial wave intensities show clear peaks around 1.44 GeV/c^2 that result from the production and decay of the tensor $K^*(1430)$. The evidence for resonant behavior in the $2^+0^-\rho D$ amplitude is somewhat equivocal; not only does the $2^+0^-\rho D$ intensity have more apparent background above the peak but its phase also moves backward relative to the phase of the $2^+0^-K^*D$ wave indicating that it may have a sizable non-resonant background contribution. These waves also show an enhancement around 2 GeV/c^2; this effect will be quantitatively discussed in a following subsection.

It is possible to fit the intensities and relative phases of these 2^+ waves to a d wave Breit-Wigner and a background amplitude, but the quality of the fit depends on the form of the background for the $2^+0^-\rho D$. To extract the $K^*(1430)$ resonance parameters in a relatively model-independent way, a fit to the $2^+0^-K^*D$, $2^+1^+K^*D$, and $2^+0^-\rho D$ differential cross sections was performed ignoring the relative phases of the two coherent $\eta-$ waves. The results of this fit are listed in Table 7.2 and the predicted lineshapes for the $2^+0^-K^*D$ and $2^+0^-\rho D$ waves are shown in Fig. 7.1(b). The quoted peak value for the $K^*\pi$ differential cross section is the sum of the $M = 0$ and $M = 1$ contributions. Because of the correlations among the fitted amplitudes, the uncertainty in the $K\rho/K^*\pi$ branching ratio is slightly less than the quoted errors on the differential cross sections would indicate. This value for the branching ratio is in good agreement with the averaged world data.[11]

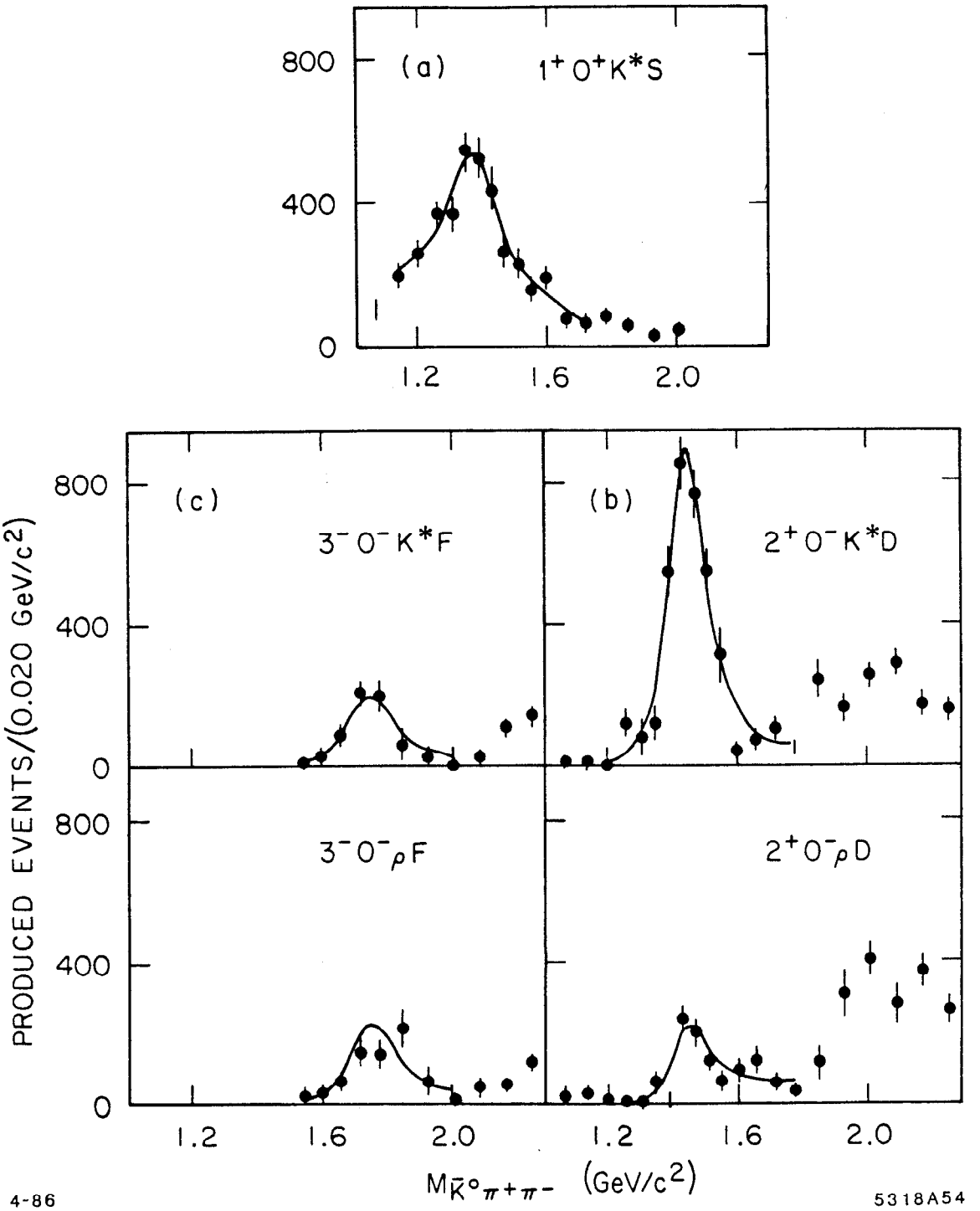

Figure 7.1. The fits to the 1^+, 2^+, and 3^- intensities. The fit of the $Q(1400)$ resonance to the $1^+0^+K^*S$ cross section is shown in (a), the fit of the $K^*(1430)$ resonance to the $2^+0^-K^*D$ and $2^+0^-\rho D$ cross sections is presented in (b), and the fit of the $K^*(1780)$ resonance to the $3^-0^-K^*F$ and $3^-0^-\rho F$ intensities is shown in (c).

Table 7.2. The 2^+ $K^*(1430)$ parameters. The differential cross sections are quoted at the peak of the resonance in events/(0.02 GeV/c^2), and are corrected for binning effects. The $K^*\pi$ differential cross section is the sum of the $M = 0$ and $M = 1$ contributions, and the $K\rho/K^*\pi$ branching ratio is corrected for isospin.

$K^*(1430) \rightarrow 2^+0^-K^*D$ / $2^+0^-\rho D$	
Mass (GeV/c^2)	$1.434 \pm 0.004 \pm 0.006$
Width (GeV/c^2)	$0.129 \pm 0.015 \pm 0.015$
χ^2/DOF	27.0/18
$d\sigma/dM_3(K^*\pi)$	$970 \pm 71 \pm 60$
$d\sigma/dM_3(K\rho)$	$213 \pm 29 \pm 15$
$BR(K\rho/K^*\pi)$	$0.293 \pm 0.032 \pm 0.020$

7.1.4 The Fits to the 3^- $K^*(1780)$

The bumps in the two 3^- partial wave cross sections around 1.75 GeV/c^2 are the expected signature of the f wave $K^*(1780)$. In fitting these amplitudes, a background contribution is hardly justified as they both show a "cleanly" produced resonant-like structure with little background at higher $\bar{K}^\circ\pi^+\pi^-$ masses. In addition, the $3^-0^-K^*F$ and $3^-0^-\rho F$ amplitudes are approximately in phase up to a mass of $\sim$ 2 GeV/c^2. Hence, the 3^- intensities and relative phases were fit to a common Breit-Wigner lineshape without a background amplitude, the relative phase offset of the two amplitudes being a fit parameter.

The results of the fit are listed in Table 7.3. Because the 3^- cross sections do not require a non-resonant component in their parametrizations, the systematic uncertainties of the differential cross sections are substantially reduced compared to the systematic uncertainties for the 2^+ $K^*(1430)$. On the other hand, the statistical errors are larger because of the smaller resonance signal. The lineshapes predicted by the fit, shown in Fig. 7.1(c), are in good agreement with the measured cross sections. The measured mass is substantially lower than the world average value of 1.780 ± 0.004 GeV/c^2, but the discrepancy is only a two standard deviation effect. The $K\rho(770)/K^*(892)\pi$ branching ratio is in mild disagreement with the 95% confidence level upper limit of 0.77 quoted in Ref. 22, but is in agreement

Table 7.3. The 3^- $K^*(1780)$ parameters. The differential cross sections are quoted at the peak of the resonance in events/(0.02 GeV/c^2), and are corrected for the effect of binning. The branching ratios are corrected for isospin, and for the $K^*(1430)$ $K\pi$ branching fraction.

$K^*(1780) \rightarrow 3^-0^-K^*F$ / $3^-0^-\rho F$ / $3^-0^-K^{**}D$	
Mass (GeV/c^2)	$1.740 \pm 0.014 \pm 0.015$
Width (GeV/c^2)	$0.171 \pm 0.042 \pm 0.020$
χ^2/DOF	16.6/17
$d\sigma/dM_3(K^*(892)\pi)$	$201 \pm 36 \pm 14$
$d\sigma/dM_3(K\rho)$	$229 \pm 53 \pm 15$
$d\sigma/dM_3(K^*(1430)\pi)$	36 ± 17
$BR(K\rho/K^*(892)\pi)$	$1.52 \pm 0.21 \pm 0.10$
$BR(K^*(1430)\pi/K^*(892)\pi)$	< 0.78 (95% CL)
$\phi(K\rho$ wrt $K^*\pi)$ (rad)	$3.26 \pm 0.10 \pm 0.05$

with most quark model predictions of approximately equal partial widths for the $K\rho$ and $K^*\pi$ decay modes. The fitted angle is the product of the production and decay amplitude phases for the $K^*(1780)$ $K\rho$ decay mode wave relative to the same product of phases for the $K^*\pi$ decay.

The 3^- $K^*(1430)\pi$ partial waves are not statistically significant and so were not included in the set of fitted partial waves. Therefore, to place an upper limit for the 3^- $K^*(1780)$ partial width into $K^*(1430)\pi$, the partial wave fits were repeated with the inclusion of the $3^-0^-K^{**}D$ wave. The measured $3^-0^-K^{**}D$ intensity in the region of the $K^*(1780)$ is then used to estimate the amount of 3^- $K^*(1430)\pi$ cross section that could be associated with the $K^*(1780)$. This value is quoted in Table 7.3, but since the $3^-0^-K^{**}D$ wave shows no significant structure this estimate should properly be used to place an upper limit on the $K^*(1780)$ partial width into the $K^*(1430)\pi$ final state. Such an upper limit is quoted in Table 7.3 for the $K^*(1430)\pi$ and $K^*(892)\pi$ branching ratio; in addition to the isospin correction, this branching ratio has also been corrected for the $K^*(1430)$ branching fraction into $K\pi$.[11]

7.1.5 *The Fits to the 1^- Amplitudes*

The behavior of the $1^-0^-K^*P$ and $1^-0^-\rho P$ cross sections and relative phases indicate that these amplitudes have at least two resonant parts, one at low mass contributing only to the $1^-0^-K^*P$ wave and the other at high mass contributing to both the $1^-0^-K^*P$ and $1^-0^-\rho P$ cross sections. A model with these ingredients provides a good description of the data.

To determine the resonance parameters in this model, the most efficient use of all the information (*i.e.* intensities and relative phases) is desirable. However, such an approach involves assuming a particular form for the parametrization of the other large waves, the $2^+0^-K^*D$ and the 3^- amplitudes, which introduces a certain amount of model-dependence into the 1^- interpretation. To show that this model-dependence is relatively weak, the 1^- amplitudes are fit to several models, with each subsequent fit introducing more model-dependence into the analysis.

The interpretation of the $1^-0^-\rho P$ amplitude is fairly straightforward as its cross section shows a clean resonant bump at a mass of ~ 1.75 GeV/c^2. The results of fitting this amplitude to a p wave Breit-Wigner are shown in Part I of Table 7.4. A similar fit to the $1^-0^-K^*P$ intensity, ignoring the other partial wave information, cannot be done in a model-independent way because of its complicated shape.

The next stage in this fitting process is to incorporate some relative phase information in the fit to the $1^-0^-\rho P$ amplitude. Because the 3^- amplitudes appear to be dominated by the $K^*(1780)$, the measured relative phases of the $1^-0^-\rho P$, the $3^-0^-K^*F$, and the $3^-0^-\rho F$ amplitudes can be used to further constrain the fit of the $1^-0^-\rho P$ wave to the resonance model. The behavior of the 3^- amplitudes are given by a Breit-Wigner defined by the $K^*(1780)$ parameters in Table 7.3, and the $1^-0^-\rho P$ amplitude is modeled by a p wave Breit-Wigner lineshape. The χ^2 fit to the measured $1^-0^-\rho P$ and 3^- amplitudes determines the p wave resonance parameters, as well as the two relative phase offsets between the three partial waves. The results of this fit are listed in Part II of Table 7.4. The fitted intensities and phases agree well with the measured amplitudes, as shown in Fig. 7.2.

The final level of sophistication is the introduction into the fit of the $1^-0^-K^*P$ and $2^+0^-K^*D$ amplitudes. The 2^+ wave, being dominated by the $K^*(1430)$, is

Table 7.4. The results of the 1^- fits. The parameters of the 1^- states determined by the three different fits are listed below. The low and high mass states are denoted as K_a^* and K_b^*, respectively.

I. Fit to the $1^-0^-\rho P$	
Mass_b (GeV/c^2)	$1.720 \pm 0.013 \pm 0.020$
Width_b (GeV/c^2)	$0.372 \pm 0.039 \pm 0.030$
$d\sigma/dM_3(K_b^* \to K\rho)$	$859 \pm 62 \pm 30$
χ^2/DOF	23.0/12
II. Fit to the $1^-0^-\rho P$, $3^-0^-K^*F$, and $3^-0^-\rho F$.	
Mass_b (GeV/c^2)	$1.717 \pm 0.011 \pm 0.020$
Width_b (GeV/c^2)	$0.376 \pm 0.033 \pm 0.010$
$d\sigma/dM_3(K_b^* \to K\rho)$	$852 \pm 51 \pm 30$
χ^2/DOF	42.0/38
$\phi(K^*(1780)\ K^*\pi$ wrt $K_b^*\ K\rho)$ (rad)	2.46 ± 0.33
$\phi(K^*(1780)\ K\rho$ wrt $K_b^*\ K\rho)$ (rad)	5.60 ± 0.36
III. Fit to the $2^+0^-K^*D$, the 1^-, and the 3^- waves.	
Mass_a (GeV/c^2)	$1.420 \pm 0.007 \pm 0.010$
Width_a (GeV/c^2)	$0.240 \pm 0.018 \pm 0.012$
$d\sigma/dM_3(K_a^* \to K^*\pi)$	$1991 \pm 133 \pm 150$
Mass_b (GeV/c^2)	$1.735 \pm 0.010 \pm 0.020$
Width_b (GeV/c^2)	$0.423 \pm 0.018 \pm 0.030$
$d\sigma/dM_3(K_b^* \to K^*\pi)$	$1146 \pm 76 \pm 170$
$d\sigma/dM_3(K_b^* \to K\rho)$	$813 \pm 42 \pm 30$
$BR(K_b^* \to K\rho/K_b^* \to K^*\pi)$	$0.97 \pm 0.09^{+0.30}_{-0.10}$
$\phi(K^*(1780)\ K^*\pi$ wrt $K_a^*\ K^*\pi)$ (rad)	$2.63 \pm 0.06 \pm 0.05$
$\phi(K^*(1780)\ K\rho$ wrt $K_a^*\ K^*\pi)$ (rad)	$5.77 \pm 0.12 \pm 0.05$
$\phi(K^*(1430)\ K^*\pi$ wrt $K_a^*\ K^*\pi)$ (rad)	$5.05 \pm 0.09 \pm 0.05$
$\phi(K_b^*\ K^*\pi$ wrt $K_a^*\ K^*\pi)$ (rad)	$3.99 \pm 0.03 \pm 0.05$
$\phi(K_b^*\ K\rho$ wrt $K_a^*\ K^*\pi)$ (rad)	$0.36 \pm 0.05 \pm 0.05$
χ^2/DOF	125/73

used to define the absolute phase behavior in the mass region below 1.6 GeV/c^2, while above that mass the absolute phase behavior is determined by the 3^- partial

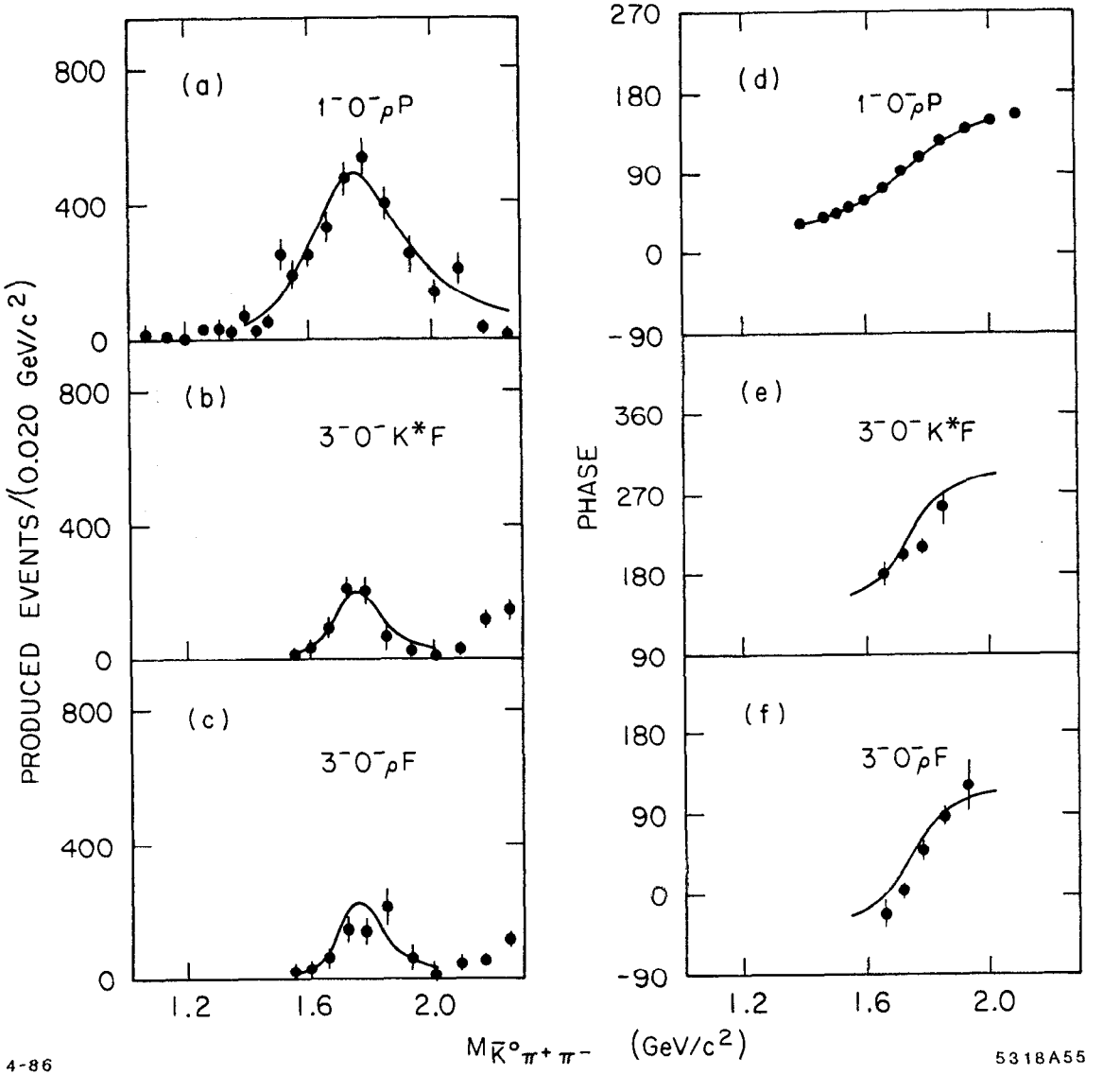

Figure 7.2. The fit to the $1^-0^-\rho P$ and the 3^- waves. The intensities and relative phases predicted by the fit to these three amplitudes are compared with the data. The relative phases have been set, bin-by-bin, by the resonant behavior of the $1^-0^-\rho P$ amplitude.

waves. The $1^-0^-K^*P$ amplitude is assumed to be dominated by a resonance in the region of 1.4 GeV/c^2, and at higher mass by the same resonance that describes the behavior of the $1^-0^-\rho P$ amplitude. A quadratic background is allowed to contribute coherently to the $1^-0^-K^*P$ amplitude, but this term is not necessary to achieve a reasonable fit.

The complete fit, which has 18 free parameters describing the 1^- amplitudes and the relative phases of the $2^+0^-K^*D$ and the 3^- waves, is used to estimate the masses, widths, and normalizations of the two 1^- resonances. The 2^+ $K^*(1430)$ and 3^- $K^*(1780)$ resonance parameters are fixed to those listed in Table 7.2 and Table 7.3, respectively. The results of the fit are listed in Part III of Table 7.4. The predicted and observed intensities and phases for the $2^+0^-K^*D$ and the 3^- waves are shown in Fig. 7.3 and the similar comparison for the two 1^- waves is shown in Fig. 7.4. This five-wave model is able to reproduce all of the features of the measured amplitudes quite well.

There are several features of the resulting model description. The $1^-0^-K^*P$ amplitude is understood as arising from the coherent sum of the two p wave resonances. The fit determines that the product of the higher mass p wave resonance's production and decay coupling phase is $\sim$ 220° forward of the same phase for the lower mass resonance. This implies that the leading edge of the broad, higher mass state interferes destructively with the lower mass resonance as the lower mass state advances through 90°. At higher mass, this interference continues to be destructive as the absolute phase of the lower mass state approaches 180° while the higher mass state resonates.

7.1.6 The Fits to the 4^+ Amplitudes

The summed 4^+ cross section shows a bump at $\sim$2.1 GeV/c^2, but the significance of this structure in the individual 4^+ partial waves is difficult to estimate. The observed enhancement is consistent with the production and decay of the g wave $K^*(2060)$ but it is not possible to unambiguously ascribe it to this state because the measured relative phases are too unreliable to determine if the amplitudes behave resonantly.

However, if one assumes that the bulk of the enhancement is due to $K^*(2060)$

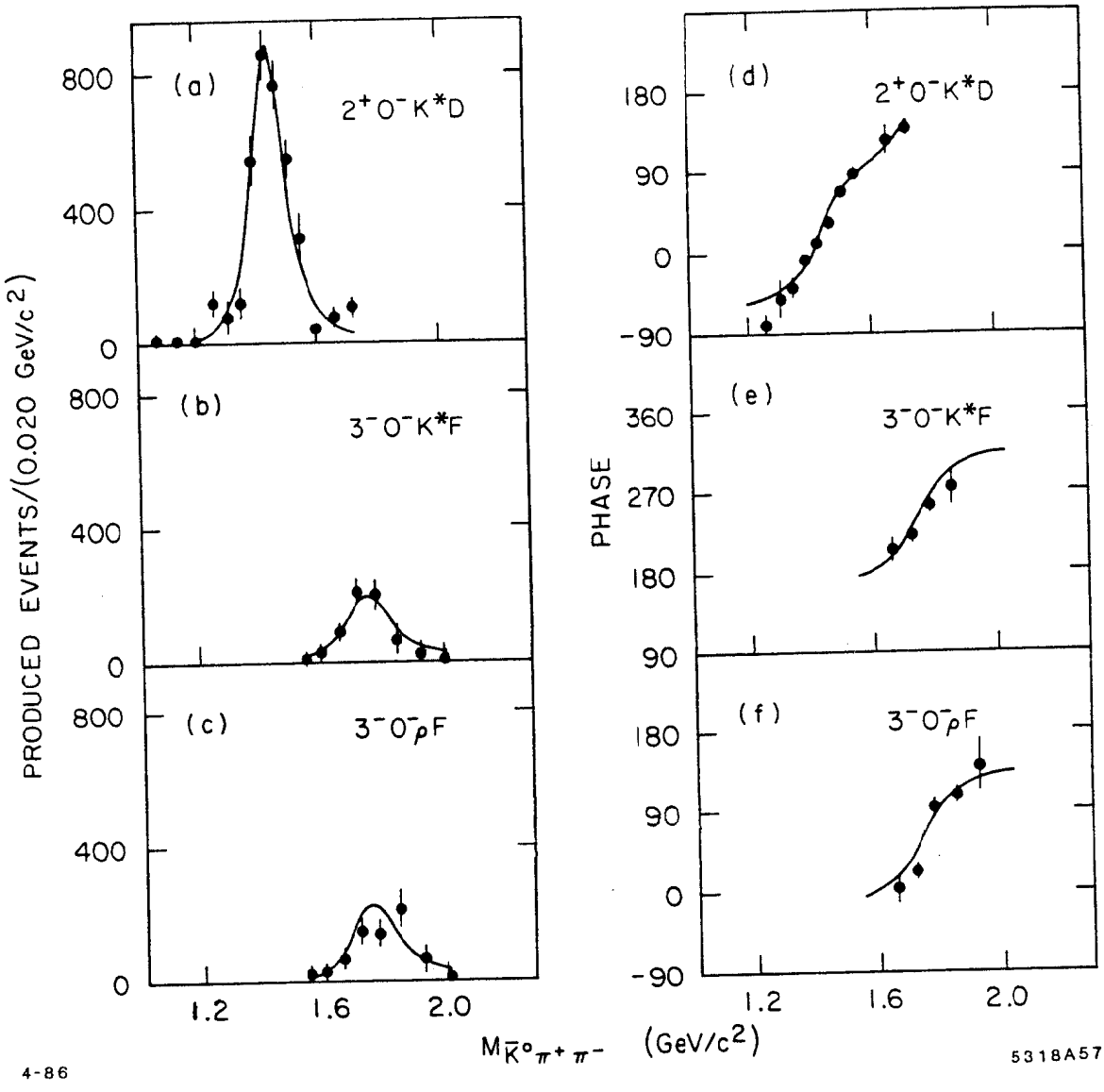

Figure 7.3. The five-wave fit predictions for the 2^+ and 3^- waves.The phases are set using the predicted behavior of the $1^-0^-K^*P$ reference wave.

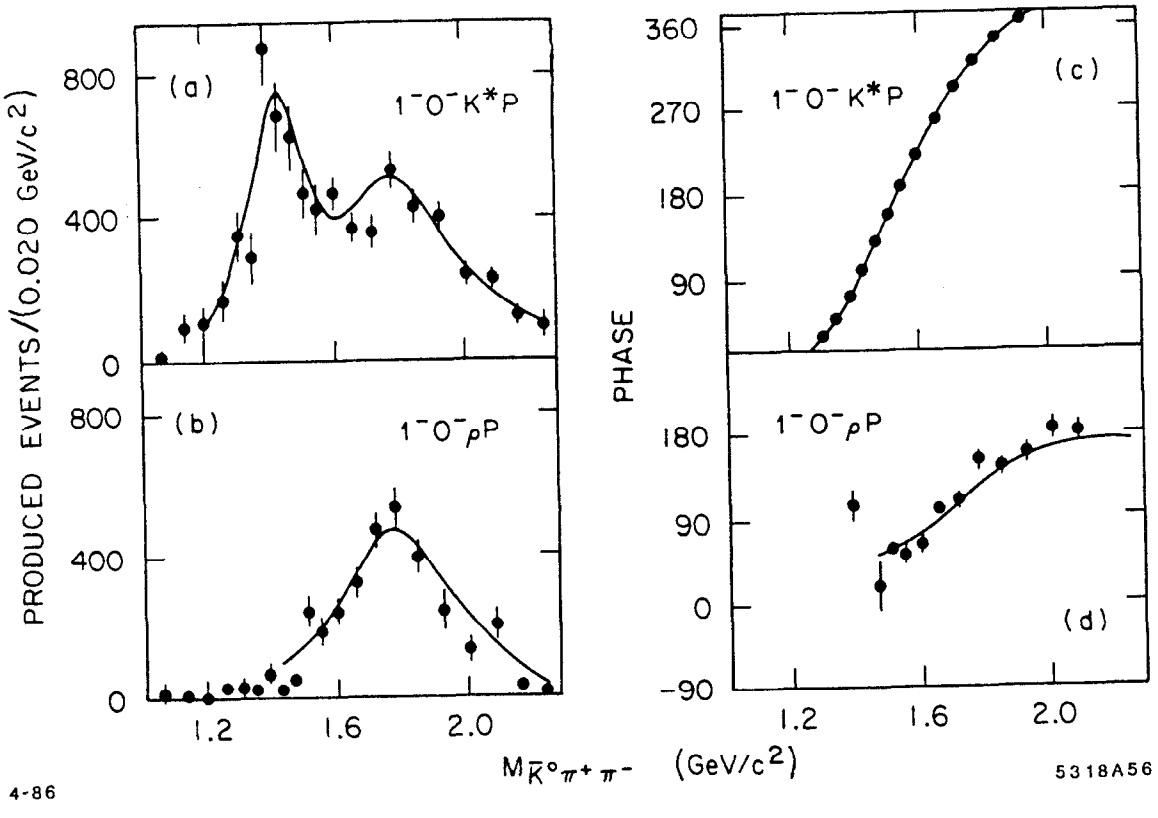

Figure 7.4. The five-wave fit predictions for the 1^- waves.The phases are set using the predicted behavior of the $1^-0^-K^*P$ reference wave.

Table 7.5. The results of the 4^+ fits. The values are obtained assuming that all of the 4^+ intensity results from $K^*(2060)$ production, and are expressed in units of events/(0.02 GeV/c^2). These values have not been corrected for isospin or for the branching fraction of the $K^*(1430)$ into $K\pi$.

Final State	$d\sigma/dM_3$ at Peak	
	Fitted Value	95% CL Upper Limit
$K^*(892)\pi$	$120 \pm 26 \pm 17$	≤ 173
$K\rho(770)$	$50 \pm 14 \pm 15$	≤ 137
$K^*(1430)\pi$	$42 \pm 14 \pm 15$	≤ 82

production and decay, it is then possible to estimate its branching fractions into the $K^*(892)\pi$, $K\rho(770)$, and $K^*(1430)\pi$ decay modes. The $4^+0^-K^*G$ intensity shows the clearest indication of a bump and so there is little systematic uncertainty involved in estimating its size. The $4^+0^-\rho G$ and the $4^+0^-K^{**}F$ partial waves, on the other hand, do not show an obvious resonant signal, which makes it difficult to determine the size of the resonant component. For this reason, upper limits are also quoted for the $K^*(2060)$ differential cross sections into these final states. The 4^+ partial wave intensities are fit to a common resonant lineshape assuming no background contribution to the amplitudes. The mass and width of the resonance are fixed at 2.060 and 0.200 GeV/c^2, respectively, these values being reasonable interpretations of the two published measurements of this state.[13,21] By assuming no background terms in the fit, conservative upper limits for the 4^+ $K\rho$ and $K^*(1430)\pi$ differential cross sections can be obtained from the fitted peak intensities and their uncertainties. (Allowing a background does not alter the fit result for the $4^+0^-K^*G$ peak intensity, but does reduce the size of the resonant contribution to the $4^+0^-\rho G$ and $4^+0^-K^{**}F$ intensities.) These fitted peak intensities and their corresponding 95% confidence level (95% CL) upper limits are given in Table 7.5.

7.1.7 The Fits to the 2^+ Amplitudes at High Mass

The $2^+0^-K^*D$ and the $2^+0^-\rho D$ intensities show a large enhancement at ~2.0 GeV/c^2, which may be evidence for a second resonant 2^+ state. To test this

Table 7.6. The fits to the high mass 2^+ amplitudes. The differential cross sections are quoted at the peak of the resonance in events/(0.02 GeV/c^2), and are corrected for mass binning effects. The $K\rho/K^*\pi$ branching ratio is corrected for isospin.

Fit to the High Mass $2^+0^-K^*D$ and $2^+0^-\rho D$ Amplitudes	
Mass (GeV/c^2)	$1.973 \pm 0.008 \pm 0.025$
Width (GeV/c^2)	$0.373 \pm 0.033 \pm 0.060$
χ^2/DOF	32.1/21
$d\sigma/dM_3(K^*\pi)$	$230 \pm 34 \pm 14$
$d\sigma/dM_3(K\rho)$	$448 \pm 36 \pm 15$
$BR(K\rho/K^*\pi)$	$1.49 \pm 0.24 \pm 0.09$
$\phi(K\rho$ wrt $K^*\pi)$ (rad)	$0.45 \pm 0.10 \pm 0.05$

hypothesis, the intensities and relative phases of these two waves are fit to a resonant lineshape. The absolute phase in this mass region is set by using the predicted phase behavior of the $1^-0^-K^*P$ reference wave from the parameters determined from the simultaneous fit to the $1^-0^-K^*P$, the $1^-0^-\rho P$, the $2^+0^-K^*D$, and the 3^- waves, described in §7.1.5.

It is not possible to achieve a good fit to the resonant model without allowing a significant background term above the fitted resonant lineshape. Therefore a coherent, linearly-rising background is introduced into the amplitude parametrization for both 2^+ waves. The fitted resonance parameters are insensitive to the detailed form of this background. The results of the fit are shown in Table 7.6. The predicted lineshapes are compared with the measured intensities and phases in Fig. 7.5. The agreement with the data is reasonable, although the measured intensities behave somewhat erratically. The measured absolute phases, which show $\sim 90°$ of forward motion, are well reproduced by the fit. These results confirm that a resonance interpretation of the 2^+ enhancement is consistent with the data.

However, a stronger conclusion is not warranted for several reasons. Firstly, although the intensities of the $2^+0^-K^*D$ and the $2^+0^-\rho D$ rise abruptly around 1.8–1.9 GeV/c^2, their persistence at above 2.1 GeV/c^2 raises questions about the uniqueness of the single resonance interpretation. In fact, the data cannot exclude

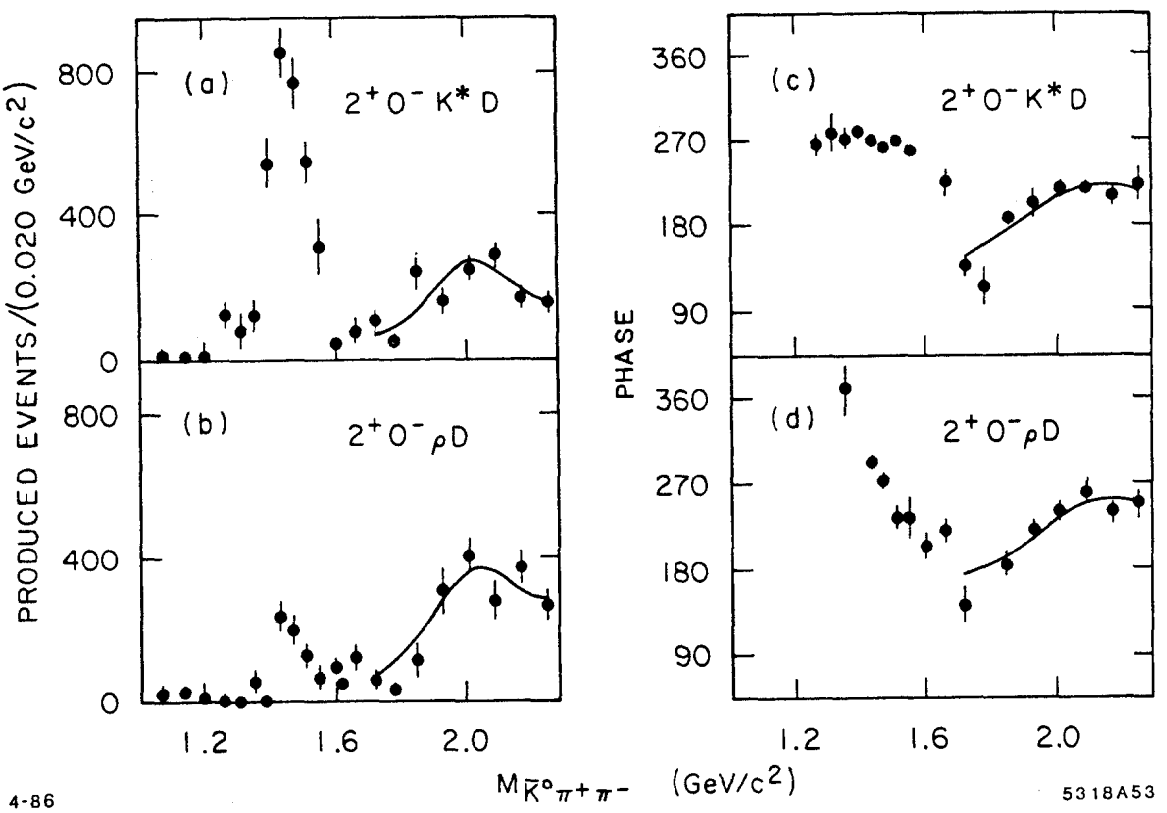

Figure 7.5. The fitted 2^+ lineshapes at high mass. The relative phases are set using the predicted behavior of the $1^-0^- K^*P$ reference wave above a mass of 1.69 GeV/c^2; below this mass, the phase of the reference wave is not set.

a two-resonance model with the second resonance being somewhat higher in mass. Secondly, the interpretation of the phase information is model-dependent because the absolute phase is set using the two-resonance model to the 1^- waves. (This is perhaps not a serious problem as the behavior of the 3^- waves constrains the absolute phase of the reference wave up to a mass of ~ 1.9 GeV/c^2.) Thirdly, the behavior of the $2^+0^-K^{**}P$ amplitude does not appear to be completely consistent with this interpretation; its intensity does not show a comparable enhancement around 2 GeV/c^2 in mass but its relative phase behavior mimics that of the other 2^+ waves. It is possible that the $2^+0^-K^{**}P$ might have a resonant component but the lack of structure in its intensity makes such an interpretation problematic.

7.2 Quark Model Assignments

7.2.1 The Well-Established States

The PWA has identified several states, some of which are well-established $q\bar{q}$ excitations. The tensor $K^*(1430)$ is the 1^3P_2 member of the $L = 1$ orbital excitation. The axial-vector $Q(1400)$ is understood to be almost equal mixtures of the two lowest-lying 1^+ strange mesons, the 1^1P_1 and the 1^3P_1. (Since the strange mesons are not charge-conjugate eigenstates, such mixing between the singlet and triplet states is allowed.) The unseen member of the $L = 1$ multiplet, the 0^+ $\kappa(1350)$, cannot decay to $\bar{K}^\circ\,\pi^+\pi^-$ because of parity conservation.

The next leading natural spin-parity state, the 3^- $K^*(1780)$, is the obvious candidate for the 3^- resonance structure in the $K^*(892)\pi$ and $K\rho$ final states. Although the observed mass of this resonance is about 0.04 GeV/c^2 below the world average of $\sim$1.780 GeV/c^2, the disagreement is only a two standard deviation effect. This state is a member of the $L = 2$ multiplet, namely the 1^3D_3.

The PWA shows evidence for the production and decay of the 4^+ $K^*(2060)$, although the resonance interpretation is ambiguous. This resonance is the leading member of the $L = 3$ multiplet, the 1^3F_4, which has been observed only in the $K\pi$ final state.

7.2.2 The Interpretation of the 1^- States

The behavior of the two 1^- partial waves is well understood by a model that

incorporates a resonant state with a mass and width of 1.42 and 0.23 GeV/c^2, respectively, coupling only to the $K^*(892)\pi$ decay mode, and a second state with a mass and width of 1.73 and 0.43 GeV/c^2, respectively, that couples to both the $K\rho$ and $K^*\pi$ final states. This confirms the essential results of the most recent $\bar{K}^\circ\pi^+\pi^-$ PWA[22] where these two states were observed and called the $K^*(1410)$ and the $K^*(1790)$. The higher mass state is now measured to be significantly lower in mass and broader than in Ref. 22, but the observed behavior of the amplitudes in the two analyses is consistent. It appears that the disagreement in mass and width results from the explicit parametrization of the data. If the measured 1^- waves are fit using the parametrization employed in Ref. 22, the fitted mass increases by ~0.05 GeV/c^2 and the width decreases by ~0.05 GeV/c^2. This difference in parametrization arises from the failure of the authors in Ref. 22 to include the effect of three-body phase space on the resonance lineshape; the increasing phase space as a function of three-body mass implies that the observed resonance peak in the differential cross section will be shifted up in mass by an amount that depends on the width of the structure. For a resonance with a width of 0.4 GeV/c^2, this mass shift turns out to be ~0.04 GeV/c^2.

In the quark model, these two vectors states may be:

1. the 2^3S_1 state, which is the first radial excitation of the $K^*(892)$;
2. the 1^3D_1 level, which is the member of the $L = 2$ multiplet containing the 3^- $K^*(1780)$; and
3. the 3^3S_1, which is the second radial excitation of the $K^*(892)$.

The other candidate $q\bar{q}$ 1^- states are higher radial excitations of these three and can be ruled out because their expected masses are too high. It is conceivable that the observed resonances could be mixtures of these three candidate states* and this possibility cannot *a priori* be excluded. However, I will argue below that the lower

---

* Such mixing of pure $q\bar{q}$ states to yield the physically observed states is not without precedent in meson spectroscopy: in the strange meson sector, the two axial vector states, the $Q(1280)$ and the $Q(1400)$, are believed to be combinations of the 1^1P_1 and the 1^3P_1 quark model states; and in the charmonium sector, the 2^3S_1 and the 1^3D_1 states mix weakly to give the observed $\Psi(3685)$ and the $\Psi(3770)$.

mass state is predominantly 2^3S_1 while the upper state must be mostly 1^3D_1.

The proximity in mass of the $K^*(1790)$ and the 3^- $K^*(1780)$ makes the association of the high mass state with the 1^3D_1 quite attractive. Besides this small splitting, the total and partial widths of the high mass 1^- state agree fairly well with those predicted by various quark model calculations. In contrast, the mass of the $K^*(1410)$ is so far below the mass of the 3^- $K^*(1780)$ that its assignment as the triplet partner to the 3^- can be safely ruled out. This means that the $K^*(1410)$ can be simply understood only as the radial excitation of the $K^*(892)$; this then raises the possibility that the 1^- $K^*(1790)$ is the second radial excitation of the $K^*(892)$, or some mixture of this state and the 1^3D_1 state.

Most theoretical predictions for the mass of the radial excitation of the $K^*(892)$ place it around 1.5-1.7 GeV/c^2, in disagreement with the assignment of the $K^*(1410)$. However, the observed decay properties of this resonance tend to support its interpretation as a radial excitation. Several quark model calculations [74–76] have indicated that the decay of a radial excitation of a $^3S_1$ state into a two-body final state with a large center-of-mass (CMS) kinetic energy is suppressed relative to decay modes with smaller values of CMS momentum; this suppression arises from the radial node(s) in the wave function of a radially excited state. Although these calculations are model-dependent because of the way relativistic effects are incorporated, the prediction of a weak two-body coupling for the radially excited vector states is a persistent result. This prediction has the following consequences: in the strange sector, the radial excitations should prefer to couple to $K^*\pi$ or $K\rho$ and not to $K\pi$; the radially excited isovectors should not couple strongly to the $\pi\pi$ decay mode; and the charmonium radial excitations should decay strongly into states such as $D^*\bar{D}$ and $D^*\bar{D}^*$ and not into $D\bar{D}$.

There are a number of experimental observations that support this predicted decay systematic. In the charmonium sector, the $\Psi(4030)$ (the 3^3S_1 $c\bar{c}$ state) prefers to decay via $D^*\bar{D}^*$ instead of $D\bar{D}$ although the former is very close to threshold. The situation with the isovectors is still quite confused, but a consistent interpretation of the data is possible that not only agrees with the model predictions but also explains several mysteries. The two candidates for the first radial excitation of the

$\rho(770)$ are the $\rho(1250)$ and the $\rho(1600)$. The $\rho(1250)$ has only been seen in the $\omega\pi$ decay mode with little evidence of it in $\pi\pi$ final states. If we assume that it is a real 1^- state, then it can be understood only as the first radial excitation of the $\rho(770)$ on the basis of the arguments used above in the case of the $K^*(1410)$. Its lack of coupling to $\pi\pi$ would then be a reflection of its radial nature. This interpretation of the $\rho(1250)$ fits in nicely with the assignment for the $K^*(1410)$, as the mass splittings of the two states is that expected of the strange and isovector states of the same nonet. This also implies that the $\rho(1600)$ is probably the 1^3D_1 partner for the 3^- $g(1690)$. However, it should be noted that the status of the $\rho(1250)$ is quite poor; the most recent photoproduction experiment analyzing the $\omega\pi$ channel could not unambiguously confirm or disprove its existence.[77]

In summary, the interpretation of the $K^*(1410)$ as the 2^3S_1 state is preferred. Its assignment as the 1^3D_1 is not tenable as this implies a large $L = 2$ multiplet mass splittings. The higher mass 1^- state is interpreted as the 1^3D_1 although it could conceivably correspond to a superposition of the 1^3D_1 and the 3^3S_1 states, or indeed to the 3^3S_1 state alone.

7.2.3 The Higher Mass 2^+ State

The second resonance-like enhancement in the 2^+ amplitudes at $\sim$1.97 GeV/c^2 has two possible quark model interpretations: (a) it is the 2^3P_2, *i.e.* the radial recurrence of the $K^*(1430)$; or (b) it is the 1^3F_2, the partner to the 4^+ $K^*(2060)$. Several comments can be made concerning the possible assignments:

1. The mass of the 2^3P_2 state predicted by Godfrey and Isgur[10] is $\sim$1.94 GeV/c^2, which is in good agreement with the estimated mass of the resonance. In contrast, the 1^3F_2 state is expected to be nearly degenerate with the $K^*(2060)$ as the multiplet splittings are expected to (and do!) decrease with increasing orbital excitation. However, because the theoretical uncertainty of these mass splittings is quite large, the orbital assignment cannot be ruled out.
2. Since a comparable signal appears to be absent in the d wave in the $K^-\pi^+n$ analysis,[21] this resonance may have a small $K\pi$ coupling, an expected property of a radial excitation.

3. A candidate for the 2^3P_0 state has been observed in the $K\pi$ data at a mass of $\sim$1.9 GeV/c^2. The association of the 2^+ state with this resonance is implied from the small mass splittings between these two states.

Although each of the above points favor the radial interpretation, all three arguments are weak and so a definite assignment is not possible; it is conceivable that both of the expected 2^+ states are being observed, which may account for the "flat-top" appearance of the 2^+ partial wave intensities above 2.0 GeV/c^2.

7.3 The Branching Fractions

It is possible to determine the $K^*(892)\pi/K\pi$ and $K\rho(770)/K\pi$ branching fractions for the natural spin-parity states using the above results and the data from analyses of the $K\pi n$ channel, since in these two channels the production cross sections are equal. The $K^-\pi^+$ data are obtained from the PWA described in Ref. 21 as these are the most accurate measurements of the two-body differential cross sections currently available.* In addition, their precise meaning (*e.g.* their systematic uncertainties) are well-understood as they come from the previous experiment (E-132) with the LASS spectrometer.

The Particle Data Group defines the branching fraction of a resonance in a production experiment as the ratio of the differential cross sections for the two final states at the peak of the resonance.[73] These peak values are determined from the resonance fits to the differential cross sections, which remove any background contributions and binning effects. The sensitivities of the two analyses are used to convert these peak values from produced events to microbarns. These values are then corrected for isospin: $\frac{2}{3}$ of the $K\pi$ final state is seen in the $K^-\pi^+$ charge mode; $\frac{4}{9}$ of the $K\pi\pi$ final state appears in the $\bar{K}^\circ\pi^+\pi^-$ mode; and $\frac{1}{3}$ of the $K\rho$ appears in the $\bar{K}^\circ\pi^+\pi^-$ final state. In addition, the $\bar{K}^\circ\pi^+\pi^-$ differential cross sections are corrected for the K°_S visibility, which is a factor of $2/0.686 = 2.916$ coming from the K°_S-K°_L ratio and the $K^\circ_S \to \pi^+\pi^-$ branching fraction.

* The E-135 $K^-\pi^+n$ event sample has the potential for significantly improving our knowledge of $K\pi$ scattering and so this would be the obvious source of data for these branching fraction calculations. A PWA of the E-135 $K^-\pi^+n$ data is underway, but these results are not yet available.

The partial waves have different meanings in the $K^-\pi^+$ and $\bar{K}^\circ\pi^+\pi^-$ analyses: The $K^-\pi^+$ partial wave amplitudes are determined at the π exchange-pole using a production model to extrapolate them from the physical region, whereas the $\bar{K}^\circ\pi^+\pi^-$ amplitudes are determined in the physical t' region. Therefore, in order to compare the two-body and three-body partial widths, the $K^-\pi^+$ partial wave amplitudes are determined in the physical region by extrapolating them back from the π-pole into the physical region and integrating them over the same t' bin as used in the $\bar{K}^\circ\pi^+\pi^-n$ analysis (*i.e.* the interval $|t'| \leq 0.3$ (GeV/c)^2).

The calculated differential cross sections of the resonances observed in this analysis are compiled in Table 7.7. The branching fractions determined from these data are listed in Table 7.8.

The branching fractions for the 2^+ $K^*(1430)$ are significantly smaller than the world average of 0.517 ± 0.056 for $BR(K^*(892)\pi/K\pi)$ and 0.11 ± 0.05 for $BR(K\rho(770)/K\pi)$.[11] However, there is considerable systematic uncertainty on these world averages due to the methods use to determine these quantities. All of the measurements contributing to the PDG average have come from analyses of small data samples where a partial wave decomposition has not been possible. Because of the large 1^- component in the peak of the $\bar{K}^\circ\pi^+\pi^-$ invariant mass distribution in the 1.44 GeV/c^2 region, the amount of $K^*(1430)$ decaying to $\bar{K}^\circ\pi^+\pi^-$ has been systematically over-estimated. To correct for this effect, the previous measurements would have to be reduced by approximately a factor of two, which would bring them into good agreement with the value quoted in Table 7.8.

The branching fractions for the 3^- $K^*(1780)$ are in modest agreement with the only other measurements[22]; the measured amount of $K^*(1780)$ decaying to $\bar{K}^\circ\pi^+\pi^-$ is in good agreement with the values quoted in Ref. 22 but the $BR(K^*\pi/K\rho)$ branching fraction differs significantly (very little $K\rho$ cross section was observed in the earlier experiment). The 1^- $K^*(1790)$ branching ratios are the first reported measurements of these quantities, as are those for the 4^+ $K^*(2060)$.

These branching fractions must be considered preliminary since the use of two different experiments to measure the two-body and three-body decay modes of these states introduces large systematic errors from the uncertainty in the sensitivities of the data samples. Also, the PWA of the $K^-\pi^+n$ event sample

Table 7.7. The $K\pi$ and $K\pi\pi$ differential cross sections. The table lists the differential cross sections determined at the peak of the resonances observed in the $K^-\pi^+$ final state[21] and in this analysis. These values are for the interval $t' \leq 0.3$ $(\mathrm{GeV/c})^2$, and have been corrected for mass binning effects, isospin, and K^0_S visibility. The $K^*(1430)$ $K\pi$ branching fraction[11] is included in the differential cross sections for the $K^*(1430)\pi$ final state.

Final State	$d\sigma/dM_3$ at Resonance μb/(0.02 GeV/c^2)
2^+ $K^*(1430)$	
$K\pi$	4.84 ± 0.68
$K^*(892)\pi$	1.58 ± 0.24
$K\rho(770)$	0.46 ± 0.08
3^- $K^*(1780)$	
$K\pi$	0.71 ± 0.12
$K^*(892)\pi$	0.32 ± 0.07
$K\rho(770)$	0.49 ± 0.13
1^- $K^*(1790)$	
$K\pi$	1.72 ± 0.41
$K^*(892)\pi$	1.87 ± 0.36
$K\rho(770)$	1.77 ± 0.21
4^+ $K^*(2060)$	
$K\pi$	0.173 ± 0.054
$K^*(892)\pi$	0.196 ± 0.051
$K\rho(770)$	0.261 ± 0.052
$K^*(1430)\pi$	0.155 ± 0.062

from E-135 is currently in progress. This should provide statistically more accurate $K\pi$ cross sections, and perhaps more importantly, should avoid the systematic uncertainty associated with the relative normalization as the data derive from the same experiment.

7.4 Hyperfine and Multiplet Splittings

With the $q\bar{q}$ assignments argued above for the two 1^- resonances and the higher 2^+ candidate state, we can now begin to look at the details of the hyperfine interactions that split the masses of the triplet and singlet states with the same

Table 7.8. The branching fractions for the resonant states. These branching fractions are derived from the data in table 1. These values are for the interval $t' \leq 0.3$ (GeV/c)^2, and have been corrected for mass binning effects, isospin, and K^0_S visibility.

2^+ $K^*(1430)$	
$BR(K^*(892)\pi/K\pi)$	0.33 ± 0.07
$BR(K\rho(770)/K\pi)$	0.09 ± 0.02
3^- $K^*(1780)$	
$BR(K^*(892)\pi/K\pi)$	0.46 ± 0.12
$BR(K\rho(770)/K\pi)$	0.69 ± 0.22
1^- $K^*(1790)$	
$BR(K^*(892)\pi/K\pi)$	1.09 ± 0.33
$BR(K\rho(770)/K\pi)$	1.03 ± 0.28
4^+ $K^*(2060)$	
$BR(K^*(892)\pi/K\pi)$	1.13 ± 0.46
$BR(K\rho(770)/K\pi)$	1.51 ± 0.56
$BR(K^*(1430)\pi/K\pi)$	0.90 ± 0.45

orbital angular momentum L, and the behavior of the multiplet mass splittings that occur between the triplet of states of the same L but different total spin J. In particular, we can see how these splittings change as the states are radially excited.

The classic examples of hyperfine splitting are the 1^1S_0 $K(494)$ and the 1^3S_1 $K^*(892)$ in the strange sector, and the π and $\rho(770)$ among the isovectors. There have been recent attempts [78,79] to understand the systematic behavior of these $L = 0$ hyperfine splittings, which have shown that with fairly weak assumptions the hyperfine splittings are approximately flavor-independent. Since the measured mass of the $K^*(1410)$ makes it approximately degenerate with the 0^- $K(1450)$, which can be only the 2^1S_0, the hyperfine splitting for the first radially excited $L = 0$ state is either small or inverted.* If the flavor-independence of the hyperfine splittings extends to the radial excitations, then this has interesting consequences

* The apparent inversion of the hyperfine splitting is somewhat troublesome as the pure $q\bar{q}$ states are not expected to demonstrate such behavior. This may be an indication that the $K^*(1410)$ is not a pure radial excitation, but has been shifted

for the spectroscopy in the other meson sectors. For example, the $\Psi(3685)$ and its singlet partner (the $\eta_c{}'$) should be very close in mass. This disagrees with the unconfirmed observation of a $c\bar{c}$ state[80] at a mass of 3.594 GeV/c^2 that has been interpreted as the η_c'.

The multiplet splitting between light-quark triplet states has recently been examined by Schnitzer[81] and Godfrey,[82] who have derived "model-independent" predictions for the systematic behavior of the multiplet splittings as a function of flavor and L. In these models, the magnitude and sign of the multiplet splittings arise from the behavior of the potential as a function of the inter-quark separation r. One interesting prediction arising from this work has been that beyond a certain average size of the $q\bar{q}$ system, the multiplet splittings will invert if the confining long-range part of the potential transforms as a Lorentz scalar whereas the multiplet ordering will remain unchanged if the long-range part transforms as a Lorentz vector. With the observation of the $K^*(1790)$ at a mass of 1.735 GeV/c^2 and its identification as the 1^3D_1 state, it would appear that this inversion has not taken place in the $L = 2$ multiplet. Unfortunately, the uncertainty on the mass of the $K^*(1790)$ is large enough that the possibility of the multiplet being inverted cannot be ruled out.

7.5 Production Mechanisms

The production angular distributions of the partial wave amplitudes reflect on the underlying processes that produce the resonant states. In the language of an exchange model, these distributions can be related directly to the scattering of the incoming K^- and a virtual meson in the particle-antiparticle sea surrounding the target proton.

In a study of the reaction $K^-p \rightarrow K^-\pi^+n$, it has been shown[20] that this process can be understood as resulting from mostly π exchange with some additional $\rho - A_2$ exchange and "absorptive corrections." Because of the proximity of the π pole to the physical t region, the resulting t' distribution is steep. In this sense, the $K^-\pi^+$ final state can be viewed as arising mainly from off-mass-shell $K\pi$ elastic scattering. Since most of the $M = 0$ natural spin-parity states

down in mass by mixing with perhaps the 1^3D_1.

observed in the $\bar{K}^\circ\pi^+\pi^-$ final state exhibit steep t' dependences, it follows that the observed $K^*(892)\pi$ and $K\rho(770)$ systems are the result of off-mass-shell $K\pi$ inelastic scattering. Hence, those natural spin-parity states observed in both the two-body and three-body channels are related by the elastic and inelastic couplings of these resonances to the $K\pi$ initial state.

On the other hand, both the $Q(1400)$ and the $K^*(1410)$ are seen in the $\bar{K}^\circ\pi^+\pi^-$ system but not in the $K^-\pi^+$ final state. This implies that they cannot be produced via π exchange in a K beam, which has visible consequences to their production angular distributions. In fact, both of these states have the characteristics expected of a state produced via a non-π-exchange production mechanism as the t' dependences of the corresponding partial wave amplitudes are shallow. The $Q(1400)$, being an axial-vector, cannot decay into $K\pi$ because of parity and angular momentum conservation, whereas the lack of $K\pi$ coupling for the $K^*(1410)$ is understood as arising from the internal dynamics of the $q\bar{q}$ system. In the case of the $Q(1400)$, which is seen only in $\eta+$ waves, its production may proceed via $\rho-A_2$ exchange. Since the $K^*(1410)$ is observed only in an $\eta-$ wave, one possible production mode is through the exchange of an axial-vector such as the $B(1235)$ or the $A_1(1270)$. Regge phenomenology predicts that the production phases of two states, one produced via π exchange and the other via B exchange differ by $\sim 90^\circ$ because of the opposite signatures of the two corresponding trajectories.[83,84] This prediction is in good agreement with the observed production phases: the phase of the $2^+0^-K^*D$ wave measured relative to the phase of the $1^-0^-K^*P$ differs by $\sim 90^\circ$ in the mass region where the 2^+ wave is dominated by the $K^*(1430)$ and the 1^- is almost entirely $K^*(1410)$. To the extent that Regge models have been shown able to describe certain aspects of the phenomenology of high energy scattering, this offset in production phase strengthens the interpretation of the partial wave t' dependences.

One final comment concerning the production of the $\bar{K}^\circ\pi^+\pi^-n$ final state should be made. The empirical observation that the unnatural spin-parity states are preferentially produced in the three-body diffractive reaction while the natural spin-parity resonances tend to appear in the charge-exchange process is underscored by the observation of four natural spin-parity resonances and only one unnatural

spin-parity state in the $\bar{K}^\circ \pi^+\pi^- n$ channel. In Regge language, this asymmetry arises partly from a large Pomeron component in diffractive production that is completely absent in the charge-exchange process. However, even the cross sections due to meson exchange processes are different; in the $K^-\pi^+\pi^- p$ channel a large part of the cross section comes from $M \neq 0$ partial waves, whereas in the $\bar{K}^\circ \pi^+\pi^- n$ case most of the production is via $M = 0$ amplitudes. Hence, the diffractive and charge-exchange reactions are fundamentally different. The meson production in the two processes is almost totally complementary, and so both types of reactions must be studied in order to obtain a more complete understanding of meson spectroscopy.

8. Conclusions

The partial wave analysis of the $\bar{K}^\circ \pi^+\pi^-$ system has uncovered the richness and diversity of the physics processes responsible for its production. The event distribution is well described by the isobar model, and the partial wave analysis successfully decomposes the system into the quantum amplitudes governing its production. Over two-thirds of the entire cross section is due to the production of K^* states that decay via an intermediate isobar state; approximately three-quarters of this resonance production occurs via natural spin-parity states ($J^P = 1^-$, 2^+, 3^-, and 4^+).

The resonant contributions to the individual partial waves are readily identified because of the absence of large non-resonant backgrounds in the partial wave amplitudes. The $1^+0^+K^*S$ amplitude shows a clear $Q(1400)$ structure; the lack of a corresponding effect in the $1^+0^+\rho S$ amplitude corroborates this identification as the $Q(1400)$ is known to have a small $K\rho$ coupling. The 2^+ $K^*(1430)$, a triplet partner to the $Q(1400)$, appears as a large enhancement in the $2^+0^-K^*D$ and $2^+0^-\rho D$ cross section around 1.44 GeV/c^2. Its measured mass, width, and branching ratio into $K\rho$ and $K^*\pi$ confirms the previously measured properties of this state.

A second enhancement in the 2^+ cross section is observed at $\sim$2 GeV/c^2 that decays via both $K\rho(770)$ and $K^*(892)\pi$ intermediate states. The measured relative phases of these waves are consistent with a resonance interpretation, and a fit to both decay modes gives a mass and width of 1.97 and 0.37 GeV/c^2, respectively. Two strange $q\bar{q}$ excitations are expected in this mass region: the radial recurrence of the 1^3P_2 $K^*(1430)$ and the partner to the 1^3G_4 $K^*(2060)$.

The 3^- $K^*(1780)$ resonance, one of the $L = 2$ triplet states, is seen decaying into both $K^*\pi$ and $K\rho$ with approximately equal strengths. Its 2^- partner is not seen, and this is consistent with the empirical observation that the unnatural spin-parity states are not copiously produced in a charge-exchange channel such as $\bar{K}^\circ \pi^+\pi^- n$.

The 1^- partial waves show resonant structure at a mass of 1.73 GeV/c^2, which is identified as resulting from the production and decay of the 1^- member of the $L = 2$ multiplet. A second 1^- resonant state is observed at a mass of $\sim$1.42

GeV/c^2 decaying only to $K^*(892)\pi$. The production angular distribution of this state indicates that it does not couple strongly to $K\pi$, which is consistent with the failure to observe this state in analyses of the $K\pi$ system in the $K\pi n$ channel.[20,21] The properties of this state are consistent with its assignment as the first radial excitation of the 1^- $K^*(892)$. These data confirm the results of a prior analysis of the $\bar{K}^\circ \pi^+\pi^- n$ final state,[22] where these two states were observed and called the $K^*(1790)$ and the $K^*(1410)$. A lower mass and larger width for the $K^*(1790)$ is inferred from this current experiment, although the partial wave data appear to be consistent with those of Ref. 22.

The 4^+ partial waves indicate an enhancement around 2.1 GeV/c^2. Although it is not possible to show that it is a resonant structure, the interpretation that it results from the production and decay of the 4^+ $K^*(2060)$ is consistent with the data.

Appendix A. The Geometry and Kinematic Fitting Program MVFIT

A.1 OVERVIEW

MVFIT is a multi-vertex fitting program that fits a set of tracks to a particular topology hypothesis. In the fit all tracks are constrained to come from common primary or decay vertices, and 3-momentum conservation is enforced at each V° or V^- decay vertex. In addition, MVFIT has the ability to impose energy constraints at any of the decay vertices (i.e. V° or V^- mass constraints), and to impose 4-momentum conservation at the primary vertex for 1-C (missing particle) and 4-C hypotheses.

A unique feature of **MVFIT** is that the fitted data consist of the coordinates on each track and any momenta measured in the dipole spectrometer, instead of a set of track vectors as is common in other kinematic fitting programs. This additional sophistication allows the fit to make maximal use of the measured information in the event.

The variables used to describe an event are:

1. X_p, Y_p, Z_p describing the position of the primary vertex;
2. $\alpha, \beta, 1/p$ for every charged helix track, the beam track, any missing neutral tracks (for 1-C hypotheses), and any V^- tracks. (α is the polar angle of each track, β is the azimuthal angle of the track's momentum vector at its parent vertex, and $1/p \equiv cB_z/p$ where p is the track's signed momentum, c is the speed of light, and B_z is the magnetic field in the solenoid.);
3. X_v, Y_v, Z_v for each V° decay vertex; and
4. S^{casc}, the path length of a V^- track (applicable for V^- topologies only).

This parametrization ensures that tracks from the same vertex share a common point. For a V^- topology, the parameters of the V^- track, the V^- decay length S^{casc}, and the primary vertex position define the location of the V^- decay vertex. This automatically ensures that the fitted V^- decay vertex is consistent with the V^- track parameters and the primary vertex position.

Conservation of 3-momentum at a decay vertex is enforced by introducing into the fit a number of constraint equations through the method of Lagrange Multipliers. To this end, an additional fit parameter (the Lagrange multiplier λ) is included in the fit for each constraint equation.

A.2 THE FITTING ALGORITHM

A least-squares fit estimates the value of the parameters describing the event. In the fit, a χ^2 function is minimized subject to the imposed constraints. The minimized function is:

$$\mathcal{F} = \sum \left(\frac{x_i - x_{pred}}{\sigma_i} \right)^2 + 2 \sum \lambda_j F_j, \qquad (A.1)$$

where the x_i are the measured track coordinates, the x_{pred} are the predicted coordinates for each track using the current set of fit parameters, the σ_i are the uncertainties associated with the x_i, the λ_j are the Lagrange multipliers, and the F_j are the constraint equations. The σ_i are convolutions of the measured coordinate uncertainties and the uncertainties in the predicted track positions resulting from multiple scattering. This method of including multiple scattering effects in the fit ignores the correlations between coordinates on each track but has been found to be adequate in most event topologies. An additional χ^2 term is added to $\mathcal{F}$ for each dipole-joined solenoid track so as to constrain the fitted track curvature to the dipole measured momentum.

The function $\mathcal{F}$ is minimized using a modified form of the Newton-Raphson algorithm, [85] which iterates the fit parameters towards a minimum of $\mathcal{F}$. This algorithm assumes that the initial fit parameters are close enough to the point where $\mathcal{F}$ has its minimum that a second-order Taylor series expansion of the function can be used to describe $\mathcal{F}$. The gradient and Hessian of $\mathcal{F}$ are evaluated analytically at the current point in parameter space, and are used to compute a new point in parameter space that is closer to the true minimum. This process is iterated until the resulting sequence of steps in the parameter space converges. The fitting algorithm is robust; it can successfully find the correct minimum even when the initial parameter values are far from the solution. Typically the fit converges within 3 to 4 iterations.

In cases where the current iteration does not appear to result in a step towards a true minimum of $\mathcal{F}$, the fit invokes a cut-stepping procedure that reduces the size of the step. In almost all such cases this simple strategy results in successful convergence after a few more iterations. The success of this approach is not due to the way the step is modified, but is due to the logic used to make the initial

decision to cut-step. Since the χ^2 of the fit has to be allowed to increase when the constraint equations are better satisfied, it is a careful balance of these two criteria that results in a stable iterative algorithm.

Once a fit converges, the χ^2 contribution of each coordinate is examined. If a contribution exceeds 12, the coordinate in question is removed from the track and the fit is again iterated until convergence is again reached. This culling of coordinates is repeated until all coordinate χ^2 contributions are less than 12, or more than five coordinates have been removed in which case the fit is considered to have failed.

There are a number of special circumstances that the fit has been designed to recognize.

1. On occasion the stepping procedure does not converge but oscillates around a poorly defined minimum point of $\mathcal{F}$. The fit recovers from such cases by judiciously cutting the step.
2. In situations when the fitted position of a decay vertex is near a chamber, the coordinates on the decay daughters are required to remain downstream of the decay vertex. In cases where the fitted vertex is stepped downstream of a daughter's coordinate, the coordinate is dropped from the fit.

A.3 CONSTRAINTS

There are three different types of constraints used in **MVFIT**; the geometry constraints which ensure that a V° points back correctly, the V° mass constraints, and the kinematic constraints imposed at the primary or V^- vertex. Momentum conservation at a V^- vertex is enforced by the same set of constraint equations that is used to enforce 4-momentum conservation at the primary vertex in a kinematic fit (this has the unfortunate feature that one cannot do V^- fits with additional kinematic constraints at the primary vertex).

The V° pointing constraints are implemented by introducing into the fit three constraint equations with their corresponding Lagrange multipliers. The three

constraint equations are

$$\begin{aligned} F &= (X_v - X_p) - t_z^2 p_x \\ G &= (Y_v - Y_p) - t_z^2 p_y \\ H &= (Z_v - Z_p) - t_z^2 p_z; \end{aligned} \tag{A.2}$$

The vector $(p_x,\ p_y,\ p_z)$ is the momentum of the V° as calculated using the fit parameters describing the V° daughter tracks. The variable t_z is introduced as a free parameter in the fit and is equal to $\sqrt{d/P_{V^\circ}}$ upon convergence (d is the decay length of the V°). Physically, the constraints are satisfied when the vertex separation vector is parallel to the momentum vector of the V°. This particular formulation of the pointing constraints has two advantages. Firstly, it is symmetric in all coordinates. Secondly, it forces the correct ordering of the parent and V° decay vertex; *i.e.* the vertex separation vector and the V° momentum vector are forced to be parallel and *not* anti-parallel.

The V° mass constraint is imposed as an energy constraint at the V° decay vertex. It has the form

$$I = E_1 + E_2 - E_{12}, \tag{A.3}$$

where E_1, E_2, and E_{12} are the energies of the two daughter tracks and the V°, respectively, calculated using the assigned masses for the three particles; $I = 0$ implies that the fitted V° invariant mass equals the assigned mass for the V° decay.

The 4-momentum constraints at the primary (or V^-) vertex are simply the 4-momentum imbalance between the initial and final state particles.

A.4 INITIALIZATION

Since the fitting algorithm assumes that the initial fit parameters are near the point where $\mathcal{F}$ has a minimum, the initialization of the fit parameters requires some care.

The initial positions of the primary and secondary vertices are taken from the least-squares fit performed by **VRHUNT**. The initial helix track parameters are taken from the independent χ^2 fit of each track in the event reconstruction, suitably modified so that the parametrized track trajectories pass through their parent vertex position and a point midway along the original fitted trajectory (this

involves a slight adjustment of the initial track angles). The initial value for the track curvature is obtained from the helix fit.

The initialization of the V^- track parameters is complicated by the additional fit parameter S^{casc}. The initial values for the α and $1/p$ of the V^- are defined by the momentum sum of the charged and neutral daughter tracks. The V^- $1/p$ and the z-separation of the primary and V^- decay vertex (determined by **VRHUNT**) are used to initialize the V^- decay length S^{casc}; β is initialized by extrapolating the azimuthal direction of the V^- from the decay vertex back to the primary vertex. This initial set of V^- track parameters along with the primary vertex position defines the initial V^- decay vertex. The track parameters of the V^- charged daughter are then modified in the same way as the other charged track parameters to yield a reasonable initial trajectory for the daughter track.

The Lagrange multipliers are initialized to 0, as there is no *a priori* knowledge of the values they will assume in the fit. The t_z's for each V° vertex are initialized to $\sqrt{d/P_{V^\circ}}$ calculated from the initial V° vertex and daughter track parameters.

A.5 Performance For the $\bar{K}^\circ\pi^+\pi^-n$ Final State

There are several criteria that can be used to judge the performance of **MVFIT** for the reaction $K^-p \to \bar{K}^\circ\pi^+\pi^-n$: (a) the speed of the algorithm; (b) the fraction of events which fail to converge; and (c) the effect on resolution for the $\bar{K}^\circ\pi^+\pi^-$ final state.

The geometry fit to the $\bar{K}^\circ\pi^+\pi^-$ final state has 22 parameters (four charged tracks with three parameters each; two vertex positions with three parameters each; and three Lagrange multipliers and one t_z for the V° pointing constraints). This large number of parameters makes the calculation of the Hessian matrix costly for a typical event, so that the time needed to perform a fit is proportional to the number of iterations, with each iteration requiring ~30 msec. Figure A.1 shows the distribution of the number of iterations for data and Monte Carlo events satisfying the **MVFIT** strip requirements (see §5.2). The distribution shows a peak at three iterations, which is the minimum number of iterations allowed for any fit. The maximum allowed number of iterations is 20; the events which have not converged after 20 iterations are considered fit failures. The second peak at 5–7 iterations is a

result of the coordinate dropping procedure. [Some of the events converging in three iterations have coordinates with excessive χ^2 contributions. For these events, the offending coordinates are removed and the fit is then reiterated until convergence. Typically the fit converges within 2—3 additional steps thus yielding the satellite peaks in the iteration distributions.] The average number of iterations for the geometry fit is 4.8 for data events and 3.7 for Monte Carlo events; the respective average elapsed times on an IBM 3081K computer are approx 140 and 110 msec. This difference in time is due to the significant background contamination in the data sample at this stage of the analysis.

Monte Carlo studies indicate that the fraction of real $\bar{K}^\circ \pi^+\pi^- n$ events that fail to converge in the geometry fit is 0.7%. The K° mass-constrained fit and the 1-C fit have even lower failure rates of 0.2% and 0.4%, respectively. This smaller failure rate is surprising in that the latter two fits place additional constraints on the events. It arises from the way in which the latter two fits are initialized: Regardless of whether the geometry fit converges, the results of this fit are used to initialize the K° mass-constrained fit. The results of the K° fit are then used to initialize the 1C-fit. Effectively, this increases the chances of the latter two fits converging immediately and not failing as a result of exceeding the maximum number of iterations.

The improvement in resolution due to **MVFIT** is significant for events with one or more badly measured tracks, but is less dramatic for well-reconstructed events. In terms of vertex position resolution, the quantity that shows the most improvement is the transverse position of the V° decay vertex. Figure A.2 shows the **MVFIT** resolution of the K° vertex x position and compares it with the resolution of the **VRHUNT** vertex measurement. The improvement of $\sim 50\%$ in resolution is due to the pointing constraint on the K° in **MVFIT**. The resolutions of the other vertex parameters improve by $\sim 10\%$ because of the fitting.

The momentum resolution of the most poorly measured tracks in the event improves substantially because of the effective increase in lever-arm when all primary tracks are constrained to come from a common vertex upstream of the first measured points on the track. This makes a small improvement in the invariant mass resolution; however, for the $\bar{K}^\circ \pi^+\pi^- n$ analysis, this is of only marginal benefit

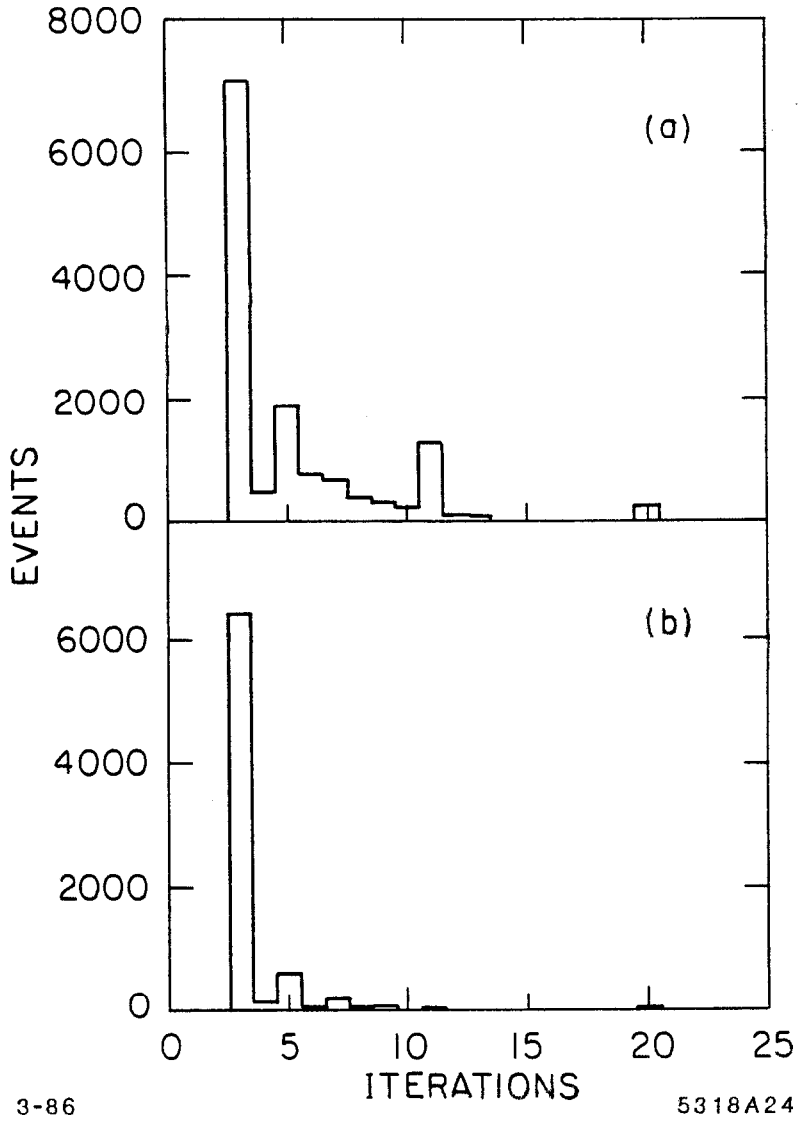

Figure A.1. The number of iterations for the geometry fit. The iteration distribution for data from the **MVFIT** strip is shown in (a); (b) shows the corresponding distribution obtained from Monte Carlo events.

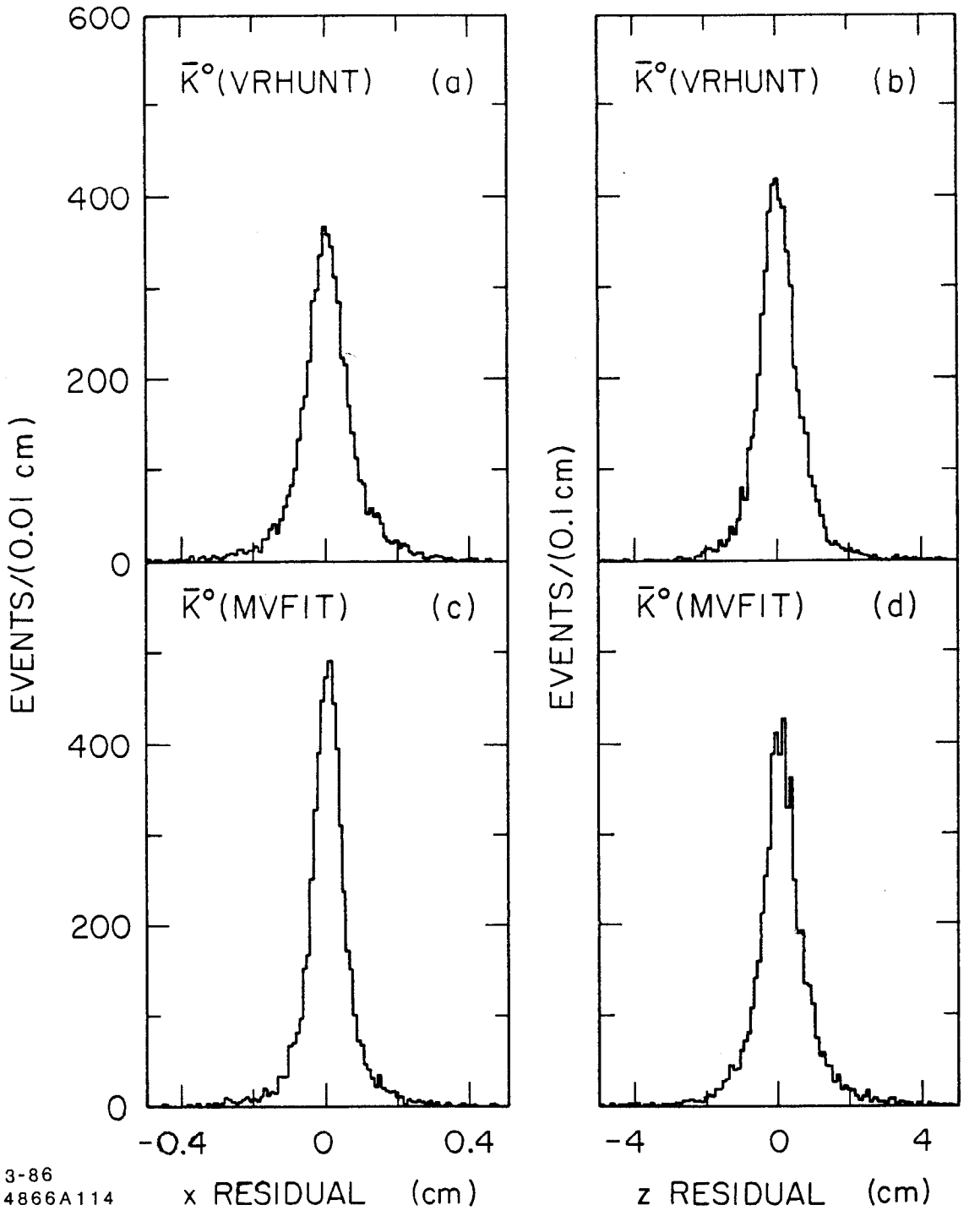

Figure A.2. The **MVFIT** K° vertex resolution. The distributions of the x and z residuals of the K° vertex determined by **VRHUNT** are shown in (a) and (b); the corresponding residual distributions from **MVFIT** are shown in (c) and (d).

since a resolution cut to remove events with such marginal tracks is still required to avoid contamination in the neutron sample.

Appendix B. The Partial Wave Set

Subsection 6.2.2 describes the criteria used to form the list of possible partial waves employed in the analysis. The resulting wave set, which has 99 $\eta+$ waves and 85 $\eta-$ waves, is listed below.

$\kappa(1300)$

$J=0$	$J=1$	$J=2$	$J=3$	$J=4$
$0^-0^+\kappa S$	$1^+0^+\kappa P$	$2^-0^+\kappa D$	$3^+0^+\kappa F$	$4^-0^+\kappa G$
	$1^+1^+\kappa P$	$2^-1^+\kappa D$	$3^+1^+\kappa F$	
	$1^+1^-\kappa P$	$2^-1^-\kappa D$	$3^+1^-\kappa F$	
		$2^-2^+\kappa D$	$3^+2^+\kappa F$	
		$2^-2^-\kappa D$	$3^+2^-\kappa F$	

$\epsilon(1250)$

$J=0$	$J=1$	$J=2$	$J=3$	$J=4$
$0^-0^+\epsilon S$	$1^+0^+\epsilon P$	$2^-0^+\epsilon D$	$3^+0^+\epsilon F$	$4^-0^+\epsilon G$
	$1^+1^+\epsilon P$	$2^-1^+\epsilon D$	$3^+1^+\epsilon F$	
	$1^+1^-\epsilon P$	$2^-1^-\epsilon D$	$3^+1^-\epsilon F$	
		$2^-2^+\epsilon D$	$3^+2^+\epsilon F$	
		$2^-2^-\epsilon D$	$3^+2^-\epsilon F$	

$K^*(892)$

$J=0$	$J=1$	$J=2$	$J=3$	$J=4$
$0^-0^+K^*P$	$1^+0^+K^*S$	$2^-0^+K^*P$	$3^+0^+K^*D$	$4^-0^+K^*F$
	$1^+0^+K^*D$	$2^+0^-K^*D$	$3^-0^-K^*F$	$4^+0^-K^*G$
	$1^-0^-K^*P$	$2^-1^+K^*P$	$3^-1^+K^*F$	$4^+1^+K^*G$
	$1^+1^+K^*S$	$2^+1^+K^*D$	$3^+1^+K^*D$	$4^+1^-K^*G$
	$1^+1^+K^*D$	$2^-1^-K^*P$	$3^-1^-K^*F$	$4^+2^+K^*G$
	$1^-1^+K^*P$	$2^+1^-K^*D$	$3^+1^-K^*D$	$4^+2^-K^*G$
	$1^+1^-K^*S$	$2^-2^+K^*P$	$3^-2^+K^*F$	
	$1^+1^-K^*D$	$2^+2^+K^*D$	$3^+2^+K^*D$	
	$1^-1^-K^*P$	$2^-2^-K^*P$	$3^-2^-K^*F$	
		$2^+2^-K^*D$	$3^+2^-K^*D$	

$\rho(770)$

$J=0$	$J=1$	$J=2$	$J=3$	$J=4$
$0^-0^+\rho P$	$1^+0^+\rho S$	$2^-0^+\rho P$	$3^+0^+\rho D$	$4^-0^+\rho F$
	$1^+0^+\rho D$	$2^+0^-\rho D$	$3^-0^-\rho F$	$4^+0^-\rho G$
	$1^-0^-\rho P$	$2^-1^+\rho P$	$3^-1^+\rho F$	$4^+1^+\rho G$
	$1^+1^+\rho S$	$2^+1^+\rho D$	$3^+1^+\rho D$	$4^+1^-\rho G$
	$1^+1^+\rho D$	$2^-1^-\rho P$	$3^-1^-\rho F$	$4^+2^+\rho G$
	$1^-1^+\rho P$	$2^+1^-\rho D$	$3^+1^-\rho D$	$4^+2^-\rho G$
	$1^+1^-\rho S$	$2^-2^+\rho P$	$3^-2^+\rho F$	
	$1^+1^-\rho D$	$2^+2^+\rho D$	$3^+2^+\rho D$	
	$1^-1^-\rho P$	$2^-2^-\rho P$	$3^-2^-\rho F$	
		$2^+2^-\rho D$	$3^+2^-\rho D$	

$\omega(783)$

$J=0$	$J=1$	$J=2$	$J=3$	$J=4$
$0^-0^+\omega P$	$1^+0^+\omega S$	$2^+0^-\omega D$	$3^-0^-\omega F$	$4^+0^-\omega G$
	$1^-0^-\omega P$	$2^+1^+\omega D$		
		$2^+1^-\omega D$		

$K^*(1430)$

$J=1$	$J=2$	$J=3$	$J=4$
$1^+0^+K^{**}P$	$2^-0^+K^{**}S$	$3^+0^+K^{**}P$	$4^-0^+K^{**}D$
$1^+1^+K^{**}P$	$2^-0^+K^{**}D$	$3^-0^-K^{**}D$	$4^+0^-K^{**}F$
$1^+1^-K^{**}P$	$2^+0^-K^{**}P$	$3^-1^+K^{**}D$	$4^+1^+K^{**}F$
$1^-0^-K^{**}D$	$2^+1^+K^{**}P$	$3^+1^+K^{**}P$	$4^+1^-K^{**}F$
$1^-1^+K^{**}D$	$2^-1^+K^{**}S$	$3^-1^-K^{**}D$	$4^+2^+K^{**}F$
$1^-1^-K^{**}D$	$2^-1^+K^{**}D$	$3^+1^-K^{**}P$	$4^+2^-K^{**}F$
	$2^+1^-K^{**}P$	$3^-2^+K^{**}D$	
	$2^-1^-K^{**}S$	$3^+2^+K^{**}P$	
	$2^-1^-K^{**}D$	$3^-2^-K^{**}D$	
	$2^+2^+K^{**}P$	$3^+2^-K^{**}P$	
	$2^-2^+K^{**}S$		
	$2^-2^+K^{**}D$		
	$2^+2^-K^{**}P$		
	$2^-2^-K^{**}S$		
	$2^-2^-K^{**}D$		

$f(1270)$

$J=1$	$J=2$	$J=3$	$J=4$
1^+0^+fP	2^-0^+fS	3^+0^+fP	4^-0^+fD
1^+1^+fP	2^-0^+fD	3^-0^-fD	4^+0^-fF
1^+1^-fP	2^+0^-fP	3^+1^+fP	4^+1^+fF
1^-0^-fD	2^+1^+fP	3^-1^+fD	4^+1^-fF
1^-1^+fD	2^-1^+fS	3^+1^-fP	4^+2^+fF
1^-1^-fD	2^-1^+fD	3^-1^-fD	4^+2^-fF
	2^+1^-fP	3^+2^+fP	
	2^-1^-fS	3^-2^+fD	
	2^-1^-fD	3^+2^-fP	
	2^+2^+fP	3^-2^-fD	
	2^-2^+fS		
	2^-2^+fD		
	2^+2^-fP		
	2^-2^-fS		
	2^-2^-fD		

REFERENCES

1. J.J. Aubert et al., Phys. Rev. Lett. **33**, 1404 (1974).
2. J.-E. Augustin et al., Phys. Rev. Lett. **33**, 1406 (1974).
3. T. Applequist and H.D. Politzer, Phys. Rev. Lett. **34**, 43 (1975).
4. E. Eichten et al., Phys. Rev. Lett. **34**, 369 (1975).
5. A. De Rujula, H. Georgi, and S.L. Glashow, Phys. Rev. **D12**, 147 (1975).
6. There are several papers on this subject. See, for example:
   E. Eichten et al., Phys Rev. **D 17**, 3090 (1978);
   T. Applequist, R.M. Barnett, and K.D. Lane, Ann. Rev. Nucl. Sci. **28**, 387 (1978); and
   W. Buchmuller and S.-H. H. Tye, Phys. Rev. **D24**, 132 (1981).
7. P.G.O. Freund and Y. Nambu, Phys. Rev. Lett. **34**, 1646 (1975).
8. J.F. Donoghue, presented at the International Europhysics Conference, Bari, Italy, 1985.
9. There is an extensive literature on this subject. Some of the more recent work has been discussed by:
   J.F. Donoghue, in Hadron Spectroscopy- 1985, edited by S. Oneda (American Institute of Physics, New York, 1985), p. 460.
   In addition, see the citations in Ref. 10.
10. S. Godfrey and N. Isgur, Phys. Rev. **D32**, 189 (1985).
11. Particle Data Group, Rev. Mod. Phys **56** (1984).
12. R. Kokoski and N. Isgur, University of Toronto preprint UTPT-85-05 (1985).
13. W.E. Cleland et al., Nucl. Phys. **B208**, 189 (1982).
14. Yu. Antipov et al., Nucl. Phys. **B86**, 365 (1975).
15. G. Otter et al., Nucl. Phys. **B93**, 365 (1975).
16. T. Tovey et al., Nucl. Phys. **B95**, 109 (1975).
17. G.W. Brandenburg et al., Phys. Rev. Lett. **36**, 703 (1976).
18. R.K. Carnegie et al., Nucl. Phys. **B127**, 509 (1977).
19. C. Daum et al., Nucl. Phys. **B187**, 1 (1981).
20. P. Estabrooks et al., Nucl. Phys. **B133**, 490 (1978).
21. D. Aston et al., Phys. Lett. **106B**, 235 (1981).

22. D. Aston et al., Nucl. Phys. **B247**, 261 (1983).
23. M. Baubillier et al., Nucl. Phys. **B202**, 21 (1982).
24. A. Etkin et al., Phys. Rev. **D22**, 42 (1980).
25. E. Konigs et al., Phys. Lett. **74B**, 282 (1978).
26. J.S.M. Vergeest et al., Phys. Lett. **62B**, 471 (1976).
27. D. Aston et al., The LASS Spectrometer, SLAC-REP-298, May 1986.
28. F.C. Winkelmann, Design and Operation of SLAC Beam Line 20-21-22, SLAC-REP-160, April 1973.
29. S. Suzuki, "Summary on Tau Calibration," SLAC Group B Analysis Memo, 1979 (unpublished).
30. G.Aiken et al., Design and Performance of the New Cathode Readout Proportional Chambers in LASS, SLAC-PUB-2642, 1980.
31. L. Bird et al., Nucl. Instrum. Methods **166**, 155 (1979).
32. B.Bertolucci, SLAC-PUB-1574, May 1975.
33. R. Fall, P. Kunz, and S. Shapiro, "Trigger Rate Equalizer," SLAC Group B Memo (unpublished).
34. Ilse Denecke, An Introduction to SLAC's Real Time System, SLAC SCS Real Time Note No. 1, Sept. 1974.
35. G. Oxoby, "Arbola" SLAC Branch Driver for PDP-11, SLAC-TN-76-3, (1976).
36. D. Horelick, IEEE Trans. Nucl. Sci. **NS22**, 517 (1975).
37. M. Breidenbach et al., A Semi-Autonomous Controller for Data Acquisition, The Brilliant ADC, SLAC-PUB-2032, 1977.
38. P.F. Kunz, Nucl. Instrum. Methods **135**, 435 (1976);
    P.F. Kunz, R. Fall, M. Gravina, and H. Brafman, "The Lass Hardware Processor," in Proceedings of the 11th Annual Microprogramming Workshop, SIGMICRO Newsleter **9**, 25 (1978);
    P.F. Kunz et al., "Experience Using the 168/E Microprocessor for Off-Line Data Analysis," IEEE Trans. Nucl. Sci. **NS-27**, 582 (1980).
39. G. Oxoby, L. Levinson, and Q. Trang, "The Bermuda Triangle, A Subsystem of the 168/E Interface Scheme Used by Group B at SLAC, SLAC-TN-79-007

(1979).

40. W.H.Barkas and M.J.Berger, Tables of Energy Losses and Ranges of Heavy Charged Particles, NASA-SP-3013 (1964).
41. V. Flaminio et al., Compilation of Cross Sections I: π^+ and π^- Induced Reactions, CERN-HERA-83-01, 1983.
42. V. Flaminio et al., Compilation of Cross Sections II: K^+ and K^- Induced Reactions, CERN-HERA-83-02, 1983.
43. V. Flaminio et al., Compilation of Cross Sections III: p and $\overline{p}$ Induced Reactions, CERN-HERA-84-01, 1984.
44. M. Roos et al, Phys. Lett. **111B**, 1 (1982).
45. P.M. Ferran et al., The 3081/E Emulator, A Processor for Use in On-Line and Off-Line Arrays, SLAC-PUB-3753, 1985.
46. G. Ascoli et al., Phys. Rev. Lett. **25**, 962 (1970).
47. G. Ascoli et al., Phys. Rev. **D7**, 669 (1973).
48. R.S. Longacre et al., Phys. Lett. **55B**, 415 (1975).
49. J.D. Hansen et al., Nucl. Phys. **B81**, 403 (1974).
50. R.J. Cashmore, "Amplitude Analysis in Three Body Final States" in 14th Scottish Universities Summer School in Physics (1973).
51. G.T. Jones, "Three Meson Partial Wave Analysis-Theory" in Daresbury Study Weekend Series #8 DL/R34, edited by J.B. Dainton and A.J.G. Hey (1975).
52. D.J. Herndon, P. Soding, and R.J. Cashmore, Phys. Rev. **D11**, 3165 (1975).
53. R.J. Cashmore, "Sources of Incoherence in 3-Body Partial Wave Analysis," in Daresbury Study Weekend Series #8 DL/R34, edited by J.B. Dainton and A.J.G. Hey (1975).
54. D. Aston, T.A. Lasinski, and P.K. Sinervo, SLAC-REP-287 (1985).
55. M.E. Rose, Elementary Theory of Angular Momentum, (Wiley, New York, 1957), p. 52.
56. J.M. Blatt and V.F. Weisskopf, Theoretical Nuclear Physics, (Wiley, New York, 1952), p. 361.
57. J. D. Jackson, Nuovo Cimento **34**, 1144 (1964).

58. W. Dunwoodie et al., Group B Physics Note # 60 (unpublished).
59. P. Estabrooks et al., Nucl. Phys. **B95**, 322 (1975).
60. M. Roos, Nucl. Phys. **B97**, 165 (1975).
61. I.J.R. Aitchison, "Corrections to the Isobar Model for Three Hadron Final States," in Daresbury Study Weekend Series #8 DL/R34, edited by J.B. Dainton and A.J.G. Hey (1975).
62. G. Ascoli and H.W. Wyld, Phys. Rev. **D12**, 43 (1975).
63. Y. Goradia and T.A. Lasinski, Phys. Rev. **D15**, 220 (1977).
64. R.L. Schult and H.W. Wyld, Phys. Rev. **D16**, 62 (1977).
65. C. Daum et al., Nucl. Phys. **B182**, 269 (1981).
66. A good review of the Deck model is:
E.L. Berger, "A Critique of the Reggeized Deck Model" in Daresbury Study Weekend Series #8 DL/R34, edited by J.B. Dainton and A.J.G. Hey (1975).
67. J. Orear, "Notes on Statistics for Physicists," Revised, CLNS-82/511, July 1982.
68. G.W. Brandenburg, SLAC Group B Internal Physics Memo # 57 (1974).
69. S. Hagopian et al., Phys. Rev. Lett. **25**, 1050 (1970).
70. B.N. Ratcliff et al., Phys. Lett. **38B**, 345 (1972).
71. D.T.Gillespie, Ph.D. thesis, Johns Hopkins University, 1968.
72. P.H. Eberhard and W.O. Koellner, Comp. Phys. Commun. **3**, 296 (1972).
73. T.G. Trippe et al., Rev. Mod. Phys. **48**, S1 (1976).
74. A. Bradley, J. Phys. **G4**, 1517 (1978).
75. E. Eichten et al., Phys. Rev. **D21**, 203 (1980).
76. S.B. Gerasimov et al., Z. Phys. **C13**, 43 (1982).
77. M. Atkinson et al., Nucl. Phys. **B243**, 269 (1984).
78. M. Frank and P.J. O'Donnell, Phys. Lett. **159B**, 174 (1985).
79. H.J. Lipkin, Argonne National Laboratory preprint ANL-HEP-PR-85-125 (1985).
80. C. Edwards et al., Phys. Rev. Lett. **48**, 70 (1982).
81. H.J. Schnitzer, Phys. Lett. **134B**, 253 (1985);
H.J. Schnitzer, Phys. Lett. **149B**, 409 (1985); and

H.J. Schnitzer, in Hadron Spectroscopy- 1985, edited by S. Oneda (American Institute of Physics, New York, 1985), p. 404.

82. S. Godfrey, in Hadron Spectroscopy- 1985, edited by S. Oneda (American Institute of Physics, New York, 1985), p. 262.
83. C.B.Chiu, Annu. Rev. Nucl. Sci. **22**, 255 (1972).
84. J.Tran Thanh Van, in Proceedings of the Sixth Rencontre de Moriond, 13-19 March 1971.
85. M.G. Kendall and A. Stuart,The Advanced Theory of Statistics, Vol. 2, 4th ed. (Macmillan, New York, 1977).